Renormalization group approach to strongly correlated and coherently driven open quantum systems

Von der Fakultät für Mathematik, Informatik und Naturwissenschaften der RWTH Aachen University zur Erlangung des akademischen Grades eines Doktors der Naturwissenschaften genehmigte Dissertation

vorgelegt von

Valentin Bruch, M. Sc.

aus Mörfelden-Walldorf

Berichter:	Univ.-Prof. Dr. rer. nat. Dante M. Kennes apl. Prof. Dr. rer. nat. Maarten R. Wegewijs
Tag der mündlichen Prüfung:	8. Mai 2023

Diese Dissertation ist auf den Internetseiten der Universitätsbibliothek verfügbar.

Abstract

In this thesis, we study open quantum systems in nonequilibrium with strong correlations and memory effects from two complementary views.

In the first part, we discuss the so-called fermionic duality relation, which can be used to simplify the description of the dynamics for a large class of fermionic models. Unlike ordinary symmetries, this relation connects the dynamics for different sets of parameters. We provide a new and simpler proof of this duality relation, which is also closer adapted to quantum information formulations of open system dynamics. This derivation highlights what prohibits or limits the generalization of the duality relation to transport observables and systems with time-dependent driving. For systems obeying ordinary symmetries associated with conservation laws, we focus on local states projected onto the symmetry sector. This projection simplifies the description of the dynamics in different formalisms, but excludes states that are entangled with some ancilla system. Applying the projection to the noninteracting resonant level model, we illustrate how it can significantly simplify the Kraus operator sum form and how the combination with fermionic duality leads to further restrictions on the dynamics.

The main part of this thesis discusses the concrete solution of the strongly correlated problem of the isotropic spin-$\frac{1}{2}$ Kondo model with time-periodic bias voltage at zero temperature. We use a recent nonequilibrium renormalization group (RG) method combined with Floquet theory to incorporate the interplay of strong correlations and coherent driving. We show in line with an experiment that such an approach is necessary for a quantitative description of transport properties by comparing our results to the simple phenomenological picture of photon-assisted tunneling, which underestimates decoherence, and to the adiabatic limit. Our findings show excellent quantitative agreement with experiments, which find side peaks of the Kondo resonance in the differential conductance. These side peaks are not completely washed out by the decoherence induced by the driving except at low driving frequency, and we predict these peaks to be sharper when the coupling to the reservoirs is asymmetric. To analyze memory effects for strong and fast harmonic driving in detail, we discuss the response to short voltage pulses. The time-resolved current after such pulses shows memory effects that arise from correlations between the two reservoirs, which are generated through the coupling to a quantum dot in the Kondo limit.

This solution of the driven Kondo model is based on the *E*-flow scheme of the real-time RG method, which we combine with a Floquet representation. This method is applicable to small open quantum systems with time-periodic external driving. Based on a perturbative expansion in the coupling between the system and the reservoirs, the real-time RG sums up large classes of terms in the coupling expansion in a self-consistent way. We provide a detailed derivation of the RG equations for a general fermionic cotunneling Hamiltonian before applying these equations to the isotropic spin $\frac{1}{2}$ Kondo model up to next-to-leading order in the renormalized coupling. We also discuss the convergence of the expansion in the coupling, numerical approximations, and subtleties arising in calculations with Floquet matrices.

Zusammenfassung

In dieser Arbeit untersuchen wir offene Quantensystem im Nichtgleichgewicht mit starken Korrelationen und Gedächtniseffekten aus zwei sich ergänzenden Blickwinkeln.

Im ersten Teil betrachten wir eine sogenannte fermionische Dualitätsrelation, welche in einer großen Klasse fermionischer System genutzt werden kann, um die Beschreibung der Dynamik zu vereinfachen. Anders als gewöhnliche Symmetrien verbindet diese Dualitätsrelation die Dynamik für unterschiedliche Systemparameter. Wir zeigen einen neuen und einfacheren Beweis dieser Relation, der zugleich besser an Beschreibungweisen offener Systeme aus dem Bereich der Quanteninformation angepasst ist. Diese Herleitung macht deutlich, was die Verallgemeinerung hin zu Transportobservablen und zeitlich getriebenen Systemen verhindert oder beschränkt. Für Systeme, die gewöhnliche, mit Erhaltungsgrößen assoziierte Symmetrien beachten, fokussieren wir uns auf lokale Zustände, die auf den Symmetriesektor projiziert sind. Diese Projektion vereinfacht die Beschreibung der Dynamik in verschiedenen Formalismen, schließt jedoch Zustände aus, die mit einem Hilfssystem verschränkt sind. Indem wir die Projektion auf das Modell einer nicht wechselwirkenden, an Reservoire gekoppelten Fermionmode anwenden, zeigen wir, wie sich die Kraus-Operatorsummenform signifikant vereinfacht und wie die Kombination mit der fermionischen Dualitätsrelation zu weiteren Beschränkungen für die Dynamik führt.

Der Hauptteil dieser Arbeit befasst sich mit der konkreten Lösung des stark korrelierten Problems des isotropen Spin-$\frac{1}{2}$ Kondomodells mit zeitperiodischer Spannung zwischen den Reservoirs bei verschwindender Temperatur. Wir nutzen eine moderne Renormierungsgruppenmethode (RG) für Systeme im Nichtgleichgewicht kombiniert mit Floquettheorie, um das Zusammenspiel von starken Korrelationen und kohärentem Treiben zu berücksichtigen. Wir zeigen in Übereinstimmung mit einem Experiment, dass ein solcher Ansatz für eine quantitative Beschreibung von Transporteigenschaften notwendig ist. Hierzu vergleichen wir unsere Ergebnisse mit einem einfacheren phenomenologischen Bild von Photon-assistiertem Tunneln, welches die Dekohärenz unterschätzt, sowie mit dem adiabatischen Grenzfall. Unsere Resultate zeigen exzellente quantitative Übereinstimmung mit Experimenten, welche Nebenmaxima der Kondoresonanz in der differenziellen Leitfähigkeit finden. Diese Nebenmaxima werden durch Dekohärenz resultierend aus dem periodischen Treiben nicht vollständig verwischt, mit Ausnahme niedriger Frequenzen. Wir erwarten, dass eine asymmetrische Kopplung zu den Reservoirs diese Nebenmaxima schärfer werden lässt. Um Gedächtniseffekte bei schnellem, starken harmonischem Treiben im Detail zu analysieren, betrachten wir die Antwort des Systems auf kurze Spannungspulse. Der zeitlich aufgelöste Strom nach einem solchen Puls zeigt Gedächtniseffekte, welche aus der Korrelation zwischen den beiden Reservoirs hervorgehen, die allein durch die Kopplung der Reservoire zu einem Quantenpunkt im Kondoregime ensteht.

Die Lösung des getrieben Kondomodells basiert auf der *E*-Fluss-Variante der Realzeit-RG, welche wir mit einer Floquetdarstellung kombinieren. Diese Methodik ist auf kleine, offene Quantensysteme mit zeitperiodischem externem Treiben anwendbar. Basierend auf einer Störungsentwicklung in der Kopplung zwischen System und Reservoirs, summiert die Realzeit-RG

große Klassen von Termen der Störungsreihe selbstkonsistent auf. Wir zeigen detailliert die Herleitung der RG-Gleichungen für einen allgemeinen, fermionischen Hamiltonoperator für Kotunnelkopplung, bevor wir diese Gleichungen auf das isotrope Spin-$\frac{1}{2}$-Kondomodell mit einer Entwicklung bis in die nachführende Ordnung in der renormierten Kopplung anwenden. Wir besprechen darüberhinaus die Konvergenz der Entwicklung in der Kopplung, numerische Approximationen, sowie Feinheiten beim Rechnen mit Floquetmatrizen.

Contents

1. Introduction

The physics of small quantum systems that are correlated with surrounding reservoirs fascinates researchers for many decades. With the advancements of quantum technology and nanoelectronics the understanding of such systems gains more and more importance. But the theoretical description of correlated quantum systems in a nonequilibrium setup often requires specialized tools. In this thesis, we will look at two tools which can simplify or completely describe open systems with strong quantum correlations.

1.1. Quantum dots

This thesis deals with theoretical methods to describe the dynamics of so-called quantum dot systems. Modern experimental techniques allow confining electrons in small, ultracold and highly controllable regions. For example, in a two-dimensional electron gas in semiconductors, electrodes can serve as separators that create a potential barrier between a small region — the dot — and the surrounding area. These dots act like zero-dimensional quantum systems with discrete energy levels [4–9]. Quantum dots with similar properties have also been realized in carbon nanotubes [10–15], individual molecules [16–19], and two-dimensional materials like graphene [20–29]. As highly controllable quantum devices, quantum dots have interesting applications as electron pumps [30–35] and single-electron sources [36–40], in electron detection [41], and in quantum computing [42]: Qubits encoded in states of a quantum dot are a promising platform on the way towards large scale quantum computation [42–46].

What makes quantum dots physically very interesting is their coupling to a dissipative environment. Here we focus on the coupling to metallic leads. In a two-dimensional electron gas, these leads can be large confined clouds of electrons, which are connected to macroscopic leads. At low temperature, the coupling to these electron reservoirs leads to fascinating quantum many-body effects such as the Kondo effect. The coupling to leads makes it possible to create a nonequilibrium state by applying a bias voltage, and to measure the charge current through the dot.

A quantum dot can often be modeled as a very simple quantum system. One can typically write down a simple-looking Hamiltonian for the quantum dot, the reservoirs, and the coupling between the dot and the reservoirs. Although it is formally well known how to compute from this Hamiltonian the dynamics and transport properties by integrating out the reservoirs [47–55], actually preforming the calculation quickly becomes very complicated. This is especially true for the interesting low-energy physics of quantum dots. Near equilibrium at very low temperature, many details of the physical realization of a quantum dot become unimportant or can be reduced to a simple-looking effective low-energy model. For the case of a small quantum dot with odd occupation number tunnel-coupled to two metallic leads, this goes so far that the low-energy

physics can be described by an effective model — the Kondo model — in which a characteristic energy scale called Kondo temperature (T_K) is the only remaining parameter characterizing the quantum dot. Thus, independent of the physical realization of the quantum dot, it will show precisely the same low-energy physics and a physical observable like the differential conductance will always follow the same universal function of T/T_K where T is the temperature of the reservoirs. This universality implies a broad applicability of the low-energy physics of a single model to many physical realizations. However, when a finite bias voltage brings the system out of equilibrium, advanced methods are required to find the universal dependence of observables such as the current on the voltage. One such method and its results will be discussed in chapters 3–6. We use units $\hbar = k_B = e = 1$ such that temperature, voltage and inverse time become directly comparable energy scales, for which the Kondo temperature marks the typical order of magnitude.

1.2. Open quantum systems

As already indicated, quantum dots can be considered open quantum systems in which a small local quantum system is coupled to a large environment consisting of electron reservoirs. To benefit from the separation of local quantum system and reservoirs, we assume that at some initial time t_0 the quantum dot is decoupled from the reservoirs and each reservoir is separately in a thermal equilibrium state. At time t_0, the coupling between the quantum dot and the reservoirs is switched on and the time evolution begins. But in contrast to the typical situation in closed quantum systems, we are only interested in the dynamics of the quantum dot and in transport properties, not in the full state of the total system. When describing the dynamics, we want to know the reduced state of the local system $\rho(t) = \mathrm{tr}_R\, \rho^{\mathrm{tot}}(t)$ instead of the total system state $\rho^{\mathrm{tot}}(t)$. Here tr_R denotes the trace over the reservoirs, which turns an infinitely large density matrix into a small, physically understandable matrix.

The main question in open system dynamics is thus how a given initial state $\rho(t_0)$ of the local system will evolve in time. In the language of open quantum systems, we answer this question by thinking of density matrices $\rho(t)$ as elements of the Liouville space, the vector space of operators acting on the underlying Hilbert space relevant to closed-system quantum mechanics[1]. The Liouville space is equipped with the Hilbert-Schmidt scalar product $(a, b) \coloneqq \mathrm{tr}(a^\dagger b)$ for elements a, b of the Liouville space, and thereby also becomes a Hilbert space [56]. We can therefore define linear maps on the Liouville space, for which we can use the well-known calculation rules for operators on a Hilbert space. These linear maps are called superoperators to distinguish them from the elements of the Liouville space — called operators — on which they act. In this framework, the time evolution is described by a superoperator $\Pi(t, t_0)$ which maps the state $\rho(t_0)$ to $\rho(t)$ and is called the propagator or dynamical map. Working only with the local state $\rho(t)$ on the quantum dot instead of the state of the full system including the reservoirs drastically reduces the state space and simplifies the computation of the dynamics. But this comes with

[1] Formally, for a given Hilbert space $\mathcal{H}$ the Liouville space contains all linear maps $a \in \mathcal{L}(\mathcal{H} \to \mathcal{H})$ for which $\mathrm{tr}(a^\dagger a) < \infty$. The latter restriction is irrelevant for the Liouville spaces considered in this thesis because those are finite-dimensional.

some new challenges, as we will see next.

The dynamical map contains all relevant information about the time evolution similar to the unitary evolution operator $U(t,t_0) = e^{-iH(t-t_0)}$ of a closed quantum system. However, in contrast to $U(t,t_0)$ the superoperator $\Pi(t,t_0)$ is not restricted to be unitary, which leads to a significant complication of calculations. For example, $\Pi(t,t_0)$ is in general not unitarily diagonalizable since it need not be normal[2]. When diagonalizing $\Pi(t,t_0)$, its left and right eigenvectors need to be computed separately, whereas in closed systems usually almost all operators are Hermitian or unitary. But in chapter 2 we will discuss a relation between $\Pi(t,t_0)$ and its adjoint which brings some simplifications of closed quantum systems to open systems.

The propagator is one way of describing the dynamics, but often one first calculates an effective Liouvillian $L(t,t_0)$, also called memory kernel. This superoperator lets us compute the time-derivative of a state in analogy to the Schrödinger equation [47, 48]:

$$\frac{d}{dt}\rho(t) = -i\int_{t_0}^{t} ds\, L(t,s)\,\rho(s). \tag{1.1}$$

In this equation, we see that the dynamics of the state at time t depends on the state at every earlier time $s < t$. Thus, there is some memory through which a state at an early time can directly influence what happens at a later time. The effective Liouvillian $L(t,s)$ describes how time s affects time t via physical processes such as electrons hopping between the system and the reservoirs. But when describing the total system as a closed quantum system, we do not see any memory in the Schrödinger equation. To understand the meaning of the memory, we recall that when reducing the total system state to the local state $\rho(t)$ we lose information. Most importantly, we discard all correlations between the system and the reservoirs or between different reservoirs. What appears as memory in an open system is information that is discarded in the open system description, although it remains relevant. Working with the state $\rho(t)$ of the local system instead of the total system state enormously simplifies calculations, but this comes at the cost that the dynamics at time t can only be inferred from the full history of the local state until t. Thus, we need to deal with memory in our description because we do not keep the full information of the total quantum state. At this point, one should remember that we have not made any approximation by using the local state with memory instead of the total state without memory.

Since the separation of local quantum system and reservoirs is not just a mathematical construction, the memory also has a physical meaning. In the presence of memory, time evolutions on the local system become possible that would not be allowed without correlations between the system and the reservoirs. In the case of time-dependent driving, we will see very explicitly in section 3.5 how the current at time t is influenced by the voltage at earlier times despite the presence of dissipation that tries to wipe out the memory. Memory effects indicate strong correlations between the system and the reservoirs or between different reservoirs, which significantly complicate the theoretical description. In some popular techniques for describing open quantum systems, the memory is completely neglected or the system of interest is approximated by a memoryless system. This is often legitimate because a system does not develop strong correlations, or because a finite reservoir temperature suppresses memory effects

[2] A linear map X is called normal if $X^\dagger X = XX^\dagger$.

on timescales longer than the inverse temperature. Complementary to such approaches, we focus on low temperatures and methods that can be used even in the presence of strong memory effects — for example in the Kondo model.

In open quantum systems driven out of equilibrium, transport properties are often of high interest [19, 57]. The current through a quantum dot in response to a bias voltage can be measured comparably easily and can signal interesting quantum effects such as the mentioned Kondo effect. While local observables like the magnetic susceptibility can be calculated using only the local state $\rho(t)$ on the quantum dot, this is not true for transport properties such as the current. To compute a nonlocal observable like the current in reservoir γ, one needs to calculate a current kernel $\Sigma_\gamma(t,s)$ which again includes memory. The current kernel is defined analogous to the effective Liouvillian, such that the current is

$$I^\gamma(t) = -i \int_{t_0}^{t} ds \ \mathrm{tr}\, \Sigma_\gamma(t,s)\, \rho(s). \tag{1.2}$$

Again, we need to use the history of the state $\rho(t)$ because the state at time t does not include all the information we need.

1.3. Renormalization group theories

A very successful idea in theoretical physics is the concept of renormalization. Various renormalization group methods have been developed since the 1960s and have greatly improved our understanding of many problems in different areas of physics. RG methods are designed for the description of quantum or classical systems, in which many degrees of freedom have significant influence on quantities of interest [58]. The key idea is to approach the solution of a problem by successively including these many degrees of freedom in an effective description. Thus, in an RG method we systematically discard individual degrees of freedom to simplify a model, but we approximately retain the effect of these discarded degrees of freedom on the remaining system in the effective description.

A descriptive example of an RG method is Kadanoff's blockspin method [59, 60], which aims to answer the question when an Ising model of classical spins on a lattice with nearest neighbor interaction becomes ferromagnetic. To reduce the number of degrees of freedom, one can coarse-grain the lattice by combining neighboring spins in blocks of 3^d spins in a d-dimensional lattice. After approximating that all spins within one block have the same value taken from a majority rule, one can treat the blocks like spins in a coarse-grained Ising model. With the involved approximations, the coarse-grained system after this RG step has the same form as the original system. By iterating this procedure, one can find an RG flow that brings the system to a ferromagnetic state with aligned spins or to a paramagnetic state. Thus, the collective phenomenon of ferromagnetism can be described although the degrees of freedom of the individual microscopic spins have been discarded by coarse graining. This ability to describe effects on different length scales makes RG methods helpful tools for the description of phase transitions [58, 61].

In this thesis, we will use an RG method to discuss the Kondo model, in which different energy scales play a role while we are only interested in a low-energy description. For such a

model, RG methods can be used that successively remove degrees of freedom at high energies, while including the effect of these degrees of freedom on the low-energy physics in an effective description. As a comparably simple example, we will review Anderson's poor man's scaling approach to the Kondo model in section 3.1.2. The concept of successively integrating out energy scales allows for the description of models in which very different energy scales play a significant role. This makes the RG not only well-suited for the Kondo problem and other problems in condensed matter physics [58, 62–64], but also for quantum field theories in particle physics [58, 65], where it was originally developed [66, 67]. The idea of renormalization has led to various RG methods that can be applied to many problems sharing the difficulty of many degrees of freedom that must be considered. This includes the numerical renormalization group [64, 68], the functional renormalization group [69–73], and the real-time renormalization group for quantum systems in nonequilibrium [53, 54, 74–76], which we will discuss in detail in chapters 4 and 5.

1.4. Time-dependent driving

Many intriguing quantum effects can be observed today in quantum materials and quantum dots. Various systems are engineered to study and control many-body effects that widen our physical understanding and may lead to new technological applications. One way of controlling quantum systems and creating new effects is fast periodic driving [77–80]. Materials can be modified by strong laser light [80] and quantum dots with interesting low-energy physics can be coupled to microwave cavities or can be directly driven by an oscillating bias voltage [18, 81–84]. Here we focus on periodically driven quantum dots in the Kondo regime, which have been realized in GaAs and a carbon nanotube with a Kondo temperature around 0.1 K to 1 K. Interesting driving effects are expected when the frequency of the external driving is of the same order, corresponding to 2 GHz to 20 GHz. A periodic voltage at such frequencies can be generated using microwave generators and applied directly to the reservoirs of a quantum dot.

A typical problem of many systems with strong external driving is the heating of the system. The external driving pumps energy into the system, heats the sample and thereby often destroys interesting quantum states, which rely on very low temperatures. But since it takes some time until the system is heated too much and quantum effects break down, for many systems there exists an accessible time interval of prethermalization after switching on the driving. During this time, the effect of the external driving on the quantum system and the emergence of new properties can be observed before the system thermalizes [80]. Heating and a limited prethermalization time are concerns in many systems with strong driving, but the model considered here has been realized in experiments which did not face this issue [82, 84]. The periodic driving is weak enough such that the power pumped into the system is small, and the large reservoirs can absorb this energy without heating up significantly.

1.5. Outline

As already indicated, this thesis mainly considers two topics concerning strongly coupled and correlated quantum dots. Chapter 2 introduces the open system transport theory and an exact

duality relation for a large class of fermionic open systems. A new proof of this duality relation is provided using a formalism that is more accessible from many common formulations of open system dynamics. We discuss superselection rules and conservation laws for open systems and combine these with the duality relation, illustrating the results using the resonant level model. The discussion of the duality relation is concluded by a brief overview of the method used in its original derivation.

Chapters 3–6 deal with the Floquet real-time renormalization group (FRTRG) applied to the Kondo model. In chapter 3 the Kondo model is introduced and the results of the FRTRG calculation are compared with experiments and more qualitative theoretical methods. The memory of a Kondo-correlated quantum dot is analyzed more in depth by computing the response current following a voltage pulse. This helps to understand the time-resolved current for strong periodic driving, which shows signatures of the strong correlations of the two reservoirs.

The method is explained in chapters 4 and 5. The concept of the FRTRG is introduced in chapter 4, where we consider a general cotunneling model. In chapter 5 the explicit RG equations for the Kondo model are derived and the initial conditions for the RG flow are explained.

Chapter 6 shows the convergence of the numerical results and some subtleties of the implementation. In the final chapter 7 we briefly summarize the main results and provide some ideas for possible follow-up research. An overview of the notation used throughout the thesis is provided in appendix K.

2. Fermionic duality

The analytic description of quantum systems often relies on symmetries and conservation laws, which simplify calculations and help understand physical results. In this chapter, we focus on a more abstract relation that simplifies calculations for many open fermionic quantum systems. This relation, called fermionic duality, is a connection between the physical system of interest and a dual system that is obtained by a parameter transform. Fermionic duality has been exploited in various setups of quantum dots with weak coupling to the reservoirs, where the dual system can help understand at first sight unintuitive effects in the physical system [85–92]. For strongly coupled systems with memory effects, fermionic duality provides a new and simple way of connecting the Schrödinger and Heisenberg picture, and can be used to construct nonperturbative approximations for the dynamics [2, 93].

Here we present a new and simpler derivation of this duality relation. This aims at facilitating the understanding of fermionic duality in different formalisms beyond its original derivation in Liouville space. We furthermore use symmetries and conservation laws to find simplified descriptions of the dynamics, for which we derive separate fermionic duality relations in different common formalisms for describing open system dynamics. The discussion of the fermionic duality relation builds upon the original derivation in Ref. [85] and its reformulation beyond weak coupling in Refs. [2, 93]. The results presented in section 2.4 have been published in Ref. [2].

2.1. Motivation and general duality relation

Fermionic duality is a valuable property of open quantum systems, which becomes useless and almost trivial in a closed system. But to understand its uncommon structure and to introduce the notation, it is helpful to first formulate it in a closed system, keeping in mind that essential simplifications of the closed system will not hold anymore in the open system case.

2.1.1. Closed system equivalent

To illustrate the concept of fermionic duality, we first consider a closed system with a constant Hamiltonian H. The evolution of a pure state $|\psi\rangle$ from time $t = 0$ to $t > 0$ is described by a unitary operator $U(t) = e^{-iHt}$. For a closed system, the duality relation states that the adjoint of the evolution is obtained by inverting the sign of all energies: $U(t)^\dagger = U(t)|_{H\mapsto -H}$. This provides a linear relation between $U(t)^\dagger$ and $U(t)$ by a parameter substitution in the energy operator H. This relation has implications for the spectral decomposition of $U(t)$. For every eigenvalue $u(t)$ of $U(t)$ also $u(t)^*|_{H\mapsto -H}$ is an eigenvalue of $U(t)$, and for every right eigenvector $|u(t)\rangle$ of $U(t)$ we know that $\langle u(t)|_{H\mapsto -H}$ is a left eigenvector of $U(t)$. However, for a closed system, this has no practical relevance because we know much more about the spectrum of $U(t)$ from the fact that

$U(t)$ is unitary. It is only for open quantum systems that a similar relation becomes interesting and can be used to simplify calculations.

A special feature of this duality relation is the parameter substitution. For closed systems, the sign of the Hamiltonian is inverted[1] and for open systems we will see that an even more precarious substitution arises. An obvious implication is that the relation is mostly useful for analytic calculations, in which parameters can easily be replaced. Physically, one can try to interpret the equations with substituted parameters as those of a dual system with different properties. Most importantly, in the dual system, all energies of the local system are inverted. However, we will see below that beyond weak coupling, this interpretation is limited because the dual system violates fundamental properties of open quantum systems. Importantly, this does not limit the practical usefulness of the fermionic duality relation, and we will use the term "dual system" to simplify the discussion, although this "system" is not physical.

2.1.2. Liouville space formulation

To understand the general duality relation, it is useful to first reformulate the closed system duality in Liouville space. We are interested in the time evolution of a density operator ρ describing the state of the system. In analogy to the operator $U(t)$, we construct a linear map $\Pi(t)$ which maps a density operator at the initial time $t = 0$ to the density operator at time $t > 0$.[2] This linear map is a superoperator, that is, it maps operators to operators. The vector space spanned by density operators on which $\Pi(t)$ acts is called Liouville space. In a closed system, we can explicitly write $\Pi(t) = U(t) \bullet U(t)^\dagger$ where $\bullet$ denotes the operator on which the linear map $\Pi(t)$ acts. In this case, the duality relation looks very similar to the relation for $U(t)$:

$$\Pi(t)^\dagger = \Pi(t)|_{H\mapsto -H}. \tag{2.1}$$

Here the adjoint of the superoperator $\Pi(t)$ is defined with respect to the Hilbert-Schmidt scalar product $(a|b) = \mathrm{tr}(a^\dagger b)$ in the usual way by $(a|\Pi(t)^\dagger|b) = [(b|\Pi(t)|a)]^*$ for all operators a, b. We use the Dirac notation in Liouville space with bras $(a| = \mathrm{tr}\, a^\dagger \bullet$, kets $|b) = b$, and superoperators acting on kets like $\Pi(t)|\rho(0))$ in analogy to the notation used for pure quantum states.

To understand why an equation of the form of Eq. (2.1) can be relevant, we note that for open quantum systems $\Pi(t)$ is in general not unitarily diagonalizable. Without fermionic duality, we do not have a simple connection between left and right eigenvectors of $\Pi(t)$. But to calculate the eigenmodes of the evolution and the amplitude of these modes depending on the initial state, we need both the left and right eigenvalues of $\Pi(t)$. For the generally complicated map $\Pi(t)$ the duality relation provides this connection between left and right eigenvectors and is thus a valuable unconventional symmetry.

[1] We only consider local systems with finite-dimensional Hilbert space, such that the spectrum of the local Hamiltonian is always bounded and the inversion of energies does not cause any problems.

[2] Compared to $\Pi(t, t_0)$ in section 1.2 we have set $t_0 = 0$ and dropped t_0 in the notation. In time-translation invariant systems as considered here, the argument t_0 is not needed because $\Pi(t, t_0)$ depends solely on the time difference $t - t_0$.

2.1.3. General duality relation

The general duality for the propagator was originally derived in Ref. [85] and we present a new proof in section 2.2.2. It holds for every system with finite-dimensional Hilbert space that is bilinearly coupled via energy-independent hopping to effectively noninteracting fermionic wideband reservoirs. These assumptions will be discussed in detail in section 2.2.1. We thus consider a local system with arbitrary Hamiltonian H_S coupled via a tunneling Hamiltonian H_V to electronic reservoirs at chemical potentials μ_α and temperatures T_α where α labels the reservoir. By μ we denote the vector of all chemical potentials. Furthermore, we introduce the notation Γ for the sum of all coupling rates contributing to the tunneling, and the superoperator $\mathcal{P} = (-\mathbb{1})^N \bullet$ for left multiplication with the fermion parity operator $(-\mathbb{1})^N$ where N is the number of electrons in the local system. With this notation, the general duality relation reads

$$\Pi(t; H_S, H_V, \mu)^\dagger = e^{-\Gamma t} \Pi(t; -H_S, iH_V, -\mu). \tag{2.2}$$

It expresses the adjoint of the propagator using a parameter substitution. To understand this parameter substitution, we need to think of the propagator as an analytic function of the vector μ and the matrices H_S and H_V (in some basis), or of the parameters appearing in H_S and H_V. Under the assumption that the propagator is an analytic function of these parameters, we can perform the parameter substitution $(H_S, H_V, \mu) \mapsto (-H_S, iH_V, -\mu)$, which maps the physical system to a dual system. We will denote quantities in this dual system with a bar, e.g., $\bar{\Pi}(t) = \Pi(t; -H_S, iH_V, -\mu)$. Due to the replacement $H_V \mapsto iH_V$ this dual system is not physical.[3] In section 2.3.4 we will see that it violates basic properties of open quantum systems. But this only limits the interpretation of the duality relation and not its usefulness in calculations. The duality relation holds in nonequilibrium, when different reservoirs have different chemical potentials and different temperatures, as long as all parameters are constant in time. The temperatures are not indicated in Eq. (2.2) because they remain unchanged in the transformation to the dual system.

2.2. Derivation of fermionic duality

The original derivation of fermionic duality in Ref. [85] used a renormalized perturbation theory based on second quantization in Liouville space, which will be briefly introduced in section 2.5. This derivation has the advantage that it is constructive because it proves that this specific renormalized perturbation theory obeys fermionic duality order by order. However, the derivation makes extended use of non-standard formulations of the dynamics in Liouville space and is not easily accessible for people not familiar with the field. The proof of fermionic duality presented here focuses on notation and methods known from standard quantum mechanics. This way, it also becomes clearer how the underlying assumptions are used and at which point

[3] In the weak coupling approximation, where only the leading order in the coupling Hamiltonian H_V is considered, the replacement $H_V \mapsto iH_V$ can be replaced by a simple sign change in the duality relation for the memory kernel and a physical dual system can be used [85]. But here we focus on the general case, allowing strong coupling and memory effects.

non-standard features arise. This is not only helpful for understanding the relation itself, but also necessary for potential extensions of the duality relation to an even broader class of systems.

2.2.1. Assumptions and Hamiltonians

Fermionic duality is an exact relation for a large class of open quantum systems. We consider an arbitrary local system with finite-dimensional Hilbert space described by a Hamiltonian H_S whose fermionic degrees of freedom obey the fermion superselection principle. The fermion superselection principle declares that there is no quantum superposition of states with even and odd number of fermions, i.e., $[\rho, (-\mathbb{1})^N] = 0$ for all physically allowed states ρ [94, 95]. Statistical mixtures of states with even and odd parity are allowed, as we will discuss in section 2.3.1. To ensure that this property is preserved, the local Hamiltonian must fulfill $[H_S, (-\mathbb{1})^N] = 0$.

The system is coupled to fermionic reservoirs, which are effectively noninteracting and described by the Hamiltonian

$$H_R = \sum_{\alpha k} (\varepsilon_{\alpha k} + \mu_\alpha) c^\dagger_{\alpha k} c_{\alpha k} = \sum_\alpha \int d\omega\, (\omega + \mu_\alpha) c^\dagger_{\alpha\omega} c_{\alpha\omega}. \tag{2.3}$$

Here $c^\dagger_{\alpha k}$ is the creation operator for an electron state with momentum k and energy $\varepsilon_{\alpha k}$. The index α is a multi-index in which we collect all other quantum numbers like the reservoir, band and spin index. For the following calculation, this allows us to ignore the spin of the fermions by treating fermions with different spins like particles from different reservoirs. In continuum notation we use the creation and annihilation operators $c^{(\dagger)}_{\alpha\omega}$ at energy ω, which are defined such that they fulfill

$$\{c_{\alpha\omega}, c^\dagger_{\alpha'\omega'}\} = \delta_{\alpha\alpha'}\delta(\omega - \omega'). \tag{2.4}$$

To obtain the continuum notation from the discrete momentum space formulation, we define the density of states $\varrho_\alpha(\omega) = \sum_k \delta(\omega - \varepsilon_k)$ and consider the continuum limit in which $\varrho_\alpha(\omega)$ can be approximated by a smooth function because the energy levels ε_k are sufficiently dense. Then the annihilation operators in continuum notation are[4] $c_{\alpha\varepsilon_k} = \sqrt{\varrho_\alpha(\varepsilon_k)}\, c_{\alpha k}$.

We now assume that the system is coupled to its reservoirs such that fermions can hop to and from the reservoirs,

$$H_V = \sum_{l\alpha k} \tilde{\tau}_{l\alpha k} d_l^\dagger c_{\alpha k} + \text{H.c.} = \sum_{l\alpha} \int d\omega\, \tau_{l\alpha} d_l^\dagger c_{\alpha\omega} + \text{H.c.}, \tag{2.5}$$

and we assume that the hopping in continuum notation $\tau_{l\alpha}(\varepsilon_k) = \tilde{\tau}_{l\alpha k}\sqrt{\varrho_\alpha(\varepsilon_k)}$ is energy-independent. Here l labels the fermion mode and spin on the local system. When studying low-energy physics,

[4] To show that this leads to the correct anticommutation relations, we consider for simplicity only a single reservoir. We consider an infinitesimal energy range $[\omega, \omega + d\omega)$ and choose as an ansatz for the annihilation operator on this interval $c'_\omega d\omega = \sum_k \Theta(\varepsilon_k - \omega)\Theta(\omega + d\omega - \varepsilon_k) c_k$. The number of states in this interval is $\varrho(\omega)d\omega = \sum_k \Theta(\varepsilon_k - \omega)\Theta(\omega + d\omega - \varepsilon_k)$ and for $d\omega \to 0$ we can write $c'_{\varepsilon_k} = \varrho(\varepsilon_k) c_k$. Computing the anticommutator for this ansatz for continuum creation and annihilation operators, we find that it takes the form of an infinitesimally broadened delta function: $\{c'_\omega d\omega, c'_{\omega'} d\omega'\} = \sum_k \Theta(\varepsilon_k - \omega)\Theta(\varepsilon_k - \omega')\Theta(\omega + d\omega - \varepsilon_k)\Theta(\omega' + d\omega' - \varepsilon_k) \approx \varrho(\omega) d\omega\, \delta_{d\omega'}(\omega - \omega') d\omega'$. Thus, to obtain the commutation relation (2.4) we need to define $c_\omega = c'_\omega / \sqrt{\varrho(\omega)}$ or $c_{\varepsilon_k} = \sqrt{\varrho(\varepsilon_k)}\, c_k$.

the assumption of energy-independent coupling is usually justified if both the coupling $\tilde{\tau}_{l\alpha k}$ and the density of states of the reservoirs $\varrho_\alpha(\varepsilon_{\alpha k})$ vary only on energy scales that are much larger than the energy scales relevant for the low-energy physics. In this case, both $\tilde{\tau}_{l\alpha k}$ and $\varrho_\alpha(\varepsilon_k)$ can be approximated by constants. An important quantity in the duality relation is the sum of all coupling rates, which is defined as $\Gamma = 2\pi \sum_{\sigma l\alpha} |\tau_{\alpha\sigma l}|^2$. In this definition, it is important to remember that we included the spin index in the multi-index α. For a system with spin-degenerate, electronic reservoirs, each reservoir contributes $4\pi|\tau_{l\alpha}|^2$ to Γ, including the sum over the spins.

Furthermore, we assume that at the initial time $t = 0$ all reservoirs are separately in equilibrium, each with its own temperature T_α and chemical potential μ_α. The state of the total system at initial time, $\rho_{\text{tot}}(0) = \rho(0) \otimes \rho_R^{\text{eq}}$, is given by an arbitrary initial state for the local system $\rho(0)$ and a grand canonical equilibrium state in each reservoir. The aim is to describe the evolution $\rho(t) = \operatorname{tr}_R \rho_{\text{tot}}(t) = \Pi(t)\rho(0)$ of the reduced state of the local system after the coupling between the system and the reservoirs is switched on at $t = 0$.

Finally, we still need to assume that a perturbative expansion of the evolution in the coupling H_V converges. This assumption is formally required because we use an expansion in the coupling in the proof, for which the duality does not hold in each order separately. However, it does hold order-by-order in a renormalized perturbation theory, which will be discussed in section 2.5. Since the renormalized perturbation theory sums up terms from bare perturbation theory in a clever order, it can be expected to converge at least as good as bare perturbation theory. The question of convergence can thus be answered best in renormalized perturbation theory and will not be addressed in the following derivation, which uses bare perturbation theory.[5]

2.2.2. Proof

In the following, we will prove the duality relation (2.2) in five steps for a time-translation invariant system. An analogous, more general and more detailed proof that also considers periodically driven systems can be found in appendix A. We start from the formal solution of the evolution of the total system including the reservoirs, using the unitary time evolution operator of the total system $U(t) = e^{-iH_{\text{tot}}t}$. The full propagator acting on an initial state denoted by $\bullet$ is

$$\Pi(t) = \operatorname*{tr}_R \left\{ e^{-i(H_S+H_R+H_V)t} (\bullet \otimes \rho_R^{\text{eq}}) e^{i(H_S+H_R+H_V)t} \right\}. \tag{2.6}$$

Step 1. In the first step, we take the adjoint of the superoperator $\Pi(t)$. By expanding the partial trace and the operator ρ_R^{eq} in the eigenbasis of ρ_R^{eq}, we can write $\Pi(t)$ as a sum of terms of the form $A \bullet B$ whose adjoint is $A^\dagger \bullet B^\dagger$. The adjoint of $\Pi(t)$ thus turns Eq. (2.6) inside out:

$$\Pi(t)^\dagger = \operatorname*{tr}_R \left\{ (\mathbb{1} \otimes \rho_R^{\text{eq}})\, e^{i(H_S+H_R+H_V)t}\, (\bullet \otimes \mathbb{1})\, e^{-i(H_S+H_R+H_V)t} \right\}. \tag{2.7}$$

In the next steps, we will manipulate this expression to reach the original form (2.6) again.

[5] The convergence of an expansion in the coupling is implicitly assumed in most approaches to open quantum system dynamics. For the exactly solvable noninteracting resonant level model, which will be used as an example, both bare and renormalized perturbation theory converge.

Step 2. We start with a basis transform in the reservoirs, where the energy ω labels the basis states. We relabel these states and thereby the creation and annihilation operators by replacing ω with $-\omega$. This can be seen as a unitary transformation — a permutation — that maps a state with energy ω to a state with energy $-\omega$. Since we eventually trace out the reservoirs, this unitary transformation does not have any effect on $\Pi(t)^{(\dagger)}$. But although $\Pi(t)^{(\dagger)}$ remains unchanged, the Hamiltonian and the equilibrium state change under this transformation. The reservoir Hamiltonian is mapped to $-\bar{H}_R = -H_R|_{\mu\mapsto-\mu}$ and the equilibrium reservoir state is mapped to $\bar{\rho}_R^{\mathrm{eq}}|_{T\mapsto-T} = \rho_R^{\mathrm{eq}}|_{T\mapsto-T,\,\mu\mapsto-\mu}$, inverting both temperature and chemical potential. The result of this step is

$$\Pi(t)^\dagger = \operatorname*{tr}_R\Big\{(\mathbb{1}\otimes\bar{\rho}_R^{\mathrm{eq}}|_{T\mapsto-T})\,e^{i(H_S-\bar{H}_R+H_V)t}\,(\bullet\otimes\mathbb{1})\,e^{-i(H_S-\bar{H}_R+H_V)t}\Big\}. \tag{2.8}$$

Step 3. This brings us to the key nontrivial steps, the technical details of which can be found in appendix A. Using only standard manipulations involving Wick's theorem,[6] we want to show in steps 3 and 4 that $\Pi(t)^\dagger$ can be written in a form similar to $\Pi(t)$:

$$\Pi(t)^\dagger = \operatorname*{tr}_R\Big\{e^{i(H_S-\bar{H}_R+iH_V+i\frac{1}{2}\Gamma)t}\,(\bullet\otimes\bar{\rho}_R^{\mathrm{eq}})\,e^{-i(H_S-\bar{H}_R-iH_V-i\frac{1}{2}\Gamma)t}\Big\}. \tag{2.9}$$

This requires an expansion of Eq. (2.8) in H_V and a resummation of this expansion.

Schematically, the proof of Eq. (2.9) can be sketched using diagrams that represent terms of this expansion of Eq. (2.8). When writing a left (right) propagator line for $e^{\pm i(H_S-\bar{H}_R)\Delta t}$ where Δt is some time interval, and indicating Wick contractions by curves, these expansion terms are of the form

$\operatorname{tr}_R\Big\{$ 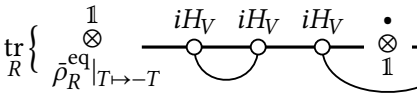 $\Big\} =$ (2.10)

$$\int_{t>t_3>t_2>t_1>0} dt_3\,dt_2\,dt_1\int_0^t dt_1'\,\operatorname*{tr}_R\Big\{(\mathbb{1}\otimes\bar{\rho}_R^{\mathrm{eq}}|_{T\mapsto-T})e^{i(H_S-\bar{H}_R)(t-t_3)}i\overbrace{H_V e^{i(H_S-\bar{H}_R)(t_3-t_2)}iH_V}$$
$$\times\, e^{i(H_S-\bar{H}_R)(t_2-t_1)}i\overbrace{H_V e^{i(H_S-\bar{H}_R)t_1}\,(\bullet\otimes\mathbb{1})\,e^{-i(H_S-\bar{H}_R)t_1'}(-iH_V)}e^{-i(H_S-\bar{H}_R)(t-t_1')}\Big\}. \tag{2.11}$$

Here we have written the tensor product vertically for brevity and explicitly indicated the trace over the reservoirs, although the trace is calculated using Wick contractions, to indicate that all terms inside the trace must be considered when calculating these contractions. In this relation, both H_R and H_V contain creation and annihilation operators $c_{\alpha\omega}^{(\dagger)}$ of the reservoirs, but we only indicate Wick contractions connected to the tunneling Hamiltonian H_V. The

[6] For a fermionic reservoir in a thermal state, Wick's theorem provides a way to calculate $R \coloneqq \operatorname{tr}_R c_1 c_2 \cdots c_n \rho_R^{\mathrm{eq}}$, where we used digits to label creation and annihilation operators and n is an even number. Wick's theorem states that the reservoir expectation value R can be calculated by summing up all possible ways of pairing up the indices $1, 2, \cdots, n$. By P we denote permutations of these indices, such that (P_1, P_2), (P_3, P_4) etc. form pairs in which the order of the indices is preserved: $P_1 < P_2$, $P_3 < P_4$ and so on. With this notation, one can prove that $R = \sum_P (-1)^P \langle c_{P_1} c_{P_2}\rangle \cdots \langle c_{P_{n-1}} c_{P_n}\rangle$ where $(-1)^P$ is -1 if P contains an odd number of permutations and $+1$ otherwise. The individual Wick contractions are $\langle c_{\eta\alpha\omega} c_{\eta'\alpha'\omega'}\rangle = \delta_{\alpha\alpha'}\delta(\omega-\omega')\delta_{\eta\bar{\eta}'} f(\eta\omega/T_\alpha)$ where η distinguishes creation ($\eta = +$) and annihilation ($\eta = -$) operators, $\bar{\eta} = -\eta$, and $f(x) = 1/(1+e^x)$ denotes the Fermi function.

reservoir Hamiltonians H_R can be eliminated and replaced by scalars using the commutation rule $H_R c_{\eta\alpha\omega} = c_{\eta\alpha\omega}(H_R + \eta\mu_\alpha + \eta\omega)$ where η distinguishes between creation ($\eta = +$) and annihilation ($\eta = -$) operators. Thus, only H_V, which is linear in the reservoir creation and annihilation operators, appears in the Wick contractions. Diagrams of the form in Eq. (2.10) contain a forward and backward propagation line on the left and right of the superoperator argument $\bullet$, respectively. These correspond to the forward and backward propagation part of the Keldysh contour, which we avoid in this derivation.

By defining modified Wick contractions, it is possible to shift $\bar{\rho}_R^{\mathrm{eq}}$ to the tensor product with the argument $\bullet$ in Eq. (2.10). This requires a distinction between contractions remaining on one propagation line and those connecting the two sides of $\bullet$. The usual Wick contraction is $\mathrm{tr}_R\, \rho_R^{\mathrm{eq}} c_{\eta_1\alpha_1\omega_1} c_{\eta_2\alpha_2\omega_2} = \mathrm{tr}_R\, \rho_R^{\mathrm{eq}} \overset{1}{\circ}\!\!\smile\!\!\overset{2}{\circ} = \delta_{\alpha_1\alpha_2}\delta_{\eta_1\bar{\eta}_2}\delta(\omega_1 - \omega_2) f(\eta_1\omega_1/T_{\alpha_1})$. With the definitions

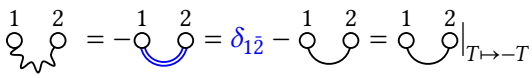

(2.12)

and the shorthand notation $\delta_{1\bar{2}} = \delta_{\alpha_1\alpha_2}\delta_{\eta_1\bar{\eta}_2}\delta(\omega_1 - \omega_2)$, we can write $\bar{\rho}_R^{\mathrm{eq}} \overset{1}{\circ}\!\!\smile\!\!\overset{2}{\circ} = \overset{1}{\circ}\!\!\sim\!\!\overset{2}{\circ}$. In the expansion this implies

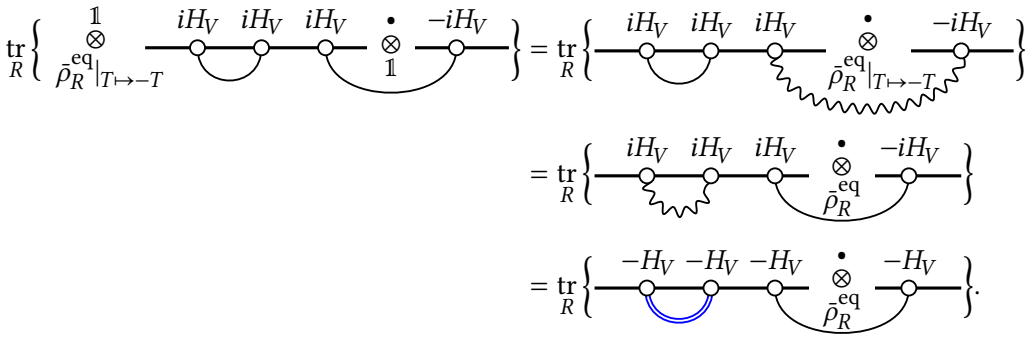

(2.13)

(2.14)

(2.15)

Here we have reversed the temperature inversion and find that a constant shift by $-\delta_{1\bar{2}}$ remains only in every contraction line that does not connect forward and backward propagator.

Step 4. We now show that the shift $-\delta_{1\bar{2}}$ in the contractions can be absorbed into an overall prefactor of the forward and backward propagator. This shift is constant in frequency — or energy — space and thus local in the time domain. The contractions can be transformed to time domain by using the interaction picture with $H_V(t) = e^{+i\tilde{H}_R t} H_V e^{-i\tilde{H}_R t}$. As verified explicitly in appendix A, in a Wick contraction $\overbrace{H_V(t_1)\cdots H_V(t_2)}$ of the coupling Hamiltonians in the time domain the shift $-\delta_{1\bar{2}}$ becomes $-\frac{1}{2}\Gamma\delta(t_2 - t_1)$. Such a time-local, scalar shift in the expansion terms can be absorbed into the definition of the propagator and leads to a prefactor $e^{-\Gamma t/2}$. When collecting all terms of the expansion, Eq. (2.15) therefore becomes

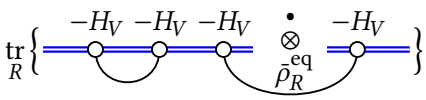

(2.16)

with the renormalized propagator double lines that include the prefactors $e^{-\Gamma t/2}$. This resummation yields Eq. (2.9).

Step 5. Eq. (2.9) is almost the duality relation (2.2), as one can see by rewriting it as

$$\Pi(t)^\dagger = e^{-\Gamma t} \operatorname*{tr}_R e^{-i(\bar{H}_S+\bar{H}_R-\bar{H}_V)t} (\bullet \otimes \bar{\rho}_R^{\mathrm{eq}}) e^{i(\bar{H}_S+\bar{H}_R+\bar{H}_V)t}, \tag{2.17}$$

identifying the dual operators $\bar{H}_S = -H_S$ and $\bar{H}_V = iH_V$. We only need to change the sign of $\bar{H}_V$ in the left propagator to find the propagator for the dual system on the right-hand side of Eq. (2.17). This sign change is achieved by the superoperator $\mathcal{P} = (-\mathbb{1})^N \bullet$ that describes left multiplication with the fermion parity operator:

$$\Pi(t)^\dagger = e^{-\Gamma t} \operatorname*{tr}_R \left[(-\mathbb{1})^N e^{-i(\bar{H}_S+\bar{H}_R+\bar{H}_V)t} \left\{ [(-\mathbb{1})^N \bullet] \otimes \bar{\rho}_R^{\mathrm{eq}} \right\} e^{i(\bar{H}_S+\bar{H}_R+\bar{H}_V)t} \right] = e^{-\Gamma t} \mathcal{P} \bar{\Pi}(t) \mathcal{P}. \tag{2.18}$$

Remarks. This proof avoids the language of Liouville space where this is possible and only uses standard methods in the key steps. This simplifies the connection to other approaches to open quantum systems, such as the Keldysh formalism. We can identify the rewriting of contractions connecting the forward and backward propagator of the total system as the key step with which we can shift ρ_R^{eq} within the equations.

But we also note that we have effectively reversed the time order in the propagators. By taking the adjoint of the unitary time evolution operators in the beginning, we reversed the time order in these operators. More precisely, in the expansion of $\Pi(t)$ we replaced the Hamiltonian $H_{\mathrm{tot}}(s)$ at time s with $H_{\mathrm{tot}}(t-s)$ (see appendix A for details). This is irrelevant as long as the Hamiltonian is constant, but it implies that for driven systems the duality relation (2.2) only holds for times t such that $H_{\mathrm{tot}}(t-s) = H_{\mathrm{tot}}(s)$ for all times $s \in [0,t]$. This strongly restricts the applicability of fermionic duality to driven systems, but for symmetric periodic driving such that $H_{\mathrm{tot}}(t) = H_{\mathrm{tot}}(-t)$, the stroboscopic evolution at times that are multiples of the driving period still respects the duality relation. Interestingly, the idea of a time reversed open system expansion is also discussed in a derivation of fluctuation relations in quantum thermodynamics [96].

The reversed time order is also an obstacle for applying fermionic duality to the calculation of transport observables, such as the current. When we compute the current, we consider a time evolution followed by a measurement of the current. When trying to derive a duality relation for the current following the same steps as in the present proof for the duality of the propagator without further tricks, one would end up first measuring the current and then evolving the system. This additional difficulty explains why we are not aware of any general fermionic duality relation for nonlocal observables such as the current.

2.3. Fermionic duality combined with superselection rules

The duality relation for the propagator in the time domain is the starting point for equivalent formulations of this duality relation in different formalisms for the description of open quantum systems. The derivation of such formulations for the Kraus operator sum form [97, 98], for the effective Liouvillian or Nakajima-Zwanzig memory kernel [47, 48] in the time domain and

in Laplace space, for the time-local quantum master equation, and for the generalized Gorini-Kossakowski-Sudarshan-Lindblad (GKSL) jump operator form [99, 100] has been reported in Refs. [2, 93]. A common property of these various formulations of fermionic duality is that they connect the physical system in the Heisenberg picture to the dual system in the Schrödinger picture. For the propagator we have seen from the general duality relation (2.2) that $\bar{\Pi}(t)$, the dual propagator in Schrödinger picture, is connected to the physical propagator in the Heisenberg picture $\Pi(t)^\dagger$. Similar relations also hold in formulations of the dynamics where the general connection between the Schrödinger and Heisenberg picture is highly nontrivial, for example the GKSL form.

A topic that has not been addressed yet is the combination of the duality relation with conservation laws and superselection rules. To fill this gap, we first review the consequences of conservation laws for open quantum systems and introduce the resonant level model, with which we will illustrate the duality relations. We will then find duality relations for the dynamics of states which are restricted to obeying conservation laws.

2.3.1. Superselection rules

Physical systems are usually restricted by symmetries and conservation laws, such as particle number conservation. In closed quantum systems, such fundamental physical properties pose restrictions on the allowed states. For example, let us consider a closed quantum system that contains a fixed, conserved number of particles. We assume that the particle number is a well-defined quantity, i.e., it is a good quantum number and superposition of states with different particle numbers are forbidden. Classical mixtures of different particle numbers — which describe a lack of knowledge about the particle number and not a quantum mechanical uncertainty — remain possible. The second assumption is that the time evolution cannot change the particle number, which implies that many matrix elements of the Hamiltonian must vanish. In the following, we will call a quantity conserved if it fulfills these two criteria of being a good quantum number and conserved by every physical time evolution in a closed quantum system.

In open quantum systems, superselection rules and conservation laws pose restrictions not only on the total system, but also on the density matrix of the local system which we aim to describe. For the example of particle number conservation, one can show that if the superposition of states with different particle numbers is forbidden in the total system, then it must also be forbidden in the local system.[7] Thus, the density matrix of the local quantum system must be block-diagonal in the eigenbasis of the particle number operator, and we can write $\rho = \bigoplus_n \rho_n$ where ρ_n is the diagonal block with n particles on the local system. For the propagator $\Pi(t)$ this has two important consequences. Firstly, many matrix elements of $\Pi(t)$ vanish because the propagator must preserve the block-diagonal structure of the input states. Secondly, many matrix elements of $\Pi(t)$ are only relevant if the input state does not obey the conservation law. In the following, we will focus on this second property. Here we only discuss the important

[7] A well-defined particle number means that every allowed density matrix must commute with the particle number operator. Since the particle number operator for a bipartite system with subsystems A and B is of the form $N_{AB} = N_A \otimes \mathbb{1}_B + \mathbb{1}_A \otimes N_B$, one can easily show that $[N_{AB}, \rho_{AB}] = 0$ implies $[N_A, \rho_A] = \mathrm{tr}_B[N_{AB}, \rho_{AB}] = 0$, where the marginal state on system A is $\rho_A = \mathrm{tr}_B \rho_{AB}$.

case of particle number conservation, but the same arguments can be used for other conserved quantities like the fermion parity $(-\mathbb{1})^N$ or — in some systems — the average spin polarization.

Restricting the allowed set of states to block-diagonal density matrices simplifies the description of the dynamics. We will denote the projection operator to the Hilbert subspace n of states containing n particles by P_n and define $\mathbb{P}_n = P_n \bullet P_n$ as the corresponding projector on the Liouville space. Although the operators P_n form a complete set of projection operators in the Hilbert space, $\sum_n P_n = \mathbb{1}$, the set of projection superoperators $\mathbb{P}_n$ is not complete, $\sum_n \mathbb{P}_n \neq \mathbb{I}$. By $\mathbb{I}$ we denote the identity superoperator. The propagator can be split into blocks $\Pi_{nm}(t) = \mathbb{P}_n \Pi(t) \mathbb{P}_m$, which describe the transition from subspace m to n. The time evolution of the different blocks of an allowed density matrix is then given by $\rho_n(t) = \sum_m \Pi_{nm}(t)\rho_m(0)$. But all blocks $\Pi_{nm}(t)$ combined only form a reduced propagator $\Pi^{\text{red}}(t) \coloneqq \Pi(t) \sum_n \mathbb{P}_n$, which contains a subset of the matrix elements of the full propagator $\Pi(t)$. Thus, working with the blocks $\Pi_{nm}(t)$ simplifies the description of the evolution by omitting matrix elements of $\Pi(t)$ that are irrelevant when the input states obey the assumed conservation laws.

These left-out matrix elements of $\Pi(t)$ only become relevant in a different physical setup that is closely connected to the concept of complete positivity, a quantum feature of evolution maps. We extend the physical setup by a reference system, with which the local system of interest may be entangled. The time evolution on this reference system is trivial, i.e., the marginal state is constant.[8] Now the combined evolution $\Pi(t) \otimes \mathbb{I}$ on system and reference should be a valid physical evolution map, which preserves the positivity of density operators. This property of every valid evolution map is called complete positivity: A superoperator $\mathcal{S}$ is called completely positive (CP) if for every positive semidefinite operator ρ on the combined local and reference system $[\mathcal{S} \otimes \mathbb{I}]\rho$ is also positive semidefinite. We will see a useful application of complete positivity in section 2.3.4. Here we notice that this is indeed a property of the full propagator $\Pi(t)$ and not just of $\Pi^{\text{red}}(t)$. More generally, the description of an evolution of a system that is entangled with some reference system requires the full propagator $\Pi(t)$. However, we are usually only interested in the evolution of the local system without any reference system that could influence the evolution or measurements. In this situation, we can restrict the description to the previously discussed block-diagonal density matrices and work only with $\Pi^{\text{red}}(t)$.

A special case of a symmetry that restricts the state space is the fermion superselection principle. Fermions have the general property that a rotation by 2π adds a phase -1 to a single fermion quantum state [95]. But since a rotation by 2π cannot make a physical difference, this phase must be a global phase. Therefore, states with an odd number of fermions cannot be in superposition with states with an even number of fermions, and every density operator must commute with the fermion parity operator $(-\mathbb{1})^{N_{\text{tot}}}$ where N_{tot} is the fermion number operator on the total system [94, 95]. This implies that also reduced density matrices must commute with the fermion parity operator on the reduced system, i.e., $[\rho(t), (-\mathbb{1})^N] = 0$, analogous to the relation we found for particle number conservation. In the derivation of fermionic duality, we used that the evolution must preserve this property. Thus, when we use a symmetry or conservation law to split the state space into subspaces between which superposition is forbidden, these subspaces

[8] One could allow for an arbitrary unitary evolution on the reference system without changing any of the definitions or statements in this paragraph.

can always be chosen such that every subspace has definite fermion parity. In the example of particle number conservation, the parity of subspace n is $(-1)^n$ such that $(-\mathbb{1})^N|\psi_n\rangle = (-1)^n|\psi_n\rangle$ for every pure state $|\psi_n\rangle$ in subspace n.

Since we usually only need $\Pi^{\mathrm{red}}(t)$, one may ask why one often calculates the full propagator $\Pi(t)$ anyway. Different methods exist for computing $\Pi(t)$, but not all of them can make use of the reduced set of input states in $\Pi^{\mathrm{red}}(t)$. For some methods, computing the full propagator is almost unavoidable. For example, when working with an effective Liouvillian as we will do in chapter 4, it is necessary to compute the effective Liouvillian for all input states to use it in a self-consistent expansion [53, 55, 74]. Once the effective Liouvillian has been found, computing the full propagator is not more difficult than computing the reduced propagator. Thus, a general simplification by use of the reduced input state space can be far from obvious. In other approaches, restricting the discussion to $\Pi^{\mathrm{red}}(t)$ does lead to significant simplifications, as we will see below using the following example.

2.3.2. Example: Resonant level model

To illustrate symmetries and superselection rules for open quantum systems as well as fermionic duality in different formulations, we will use the noninteracting resonant level model. In this model, we consider a single fermionic level tunnel-coupled to reservoirs of spinless fermions. This simplest model with memory effects that obeys fermionic duality is used as an exactly solvable toy model and for the description of transport through single molecules [101, 102]. The Hamiltonian of the resonant level model with multiple reservoirs labeled by α is

$$H_{\mathrm{tot}} = \varepsilon d^\dagger d + \sum_\alpha \int d\omega\, (\omega + \mu_\alpha) c_{\alpha\omega}^\dagger c_{\alpha\omega} + \sum_\alpha \sqrt{\frac{\Gamma_\alpha}{2\pi}} \int d\omega \left(d^\dagger c_{\alpha\omega} + c_{\alpha\omega}^\dagger d \right), \tag{2.19}$$

where $d^\dagger$ is the fermion creation operator for the fermionic mode at energy ε. The total coupling rate that appears in the duality relation is $\Gamma = \sum_\alpha \Gamma_\alpha$, and the dual system is defined by the parameter substitution $(\Gamma_\alpha, \mu_\alpha, \varepsilon) \mapsto (-\Gamma_\alpha, -\mu_\alpha, -\varepsilon)$. Detailed derivations of the dynamics of a resonant level connected to a single reservoir are presented in Ref. [102] using various methods. A derivation of the dynamics and the current with multiple leads is reviewed in appendix B using a method from Refs. [103, 104].

For the resonant level model, the structure of valid density matrices is restricted by the fermion superselection principle, which splits the state space into two one-dimensional subspaces of occupancy 0 or 1. In the occupancy basis, the propagator can be written as a block-diagonal matrix

$$\Pi(t) = \begin{array}{c} (ab| \\ \downarrow \\ 00 \\ 11 \\ 01 \\ 10 \end{array} \begin{array}{c} |cd) \to \\ \\ \left(\begin{array}{c|c} \multicolumn{2}{c}{\begin{array}{cc} 00 & 11 \end{array}} & \begin{array}{cc} 01 & 10 \end{array} \\ \hline \multicolumn{2}{c|}{\Pi^{\mathrm{red}}(t)} & \multicolumn{2}{c}{0} \\ \hline \multicolumn{2}{c|}{0} & \multicolumn{2}{c}{\Pi(t) - \Pi^{\mathrm{red}}(t)} \end{array} \right) \end{array}, \tag{2.20}$$

where we indicate the matrix elements $(ab|\Pi(t)|cd) = \langle a|\big[\Pi(t)(|c\rangle\langle d|)\big]|b\rangle$ describing a transition from state $|c\rangle\langle d|$ to $|a\rangle\langle b|$. Half of the 16 matrix elements of $\Pi(t)$ vanish, because transitions

between states obeying the superselection principle and operators that do not obey it are forbidden. Four matrix elements form $\Pi^{\mathrm{red}}(t)$ and describe the evolution of states obeying the superselection principle. The remaining four matrix elements describe the evolution of operators $|0\rangle\langle 1|$ and $|1\rangle\langle 0|$ which never occur in our system obeying the superselection principle. Since the occupancy subspaces 0 and 1 of the Hilbert space are one-dimensional, the superoperators $\Pi_{nm}(t)$ become scalars and are the matrix elements of $\Pi^{\mathrm{red}}(t)$. Trace preservation adds another constraint to each column of the matrix $\Pi^{\mathrm{red}}(t)$ such that only two independent matrix elements remain. Below we will see that fermionic duality restricts the propagator even further such that only one independent matrix element remains.

2.3.3. Duality for the propagator

The duality relation (2.2) for the propagator can be projected to subspaces defined by selection rules and conservation laws. This leads to a cross connection of the components $\Pi_{nm}(t)$ and $\Pi_{mn}(t)$:

$$\Pi_{nm}(t)^\dagger = (-1)^{n+m} e^{-\Gamma t} \bar{\Pi}_{mn}(t). \tag{2.21}$$

Thus, fermionic duality also holds for the reduced propagator $\Pi^{\mathrm{red}}(t)$ and for the propagator $\Pi_{nn}(t)$ with $n = m$ that describes the evolution within subspace n. This is of practical interest because often only a subspace of the state space is relevant, and approximations of the propagator only aim to describe such a subspace. A prominent example is the Kondo limit of the Anderson model, which describes a low-energy subspace of a singly occupied quantum dot and will be discussed in chapter 3. However, in this Kondo limit the corresponding subspace in the dual system is a high-energy subspace of unpaired particles in a strong pairing potential, to which a simplified low-energy description cannot be applied. This restrains us from using fermionic duality for the Kondo model.

Interestingly, the duality relation (2.21) includes the same prefactor $e^{-\Gamma t}$ for every subspace propagator $\Pi_{nn}(t)$. This is remarkable considering that different fermion modes on the local system are coupled to the reservoirs with different coupling strengths. To understand the appearance of the total tunneling rate Γ we remember that we defined the subspaces n by the particle number, which is a combined property of all fermion modes on the local system. The definition of the subspaces does not prefer any specific fermionic mode, such that the bare sum of all coupling rates Γ is relevant for each subspace. This is reflected in the duality relation (2.21). Other conservation laws which could define subspaces must have the same property of treating all fermion modes equally.

For the resonant level model, we have already seen that the four blocks $\Pi_{nm}(t)$ are scalars. The matrix elements of the resonant level model are

$$\Pi(t) = \begin{array}{c} \\ 00 \\ 11 \\ 01 \\ 10 \end{array} \begin{array}{c} \begin{array}{cccc} 00 & 11 & 01 & 10 \end{array} \\ \left(\begin{array}{cc|cc} \Pi_{00} & \Pi_{01} & \multicolumn{2}{c}{\multirow{2}{*}{0}} \\ \Pi_{10} & \Pi_{11} & & \\ \hline \multicolumn{2}{c|}{\multirow{2}{*}{0}} & e^{i\epsilon t-\Gamma t/2} & 0 \\ & & 0 & e^{-i\epsilon t-\Gamma t/2} \end{array}\right) \end{array}, \tag{2.22}$$

where we marked in green all transition rates which are self-dual and in blue those which are related to each other by the duality. The lower right matrix block — describing the evolution of density operators that violate the superselection principle — also obeys the duality relation, but in the following we will focus on $\Pi^{\mathrm{red}}(t)$. The duality relations for the components of the reduced propagator are[9]

$$\Pi_{nn}(t) = e^{-\Gamma t}\bar{\Pi}_{nn}(t), \qquad \Pi_{01}(t)^* = -e^{-\Gamma t}\bar{\Pi}_{10}(t). \tag{2.23}$$

With the sum rules $\Pi_{00}(t) + \Pi_{10}(t) = \Pi_{01}(t) + \Pi_{11}(t) = 1$ that express trace preservation, this duality relation allows us to construct all components $\Pi_{nm}(t)$ of $\Pi^{\mathrm{red}}(t)$ just from, for example, $\Pi_{00}(t)$.[10] Without knowing any further details of the model, we can conclude that

$$\Pi_{01}(t) = \frac{1}{2}\left(1 - e^{-\Gamma t}\right)[1 + p(t)], \qquad \Pi_{00}(t) = \frac{1}{2}\left(1 + e^{-\Gamma t}\right) + \frac{1}{2}\left(1 - e^{-\Gamma t}\right)p(t), \tag{2.24}$$

$$\Pi_{10}(t) = \frac{1}{2}\left(1 - e^{-\Gamma t}\right)[1 - p(t)], \qquad \Pi_{11}(t) = \frac{1}{2}\left(1 + e^{-\Gamma t}\right) - \frac{1}{2}\left(1 - e^{-\Gamma t}\right)p(t), \tag{2.25}$$

where $p(t)$ is some real-valued function fulfilling $\bar{p}(t) = -p(t)$. Thus, only one scalar function must be determined to obtain the full dynamics restricted to input states without superpositions of $|0\rangle$ and $|1\rangle$. This function $p(t)$ is derived explicitly in Ref. [102], and can be expressed most compactly with the help of two further functions that are relevant for the dynamics in other formulations (see below):

$$k(t) = \sum_{\alpha} 2T_\alpha \frac{\sin([\varepsilon - \mu_\alpha]t)}{\sinh(\pi T_\alpha t)}, \tag{2.26}$$

$$g(t) = \int_0^t ds\, e^{-\frac{1}{2}\Gamma s} k(s), \tag{2.27}$$

$$p(t) = \frac{\Gamma}{1 - e^{-\Gamma t}} \int_0^t ds\, e^{-\Gamma(t-s)} g(s). \tag{2.28}$$

This function $p(t)$ indeed fulfills the duality relation $\bar{p}(t) = -p(t)$, illustrating that fermionic duality often reveals quite subtle properties which strongly simplify calculations, or constitutes a highly nontrivial check on results beyond ordinary symmetries.

2.3.4. Kraus operator sum form

A generic form in which the propagator can be expressed is the Kraus operator sum, $\Pi(t) = \sum_i \lambda_i K_i \bullet K_i^\dagger$ with $\lambda_i > 0$. The coefficients λ_i are usually absorbed into the definition of the Kraus operators K_i, but when working with fermionic duality it is more convenient to use normalized Kraus operators which fulfill $\mathrm{tr}\, K_i^\dagger K_j = \delta_{ij}$ and to write the coefficients λ_i separately. The operator sum form is obtained when simulating the evolution by replacing the reservoirs with an auxiliary system and doing measurements on this auxiliary system. In this simulation,

[9] We use that $\Pi_{nn}(t)$ must preserve the Hermiticity of states on which it acts. In a one-dimensional subspace, this implies that $\Pi_{nn}(t)$ is a real number.

[10] One can use, for example, $\Pi_{11}(t) = 1 + e^{-\Gamma t}[1 - \bar{\Pi}_{00}(t)^*] = 1 + e^{-\Gamma t} - \Pi_{00}(t)$.

each individual term in the operator sum form corresponds to one measurement outcome followed by an operation on the system that depends on that measurement outcome. This physical interpretation complements a solid mathematical background with the theorem by Sudarshan [97] and Kraus [98] that a superoperator is CP if and only if it can be expressed in the operator sum form with positive coefficients $\lambda_i > 0$. One can show (see appendix C) that since $\Pi(t)$ is CP, also each subspace propagator or transition between subspaces $\Pi(t)_{nm}$ for fixed (n, m) must be CP. It follows that every block $\Pi(t)_{nm}$ has its own Kraus operator sum form with its own duality relation.

The canonical Kraus operator sum form for $\Pi_{nm}(t)$ is

$$\Pi_{nm}(t) = \sum_{i=1}^{d_n d_m} \lambda_i^{nm}(t)\, K_i^{nm}(t) \bullet K_i^{nm}(t)^\dagger \tag{2.29}$$

with coefficients $\lambda_i^{nm}(t) \geq 0$ and normalized Kraus operators fulfilling $\mathrm{tr}\, K_i^{nm}(t)^\dagger K_j^{n'm'}(t) = \delta_{ij}\delta_{nn'}\delta_{mm'}$. Here d_n denotes the dimension of subspace n and the Kraus operator K_i^{nm} maps subspace m to subspace n, $K_i^{nm} = P_n K_i^{nm} P_m$. These Kraus operators obey the sum rule

$$\sum_{in} \lambda_i^{nm}(t) K_i^{nm}(t)^\dagger K_i^{nm}(t) = P_m \tag{2.30}$$

for every subspace m to ensure that the evolution is trace preserving. Importantly, the operators $K_i^{nm}(t)$ are the Kraus operators of the reduced propagator $\Pi^{\mathrm{red}}(t) = \sum_{nm} \Pi_{nm}(t)$ and not those of the full propagator $\Pi(t)$. Both $\Pi(t)$ and $\Pi^{\mathrm{red}}(t)$ have d^2 canonical Kraus operators.[11] But Kraus operators of the full propagator are generally more complicated because they can act on multiple input subspaces, whereas $K_i^{nm}(t)$ only acts on one subspace m. The only restriction on the Kraus operators of the full propagator is that they must preserve the separation of subspaces.[12] For example, in the resonant level model two canonical Kraus operators of the full propagator $\Pi(t)$ are of the form $\alpha(t)|0\rangle\langle 0| + \beta(t)|1\rangle\langle 1|$ where $\alpha(t)$ and $\beta(t)$ are relatively complicated expressions [102]. The Kraus operators for $\Pi^{\mathrm{red}}(t)$ are only allowed to act on a single subspace (0 or 1) such that we obtain the simpler operators $|0\rangle\langle 0|$ and $|1\rangle\langle 1|$. Thus, by restricting the description from $\Pi(t)$ to $\Pi^{\mathrm{red}}(t)$ we do not reduce the number of Kraus operators, but we restrict the space in which these operators live and thereby simplify the Kraus operators. This shows that for the Kraus operator sum form, it can make a significant difference whether one works with $\Pi(t)$ or with $\Pi^{\mathrm{red}}(t)$.

The fermionic duality relation connects pairs of Kraus operators. This result of Ref. [93] is valid for Kraus operators of the full propagator and for those of $\Pi^{\mathrm{red}}(t)$. Provided the coefficients $\lambda_i^{nm}(t)$ differ for different index i,[13] the duality connects every Kraus operator K_i^{nm} to a dual

[11] Fewer Kraus operators might be needed because some coefficients vanish, $\lambda_i^{nm}(t) = 0$. For example, at $t = 0$ the propagator is just $\Pi(t) = \mathbb{I} = \mathbb{1} \bullet \mathbb{1}$.

[12] Mathematically, this means that if a Kraus operator K_i of the full propagator maps a state in subspace m to a state in subspace n, then it must fulfill $K_i P_m = P_n K_i$.

[13] The coefficients $\lambda_i^{nm}(t)$ are the eigenvalues of the operator choi$[\Pi_{nm}(t)]$ defined in appendix C. If this operator is nondegenerate, the orthonormal Kraus operators are unique up to a phase prefactor. In this case, the duality relation (2.31) holds. If choi$[\Pi_{nm}(t)]$ is degenerate, i.e., if there exists a set of indices $\{i_l\}_l$ with equal coefficients

partner $\bar{K}_j^{mn}$ such that

$$\lambda_i^{nm}(t) = (-1)^{n+m} e^{-\Gamma t} \bar{\lambda}_j^{mn}(t), \qquad K_i^{nm}(t) = e^{i\varphi_i^{nm}} \bar{K}_j^{mn}(t)^\dagger, \tag{2.31}$$

where $e^{i\varphi_i^{nm}}$ is a phase that arises from the general gauge freedom of choosing the Kraus operators for the same propagator. It is always possible to choose Kraus operators such that these phases vanish, $\varphi_i^{nm} = 0$ for all n, m and i. Thus, when we calculate one Kraus operator explicitly, we can typically get another one using fermionic duality. But we also note that in Eq. (2.31) it is possible that $i = j$ such that for $n = m$ the duality relation can connect a Kraus operator to itself. For such self-dual Kraus operators and coefficients, the duality relation mainly provides a check of the results. Eq. (2.31) follows from Eqs. (2.21) and (2.29), and a brief proof using the Choi operator is provided in appendix C.2. With the subspace-separate decomposition discussed here, we have shown that also the Kraus operators of the reduced propagator $\Pi^{\mathrm{red}}(t)$ fulfill a duality relation, extending the discussion of the full propagator in [2, 93]. These Kraus operators K_i^{nm} are naturally grouped by the different subspaces (n, m). This makes it simpler to determine which Kraus operators can be duality partners and which operators can — or must — be self-dual.

The duality relation for the coefficients $\lambda_i^{nm}(t)$ shows a surprising consequence. For every physical system with CP dynamics, these coefficients must be positive, $\lambda_i^{nm}(t) \geq 0$. But the duality relation implies that the coefficients of the Kraus operator of the dual system can be negative. More precisely, all dual coefficients for Kraus operators connecting two subspaces with different fermion parity are negative. Thus, the evolution map of the dual system is not CP. Only the evolution within each parity block is CP and could be interpreted as dynamics of a physical system, while transitions between the two parity blocks are completely negative since they have only negative coefficients in the operator sum form. This means that the dual system is unphysical on a fundamental level [2, 93]. Thus, beyond weak coupling, fermionic duality does not lead to physically observable effects, but it remains a powerful and useful tool that offers simplifications in analytic calculations which no physical symmetry can yield.

In the resonant level model, the Kraus operators are specially simple. Since the subspaces for occupancy 0 or 1 are just one-dimensional, the normalized Kraus operators can be written down directly:

$$K^{00} = |0\rangle\langle 0| = dd^\dagger, \quad K^{11} = |1\rangle\langle 1| = d^\dagger d, \quad K^{01} = |0\rangle\langle 1| = d, \quad K^{10} = |1\rangle\langle 0| = d^\dagger. \tag{2.32}$$

The prefactors λ_{nm} of these Kraus operators are just the components Π_{nm} of the propagator. Although we have already calculated these [Eqs. (2.24)–(2.25)], it is illustrative how the relations between these prefactors are obtained in the entirely different Kraus operator formalism. In general, these prefactors are restricted by the sum rule Eq. (2.30) that ensures trace preservation. Furthermore, in the duality relation (2.2), trace preservation implies that $(-\mathbb{1})^N$ must be an eigenmode of the dynamics with decay rate Γ [103–105]. This leads to another general sum

$\lambda_{i_l}^{nm}(t)$, then there exist corresponding degenerate dual coefficients such that $\lambda_{i_l}^{nm}(t) = (-1)^{n+m} e^{-\Gamma t} \bar{\lambda}_{j_l}^{mn}(t)$ and the duality guarantees that the operators $\{K_{i_l}^{nm}(t)\}_l$ span the same vector space as the operators $\{\bar{K}_{j_l}^{mn}(t)^\dagger\}_l$. This implies that there exists always a choice of Kraus operators which fulfill Eq. (2.31), but only if all coefficients are different all choices of orthonormal Kraus operators fulfill this relation.

rule [93], which is quite unusual in quantum information:

$$\sum_{im}(-1)^{n+m}\lambda_i^{nm}(t)K_i^{nm}(t)K_i^{nm}(t)^\dagger = e^{-\Gamma t}P_n. \tag{2.33}$$

This is precisely the dual relation to Eq. (2.30). Combining these very general sum rules, we find

$$\lambda_{00}+\lambda_{10}=1, \qquad \lambda_{11}+\lambda_{01}=1, \tag{2.34}$$

$$\lambda_{00}-\lambda_{01}=e^{-\Gamma t}, \qquad \lambda_{11}-\lambda_{10}=-e^{-\Gamma t}, \tag{2.35}$$

leading to the result derived earlier in Eqs. (2.24)–(2.25). This illustrates how fermionic duality and the restriction to physically allowed input states provide constraints on the dynamics that simplify calculations and results.

2.3.5. GKSL form

Similar to the Kraus operator sum form for the propagator, one can also find an operator sum form for the generator of the dynamics. In the time-local or time-convolutionless quantum master equation the dynamics is described by a generator $\mathcal{G}(t)$, which hides all memory effects in a time-local form [106, 107]:[14]

$$\frac{d}{dt}\rho(t) = -i\mathcal{G}(t)\rho(t). \tag{2.36}$$

This quantum master equation comes with the obstacle that for some systems $\mathcal{G}(t)$ can diverge at isolate points in time. Such divergences mark times when $\Pi(t)$ is not invertible because multiple initial states lead to the same local state at time t. The discussion of these physical divergences is beyond the scope here, and we only consider evolutions and times t such that $\Pi(t)$ is invertible and $\mathcal{G}(t)$ is well-defined. The general duality relation for this generator provides a simple way of obtaining the generator in Heisenberg picture $\mathcal{G}^H(t)$ [2, 93]:

$$\mathcal{G}^H(t) = \left[\Pi^{-1}(t)\mathcal{G}(t)\Pi(t)\right]^\dagger = -\mathcal{P}\bar{\mathcal{G}}(t)\mathcal{P} + i\Gamma\mathbb{I}. \tag{2.37}$$

Here, $\mathcal{G}^H(t)$ is defined as the generator in the Heisenberg picture by

$$\frac{d}{dt}\Pi(t)^\dagger = i\mathcal{G}^H(t)\Pi(t)^\dagger. \tag{2.38}$$

The generator can be written as a sum of generally time-dependent jump operators, analogous to the Kraus operator sum. As derived in appendix C.3, the contribution of jumps from subspace m to n in the GKSL jump operator sum is

$$-i\mathcal{G}^{nm}(t) = -i\delta_{nm}[H_n'(t),\bullet] + \sum_{i=1}^{d_n d_m-\delta_{nm}} j_i^{nm}(t)\left[J_i^{nm}(t)\bullet J_i^{nm}(t)^\dagger - \frac{1}{2}\left\{J_i^{nm}(t)^\dagger J_i^{nm}(t),\bullet\right\}\right], \tag{2.39}$$

[14] It is a common misconception that a time-local quantum master equation can only describe systems without memory effects. By defining $\mathcal{G}(t) = i[d\Pi(t)/dt]\Pi(t)^{-1}$ the memory effects are only hidden in the time-dependence of $\mathcal{G}(t)$ and not ignored. $\mathcal{G}(t)$ contains not only information about what happens at time t, but also about processes that affect the state at time t. The generator $\mathcal{G}(t)$ in which the memory is hidden can also be used to quantify the memory of the system [108, 109].

where the jump operators fulfill $P_n J_i^{nm}(t) P_m = J_i^{nm}(t)$. Here one should note that with this definition $\mathcal{G}^{nm}(t) \neq \mathbb{P}_n \mathcal{G}(t) \mathbb{P}_m$ even though $\Pi^{nm}(t) = \mathbb{P}_n \Pi(t) \mathbb{P}_m$. We have split the generator into trace-destroying contributions of different jump operators, $\mathrm{tr}[\mathcal{G}^{nm}(t)\bullet] = 0$, whereas the superoperators $\mathbb{P}_n \mathcal{G}(t) \mathbb{P}_m$ are not trace-destroying. Like the canonical Kraus operators, we also choose the canonical jump operators to be normalized to $\mathrm{tr}\, J_i^{nm}(t)^\dagger J_j^{n'm'}(t) = \delta_{ij}\delta_{nn'}\delta_{mm'}$. The Hermitian operators $H_n'(t) = P_n H_n'(t) P_n$ in subspace n are not simply the close system Hamiltonians, but include effects from the coupling to the reservoirs.

Eq. (2.39) defines the contributions to the reduced generator $\mathcal{G}^{\mathrm{red}}(t) = \sum_{nm} \mathcal{G}^{nm}(t) \mathbb{P}_m = \sum_m \mathcal{G}(t) \mathbb{P}_m$, which generates the reduced propagator $\Pi^{\mathrm{red}}(t)$ defined in section 2.3.1.[15] As discussed for the relation between the reduced and full propagator, the reduced generator $\mathcal{G}^{\mathrm{red}}(t)$ is exactly equivalent to the full generator when acting on states obeying particle number conservation, by which we have defined the subspaces. Similar to the Kraus operators of $\Pi^{\mathrm{red}}(t)$ also the jump operators of $\mathcal{G}^{\mathrm{red}}(t)$ are, in general, simpler than those of the full generator $\mathcal{G}(t)$. An operator $J_i^{nm}(t)$ is restricted to mapping subspace m to subspace n, while jump operators of the full generator can act on multiple subspaces without mixing these subspaces.

The Heisenberg picture generator defined in Eq. (2.38) can be written in a slightly modified GKSL form. The main difference is that in the Heisenberg picture the generator is not trace-destroying, but instead destroys the identity operator, $\mathcal{G}^H(t)\mathbb{1} = 0$. This leads to the GKSL form

$$i\mathcal{G}^{Hnm}(t) = i\delta_{nm}[{H_n'}^H(t), \bullet] + \sum_{i=1}^{d_n d_m - \delta_{nm}} j_i^{Hnm}(t) \left[J_i^{Hnm}(t) \bullet J_i^{Hnm}(t)^\dagger - \frac{1}{2} \left\{ J_i^{Hnm}(t) J_i^{Hnm}(t)^\dagger, \bullet \right\} \right] \tag{2.40}$$

for the reduced generator in the Heisenberg picture, where one should note that the order of the jump operators in the anticommutator has changed compared to Eq. (2.39). But although this form looks very similar to the GKSL form in the Schrödinger picture, the general relation between the jump operators and rates in the Schrödinger and Heisenberg picture is very complicated, as the general relation for the generators in Eq. (2.37) shows. Calculating the generator in Heisenberg picture without fermionic duality requires a similarity transform with the full propagator, which makes it virtually impossible to obtain Heisenberg picture jump operators from Schrödinger picture jump operators without completely recalculating the GKSL form. This is in stark contrast to the following simple relation providing the Heisenberg picture GKSL form using fermionic duality:

$${H_n'}^H(t) = -\bar{H}_n'^H(t), \qquad J_i^{Hnm}(t) = \bar{J}_i^{mn}(t), \qquad j_i^{Hnm}(t) = (-1)^{n+m} \bar{j}_i^{mn}(t). \tag{2.41}$$

This duality relation provides one possible set of jump operators, which are generally nonunique similar to the Kraus operators. By convention, we use the same index i in the Schrödinger and Heisenberg picture. Thus, using fermionic duality we can easily switch between the Schrödinger and Heisenberg picture, and retain the structure of an already simplified analytic result — a highly nontrivial[16] simplification.

[15] Formally, $\Pi^{\mathrm{red}}(t) = \mathcal{T}_{\leftarrow} \exp\left[-i \int_0^t ds\, \mathcal{G}^{\mathrm{red}}(s) \right] \sum_m \mathbb{P}_m$.

[16] except if $[\mathcal{G}(t), \mathcal{G}(s)] = 0$ for all times t, s

For the resonant level model, the general GKSL form in Eq. (2.39) implies that only two jump operators are required to describe the dynamics. These are simply the creation and annihilation operators, $J^{01} = d$ and $J^{10} = d^\dagger$, which connect the even and odd parity sector. Since the subspaces have dimension $d_n = 1$, the commutator in Eq. (2.39) will always be trivial and we can set $H_n' = 0$. We can furthermore use that $(-\mathbb{1})^N$ is an eigenmode of the dynamics [as discussed above Eq. (2.33)] and must be an eigenvector with eigenvalue $-\Gamma$ of $-i\mathcal{G}(t)$ and of $-i\mathcal{G}^{\mathrm{red}}(t)$. This yields the sum rule $j^{01} + j^{10} = \Gamma$ for the jump rates [2, 93].[17] Thus, the generator must be of the form

$$-i\mathcal{G}^{\mathrm{red}}(t) = \frac{\Gamma}{2} \sum_{\eta=\pm} [1 - \eta g(t)] \left[d_\eta \bullet d_\eta^\dagger - \tfrac{1}{2} \left\{ d_\eta^\dagger d_\eta, \bullet \right\} \right], \tag{2.42}$$

where only the function $g(t)$ is taken from a separate calculation, in this case from Eq. (2.27). This shows once more how for the resonant level model, fermionic duality and general symmetry restrictions reduce the problem of describing the dynamics to determining a single scalar function of time.

2.4. Divisibility and Markovianity

The previously discussed GKSL form is especially interesting because it contains quantitative information about the memory of the system. Defining memory seems straightforward in a classical system, where one can ask and measure whether the evolution of a state at time t depends only on the state immediately before t or also on earlier times. But in a quantum system, we cannot directly observe how a quantum state evolves without changing the state by measuring it. If we measure the state at different times $t_1, t_2, \ldots$ to find out whether the state measured at time t_{n+1} depends only on time t_n, then these measurements will change the evolution. This difficulty has led to multiple definitions of memoryless or Markovian evolutions in quantum systems [56, 108–111].

2.4.1. Definitions of non-Markovianity

The strictest definition of Markovianity declares that a time evolution is Markovian or memoryless if and only if it can be split at any time s such that $\Pi(t) = \Pi(t-s)\Pi(s)$ for all $t > s > 0$, breaking all correlations between local system and reservoirs at time s. If this relation is fulfilled, the evolution from time s to t depends solely on the state of the local quantum system at time s and not on the previous evolution or on the correlation with the reservoirs at time s. This strict definition of Markovianity is called semigroup divisibility because only semigroup evolutions — $\Pi(t) = e^{-i\mathcal{G}t}$ with constant generator $\mathcal{G}$ — are Markovian in this sense.

A less restrictive definition of Markovianity is the CP-divisibility of the dynamics [108–111]. The main idea behind this approach is the following. If the evolution of a system between any two times t_1 and t_2 were allowed for *some* physical system that has no correlation with the reservoirs at time t_1, then the memory effects must be weak. On the other hand, if for every

[17] The general sum rule for jump rates due to fermionic duality is $\sum_{mi} j_i^{mn}(t) = d_n\Gamma + \sum_{mi}(-1)^{n+m} j_i^{nm}(t)$ in each subspace n. Summing over n yields the sum rule $\sum_{nmi} j_i^{nm}(t)[1 - (-1)^{n+m}] = d\Gamma$ in which only jump rates of parity-changing jump operators $[(-1)^{n+m} = -1]$ play a role [2, 93].

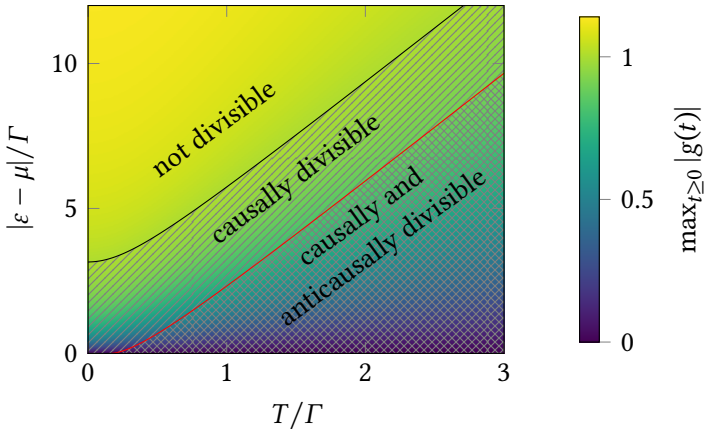

Figure 2.1.: Overview of parameter $\max_{t\geq 0} |g(t)|$ in the jump rates of the single reservoir resonant level model that indicates causal divisibility of both $\Pi(t)$ and $\Pi^{\mathrm{red}}(t)$. The model has causally divisible dynamics if $|g(t)| \leq 1$ for all times. The boundaries of the parameter regimes of causal and anticausal divisibility are marked by black and red curves, respectively. See figure 2.2 for the construction of the red curve.

possible physical system the evolution from time t_1 to t_2 can only be explained by the presence of correlations with some environment or reservoirs, then this memory must be relevant and the system is called non-Markovian. Mathematically, this reasoning is formulated by defining a divisor $\Pi_D(t_2, t_1) = \Pi(t_2)\Pi^{-1}(t_1)$ that continues an evolution that was interrupted at time t_1. If $\Pi_D(t_2, t_1)$ is CP for all times $t_2 > t_1$, then the evolution is called CP-divisible. The CP-property of the divisor $\Pi_D(t_2, t_1)$ can be understood as the possibility of a simulation task. If $\Pi_D(t_2, t_1)$ can be simulated by some setup in which at time t_1 system and environment are decoupled, then the evolution is CP-divisible. A seminal result is that this is the case if and only if the jump rates $j_i(t)$ of the full generator $\mathcal{G}(t)$ are nonnegative for all times t [108–110, 112].[18] Thus, the sign of the jump rates indicates how strong the memory effects in the system are. We call an evolution fulfilling this definition of Markovianity causally divisible. The resonant level model has causally divisible dynamics in the parameter region shown in figure 2.1, which is determined by the parameter $g(t)$ appearing in the jump rates.

We recall from section 2.3.1 that when discussing complete positivity it makes a difference whether we consider the full propagator $\Pi(t)$ or the reduced propagator $\Pi^{\mathrm{red}}(t)$. For both, one can define a divisor and CP-divisibility, which is determined using the jump rates of either the full or the reduced generator. One can show that CP-divisibility of the full evolution always implies CP-divisibility of the reduced evolution.[19] Thus, compared to the common definition of CP-divisibility by the full evolution, CP-divisibility of the reduced evolution is a weaker criterion which only considers the evolution of states that are allowed by conservation laws. The following discussion of CP-divisibility in Schrödinger and Heisenberg picture is valid for both definitions via the reduced or the full evolution.

2.4.2. Divisibility in the Schrödinger and Heisenberg picture

The definition of divisibility discussed so far only considers the evolution of states in the Schrödinger picture. But one can construct an analogous criterion for memory effects in the

[18] This follows from the form $\Pi_D(t_2, t_1) = \mathcal{T}_{\leftarrow} \exp\left[-i \int_{t_1}^{t_2} ds\, \mathcal{G}(s)\right]$ of the divisor.

[19] In appendix C.2 we show that complete positivity of $\Pi(t)$ implies complete positivity of $\Pi^{\mathrm{red}}(t)$. The same proof can be used to show that if $\Pi_D(t, s)$ is CP, then also $\Pi_D^{\mathrm{red}}(t, s)$ is CP.

Heisenberg picture. Surprisingly, the divisibility criteria in the Schrödinger and Heisenberg picture can be quite different. In the Schrödinger picture, we think of the time evolution of states with a causal order such that the state $\rho(t+\Delta t)$ shortly after time t mainly depends on $\rho(t)$. In an evolution without memory, the divisor $\Pi_D(t+\Delta t,t)=\Pi(t+\Delta t)\Pi(t)^{-1}$ bringing states from time t to $t+\Delta t$ is a valid evolution map and thereby CP. This quantifies that the evolution from time t to $t+\Delta t$ is not dominated by memory, which could make the state at time $t+\Delta t$ strongly depend on earlier times.

In contrast, in the Heisenberg picture, the state of the system is kept constant and observables evolve in time. In analogy to the Schrödinger picture, an observable $A(t+\Delta t)$ measured shortly after time t should mainly depend on the same observable $A(t)$ at an earlier time. The dependence on $A(s)$ at times $s<t$ can be understood as a different type of memory. In terms of the observable propagator $\Pi^H(t)$ — which is CP like $\Pi(t)$ — we expect that without strong memory effects the map $\Pi_D^H(t+\Delta t,t):=\Pi^H(t+\Delta t)\Pi^H(t)^{-1}$ from $A(t)$ to $A(t+\Delta t)$ should be CP and thereby a valid evolution map for observables. Here we defined a divisor in analogy to the Schrödinger picture, and we call the evolution anticausally divisible if $\Pi_D^H(t_2,t_1)$ is CP for all times $t_2>t_1$. Although this definition follows very similar arguments, the Heisenberg picture divisor $\Pi_D^H(t_2,t_1)=[\Pi(t_1)^{-1}\Pi(t_2)]^\dagger$ differs from the Schrödinger picture divisor $\Pi_D(t_2,t_1)=\Pi(t_2)\Pi(t_1)^{-1}$ because $\Pi(t_1)^{-1}$ and $\Pi(t_2)$ in general do not commute. This has the consequence that causal and anticausal divisibility are, in general, very different criteria, as we can see for the resonant level model in figure 2.1. Analogous to the causal divisibility, an evolution is anticausally divisible if all Heisenberg picture jump rates $j_i^H(t)$ are nonnegative for all times t [2].[20]

When thinking of the evolution of states, the Heisenberg picture divisor seems to have reverse causal order. The map $\Pi_D^H(t_2,t_1)^\dagger=\Pi(t_1)^{-1}\Pi(t_2)$ describes first an evolution of states from 0 to t_2 followed by the reverse evolution from t_1 to 0. Formulated as a simulation task in the Schrödinger picture, the anticausal divisibility requires that some physically allowed time evolution can bring the system into a state at time $t_1<t_2$ such that the normal time evolution starting from time t_1 will yield the same state at time t_2 as the evolution from 0 to t_2 with the physical system would yield. The uncommon order of forward and backward evolution in $\Pi_D^H(t_2,t_1)^\dagger$ and the rather complicated simulation task illustrate that the anticausal divisibility is unintuitive in the common description of quantum mechanics, in which states evolve while observables are constant. These issues arise because when working in the Schrödinger picture, we commonly think of $\Pi(t)$ as a time-ordered map which can naturally be split into successive evolutions over short time intervals. This is expressed in the form $\Pi(t)=\mathcal{T}_{\leftarrow}\exp\big[-i\int_0^t ds\,\mathcal{G}(s)\big]$. Since $\Pi^H(t)$ is the adjoint of $\Pi(t)$, it has the reverse time order when constructing $\Pi^H(t)$ based on $\Pi(t)$. But when directly constructing the evolution map in the Heisenberg picture, one can find a time-ordered form for $\Pi^H(t)$, which we formulate as $\Pi^H(t)=\mathcal{T}_{\leftarrow}\exp\big[i\int_0^t ds\,\mathcal{G}^H(s)\big]$. Thus, anticausal divisibility is a criterion that naturally arises when working only in the Heisenberg picture, but which is far from obvious when constructing the Heisenberg picture propagator from the Schrödinger picture.

[20] The Heisenberg picture divisor fulfills $\Pi_D^H(t_2,t_1)=\mathcal{T}_{\leftarrow}\exp\big[i\int_{t_1}^{t_2} ds\,\mathcal{G}^H(s)\big]$, which leads to this result.

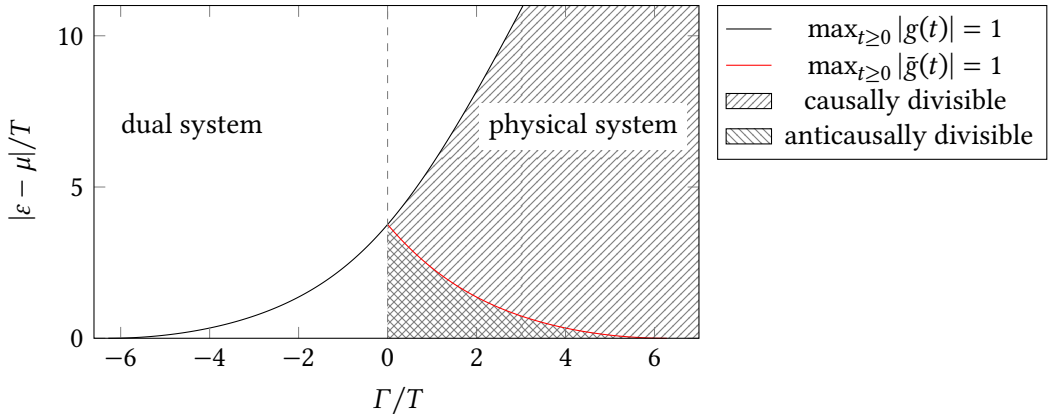

Figure 2.2.: Causal and anticausal divisibility in joint plot of physical and dual parameter regime with positive and negative coupling rate Γ, respectively. We only define divisibility for the physical system ($\Gamma \geq 0$). The region of causal divisibility is limited by the black curve where $\max_{t\geq 0} |g(t)| = 1$. This curve remains well-defined for negative Γ. By mirroring the black curve at $\Gamma = 0$ we obtain the red curve of $\max_{t\geq 0} |\bar{g}(t)| = 1$, which marks the boundary of the anticausally divisible parameter region. The red curve ends at $\Gamma = 2\pi T$, where $\max_{t\geq 0} |\bar{g}(t)|$ diverges if $\varepsilon - \mu \neq 0$.

2.4.3. Divisibility of the resonant level model

The difference between the two definitions of divisibility can be understood best for an example system. In figure 2.1 the parameter regions of causal and anticausal divisibility are shown for the resonant level model with a single reservoir. One can see that the region of causal divisibility is larger and includes the region of anticausal divisibility, making anticausal divisibility the stricter criterion for this model. The strictest criterion of semigroup divisibility is only fulfilled at $\varepsilon - \mu = 0$ and always implies causal and anticausal divisibility. In this simple model, the reduced evolution $\Pi^{\text{red}}(t)$ is CP-divisible if and only if $\Pi(t)$ is CP-divisible.

To understand whether a system has anticausally divisible dynamics, we need to analyze its Heisenberg picture generator. As discussed before, this generator can be calculated easily from the Schrödinger picture for systems obeying fermionic duality, but obtaining it without the duality trick is much more cumbersome. Figure 2.2 illustrates how fermionic duality determines for which parameters the resonant level model has anticausally divisible dynamics. When plotting quantities like $g(t)$ as a function of Γ and $|\varepsilon - \mu|$ we can view the dual system ($\Gamma < 0$) as an analytic continuation of the physical system ($\Gamma \geq 0$). The curve separating the region of causal divisibility from the non-divisible region also has an analytic continuation to the dual system. By mirroring this curve at $\Gamma = 0$ we obtain the boundary of the anticausally divisible parameter region in the physical system. This illustrates how fermionic duality is deeply connected to analytic properties of the model.

The resonant level model shows that although both causal and anticausal divisibility are defined analogously in two different views on the dynamics, they are very different criteria for categorizing memory effects. Fermionic duality makes it much simpler to compare both criteria. The abstract discussion of Markovianity in the present section will be complemented by a practical analysis of memory effects visible in transport observables in section 3.4.

2.5. Renormalized perturbation theory

The duality relation is useful for exact analytic results [2, 93] and for calculations using the approximation of weak coupling [85–92]. But when studying open quantum systems, one often works with approximate results beyond the weak coupling approximation, which are not guaranteed to obey fermionic duality. When expanding the effective Liouvillian [or memory kernel, see Eq. (1.1)] or the propagator $\Pi(t)$ in the coupling and truncating this expansion, fermionic duality will in general not hold anymore. An approach which does obey fermionic duality in a truncated expansion is the renormalized perturbation theory of Refs. [103, 104]. This method defines an expansion in the coupling around the infinite temperature solution in such a way that fermionic duality holds order by order, and was used in the original derivation of fermionic duality [85]. This renormalized perturbation theory is suited for fermionic open quantum systems in the wideband limit in nonequilibrium that obey the fermion superselection principle, and has been used in a recent renormalization group approach [113]. A detailed proof of fermionic duality using this method can be found in Refs. [85, 93]. Here we review the main ideas of this renormalized perturbation theory, which is applied in appendix B to compute transport properties of the resonant level model with multiple reservoirs.

At the core of this renormalized perturbation theory is the idea of using second quantization in Liouville space. With this aim, one defines so-called causal superfermions [103, 104]

$$G^q_{\eta l} = \frac{1}{\sqrt{2}}\left[d_{\eta l} + q(-\mathbb{1})^N \bullet (-\mathbb{1})^N d_{\eta l}\right], \tag{2.43}$$

$$J^q_{\eta\alpha\omega} = \frac{1}{\sqrt{2}}\left[c_{\eta\alpha\omega} + q(-\mathbb{1})^{N_R} \bullet (-\mathbb{1})^{N_R} c_{\eta\alpha\omega}\right] \tag{2.44}$$

for system and reservoirs, which have a causality index q additional to the particle-hole index η. Like fermion creation and annihilation operators, these superoperators square to zero and can be combined to products which form a complete basis for the superoperator space. Moreover, for the reservoir superoperators $J^q_{\eta\alpha\omega}$ a variant of Wick's theorem can be derived. A term of the form $\mathrm{tr}_R(J^{q_1}_{\eta_1\alpha_1\omega_1}\cdots J^{q_n}_{\eta_n\alpha_n\omega_n}\rho_R)$ can be computed by finding all possible pair contractions of these superoperators.

To understand how to compute the propagator using these superfermions, we start from the formal solution

$$\Pi(t) = \operatorname*{tr}_R e^{-i(L_S+L_R+L_V)t}(\bullet \otimes \rho_R) \tag{2.45}$$

where bare Liouvillians $L_S = [H_S, \bullet]$, $L_R = [H_R, \bullet]$ and $L_V = [H_V, \bullet]$ are used instead of Hamiltonians. Next one expands in L_V, expresses L_V in terms of causal superfermions, and defines an interaction picture for causal superfermions by

$$J^q_{\eta\alpha}(t) = \int d\omega\, e^{iL_R t} J^q_{\eta\alpha\omega} e^{-iL_R t}. \tag{2.46}$$

For a hopping term of the form in Eq. (2.5) the expansion then takes the form

$$\Pi(t) = \sum_n \int_{t>t_n>\ldots>t_1>0} dt_n \ldots dt_1\, [\text{local system part}(t, t_n, \ldots, t_1)] \operatorname*{tr}_R J^{q_n}_{\eta_n\alpha_n}(t_n)\cdots J^{q_1}_{\eta_1\alpha_1}(t_1)\rho_R. \tag{2.47}$$

Here we focus on the reservoir part. A central property of the superfermions is that Wick's theorem now allows only two types of contractions:

$$\operatorname*{tr}_R J^-_{\eta\alpha}(t) J^-_{-\eta\alpha}(s)\rho_R \propto \frac{T_\alpha}{\sinh\left(\pi T_\alpha[t-s]\right)}, \tag{2.48}$$

$$\operatorname*{tr}_R J^-_{\eta\alpha}(t) J^+_{-\eta\alpha}(s)\rho_R \propto \delta(t-s). \tag{2.49}$$

Thus, half of the contractions are local in time, and all remaining time-nonlocal contractions vanish in the infinite temperature limit. As explained in detail in Refs. [103, 104] one can now first sum up all time-local contractions. The remaining terms constitute an expansion of $\Pi(t)$ around its infinite temperature limit. We spare the details of calculating the evolution of the local system in Eq. (2.47), but note that by first summing up the time-local contributions, we reduce the number of terms that appear in this calculation.

In the expansion of $\Pi(t)$ around its infinite temperature limit, fermionic duality holds for each expansion order.[21] For systems that are not exactly solvable, one can thus calculate the memory kernel by truncating the series expansion at some order in H_V. Remarkably, for the resonant level model the leading order of this renormalized expansion of the effective Liouvillian and of the generator $\mathcal{G}(t)$ is exact, and also for the $U = 0$ Anderson model [see Eq. (3.1)] the generator remains exact in leading order [114].

This renormalized perturbation theory illustrates the idea of renormalization in a single discrete step. Instead of expanding the dynamics around the bare theory of a decoupled system ($H_V = 0$), one approaches the solution in two steps. The first step — a renormalization step — brings us from the bare theory to the infinite temperature solution with the aim of simplifying the further calculation towards finite temperature. This step does not involve any approximations. In the second step, we calculate the finite temperature result and benefit from the renormalization step, which reduces the number of terms in the expansion. The idea of approaching the solution in renormalization steps that involve only few approximations also appears in RG methods. One typically uses not just discrete renormalization steps, but combines infinitesimal steps to an RG flow in which the effective Liouvillian is continuously updated. For example, in the T-flow RG one starts from the infinite temperature solution and then continuously lowers the temperature to describe the dynamics at finite temperature [113]. Such methods have many advantages, such as the ability to include different energy scales in the description and to describe even highly correlated systems such as the Kondo model, as we will see in the remaining chapters of this thesis.

2.6. Summary

Fermionic duality is an exact relation that connects the Heisenberg picture of the dynamics to an unphysical dual system in the Schrödinger picture, which can be obtained from the physical system by a simple parameter substitution. This relation can be used to simplify the analytic

[21] When calculating the dynamics, one usually calculates first the effective Liouvillian as defined in Eq. (1.1). For the effective Liouvillian calculated using this renormalized perturbation theory, fermionic duality also holds for every truncation order of the expansion around the infinite temperature result.

description of a large class of fermionic open quantum systems. Fermionic duality was originally derived using a renormalized perturbation theory in Liouville space [85]. This method is well suited to study open fermionic quantum systems in the wideband limit and obeys the duality relation order by order in a perturbative expansion, in contrast to most other methods. Here we complemented the original derivation with a new proof of the duality relation, which is closer adapted to quantum information formulations of open system dynamics.

We reviewed how for open quantum systems symmetries and conservation laws restrict the set of physically allowed states and split the state space into subspaces. Restricting the description of the dynamics to these subspaces can lead to simplifications, such as simpler Kraus and jump operators. Going beyond Refs. [2, 93], we showed how fermionic duality can be used for these subspaces to further simplify calculations. For the noninteracting resonant level model, one can directly obtain normalized Kraus operators and Lindblad jump operators only from knowing the Hilbert space of the local system and the fermion superselection principle. Using the fermionic duality, the normalization coefficients of all Kraus operators and all jump rates can be obtained from just two scalar functions of time.

The jump rates can be used to quantify the memory or Markovianity of the dynamics. Fermionic duality makes it possible to obtain the jump rates in the Heisenberg picture from those in the Schrödinger picture by a simple parameter substitution. Without fermionic duality, this would require a considerable effort. Like in Schrödinger picture, also the Heisenberg picture jump rates can indicate the presence of memory and a non-standard type of non-Markovianity. The example of the resonant level model indicates that the jump rates in the Heisenberg picture provide a more sensitive measure for the presence of memory than CP-divisibility in the Schrödinger picture.

3. Periodically driven Kondo model

In this chapter, we turn to quantum dots in a regime where quantum many-body effects are especially prominent. The Kondo model describes a limiting case of a quantum dot in which a strongly correlated quantum state is formed by the dot and the reservoirs. This affects observables like the current and challenges the intuitive classical understanding of electron transport. Here, we introduce this model and analyze its response to different periodic bias voltage profiles. The results are obtained using the FRTRG method that will be discussed in full detail in chapters 4 and 5. For harmonic driving, we compare our results to more qualitative methods and to experiments. Finally, using a pulsed voltage, we aim to gain a better understanding of memory effects in the system. The results presented here have been published in Ref. [3] except for section 3.2.3 and figure 3.6.

3.1. Model

The Kondo model describes a limiting case of a quantum dot [115, 116]. The physical system of interest is a small quantum dot with large level spacing and strong Coulomb repulsion of the on-site electrons, which is coupled to two metallic leads. Such systems can be realized in two-dimensional electron gases [8, 9, 81, 117–121], in carbon nanotubes [11–15], in single-molecule transistors [16, 17, 122, 123], and in bilayer graphene [29]. In such a system at very low temperature, almost all electron levels of the dot are either always occupied or never reached, as illustrated in figure 3.1(a). The dot energy levels can be tuned by applying a gate voltage to the dot such that due to the strong Coulomb repulsion, one electron level is always occupied by exactly one electron as depicted in figure 3.1(b). In this Coulomb blockade regime, a classical description predicts a complete suppression of conductance through the quantum dot at low temperature because no electron has enough energy to hop onto or out of the dot and the coupling energy is insufficient to overcome this constraint. Without extra energy, no electron can get from one reservoir to the other one through the quantum dot. But quantum mechanics allows for virtual processes in which a high-energy state is occupied for a very short time. The Kondo model describes the low-energy physics of such a quantum dot, where these virtual processes are dominant and lead to an interesting strongly correlated quantum state. Here we briefly review how the model is derived and motivate its low-energy physics, mostly following Ref. [124].

The Kondo model is not only realized in quantum dots, but was originally developed to describe electron scattering at magnetic impurities in dilute magnetic alloys at low temperature [125]. In such materials, the Kondo effect leads to a higher resistivity at very low temperature [126]. The Kondo model is also realized in single atoms or molecules forming a localized magnetic moment on a surface, where signatures of the Kondo model can be detected using a scanning

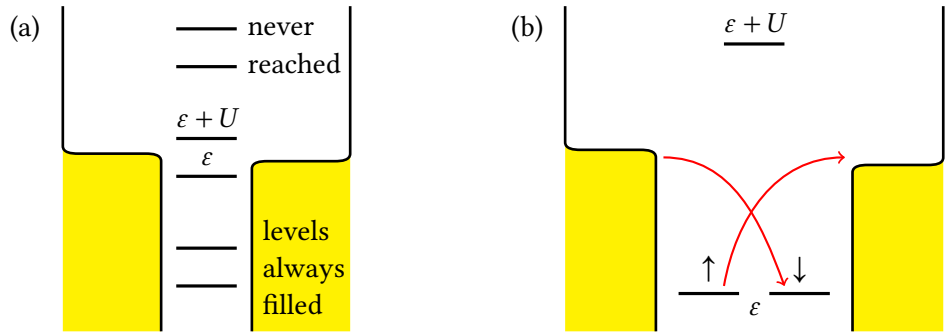

Figure 3.1.: (a) Ground state energies in a spin-degenerate quantum dot in the Coulomb blockade regime, coupled to two reservoirs (left and right). Horizontal lines indicate the energy required for adding a single electron to the dot for different occupancies of the dot. The dot fills with electrons as long as this energy lies below the Fermi level. Energies deep in the Fermi sea or far above the Fermi level correspond to occupancies that are never reached and can be ignored. In the depicted quantum dot, removing an electron costs energy $-\varepsilon > 0$ and adding an electron costs $U + \varepsilon > 0$. (b) Ignoring all configurations that are never reached, we obtain the Anderson model describing a single spin-degenerate level with strong Coulomb interaction. In the Kondo limit, the dot is always occupied by exactly one electron because the energies $-\varepsilon$ and $U + \varepsilon$ for removing or adding an electron are high. A spin-flipping cotunneling process bringing an electron from the left to the right reservoir is indicated by red arrows. In such virtual processes, a high-energy state is occupied for a very short time. For illustration of this process, we display the spin configuration separately. The Kondo model is an effective description for the two low-lying states ↑ and ↓, in which these virtual processes are included in an effective description.

tunneling microscope (STM) [127–135]. But here we focus on the realization in quantum dots in the Coulomb blockade regime, because in such systems a periodically driven Kondo model has been realized experimentally [18, 81–84].

3.1.1. Derivation of the Kondo model

To derive the Kondo model for a quantum dot in the Coulomb blockade regime, we start from the Anderson model [136], for which we sketched some relevant energies in figure 3.1(b). The Anderson Hamiltonian

$$H_{\text{Anderson}} = \sum_{k\sigma\alpha} (\epsilon_{k\alpha} + \mu_\alpha) c^\dagger_{k\sigma\alpha} c_{k\sigma\alpha} + \sum_{k\sigma\alpha} (v_\alpha c^\dagger_{k\sigma\alpha} d_\sigma + \text{H.c.}) + \varepsilon \sum_\sigma d^\dagger_\sigma d_\sigma + U d^\dagger_\uparrow d_\uparrow d^\dagger_\downarrow d_\downarrow \tag{3.1}$$

describes a single-level quantum dot with spin-degenerate dot level $\varepsilon < 0$ and on-site repulsion energy $U > |\varepsilon|$ coupled to two reservoirs labeled $\alpha = L, R$ with reservoir energies $\epsilon_{k\alpha}$ and chemical potentials μ_α. Here $c^{(\dagger)}_{k\sigma\alpha}$ are creation and annihilation operators in reservoirs α with spin σ and momentum k, and $d^{(\dagger)}_\sigma$ are creation and annihilation operators on the quantum dot.

In the Anderson model, we use different approximations that become valid when focussing on low-energy physics. As indicated in figure 3.1(a), it is often sufficient to consider a single electron level quantum dot when a large level spacing of a realistic dot ensures that only a single level can contribute to the dynamics at very low temperature. In Eq. (3.1) we assume that the coupling

between dot and reservoirs described by the hopping term with coefficients v_α is independent of momentum or energy of the reservoir electrons. This approximation is justified because the coupling strength typically varies on energy scales that are much larger than the low-energy scales which we consider here. For the same reason, we also consider wideband reservoirs here like in chapter 2, but we will see in section 3.1.2 that the reservoirs in the Kondo model should have a large but finite bandwidth. Thus, the relatively simple form of the Anderson Hamiltonian is a consequence of our focus on the low-energy physics. We will now extract the low-energy physics of the Anderson model and thereby reduce it further to the Kondo model.

To reach the Kondo regime, we assume that the level ε lies deep in the Fermi sea while $U+\varepsilon$ lies far above the Fermi level as sketched in figure 3.1(b). This defines a separation of energy scales, with a high-energy sector defined by $-\varepsilon$ and $U+\varepsilon$. Here we measure level energies relative to the Fermi level. On the low-energy scale we have the hopping parameters $|v_\alpha|$, the reservoir temperature, and the voltage included in the chemical potentials μ_α. Processes involving the high-energy sector — such as an electron hopping onto the dot and back — can only occur as virtual processes. The Kondo model describes the effective low-energy physics through a Hamiltonian which only considers the two low-energy states (↑ and ↓) and includes the effect of the virtual processes on these low-energy states in an effective coupling term. The virtual tunneling processes of electrons hopping from the reservoirs onto the dot and back have amplitudes of the order of $|v_\alpha v_{\alpha'}|/(-\varepsilon)$ or $|v_\alpha v_{\alpha'}|/(U+\varepsilon)$ where α and α' are the involved reservoirs. These tunneling processes can either leave the spin of the dot unchanged, or flip the dot spin. In figure 3.1(b) a spin-flipping process is illustrated. Such virtual processes lead to the screening of the spin on the dot and couple the reservoirs if multiple reservoirs are connected to the dot.

A derivation of the low-energy Hamiltonian by a Schrieffer-Wolff transformation [137] is reviewed in appendix D and leads to the Kondo Hamiltonian

$$H = \int d\omega \sum_{\sigma\alpha} (\omega + \mu_\alpha) c^\dagger_{\omega\sigma\alpha} c_{\omega\sigma\alpha} + \frac{1}{2} \sum_{\alpha\alpha'\sigma\sigma'} \bar{J}_{\alpha\alpha'} \mathbf{S}\cdot\boldsymbol{\sigma}_{\sigma\sigma'} \iint d\omega\, d\omega'\, c^\dagger_{\omega\sigma\alpha} c_{\omega'\sigma'\alpha'}, \tag{3.2}$$

which contains the essence of the low-energy physics. In this thesis, we apply the FRTRG directly to this Hamiltonian and not the previously discussed Anderson Hamiltonian. In the Kondo Hamiltonian, we ignore a potential scattering term for electron cotunneling that does not couple to the dot spin (see appendix D). This term only has a small contribution to the conductance through the dot when the coupling v_α between dot and reservoirs is small [138, 139]. Below we will focus on the limit $v_\alpha \to 0$ such that neglecting this term is well justified.

The exchange coupling matrix appearing in the Kondo Hamiltonian due to the virtual tunneling is given by

$$\bar{J}_{\alpha\alpha'} = 2 v_\alpha v^*_{\alpha'} \sqrt{\varrho_\alpha \varrho_{\alpha'}} \left(\frac{1}{-\varepsilon} + \frac{1}{U+\varepsilon} \right). \tag{3.3}$$

The phases of the couplings v_α can be absorbed into the phase of the reservoir operators $c_{\omega\sigma\alpha}$, such that we can assume that $\bar{J}_{\alpha\alpha'}$ is a real symmetric matrix. We parametrize this coupling matrix by a scalar coupling J and asymmetry factors, $\bar{J}_{\alpha\alpha'} = 2\sqrt{x_\alpha x_{\alpha'}} J$, where $x_L + x_R = 1$. By ϱ_α we denote the density of state in reservoir α, which is approximately constant at the Fermi energy. Thinking of the underlying Anderson model, we can interpret the coefficients x_α as prefactors

of the coupling rates, $\Gamma_\alpha \propto x_\alpha$ with $\Gamma_\alpha \propto |\nu_\alpha|^2$ defined as in chapter 2. In all results presented here we assume symmetric coupling with $\bar{J}_{\alpha\alpha'} = J$ except when the asymmetry is explicitly specified. Remembering that $|\varepsilon|$ and $U + \varepsilon$ are large energies and $|\nu_\alpha|^2$ is small, we find that the bare coupling J must be small. But we will see below that a weak bare coupling J can lead to a strong effective coupling and an, at first sight, surprisingly high differential conductance.

3.1.2. Poor man scaling

What makes the Kondo model especially interesting is a strong effective coupling of the quantum dot to the reservoirs at low energies. Virtual cotunneling processes involving states with relatively high energies affect the low-energy physics such that in an effective low-energy description the coupling is increased. This effect and the emergence of a strong coupling regime can be understood qualitatively using Anderson's poor man's scaling approach [63], which furthermore illustrates concepts of RG methods.

In the Kondo model with finite bare coupling J we need to consider a finite reservoir bandwidth, as the following calculation will show. In the poor man's scaling approach, we consider a hard cutoff for the reservoir density of states at energy D. Thus, the reservoirs have a constant density of states in the energy range $\omega \in [-D, D]$ and no states outside this energy window. Now we want to reduce the high-energy cutoff to $D' = D - \delta D$ and modify the Hamiltonian such that the low-energy physics remains unchanged. We will see that in the Hamiltonian we only need to change the coupling. This leads to an effective coupling $J(D)$ which increases as D is lowered. We assume that both reservoirs have the same chemical potential and zero temperature.

As just outlined, we need to calculate an effective Hamiltonian that includes the effect of reservoir states in the energy window $|\omega| \in (D - \delta D, D]$ on states with lower energy. In leading order in the coupling, there are two processes through which states in this energy window contribute to the effective Hamiltonian. A low-energy electron, i.e., a reservoir electron near the Fermi level, can be scattered to the energy range $(D - \delta D, D]$ before it is scattered back to low energy. In the second process, an electron deep in the Fermi sea can be scattered to a state near the Fermi level and a low-energy electron fills the hole in the Fermi sea.

The contribution of these processes to the effective Hamiltonian can be computed using the T-matrix formalism, see appendix D.3 for a brief derivation. In the T-matrix formalism, we start from those matrix elements or matrix blocks of the Hamiltonian which describe the transition from a low-energy reservoir state to a high-energy reservoir state and vice versa. For an electron scattering from the state (α, σ, ω) to $(\alpha', \sigma', \omega')$, this matrix block is given by the operator

$$V_{\alpha'\sigma',\alpha\sigma} = \frac{1}{2}\bar{J}_{\alpha'\alpha}\mathbf{S}\cdot\boldsymbol{\sigma}_{\sigma'\sigma}. \tag{3.4}$$

This is a matrix element in reservoir state space, and an operator on the Hilbert space of the local system. For a virtual process in which a reservoir electron is scattered from state (α, σ, ω) to $(\alpha', \sigma', \omega')$ via the energy window $(D - \delta D, D]$, the T-matrix formalism yields the effective coupling term (see appendix D.3)

$$\delta H_{\alpha'\sigma'\omega',\alpha\sigma\omega} = \int_{D-\delta D}^{D} d\omega'' \sum_{\alpha''\sigma''} \frac{1}{2}\left(\frac{V^\dagger_{\alpha'\sigma',\alpha''\sigma''}V_{\alpha''\sigma'',\alpha\sigma}}{\omega' - \omega''} + \frac{V^\dagger_{\alpha'\sigma',\alpha''\sigma''}V_{\alpha''\sigma'',\alpha\sigma}}{\omega - \omega''}\right). \tag{3.5}$$

The first process of an electron scattering to a high-energy state and back to the low-energy sector yields an effective coupling term[1]

$$\delta H^{\text{particle}}_{\alpha'\sigma'\omega',\alpha\sigma\omega} = \frac{1}{2}\delta D\left(\frac{1}{\omega'-D}+\frac{1}{\omega-D}\right)\frac{1}{4}(\bar{J}^2)_{\alpha'\alpha}\sum_{ij}(\sigma^i\sigma^j)_{\sigma'\sigma}S^iS^j \tag{3.6}$$

if δD is infinitesimal.

The second process is obtained from the first one by exchanging particles and holes. Scattering a hole with parameters $(\alpha,\bar{\sigma},-\omega)$ — corresponding to an electron state (α,σ,ω) — to a hole $(\alpha',\bar{\sigma}',-\omega')$ is described by the operator $V'_{\alpha'\sigma',\alpha\sigma} = -\bar{J}_{\alpha\alpha'}\mathbf{S}\cdot\boldsymbol{\sigma}_{\sigma\sigma'}/2$. Inserting this scattering term and the hole energies in Eq. (3.5) yields the effective matrix element for holes

$$\delta H^{\text{hole}}_{\alpha\bar{\sigma}-\omega,\alpha'\bar{\sigma}'-\omega'} = \frac{1}{2}\delta D\left(\frac{1}{-\omega'-D}+\frac{1}{-\omega-D}\right)\frac{1}{4}(\bar{J}^2)_{\alpha'\alpha}\sum_{ij}[(\sigma^i)^\top(\sigma^j)^\top]_{\sigma\sigma'}S^iS^j \tag{3.7}$$

for this process. When transforming these results for holes back to matrix elements for particles, we need to take the transpose and obtain another minus sign from the anticommutation of fermionic operators.[2] Focussing on the low-energy physics we can now approximate that $|\omega|,|\omega'|\ll D$, and we can neglect ω and ω' in Eqs. (3.6) and (3.7), such that the total contribution to the effective Hamiltonian simplifies to

$$\begin{aligned}\delta H_{\alpha'\sigma'\omega',\alpha\sigma\omega} &= \delta H^{\text{particle}}_{\alpha'\sigma'\omega',\alpha\sigma\omega} - \delta H^{\text{hole}}_{\alpha'\bar{\sigma}'-\omega',\alpha\bar{\sigma}-\omega} &(3.8)\\ &= -\frac{\delta D}{D}\frac{1}{4}(\bar{J}^2)_{\alpha'\alpha}\sum_{ij}[\sigma^i,\sigma^j]_{\sigma'\sigma}S^iS^j &(3.9)\\ &= \frac{1}{2}\frac{\delta D}{D}(\bar{J}^2)_{\alpha\alpha'}\mathbf{S}\cdot\boldsymbol{\sigma}_{\sigma'\sigma}. &(3.10)\end{aligned}$$

This is of the same form as the coupling term in the original Hamiltonian. Here, we recognize a key idea of many RG methods, which is the self-similarity of a model under a change of an RG flow parameter. In the effective Hamiltonian, only the coupling has to be modified by[3]

$$J(D) - J(D-\delta D) = -2\frac{\delta D}{D}J^2. \tag{3.11}$$

This leads to the differential equation $\partial_D J = -2J^2/D$ with the solution

$$J(D) = \frac{1}{J_0^{-1}+2\log(D/D_0)}, \tag{3.12}$$

in which J_0 and D_0 denote the bare, non-renormalized coupling and bandwidth, respectively. With this poor man's scaling result, we can understand how the effective coupling increases as more and more reservoir states are included in the effective description by lowering the cutoff D.

[1] We use that $\bar{J}$ is a real-symmetric matrix. The adjoint in Eq. (3.5) denotes $V^\dagger_{\alpha\sigma,\alpha'\sigma'} = (V_{\alpha'\sigma',\alpha\sigma})^\dagger$.

[2] In second quantization, this second process is $\delta H^{\text{hole process}} = \sum_{\alpha\alpha'\sigma\sigma'}\iint d\omega d\omega'\,\delta H^{\text{hole}}_{\alpha\bar{\sigma}-\omega,\alpha'\bar{\sigma}'-\omega'}c_{\alpha\sigma\omega}c^\dagger_{\alpha'\sigma'\omega'} = -\sum_{\alpha\alpha'\sigma\sigma'}\iint d\omega d\omega'\,\delta H^{\text{hole}}_{\alpha'\bar{\sigma}'-\omega',\alpha\bar{\sigma}-\omega}c^\dagger_{\alpha\sigma\omega}c_{\alpha'\sigma'\omega'} + \text{const.}$

[3] We use that $\bar{J}_{\alpha\alpha'} = 2\sqrt{x_\alpha x_{\alpha'}}J$ and $\sum_\alpha x_\alpha = 1$.

In the poor man's scaling result, the coupling does not just increase as the cutoff D is decreased, but it even diverges at a fixed value for D. This implies that there exists an emergent energy scale at which our assumption of weak coupling breaks down and the effective Hamiltonian describes a strong coupling problem. This characteristic low-energy scale of the model is called the Kondo temperature. In the strong coupling regime the previous derivation is not valid anymore, but we can estimate the Kondo temperature using the value of D where $J(D)$ diverges:

$$T_K \sim D_0 e^{-\frac{1}{2J_0}}. \tag{3.13}$$

An immediate consequence of this result is that we cannot take the wideband limit of $D_0 \to \infty$ because T_K diverges, except if we send $J_0 \to 0$ at the same time. This explains why perturbation theory in the coupling diverges for the Kondo model when using the simplifications of the wideband limit. A remarkable feature of the poor man's scaling derivation is that the low-energy scale T_K only emerges when including cotunneling processes from a large energy range $[T_K, D_0]$. This property makes the Kondo model a prototypical RG problem because many RG techniques can include the interplay of effects arising on different energy scales.

The scaling idea which leads to Eq. (3.12) has another important implication. All parameter combinations that lead to the same Kondo temperature T_K lie on one RG flow path and should generate the same effective low-energy physics because the RG flow distills the low-energy physics from the model. This implies that when measuring energy in units of the Kondo temperature, the low-energy physics is always the same, independent of all parameters. This property is called universality. In the poor man's scaling picture this result seems exact, but in a more precise description this universality is only found in the limit $J_0 \to 0$ and $D_0 \to \infty$ such that T_K remains finite. Since J_0 is usually small [see Eq. (3.3)], this limit is indeed a physically relevant case. In this case, the details of the high-energy cutoff in the reservoir density of states do not play any role. A smooth function suppressing the reservoir density of states at high energies instead of a hard cutoff may lead to a different Kondo temperature, but does not change the low-energy physics in any other way. Thus, for any physical realization of a quantum dot in the Kondo regime — typically with a complicated density of states which is approximately constant on the scale of T_K — only the Kondo temperature is required to describe the low-energy physics and to calculate observables, such as the current between the two reservoirs.

The poor man's scaling provides a qualitative view on the idea of scaling and the emergence of the low-energy scale T_K. It shows that although the initial coupling J_0 is very small — as derived from the Anderson model — the large reservoirs lead to a strong renormalized coupling at low energies. Even though this poor man's scaling result is qualitatively insightful, it only provides a very rough estimate of T_K. A more precise result is

$$T_K \approx D_0 \sqrt{J_0} e^{-\frac{1}{2J_0}}. \tag{3.14}$$

for the Lorentzian cutoff function $D(\omega) = D_0^2/(D_0^2 + \omega^2)$ of the reservoir density of states [126], which will be recovered using the FRTRG in section 5.2.5.

3.1.3. Equilibrium properties

The strong effective coupling leads to interesting ground state and low-energy properties of the equilibrium Kondo model. These properties have been calculated using Fermi liquid theory [140], the Bethe ansatz [141–146], the numerical renormalization group [64, 147–149], and conformal field theory [150, 151]. Here we briefly review some important results of the spin-$\frac{1}{2}$ Kondo model in and near equilibrium.

The strong effective coupling at low temperature indicates that there will be a strong correlation of the dot spin and the reservoirs. Since the coupling is antiferromagnetic, $\bar{J}_{\alpha\alpha} > 0$, the local spin S and the reservoir spins $\mathrm{S}_{\mathrm{res}} = \sum_{\sigma\sigma'\alpha\alpha'} \iint d\omega\, d\omega' \boldsymbol{\sigma}_{\sigma\sigma'} c^\dagger_{\omega\sigma\alpha} c_{\omega'\sigma'\alpha}$ form a singlet ground state. In this regime with strong effective coupling, tunneling between the two reservoirs becomes resonant. At zero temperature, an incoming electron tunnels to the other reservoir with 100% probability and is never reflected [115, 138, 139]. Thus, for symmetric coupling to the two reservoirs the differential conductance reaches the maximal possible value for a single spin-$\frac{1}{2}$ tunneling channel, $G = 2e^2/h$ [138, 139]. This unitary differential conductance is the most prominent and directly measurable consequence of the Kondo ground state, and has been observed experimentally [119]. It is accompanied by a resonance in the density of states at the Fermi level. It is characteristic of the Kondo model that this resonance is weakened by temperature, such that finite temperature and a bias voltage reduced the differential conductance [115, 116, 152, 153]. As motivated using the poor man's scaling, this suppression follows a universal function $G(T/T_K, V/T_K)$, which does not depend on any details of the quantum dot in which the Kondo model is realized [124, 154, 155]. It is therefore common to define the Kondo temperature by the temperature or bias voltage, at which the differential conductance is reduced to half of its equilibrium value. Since we focus on zero temperature here, we define T_K via a constant bias voltage by

$$G(eV = k_B T_K) = \frac{1}{2} G(V = 0). \tag{3.15}$$

3.2. Harmonic driving

When discussing a periodic bias voltage, we typically consider a harmonic driving of the form

$$V(t) = \mu_L(t) - \mu_R(t) = V_{\mathrm{avg}} + V_{\mathrm{osc}} \cos(\Omega t). \tag{3.16}$$

This driving profile is the simplest case both for experiments and for theoretical descriptions. Figure 3.2 shows an overview of the differential conductance for this driving profile, and in this section we will discuss the different effects visible in this overview.

Different theoretical methods have been applied to the Kondo model with harmonic driving to predict the low-energy physics of quantum dots [156–159], and experiments have measured the conductance though quantum dots in the Kondo limit with this driving profile [18, 81–84]. Like most of these works, we focus our discussion on the differential conductance $G = dI_{\mathrm{avg}}/dV_{\mathrm{avg}}$ for direct current. In Ref. [159], Kaminski, Nazarov, and Glazman derived expressions for the differential conductance through the periodically driven Kondo model in different limiting cases, which provide a qualitative overview over different parameter regimes for $V_{\mathrm{avg}} = 0$. But this

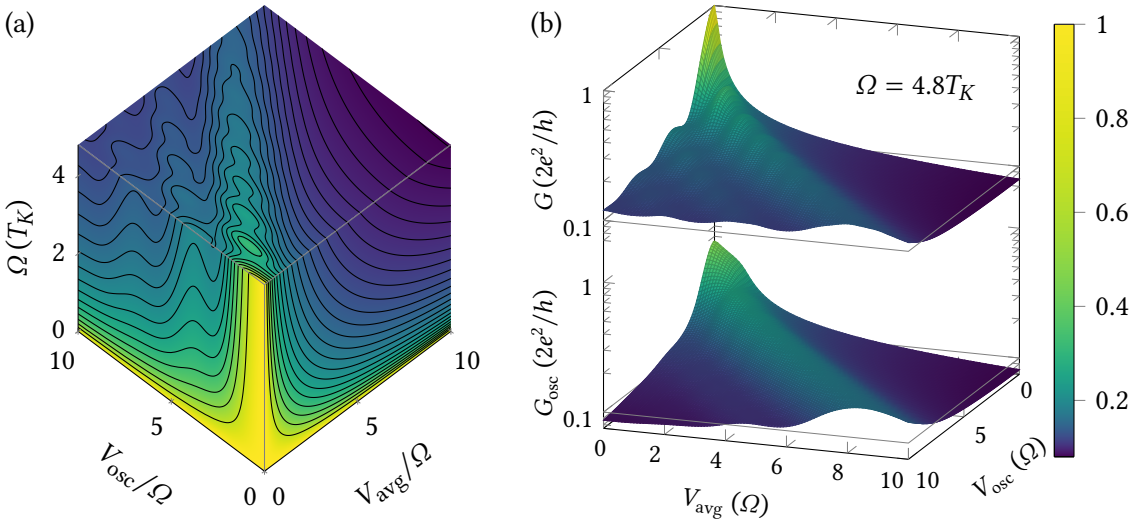

Figure 3.2.: Overview of the differential conductance G through the Kondo model. (a) G with contour lines as a function of $V_{\mathrm{avg}}, V_{\mathrm{osc}}$ and Ω at either $V_{\mathrm{avg}} = 0$, $V_{\mathrm{osc}} = 0$, or $\Omega = 4.8T_K$. The contour lines show $G = (2e^2/h)/n$ for $n = 2, 3, \ldots$. One can see oscillations in G as a function of V_{osc}/Ω and V_{avg}/Ω, which will be explained in section 3.2.2. (b) Differential conductance for direct and alternating current $G = dI_{\mathrm{avg}}/dV_{\mathrm{avg}}$ and $G_{\mathrm{osc}} = dI_{\mathrm{osc}}/dV_{\mathrm{osc}}$ at fixed frequency $\Omega = 4.8T_K$. A peak structure with multiple side peaks is visible in G, while G_{osc} only shows a broad maximum at $V_{\mathrm{avg}} \approx V_{\mathrm{osc}}$.

description does not include the effects of phonon-assisted tunneling that were predicted in Ref. [158] using a perturbative expansion in the coupling and by Ref. [160] using an interpolated effective self-energy. Other works discussed an ac gate voltage modulating the level energy of a quantum dot in the Kondo regime [159–162]. In all these approaches, the decoherence due to the periodic driving could not be considered without simplifying assumptions. Here, we complement these approaches with the FRTRG, which includes the interplay of periodic driving and strong coupling.

3.2.1. Analytic predictions and limiting cases

As mentioned above, the differential conductance through the Kondo model reaches the maximal possible value in equilibrium. When the periodic driving is switched on, G is mainly reduced by two effects. The first one is an overall suppression of the Kondo resonance because the driving adds decoherence and takes the system further away from the strongly correlated Kondo ground state. Stated simply, we are moving away from equilibrium. The second effect is the appearance of photon side bands in the differential conductance. Electrons can get excited by the periodic driving and will then contribute to side resonances of the Kondo resonance where V_{avg} is an integer multiple of the frequency Ω, instead of contributing to the Kondo resonance at $V_{\mathrm{avg}} = 0$. This generally reduces the Kondo peak at $V_{\mathrm{avg}} = 0$. The FRTRG takes both effects into account and provides quantitative results for transport properties, whereas the methods to which we will compare our results below only describe both effects separately.

We first look at the overall suppression of the Kondo resonance due to decoherence. To

this end, we compare our results to the analytic approximations by Kaminski, Nazarov, and Glazman [159], who use expansions around different limiting cases to provide an overview of the differential conductance for $V_{\text{avg}} = 0$. Two intuitive limiting cases are the equilibrium limit found at $V_{\text{avg}}, V_{\text{osc}} \ll T_K$ (arbitrary Ω), and the adiabatic limit $\Omega \ll \max\{V_{\text{osc}}, V_{\text{avg}}, T_K\}$. By adiabatic we mean the limit $\Omega \to 0$, such that the voltage is approximately constant at every time and $G(t) = G[V_{\text{avg}} = V(t)]$. It may seem surprising that for $\Omega \ll V_{\text{osc}}$ the system responds approximately adiabatically to the bias voltage, since Ω may still be larger than the Kondo temperature which is our reference energy scale. However, the large bias voltage adds decoherence and thereby increases the relaxation rate of the Kondo spin such that for sufficiently large bias voltage Ω will be small compared to the relaxation rate. The fast relaxation of the system due to strong decoherence prevents memory effects and the system responds adiabatically. The third limit $\Omega \gg \max\{V_{\text{osc}}, T_K\}$ can also be understood intuitively. On the relevant timescales, the rapid oscillations will average out and can be neglected. Thus, setting $V_{\text{osc}} = 0$ is a good approximation if $\Omega \gg \max\{V_{\text{osc}}, T_K\}$. Kaminski et al. also find expressions for G at smaller Ω or larger V_{osc} by computing the relaxation rate and either treating decoherence perturbatively where it is weak, or using perturbation theory to compute the conductance for stronger decoherence.

A comparison to the expressions in Ref. [159] and to the adiabatic approximation is shown in figure 3.3. Here, the adiabatic approximation is based on a real-time RG[4] calculation at vanishing oscillating voltage. One can see that the adiabatic approximation provides a good estimate of the differential conductance if one of the energy scales V_{avg}, V_{osc}, and T_K is dominant and much larger than the other scales, including frequency. But near $V_{\text{avg}} \approx V_{\text{osc}}$ the adiabatic approximation breaks down unless the driving is slow compared to T_K. The adiabatic approximation predicts a sharp peak of G at $V_{\text{avg}} = V_{\text{osc}}$, but the FRTRG results show a broader peak shifted towards $V_{\text{avg}} < V_{\text{osc}}$. This effect can be relevant for experiments, in which the adiabatic regime can be used to calibrate V_{osc}, as we will see in section 3.3. The approximations by Kaminski et al. for $V_{\text{avg}} = 0$ show good qualitative agreement with our results for most parameter regimes, but significant deviations in the adiabatic limit except at $V_{\text{osc}} \gg T_K$. These deviations originate from the analytic estimate for the differential conductance at constant bias voltage, on which we do not focus in this work. To conclude, the overall suppression of the differential conductance in cases where one energy scale is dominant has been explained and derived analytically in Ref. [159] and the FRTRG qualitatively agrees with these results. But in figure 3.3 we also see oscillations that are ignored by the previously discussed approximations. These will be discussed next using a different physical picture.

3.2.2. Photon-assisted tunneling

The periodic driving leads not only to a suppression of the Kondo resonance, but also to the absorption and emission of photons by reservoir electrons. This shifts the reservoir electron energies by integer multiples of the driving frequency and leads to side peaks of the Kondo resonance in the differential conductance at $V_{\text{avg}} = n\Omega$ where n is an integer. Similar effects have been predicted [163] and observed [164] in quantum dots and are well-known in different

[4]The FRTRG is an extension of this E-flow real-time RG, and both are equivalent at $V_{\text{osc}} = 0$.

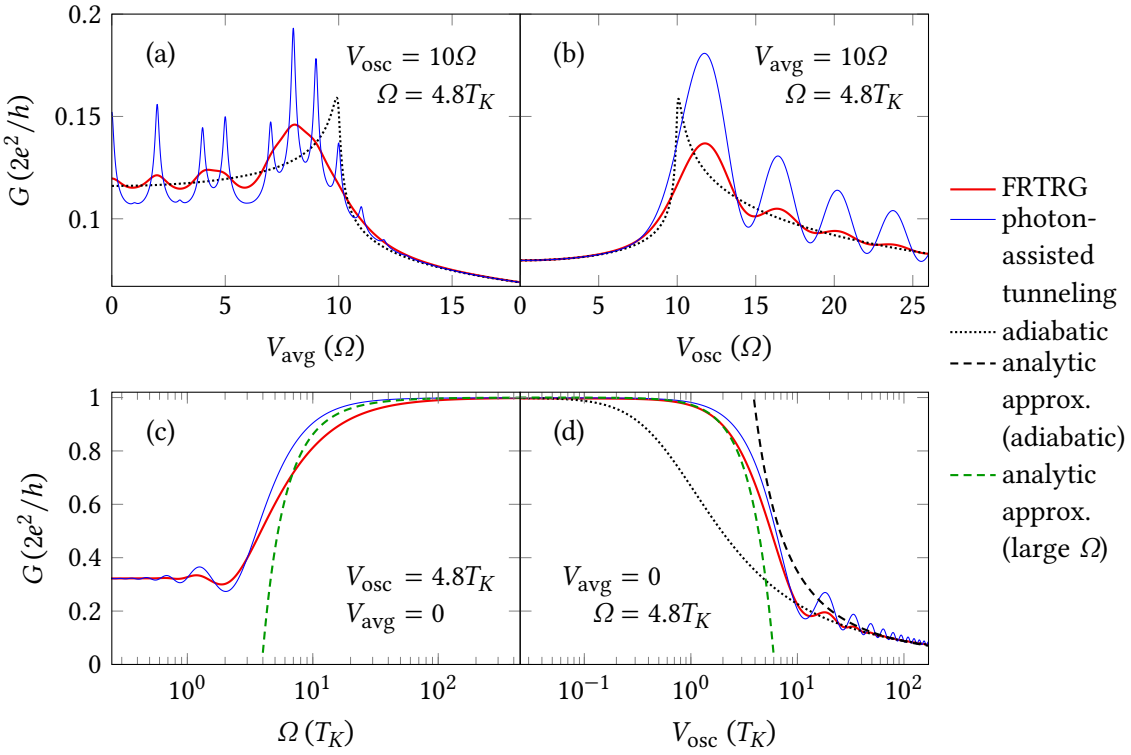

Figure 3.3.: Differential conductance as a function of V_{avg}, V_{osc}, and Ω, calculated with different approaches. (a) Side peaks of the Kondo resonance in $G(V_{\mathrm{avg}})$ at high V_{osc}/Ω. In the FRTRG results (red) the peaks are washed out, but the different weights of different peaks remain visible. The phenomenological Eq. (3.18) (blue) predicts the peaks and their weights, but ignores the decoherence that suppresses them. The adiabatic approximation (dotted) has a sharp peak at $V_{\mathrm{avg}} = V_{\mathrm{osc}}$, which is shifted compared to the maximum in $G(V_{\mathrm{avg}})$ predicted by the FRTRG. Aside from the shifted peak, the adiabatic approximation yields a reasonable estimate because $V_{\mathrm{osc}} \gg \Omega$ is a dominant energy scale. (b) At constant, resonant V_{avg} (V_{avg}/Ω is an integer), the side resonance leads to broad maxima in $G(V_{\mathrm{osc}})$, which are again overestimated in Eq. (3.18). The dominant energy scale $V_{\mathrm{avg}} \gg \Omega$ makes the adiabatic approximation a reasonable estimate. (c) G as a function of Ω at constant V_{osc} starts from the adiabatic limit at low frequency and reaches the unitary conductance for very fast driving. Small oscillations are again due to photon-assisted tunneling and overestimated by the phenomenological approximation. At high frequencies, the analytic result of Ref. [159] predicts a faster convergence to $G = 2e^2/h$. (d) $G(V_{\mathrm{osc}})$ at $V_{\mathrm{avg}} = 0$ again shows small oscillations that qualitatively follow the result calculated for photon-assisted tunneling. The analytic results from Ref. [159] show good agreement except in the transition from weak to strong driving, but do not predict the weak oscillations in $G(V_{\mathrm{osc}})$. The adiabatic approximation becomes valid at very strong driving.

transport models [165]. Subsequently, we will focus on these effects to qualitatively understand the oscillations appearing in figures 3.2 and 3.3.

To this end, we will for now pretend that the oscillating voltage only changes the density of states in the reservoirs. All other effects of the driving, such as the damping of the Kondo resonance due to stronger decoherence, are neglected. To simplify the discussion, we assume that an oscillating voltage is applied to the right reservoirs while the chemical potential of the left reservoir is kept constant. In the Kondo limit, this assumption is justified because only the voltage $\mu_L(t) - \mu_R(t)$ is relevant and a shift in both chemical potentials has no effect.[5] The oscillating chemical potential changes the density of states in the right reservoir through the absorption and emission of photons from the driving field, such that replicas of the equilibrium density of states appear shifted by multiples of the driving frequency (see appendix E). The resulting effective density of states for the right reservoir at energy E is [163]

$$\varrho_R^{\text{eff}}(E) = \sum_n \mathcal{J}_n^2\left(\frac{V_{\text{osc}}}{\Omega}\right)\varrho_R^{\text{eq}}(E + n\Omega), \tag{3.17}$$

where $\mathcal{J}_n$ denotes the n^{th} Bessel function. This has immediate consequences for the differential conductance, which is linear in the density of states of each of the two reservoirs, evaluated at the Fermi level of the respective reservoir. Since the effective density of states in the right reservoir is a linear combination of the density of states at different energies, the same is true for the differential conductance. Thus, when only accounting for photon-assisted tunneling and no other effects of the periodic driving, the differential conductance at finite V_{osc} can be approximated by

$$G(V_{\text{avg}}, V_{\text{osc}}) \approx \sum_{n=-\infty}^{\infty} \mathcal{J}_n^2\left(\frac{V_{\text{osc}}}{\Omega}\right) G(V_{\text{avg}} + n\Omega, 0). \tag{3.18}$$

To evaluate the right-hand side of this phenomenological approximation, we only need to know the differential conductance as a function of a static bias voltage. This crude approximation is a simplified result of a perturbative calculation of the current through the Kondo model by Goldin and Avishai [158] and is shown in blue in figure 3.3. Eq. (3.18) was also shown to be exact for a Kondo model with a nonisotropic coupling chosen in such a way that the model becomes analytically solvable [157].

The qualitative form of Eq. (3.18) is helpful for understanding the results of the FRTRG. First, we note that the Kondo resonance in the conductance in equilibrium will lead to satellite replicas at $V_{\text{avg}} = n\Omega$ where $|n| \lesssim V_{\text{osc}}/\Omega$ is an integer. The weight of these satellite peaks is determined by the Bessel functions $\mathcal{J}_n^2(V_{\text{osc}}/\Omega)$, whose qualitative dependence on n and its argument is well known. These results agree well with the FRTRG analysis, although the peaks are additionally suppressed and broadened by decoherence, as one can see in figure 3.3(a). Using Eq. (3.18), one can predict which peaks are high and which ones are suppressed, but not how high the peaks will actually be. This important question can be addressed with the FRTRG, and we will see below in figure 3.6 that a good quantitative agreement with experiments requires a method like

[5] In the Kondo model, there are no energy levels besides the reservoirs. Thus, a shift of all chemical potentials $\mu_\alpha(t)$ shifts all energy levels and is equivalent to an irrelevant scalar shift in the Hamiltonian.

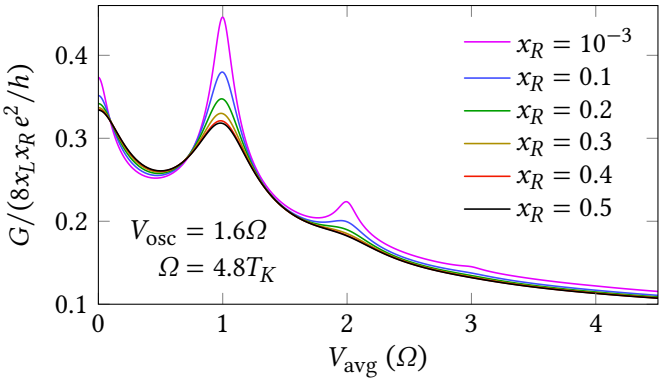

Figure 3.4.: Differential conductance G normalized to the equilibrium value $G(V_{\mathrm{avg}} = V_{\mathrm{osc}} = 0) = 8x_Lx_Re^2/h$ for different values of the asymmetry x_R. The peaks at integer values of V_{avg}/Ω become sharper for higher asymmetry. In the limit of very strong asymmetry — here shown with $x_R = 10^{-3}$ — the curve follows the phenomenological approximation in Eq. (3.18).

the FRTRG that goes beyond Eq. (3.18). There exists, however, a limit in which Eq. (3.18) becomes exact, as we will discuss next.

3.2.3. Asymmetric coupling

The conductance of the Kondo model is not only affected by the voltage $V(t)$, but also by the asymmetry in the coupling to the two reservoirs. Both a balanced coupling [119] and asymmetric coupling [118] can be realized in quantum dots, but a relatively balanced coupling is more common [118]. When realizing the Kondo model in atoms or molecules on surfaces with a bias voltage induced through an STM tip, the asymmetry depends on the distance of the STM tip. In this setup, a strong asymmetry can be realized [128]. The FRTRG can be used to quantitatively compute the conductance with and without asymmetry. Here we discuss the effect of an asymmetry, which can be understood qualitatively using analytic insights.

The dominant effect of an asymmetry is the reduction of the equilibrium conductance to $G = 4x_Lx_R(2e^2/h)$ [115, 116], which follows the intuition that the conductance is proportional to the coupling to each reservoir. Here we recall the notation of asymmetry prefactors $x_\alpha \propto \Gamma_\alpha$ of the coupling rates to the reservoirs, defined such that $x_L + x_R = 1$. Aside from the overall suppression of the conductance, an asymmetry also leads to changes in the dependence of the differential conductance on the bias voltage. To see these effects, we normalize G to its equilibrium value $4x_Lx_R(2e^2/h)$. In figure 3.4 we show that the side peaks in the differential conductance due to photon-assisted tunneling become sharper for more asymmetric coupling. In experiments, this effect may become detectable for $x_L \gtrsim 2x_R$ if V_{osc} is calibrated with sufficient accuracy. We find that the differential conductance normalized to $4x_Lx_R$ always lies between the value for symmetric coupling and a strong asymmetry limit with significantly sharper peaks, which we will discuss next.

To understand the limit $x_R \to 0$ of a strong asymmetry, we assume again for simplicity that the left reservoir is kept at constant chemical potential while the right reservoir is connected to an oscillating potential. A Kondo resonance forms in the density of states of both reservoirs and in the right reservoir the oscillating voltage leads to an effective density of states as in Eq. (3.17). But in contrast to the case of symmetric coupling, the right reservoir is so weakly coupled to the dot that its effective density of states has no significant effect on the left reservoir. This suggests that the approximation in Eq. (3.18) is exact in this limit. Indeed, one can show that

the phenomenological Eq. (3.18) holds term-by-term in a perturbative expansion in the coupling when considering only the leading order in x_R (see appendix F). The FRTRG confirms that Eq. (3.18) is exact in the limit $x_R \to 0$ and furthermore shows that $G(V_{\text{avg}})/(4x_L x_R)$ at $V_{\text{osc}} = 0$ only weakly depends on the asymmetry parameter x_R.

Knowing that in the limit of a strong asymmetry the differential conductance follows Eq. (3.18) which predicts sharp side peaks, we qualitatively understand that an asymmetry will lead to sharper side peaks compared to the balanced coupling. This property of the Kondo model may help to observe side resonances in experiments, as our comparison with experimental data in figure 3.5 suggests. In realistic quantum dots an asymmetry in the coupling is expected to shift the Kondo peak away from zero bias to finite V_{avg} [117, 118, 166]. But in the universal limit of the Kondo model, the particle-hole symmetry prevents such a shift. We therefore cannot see this effect in the FRTRG results.

3.3. Comparison to experiments

A periodically driven Kondo quantum dot has been realized in multiple experiments [18, 81–84]. Here, we compare our results to two of these experiments that have found side peaks of the Kondo resonance in the differential conductance due to photon-assisted tunneling. In 2004, Kogan, Amasha, and Kastner [82] first observed such side peaks in a GaAs quantum dot. In 2018, Bruhat et al. [84] published measurements of the differential conductance through a carbon-nanotube-based quantum dot at multiple frequencies. We compare our predictions to these measurements in figures 3.5 and 3.6, and find excellent quantitative agreement. Other experiments found limited [18] or no indications [81] for the aforementioned side peaks.

3.3.1. Results

In figure 3.5 we compare our prediction to the differential conductance measured by Kogan et al. in a single electron transistor realized in a semiconductor quantum dot at low temperature ($T \sim 0.16 T_K$). The measured values (dots) are compared to FRTRG results for an asymmetrically coupled Kondo model with $x_L = 4x_R$ (colored curves) and for symmetric coupling (black curves). All theoretical predictions in these comparisons are shifted by a constant background conductance and scaled by a prefactor of G to match the experimental values. An asymmetric coupling can partially explain the relatively strong suppression of the Kondo peak in this experiment — by a factor 0.096 in our fit for a symmetrically coupled dot — and leads to sharper peaks, as explained in section 3.2.3. A good agreement between theory and experiment can also be reached when a lower Kondo temperature and a more symmetrically coupled quantum dot is assumed. But here we work with the Kondo temperature estimated based on a measurement at $V_{\text{osc}} = 0$. As will be discussed in more detail below, for this prediction we assumed a correction factor 1.42 for the calibration of V_{osc}.

In figure 3.6, measurements by Bruhat et al. at two different frequencies but in the same quantum dot are shown. In this case, we only consider symmetric coupling to the reservoirs and modify the calibration of V_{osc} by factors 0.89 and 1.07 for frequencies 19 GHz and 12 GHz, respectively. Aside from the modified calibration, the constant background conductance and

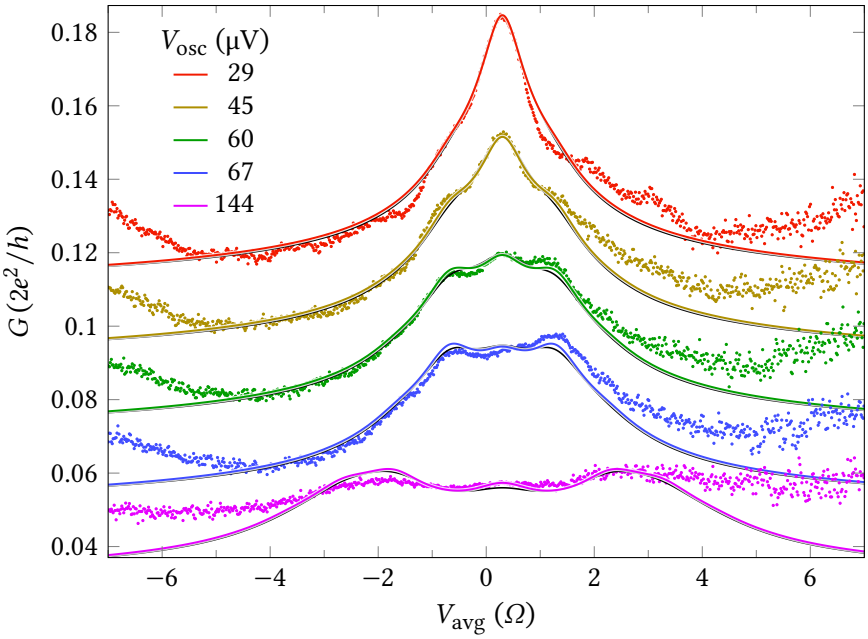

Figure 3.5.: Differential conductance through a semiconductor quantum dot measured by Kogan et al. [82] (dots) at driving frequency $\Omega/2\pi = 13.47\,\mathrm{GHz}$ compared to the FRTRG prediction (solid curves). The scale on the y axis refers to the lowest curve, and all subsequent curves are separated by $0.02(2e^2/h)$ for clarity. The voltage V_{avg} of the theoretical prediction is shifted by 0.3Ω to match the experiment. The colored curves show the prediction for an asymmetrically coupled Kondo model with $x_L = 4x_R$, while the black curves show symmetric coupling. The calibration of V_{osc} in the experiment yields the values indicated in the legend. For the theoretical prediction, V_{osc} is increased by 42% as explained in section 3.3.2. The FRTRG results show $\Omega = 1.05T_K$ with G reduced by a prefactor 0.15 (or 0.096 for symmetric coupling) and shifted by $0.021(2e^2/h)$.

overall prefactor of G are the only two fit parameters in our prediction. These parameters are the same for both frequencies and all values for V_{osc}. We find very good agreement between the FRTRG predictions and the measurements for both frequencies, but at large V_{osc}/Ω an offset between theory and experiment indicates stronger background conductance. In the prediction for $f = 12\,\mathrm{GHz}$ we can estimate this background conductance based on the background measured at a very weak driving of $V_{\mathrm{osc}} = 20\,\mu\mathrm{V}$. Since the background conductance results from nonuniversal terms which are not related to Kondo physics and in which only higher energy scales than the Kondo temperature appear, we can assume that this background responds adiabatically to the periodic driving. The FRTRG results shifted by the adiabatic background conductance are shown by black curves in figure 3.6 in excellent agreement with the experimental data. We stress that to reach this agreement at different frequencies and a large range of values for V_{osc} we only had to modify the calibration of V_{osc} and fit the background conductance and overall suppression of the differential conductance. All other parameters were directly taken from Ref. [84]. A comparison to the phenomenological Eq. (3.18), shown as thin gray curves in figure 3.6, confirms that this approximation can qualitatively predict the Kondo side peaks, but does not yield a good quantitative description.

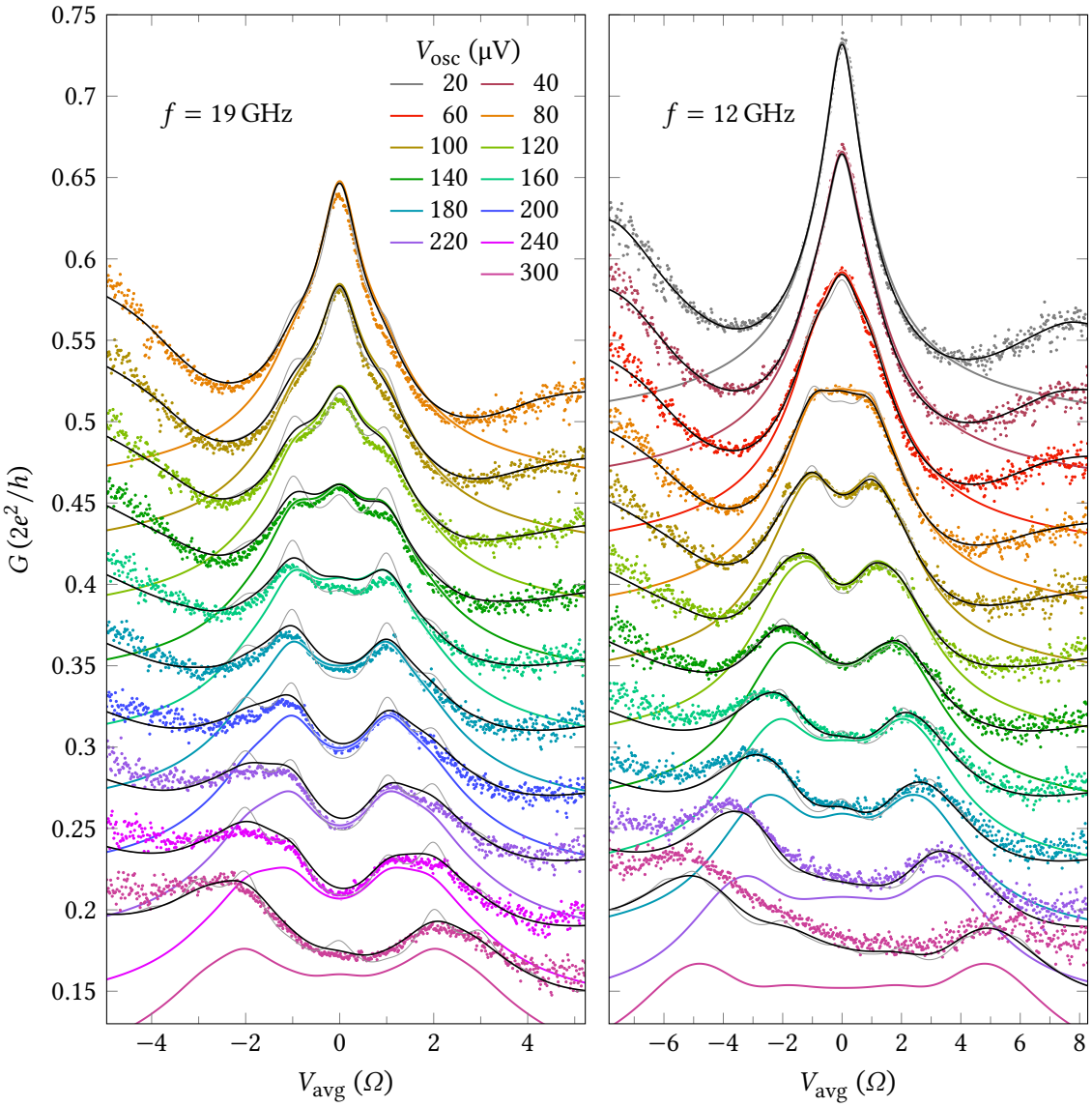

Figure 3.6.: Differential conductance through a carbon-nanotube-based quantum dot at two different frequencies measured by Bruhat et al. [84] (dots), compared to FRTRG prediction (colored solid curves). The scale on the y axis refers to the lowest curves, and all subsequent curves are separated by $0.04(2e^2/h)$. The black curves show FRTRG results plus a background conductance estimated based on the measurement at $f = 12\,\mathrm{GHz}, V_{\mathrm{osc}} = 20\,\mu\mathrm{V}$. For $f = 12\,\mathrm{GHz}$ these curves show almost perfect agreement with the experiment, while for $f = 19\,\mathrm{GHz}$ we find a small offset between these corrected predictions and the measurements. Thin gray curves show results from Eq. (3.18) plus the estimated background to indicate that an accurate theoretical description must go beyond this phenomenological approximation. In the experiment, V_{osc} was calibrated separately for both frequencies, leading to the values in the legend. For the FRTRG predictions we multiply V_{osc} by a correction factor 0.89 for $f = 19\,\mathrm{GHz}$ and 1.07 for $f = 12\,\mathrm{GHz}$. The FRTRG predictions are shifted by $0.062(2e^2/h)$ to account for a background conductance and multiplied by 0.282 to include an overall suppression. For the FRTRG calculations, we used $\Omega_{12\,\mathrm{GHz}} = 0.76T_K$ and $\Omega_{19\,\mathrm{GHz}} = 1.20T_K$.

3.3.2. Details of experiments and fit parameters

Both experiments used quantum dots with Kondo temperatures of a few 100 mK and driving frequencies in the microwave range between 12 GHz and 19 GHz. Kogan, Amasha, and Kastner worked with a GaAs quantum dot at temperature $T \sim 0.3T_K$, and later Bruhat et al. used a carbon-nanotube-based quantum dot at approximately zero temperature ($T < 0.03T_K$). In both experiments, the frequency and average bias voltage V_{avg} are known with high precision, but the Kondo temperature and the calibration of the oscillating voltage V_{osc} require some discussion.

Kondo temperature. The Kondo temperature enters our prediction through the ratio Ω/T_K and determines the width of the peaks in figures 3.5 and 3.6. Different definitions of the Kondo temperature exist in the literature. Here, we compare FRTRG results to measurements at $V_{\mathrm{osc}} = 0$ in both experiments to determine the values of T_K for these experiments. Bruhat et al. provide relatively precise values for the Kondo temperature, which is possible due to the low sample temperature. Their method for determining the Kondo temperature can be compared to our definition of T_K for the FRTRG, yielding $T_K = 65\mu eV$.[6] In the measurement by Kogan et al., the finite temperature leads to a less precise estimate for the Kondo temperature and may also affect the data shown in figure 3.5. For this experiment, we find $T_K \approx 53\mu eV$ by a comparison to the measurement at $V_{\mathrm{osc}} = 0$ shown in Ref. [82].

Calibration of V_{osc}. For the calibration of V_{osc} the two experiments used different methods, but in both cases we find that the FRTRG results only agree with the measured data if this calibration is modified. Kogan et al. calibrated V_{osc} by comparing the differential conductance to the adiabatic limit after increasing the Kondo temperature to bring it to an approximately adiabatic regime. As we have seen in section 3.2.1, the adiabatic limit of the differential conductance shows a peak in G at $V_{\mathrm{avg}} = V_{\mathrm{osc}}$, but in the FRTRG results this peak is shifted towards smaller V_{avg}. As long as the system is not in a completely adiabatic regime, we therefore expect this calibration procedure to underestimate V_{osc}. However, to make the FRTRG results match the measurement we need to increase V_{osc} by 42%, which is more than we would expect from the calibration procedure.

Bruhat et al. also used the comparison to an adiabatic response of the system for the calibration of V_{osc}, but in this case, the calibration was not done in the Kondo regime. The two different frequencies $f = 19\,\mathrm{GHz}$ and $f = 12\,\mathrm{GHz}$ require a separate calibration of V_{osc}.[7] To find good agreement between FRTRG results and the experiment we multiply V_{osc} as calibrated in the experiment by correction factors 0.89 for $f = 19\,\mathrm{GHz}$ and 1.07 for $f = 12\,\mathrm{GHz}$, accounting for a calibration uncertainty of the order of 10% in the experiment.

Background conductance and suppression of G. The FRTRG describes the universal Kondo physics, where only cotunneling processes that contribute to the Kondo resonance exist. But in a realistic setup the nonuniversal processes do not vanish and not only the Kondo peak

[6] By comparing FRTRG calculations at $V_{\mathrm{osc}} = 0$ to figure 1(d) of Ref. [84], we find that we need to multiply the Kondo temperature determined by Bruhat et al. with 2.3 to obtain T_K. They find a Kondo temperature of $28.2\mu eV$, such that we use $T_K = 65\mu eV$.

[7] The calibration of different frequencies in Ref. [84] is not completely independent, since an absolute and a relative calibration method are combined to reach a consistent calibration for different frequencies.

contributes to the differential conductance. We expect a background conductance that should be approximately constant at the Kondo peaks, but grows as V_{avg} approaches the energies ε or $\varepsilon + U$ characterizing the quantum dot. In the comparison to the experiments, we therefore shift G by a constant offset. A more precise estimate of the background conductance is obtained in figure 3.6 by using the background at weak driving, as indicated by the black curves. Furthermore, the differential conductance can be suppressed by asymmetric coupling, finite temperature and possibly other effects. We thus use a prefactor of G as another fit parameter for the theoretical description. Both the shift and prefactor of G are parameters of the quantum dot, and in figure 3.6 we use the same parameters for all frequencies and all values of V_{osc}.

Asymmetry. As discussed in section 3.2.3 an asymmetric coupling affects the overall conductance. In figure 3.5 we see a relatively strong suppression of G, for which our fit predicts a height of the equilibrium Kondo resonance of $G(V_{\mathrm{avg}} = V_{\mathrm{osc}} = 0) \approx 0.19\, e^2/h$ compared to $0.55\, e^2/h$ in the experiment by Bruhat et al. At the same time, the Kondo temperature taken from the measurement at $V_{\mathrm{osc}} = 0$ in Ref. [82] seems too large when comparing the measurements to our prediction for a symmetrically coupled quantum dot. But with an asymmetric coupling to the dot the side peaks of the Kondo resonance become sharper — similar to the effect of a lower Kondo temperature — and the equilibrium conductance $G(V_{\mathrm{avg}} = V_{\mathrm{osc}} = 0)$ is reduced. The measurements by Kogan et al. furthermore show a shift of the Kondo peak to finite V_{avg}, which may indicate an asymmetric coupling [118, 166]. Because of these indications, we compare the measurement by Kogan et al. to an asymmetrically coupled Kondo model with $x_L = 4x_R$.

3.4. Voltage pulses

With the FRTRG, it is possible to compute the response current for an arbitrary periodic bias voltage $V(t)$. This enables a detailed study of memory effects, which are tightly connected to the strong correlation between quantum dot and reservoirs. Here we mean by memory effects that an observable — the current — at time t depends on the bias voltage $V(t')$ applied before time t. This memory arises from correlation between the reservoirs which are included in the FRTRG calculation. Here, we analyze this memory for short voltage pulses, which will then help us understand rapid oscillations in the response current for strong harmonic driving. This analysis of memory in transport observables complements the discussion of memory in the time-evolution of the local system in section 2.4.

The response current for a short voltage pulse is shown in figure 3.7(a). We consider Gaussian voltage pulses that are repeated in intervals that are sufficiently long, such that after each pulse, the system approximately reaches the equilibrium state before the next pulse arrives. In figure 3.7 one can see that the response current consists of two components. During the pulse, a strong current sets in with no delay. This is what we will call the immediate response. After the voltage pulse, a much weaker, slowly decaying current remains, to which we refer as the retarded current. This retarded current is caused by the memory of the system and can flow in different directions, as the orange curve in figure 3.7(a) shows. In the following, we will focus on this component of the current, providing some qualitative understanding.

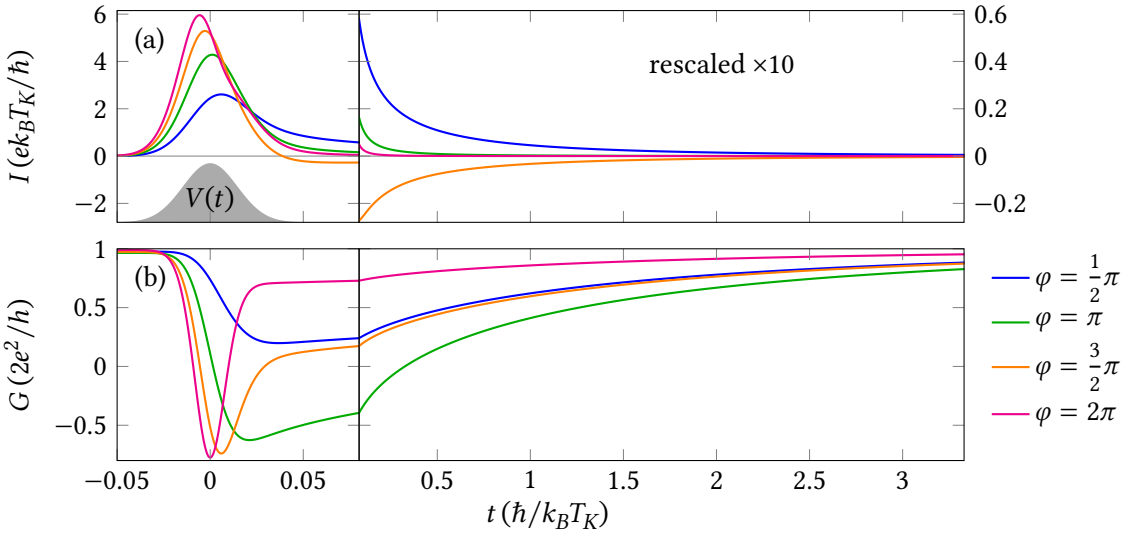

Figure 3.7.: (a) Current through a Kondo quantum dot in response to short Gaussian voltage pulses with different phases $\varphi = \int dt V(t)$. The right panel continues the plot with scaled axes (×10 on y axis, ×0.1 on x axis). During the pulse the current follows the voltage (indicated in gray) and after the pulse a decaying current depending on the phase φ remains. For $\varphi = 3\pi/2$, this current flows in the reverse direction. (b) Transient differential conductance $G(t) = dI(t)/dV_{\text{avg}}$ as indicator for the recovery of the Kondo resonance after a voltage pulse. For $\varphi = 2\pi$, the unitary conductance is quickly restored, whereas for $\varphi = \pi$ the recovery of the Kondo resonances takes a relatively long time. $\varphi = \pi/2$ and $\varphi = 3\pi/2$ show almost the same $G(t)$ after the pulse. Here the pulse duration (full width at half maximum) is $0.034\hbar/(k_B T_K)$ and the time between two pulses is $14.4\hbar/(k_B T_K)$.

To understand the retarded current, we consider a single, very short voltage pulse, which can be characterized by the phase $\varphi = \int dt V(t)$ accumulated between the two reservoirs. Let us again assume that the pulse is applied to the chemical potential of the right reservoir, while the left reservoir is kept at constant chemical potential. Then all electron states in the right reservoir obtain a phase $e^{i\varphi}$ due to the pulse. Without correlations between the reservoirs, this phase would be irrelevant due to the $U(1)$ gauge freedom in the definition of the electron states. But in the Kondo model, the reservoirs and the quantum dot spin form a strongly correlated state, in which the two reservoirs are entangled. In this case, the phase $e^{i\varphi}$ does have an effect. Let us consider a typical process that contributes to the correlations between the two reservoirs. An electron is transported through the dot from the left reservoir to the right reservoir in a cotunneling process, either before or after the pulse. These two paths — earlier or later cotunneling — can interfere and leave the reservoirs in an entangled state during the pulse. In this simple process, the phase $e^{i\varphi}$ is a relative phase between two interfering quantum states, which can affect the current. Such correlations between the two reservoirs form the memory of the system, which contains information about $e^{i\varphi}$ and makes it possible that a current flows after the voltage pulse has ended.

This brief motivation of the correlations that constitute the memory already indicates that only $e^{i\varphi}$ can influence these correlations, such that the phases φ and $\varphi + 2\pi$ should lead to the same retarded current. In this simplified view — which ignores cotunneling during the voltage

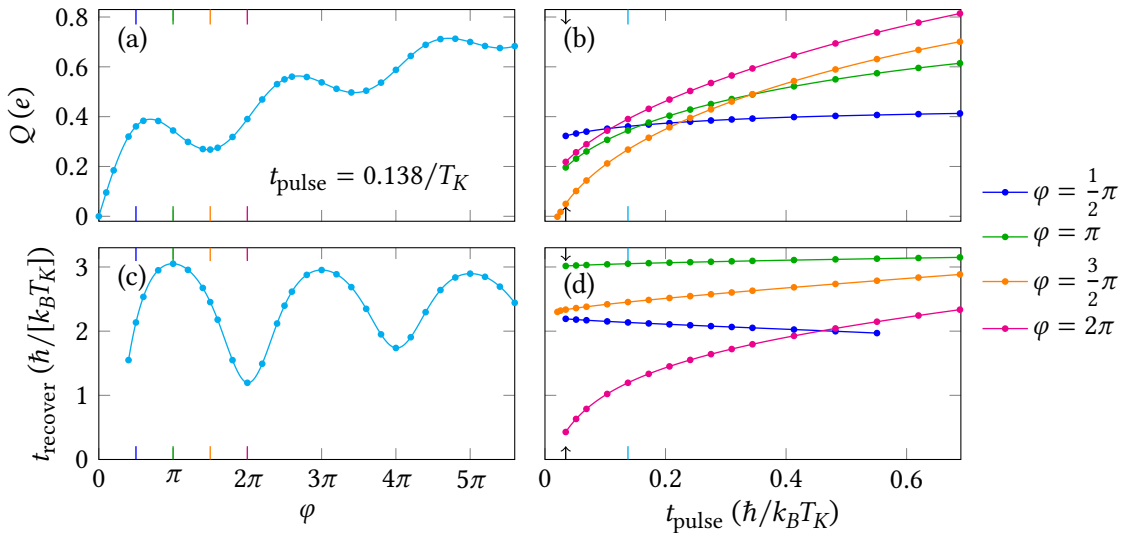

Figure 3.8.: (a) Charge transported in response to a voltage pulse as a function of the pulse phase φ at constant pulse duration. Oscillations with φ are clearly visible. (b) Transported charge as a function of pulse duration (full width at half maximum) at fixed φ. Black arrows mark the parameters show in figure 3.7. For short pulses, the retarded current increases Q for $\varphi = \pi/2$ and reduces Q for $\varphi = 3\pi/2$. At very short pulses, the retarded current is dominant, and the transported charge becomes negative for $\varphi = 3\pi/2$. (c,d) Time after the pulse when the transient differential conductance $G(t)$ reaches 80% of its equilibrium value. The recovery time is shortest when φ is an integer multiple of 2π. The pulses are repeated with period $T = 14.4\hbar/(k_B T_K)$.[9]

pulse[8] — the memory cannot contain information about anything else than $e^{i\varphi}$. Thus, a pulse with phase $\varphi = 3\pi/2$ (orange in figure 3.7) should lead to the same retarded current as a negative pulse with phase $\varphi = -\pi/2$ (blue curve shows $\varphi = +\pi/2$). Since weak pulses must lead to a current in the direction of the voltage pulse as expected from linear response theory, the strong pulse with $\varphi = 3\pi/2$ must lead to a retarded current in the reverse direction. This effect can be seen in figure 3.7(a). We can see that the current after a pulse with $\varphi = 3\pi/2$ (orange) is similar — albeit weaker — to the reverse of the current after a pulse with $\varphi = \pi/2$ (blue). This suggests that the retarded current will oscillate as a function of φ similar to $\sin\varphi$. The main signatures of this qualitative result are the suppression of the retarded current for $\varphi = 0 \mod \pi$ and the reverse retarded current for $\pi < |\varphi| < 2\pi$.

The phase φ also mainly determines how strongly the Kondo state is destroyed by the pulse. To quantify this, we look at the transient differential conductance $G(t) = dI(t)/dV_{\text{avg}}$ which asymptotically approaches its equilibrium value $G(t) = 2e^2/h$ after a pulse as shown in figure 3.7(b). The deviation of $G(t)$ after a pulse from its equilibrium value indicates how strongly the Kondo state was destroyed. From figure 3.7(b) we can identify three main features in the dependence of $G(t)$ on φ. Firstly, for $\varphi = 2\pi$ the Kondo state is hardly affected and recovers quickly. This

[8] Electrons can also cotunnel through the dot during the pulse. Such processes depend on details of the pulse and not only on φ. To qualitatively understand the retarded response to very short pulses, we neglect such processes.

[9] The data point in figure 3.8(b) and (d) for $\varphi = 3\pi/2$ with shortest t_{pulse} was generated with a shorter pulse repetition time of $T = 10.8\hbar/(k_B T_K)$. Because of this, the retarded current might be underestimated.

is expected because we have already seen that the memory mainly depends on $e^{i\varphi}$. For $\varphi = 2\pi$ this phase factor becomes trivial such that the dominant contribution to the memory vanishes. Secondly, $\varphi = 3\pi/2$ and $\varphi = \pi/2$ have very similar effects. Since the sign of φ cannot have any influence on $G(t)$, this establishes that only $\varphi \mod 2\pi$ is relevant. Thirdly, the effect on the Kondo state is maximal for $\varphi = \pi$, although this pulse has a very weak retarded current, as the green line in figure 3.7(a) shows. Thus, only pulses which strongly affect the Kondo resonance can lead to a strong retarded current, but not all pulses that destroy the Kondo resonance also lead to a significant retarded current.

To further test our qualitative understanding of the effect of φ on the current and on the Kondo resonance, we look at the total charge Q transported in response to a voltage pulse and the time t_{recover} after which the Kondo resonance is largely restored. In figure 3.8 these quantities are plotted as a function of the phase φ and the pulse duration. Oscillations in Q as a function of φ [figure 3.8(a)] for short pulses confirm the relevance of the phase-dependent retarded current for the total transported charge. The recovery time of the Kondo resonance also oscillates as a function of φ [figure 3.8(c)], and indicates that even a strong pulse with $\varphi = 4\pi$ can have a significantly smaller effect on the Kondo resonance than a weaker pulse with phase $\varphi = \pi$. Both Q and t_{recover} plotted as a function of the pulse duration show that the effect of φ is especially prominent for very short pulses [figure 3.8(b,d)]. For slow pulses, an adiabatic response is approached, in which the pulse height is relevant but $e^{i\varphi}$ does not play any role. In the case of very short pulses, the phase strongly affects the recovery time and the retarded current becomes the dominant contribution to the transported charge. In the limit of extremely short pulses, this can lead to a negative total transported charge ($Q < 0$) for a positive voltage pulse with phase $\varphi = 3\pi/2$. However, we do not expect this regime of extremely short and strong pulses to be of practical relevance because the strong voltage would push a realistic system out of the Kondo regime.

3.5. Higher harmonics for harmonic driving

Having seen how the phase φ of a voltage pulse influences the current, we can now also understand the response to different driving profiles. In the simple case of harmonic driving, at high V_{osc} the current shows contributions from many higher harmonics and rapid oscillations in the time domain as shown in figure 3.9(a). These rapid oscillations can be understood as oscillations of a cumulative phase $e^{i\varphi(t)}$ as we have seen for the voltage pulses. For an arbitrary bias voltage profile, we define the phase $\varphi(t) = \int_{t^*}^{t} ds\, V(s)$ accumulated by reservoir electrons between a constant reference time t^* and time t. The current measured at time t probes correlations between the system and the reservoirs that are created before t, as we have seen in the definition of the current kernel $\Sigma_\gamma(t, s)$ in Eq. (1.2). For different starting times s, this current kernel depends on different relative phases $\varphi(t) - \varphi(s)$, which affect these correlations. However, if we choose t^* such that $\varphi(t)$ is nearly constant around t^*, then a finite time interval around t^* will contribute approximately the same phase $\varphi(t)$. The constructive interference of terms from times around t^* makes $\varphi(t)$ a relevant phase contributing to the current at time t, similar to the effect of the constant phase φ on the retarded current for voltage pulses. We can identify interference effects

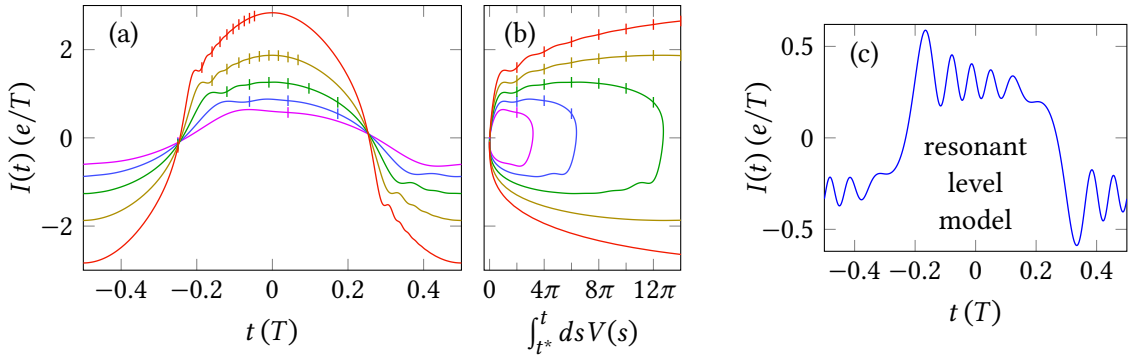

Figure 3.9.: (a) Current as a function of time for $V(t) = V_{\mathrm{osc}} \cos(\Omega t)$ in the Kondo model at $\Omega = T_K$ with time measured relative to the driving period $T = 2\pi/\Omega$. The colors mark (from pink to red) $V_{\mathrm{osc}} = 5\Omega, 10\Omega, 20\Omega, 40\Omega$, and 80Ω. (b) $I(t)$ versus $\int_{t^*}^{t} ds\,V(s)$ parametrized by t. This visualization shows that the rapid oscillations in $I(t)$ result from the phase accumulated between time $t^* = -T/4$ and t. Marks in (a) and (b) indicate where $\int_{t^*}^{t} ds\,V(s)$ is an integer multiple of 2π. (c) Current through the noninteracting resonant level model at zero temperature with two reservoirs for comparison (compare also Ref. [167]). One can see oscillations like in the Kondo model. Here the voltage is applied to the left reservoir, $\mu_L = 16\Omega$, and the current is measured in the left reservoir while the dot level and the right reservoir are kept at $\varepsilon = \mu_R = 0$. The coupling to both reservoirs is $\Gamma_L = \Gamma_R = 0.1\Omega$.

depending on this phase as long as $t - t^*$ is smaller than the coherence time. Such interference effects are indeed visible as rapid oscillations in figure 3.9(a).

Similar oscillations also appear in noninteracting systems where they are well-known [167], and have been predicted for the harmonically driven Kondo model with a specific nonisotropic coupling [157]. For comparison, figure 3.9(c) shows similar oscillations in the analytically solvable noninteracting resonant level model coupled to two reservoirs (see section 2.3.2 and appendix B). But although the Kondo model and the resonant level model show a very similar effect, one has to distinguish carefully which correlations enable this effect. In the resonant level model, the rapid oscillations in the current result from correlations only between the level (or quantum dot) and one reservoir. The two reservoirs are not correlated. Thus, only the chemical potentials relative to the dot level determine the phase $\varphi(t)$ that dictates the oscillations in the current. In contrast, in the Kondo model the oscillations signal correlations between the two reservoirs which are mediated through the Kondo quantum dot. This can be verified by checking that only the relative voltage $\mu_L - \mu_R$ between the two reservoirs affects the oscillations, and thereby provides an important experimental check to identify correlations mediated by a quantum dot in the Kondo regime. Thus, rapid oscillations in the current in a Kondo quantum dot driven by a fast and strong harmonic bias voltage are a signature of the strong quantum correlations between the two reservoirs.

The interesting time-dependence of the current is not clearly visible in its Fourier modes. As shown in figure 3.10, the Fourier modes of the current for harmonic driving mainly follow an algebraic decay until mode index $n \approx V_{\mathrm{osc}}/\Omega$, which is consistent with the adiabatic limit. Higher modes with $n \gtrsim V_{\mathrm{osc}}/\Omega$ are suppressed exponentially, such that the current in the time domain is smooth on the timescale $1/V_{\mathrm{osc}}$ corresponding to the largest energy scale among

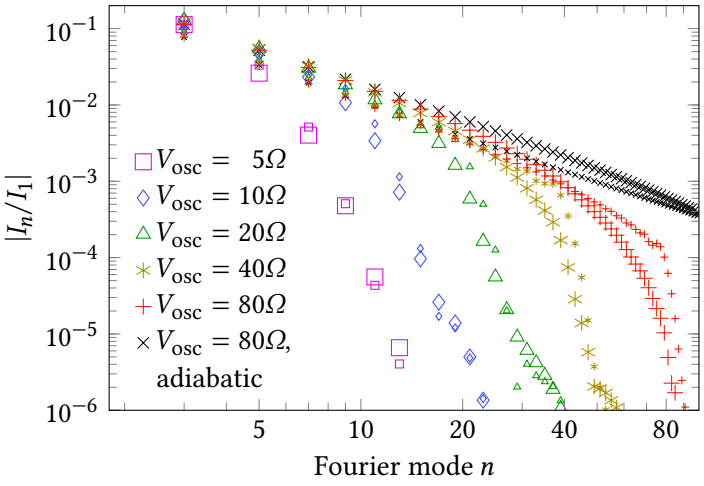

Figure 3.10.: Fourier modes $|I_n|$ of the current relative to the first mode for $V(t) = V_{\text{osc}} \cos(\Omega t)$ in the Kondo model for $\Omega = T_K$ (big markers) and for $\Omega = 20T_K$ (small markers) at different values for V_{osc}. At high frequency, the amplitude $|I_n|$ of Fourier mode n drops approximately algebraically as a function of n for $n\Omega < V_{\text{osc}}$ before it is suppressed exponentially for $n\Omega > V_{\text{osc}}$. At lower frequency, high modes are already suppressed before reaching $n\Omega = V_{\text{osc}}$. In both cases, many higher harmonic modes show a significant contribution to the current.

the parameters. The rapid oscillations of the current do not have a strong signature in Fourier space because their frequency is not constant. This intuitive structure in Fourier space stands in contrast to the interesting oscillations in the time domain, and suggests that a measurement of the time-dependent current may be more interesting than measuring the higher Fourier modes.

3.6. Summary

The periodically driven Kondo model combines strong quantum correlations with nonequilibrium and memory effects. We have seen how an oscillating bias voltage with sufficiently high frequency leads to photon-assisted tunneling and satellite peaks. The rich structure of the differential conductance as a function of frequency, average voltage and oscillating voltage can be understood roughly using the qualitative pictures of photon-assisted tunneling and decoherence, combined analytic approximations for limiting cases. However, a quantitative description of experimental observables covering the whole range from weak to strong and slow to fast driving requires an advanced method like the FRTRG. We have motivated and showcased its application here and will discuss its details in the next chapters. The FRTRG shows excellent quantitative agreement with two experiments and with all known limiting cases.

We exploited that transport through a highly correlated quantum dot can be analyzed for a variety of periodic driving profiles with high time-resolution using the FRTRG. This allowed us to analyze memory effects using transport observables, complementing the discussion of memory in the evolution of states in section 2.4. Applying the FRTRG to a train of well-separated short voltage pulses, we conclusively showed that the memory in the transport response is caused by correlations of the two leads. We quantitatively showed that a voltage pulse causes a retarded current mainly through its cumulative voltage phase $\varphi = \int dt V(t)$. In the case of fast harmonic driving, this phase leads to rapid oscillations in the response current as a function of time, which are a direct effect of the strong correlations between the two reservoirs. We suggest that this can be used to experimentally detect evidence for these strong correlations by verifying the dependence of the rapid oscillations on bias only, being independent of the level position.

4. Floquet real-time RG

The Kondo model with a finite bias voltage as discussed in the previous chapter is a prototypical example of an open system far from equilibrium with strong coupling and memory effects. The analysis of such models is difficult due to the large number of electrons in the reservoirs that combine to a quantum many-body state. As bare perturbation theory breaks down and the total system size makes some numerical approaches unfeasible, renormalization group methods play a key role in making predictions for such models.

In this chapter, the Floquet real-time renormalization group is introduced as a method to describe such systems. The overall concept of the FRTRG and the notation used in this method are introduced on a general level. Afterward, the details of the method are presented by deriving the RG equations for a quantum system at zero temperature, which interacts with metallic reservoirs only via two-particle interactions or cotunneling. This restricts the derivation to Kondo-type models. Other model-specific details are postponed to chapter 5 to keep the derivation as simple as possible. The discussion of the initial condition for the RG flow — an essential part of the method — is only briefly touched in this chapter and mainly postponed to chapter 5. This derivation has been presented in Ref. [3] and closely follows Ref. [76], in which the case of a constant bias voltage was considered. The full derivation of the FRTRG for the Kondo model takes 16 steps in this chapter and in chapter 5. An overview of the notation is provided in appendix K and the steps are listed in table 5.2.

4.1. Main idea of the real-time RG

In many problems of condensed matter theory, effects on different energy scales must be considered. Processes involving higher energy scales may effectively modify the low-energy properties of a system. For example, in the Kondo model, electrons and holes in the conduction band even far away from the Fermi energy contribute to the Kondo resonance at low energy. A theory describing the low-energy physics should include such effects. As explained in section 3.1.2, one should gradually integrate out high energy scales to obtain an effective theory for the low-energy physics.

Here we focus on the real-time RG (RTRG), which has been developed for open quantum systems in the time domain [53, 54, 168, 169] and in Laplace space [55, 74–76]. In this method, an effective low-energy description is reached by integrating out hopping or cotunneling processes between the system and the reservoirs starting from short duration or high energy. A special case of the RTRG is the E-flow scheme, which describes the dynamics in Laplace space. The Laplace variable E naturally provides a way of successively including high energies. We define the Laplace transform of a function $f(t)$ with the sign convention $\tilde{f}(E) = \int_0^\infty dt\, e^{iEt} f(t)$ such that it is always well-defined if $\operatorname{Im} E$ is sufficiently large. This gives the Laplace variable E the meaning of an

energy in analogy to quantum time evolution formulas. For very high Im E only very short times of the function $f(t)$ matter. When describing the dynamics of a quantum system, at large Im E only correlations on very short timescales can play a role and for sufficiently large Im E all finite time correlations can be neglected, which simplifies the description considerably. In the E-flow scheme, this property of the Laplace transform is used by first deriving the dynamics at large Im E and then successively including lower energy scales in the effective description by lowering Im E. This requires that we find RG equations for the E-derivatives of the effective Liouvillian, the effective coupling between the system and the reservoirs, and transport observables of interest. We will see that such equations can be found using a self-consistent expansion in the effective coupling. Eventually, this will lead to a numerically solvable ordinary differential equation which lets us include all energy scales down to $E = 0$ in the effective low-energy description.

The self-consistent formulation and the successive inclusion of all energy scales in the RG procedure avoid some common approximations and make the RTRG a powerful method. These aspects significantly improve the underlying expansion in the coupling between the system and the reservoirs. Still, due to the expansion in the coupling, the applicability to a strongly coupled system is a priori not guaranteed. But in the Kondo model, where the bare coupling is small, the RTRG can also be applied in the regime of strong renormalized coupling, as we will discuss in section 6.1.1.

4.2. Liouville-Floquet space and diagrammatic language

The E-flow scheme of the RTRG is formulated in Liouville-Laplace space. Functions of time are transformed to Laplace space and states of the open quantum system are density matrices, elements of the Liouville space instead of the usually more familiar Hilbert space. In this framework, dynamics and transport properties can be calculated conveniently using a diagrammatic language that will be explained below. To describe systems with time-dependent driving, it is useful to extend the Laplace space using Floquet theory.

4.2.1. Floquet theory

Time-periodic physical problems have been studied in various contexts. Here we work in frequency space to handle the periodic driving and all time dependence. Following the Floquet Green's function formalism, [170–176] we express the Fourier series of time-periodic functions in matrices, which allows for an efficient numerical solution.

For an intuitive understanding of the formalism, we start in the time domain. As in chapter 2 we study the dynamics of a local system that is coupled to reservoirs, and this coupling is switched on at some initial time t_0. A physical observable measured at some time t is, in general, a function $f(t, t_0)$ of t and t_0. In contrast to the case of a system without external driving where observables depend solely on $t - t_0$, we must consider here that an observable depends on t and t_0 separately. Since the external driving is periodic with period T, the function f must be invariant under a global shift of all times by T, $f(t + T, t_0 + T) = f(t, t_0)$. By writing f as a function of $(t - t_0, t)$ we can apply a Laplace transform in the first argument $(t - t_0)$ and a Fourier series

expansion in the second argument (t) using the periodicity in the second argument [170, 177]:

$$\tilde{f}_n(E) \coloneqq \frac{1}{T}\int_0^\infty ds\, e^{iEs}\int_0^T dt\, e^{in\Omega t} f(t, t-s). \tag{4.1}$$

As defined before for the undriven case, $\tilde{f}_n(E)$ is analytic in the upper half of the complex plane. In this transformation, $f(t, t_0)$ need not be an observable, but it can be any physical quantity depending only on the times t and t_0.

The representation $\tilde{f}_n(E)$ contains all the required information and could be used in further calculations, but it is much more convenient to define the Floquet matrix [170–172]

$$\hat{f}(E)_{nm} \coloneqq \tilde{f}_{n-m}(E + m\Omega). \tag{4.2}$$

This Floquet matrix is defined such that convolutions of functions in the time domain become convenient matrix products of the corresponding Floquet matrices. A proof of this property can be found in appendix G. Since an expansion of the dynamics in the time domain typically requires many convolutions, the description in Floquet space with numerically much cheaper matrix products is advantageous.

It is useful to consider how the special case without driving is recovered, in which Floquet theory is not needed. In this limit, the system is invariant under arbitrary global time translations and a function $f(t, t_0)$ can only depend on the time difference $t - t_0$. Such functions are described by diagonal Floquet matrices $\hat{f}(E)_{nm} = \delta_{nm}\tilde{f}(E + n\Omega)$ where $\tilde{f}(E) = \int_0^\infty ds\, e^{iEs} f(s)$ is the Laplace transform of $f(t - t_0)$. We will denote such diagonal matrices by

$$\hat{f}(E) = \tilde{f}(E + \hat{N}\Omega), \qquad \hat{N}_{nm} = n\delta_{nm}, \tag{4.3}$$

where $\hat{N}$ is a diagonal Floquet matrix. For a system without time-dependent driving, all Floquet matrices are diagonal and it is sufficient to consider only a single matrix element $\hat{f}(E)_{00}$. Since this is just the Laplace transform of $f(t - t_0)$, the Floquet formalism reproduces the common description of time-translation invariant systems. The E-flow RTRG for time-translation invariant systems is therefore a special case of the FRTRG.

4.2.2. State evolution in Floquet-Liouville space

Now we want to use the previously introduced Floquet theory to describe open system dynamics in Liouville space. We will first consider a general model of a local system with time-constant Hamiltonian H_S coupled via a coupling Hamiltonian $H_V(t)$ to reservoirs described by the Hamiltonian $H_R(t)$. Here both $H_V(t)$ and $H_R(t)$ are periodic in time with the same period $T = 2\pi/\Omega$.[1]

In the time domain, we can formally write down the unitary evolution of the total system and trace out the reservoir degrees of freedom, assuming that at time t_0 the reservoirs are in an equilibrium state ρ_R^{eq}. The same formal solution for the state $\rho(t)$ at time t as given in Eq. (2.6)

[1] We will see in section 5.3.2 that for the periodically driven Kondo model we can either keep the time-dependence in the reservoir Hamiltonian $H_R(t)$ or (partially) shift the time dependence to the coupling Hamiltonian $H_V(t)$ by a unitary transformation.

can be written in Liouville space when defining Liouvillians as commutators with Hamiltonians, e.g., $L_S = [H_S, \bullet]$:

$$\rho(t) = \Pi(t, t_0)\rho(t_0) = \operatorname*{tr}_R \Big\{ \mathcal{T}_{\leftarrow} e^{-i\int_{t_0}^{t} ds \left[L_S + L_V(s) + L_R(s)\right]} [\rho(t_0) \otimes \rho_R^{\mathrm{eq}}] \Big\}. \tag{4.4}$$

The transformation from a time ordered integral to Floquet space can be done using the following general relation, which is proven in appendix G. For any time-periodic function $f(t)$ the time-ordered integral $h(t, t_0) := \mathcal{T}_{\leftarrow} \exp\big[\int_{t_0}^{t} ds\, f(s)\big]$ has the Floquet matrix

$$\hat{h}(E) = \frac{i}{E + \hat{N}\Omega - i\hat{f}} \qquad \text{with} \qquad \hat{f}_{nm} := \frac{1}{T}\int_0^T dt\, e^{i(n-m)\Omega t} f(t). \tag{4.5}$$

Applying this in Eq. (4.4) with $f(t) = -i[L_S + L_V(t) + L_R(t)]$ yields the Floquet matrix for the propagator:

$$\hat{\Pi}(E) = \operatorname*{tr}_R \Big\{ \frac{i}{E + \hat{N}\Omega - L_S - \hat{L}_V - \hat{L}_R} (\bullet \otimes \rho_R^{\mathrm{eq}}) \Big\}. \tag{4.6}$$

This is a convenient starting point for an expansion in $\hat{L}_V$. Here the Floquet matrices $\hat{L}_R$ and $\hat{L}_V$ are defined analogous to $\hat{f}_{nm}$ in Eq. (4.5).

When expanding the evolution in the coupling $\hat{L}_V$ it will be useful to express the propagator $\hat{\Pi}(E)$ in terms of an effective Liouvillian $\hat{L}(E)$. In the time domain, the effective Liouvillian is usually called the memory kernel of the evolution and has been introduced in Eq. (1.1):

$$\frac{d}{dt}\rho(t) = -i\int_{t_0}^{t} ds\, L(t, s)\, \rho(s). \tag{4.7}$$

We remind from section 1.2 that the open system description using reduced states $\rho(t)$ discards information about the reservoirs, but this information reappears partially as memory in $L(t, s)$. Replacing $\rho(t)$ with $\Pi(t, t_0)$ and transforming to Floquet space yields

$$\hat{\Pi}(E) = \frac{i}{E + \hat{N}\Omega - \hat{L}(E)}. \tag{4.8}$$

Thus, $\hat{L}(E)$ and $\hat{\Pi}(E)$ are closely related, and it is sufficient to know $\hat{L}(E)$ to describe the dynamics. In the following, we will mainly work with $\hat{L}(E)$ because an expansion of $\hat{L}(E)$ in $\hat{L}_V$ contains significantly fewer terms than an expansion of $\hat{\Pi}(E)$. More precisely, an expansion of $\hat{\Pi}(E)$ in $\hat{L}_V$ will yield the same result as expanding Eq. (4.8) in a geometric series, in which we insert the expansion of $\hat{L}(E)$. We will see below that a diagrammatic language can help us to select those terms from an expansion of Eq. (4.6) that contribute to $\hat{L}(E)$.

4.2.3. Expanding in the coupling (step 1)

The first step in the derivation of the FRTRG is the construction of this series expansion for $\hat{L}(E)$. Here we derive this series for a general cotunneling model with noninteracting reservoirs. Like in chapter 2, we assume that the reservoir Hamiltonian is of the form

$$H_R(t) = \sum_{\alpha} \int d\omega [\omega + \mu_\alpha(t)] \sum_{\sigma} c^{\dagger}_{\alpha\sigma\omega} c_{\alpha\sigma\omega}, \tag{4.9}$$

but here we allow for time-dependent chemical potentials $\mu_\alpha(t)$ in the reservoirs labeled by α. The creation and annihilation operators fulfill the anticommutation relation[2]

$$\{c_{\alpha\sigma\omega}, c^\dagger_{\alpha'\sigma'\omega'}\} = D(\omega)\delta_{\alpha\alpha'}\delta_{\sigma\sigma'}\delta(\omega-\omega'), \tag{4.10}$$

where $D(\omega) = D^2/(D^2+\omega^2)$ is a high-energy cutoff function for a bandwidth D, which is assumed to be much larger than all other energy scales. We will eventually consider the limit $D\to\infty$ — combined with weak coupling as discussed in section 3.1.2 — such that for the low-energy physics $D(\omega)$ will always appear to be constant. In this limit, the details of this high-energy cutoff function are irrelevant, as motivated at the end of section 3.1.2.

To express the problem in Liouville spaces we introduce a more compact notation. We define multi-indices labeled by digits as $1 \equiv (\alpha_1, \sigma_1, \omega_1, \eta_1)$, which include the reservoir index $\alpha = L, R$, a spin index $\sigma = \uparrow, \downarrow = \pm$, the energy $\omega \in \mathbb{R}$, and an index distinguishing between creation ($\eta = +$) and annihilation operators ($\eta = -$). The subscript 1 of the components of the multi-index will be dropped as long as the notation remains unambiguous. For example, we write $c_1 = c_{\alpha\omega\sigma}$ for $\eta = -$ and $c_{1'} = c^\dagger_{\alpha'\omega'\sigma'}$ for $\eta' = +$.

Next we introduce fermionic field superoperators K_1^p acting on operators in Liouville space,

$$K_1^+ = c_1\bullet, \qquad\qquad K_1^- = \bullet c_1, \tag{4.11}$$

for which the upper index $p = \pm$ distinguishes between left and right multiplication with a creation or annihilation operator [55]. This is equivalent to the distinction of forward and backward propagation in the usual Keldysh formalism [52] and we will therefore refer to the index p as Keldysh index. In this notation, the reservoir Liouvillian becomes[3]

$$L_R(t) = \frac{1}{2}\sum_{1p}\eta[\omega+\mu_\alpha(t)]K_1^pK_{\bar 1}^p, \qquad\qquad \hat L_R = \frac{1}{2}\sum_{1p}\eta(\omega+\hat\mu_\alpha)K_1^pK_{\bar 1}^p. \tag{4.12}$$

Here $\bar 1 = (\alpha, \sigma, \omega, \bar\eta)$ flips the index η, $\bar\eta = -\eta$, and $\hat\mu_\alpha$ is defined analogous to $\hat f$ in Eq. (4.5). The sum over multi-index 1 implicitly includes an integral over ω.

Since we aim to expand in the coupling Liouvillian $\hat L_V$, it is especially important to write $\hat L_V$ in a suitable form. In general, $L_V(t)$ can be written in the form

$$L_V(t) = G_1^{(0)p}(t)K_1^p + \frac{1}{2}p'G_{11'}^{(0)pp'}(t)\,{:}\,K_1^pK_{1'}^{p'}\,{:} + \ldots, \tag{4.13}$$

where the bare vertices $G_{1\ldots}^{(0)p\ldots}$ are superoperators acting only on the local system whose explicit form is not yet relevant here, and we implicitly sum over all indices that occur only on one side of the equation. The one-point vertex $G_1^{(0)p}$ results from terms in $H_R(t)$ which are linear in reservoir creation and annihilation operators, the two-point vertex $G_{11'}^{(0)pp'}$ originates from terms

[2] We have seen in section 2.2.1 how to absorb the density of states into the definition of creation and annihilation operators in the frequency domain. Here we slightly modify the calculation leading to Eq. (2.4) by using $\varrho(\omega) = \varrho_0 D(\omega)$ and defining $c_{\varepsilon_k} = D(\varepsilon_k)\sqrt{\varrho_0}c_k$. The constant ϱ_0 can be absorbed in the coupling.

[3] In contrast to Eq. (4.14), in Eq. (4.12) we did not write normal ordering. We could equivalently write ${:}\,K_1^pK_{\bar 1}^p\,{:}$ instead of $K_1^pK_{\bar 1}^p$ because in the sum over p and η both terms are equal.

that are quadratic in the reservoir field operators, and likewise for higher-order terms. By $:\ldots:$ we denote normal ordering, that is, no reservoir contraction between superoperators within the normal ordering is allowed.[4]

The formalism allows the inclusion of different vertices, leading to different RG equations. But in the Kondo model only the two-point vertex is present, and we restrict the derivation to this case in the following. We can furthermore choose the remaining two-point vertex to be antisymmetric, $G^{(0)p'p}_{1'1} = -G^{(0)pp'}_{11'}$. Indeed, using that the fermionic superoperators K_1^p commute for different Keldysh indices ($[K_1^\pm, K_{1'}^\mp] = 0$) and anticommute inside the normal ordering for equal Keldysh indices ($:K_{1'}^\pm K_1^\pm := -\ :K_1^\pm K_{1'}^\pm:$), we see that only the antisymmetric component of the two-point vertex remains. Thus, the coupling Liouvillian is

$$\hat{L}_V = \frac{1}{2} p' \hat{G}^{(0)pp'}_{11'}\ :K_1^p K_{1'}^{p'}:, \qquad \hat{G}^{(0)p'p}_{1'1} = -\hat{G}^{(0)pp'}_{11'}, \tag{4.14}$$

where the Floquet matrix $\hat{G}^{(0)pp'}_{11'}$ is defined through the time-dependent vertex as in Eq. (4.5).

We are now ready to expand Eq. (4.6) in $\hat{L}_V$ and trace out the reservoirs. To illustrate the strategy, we consider in detail the leading nontrivial order in $\hat{L}_V$. Expanding Eqs. (4.6) and (4.8) up to second order in $\hat{L}_V$ and first order in $[\hat{L}(E) - L_S]$ yields

$$\begin{aligned}\hat{\Pi}(E) &= \frac{i}{E + \hat{N}\Omega - L_S} \\ &\quad + i\frac{1}{E + \hat{N}\Omega - L_S} \operatorname*{tr}_R \Big\{ \hat{L}_V \frac{1}{E + \hat{N}\Omega - L_S - \hat{L}_R} \hat{L}_V \frac{1}{E + \hat{N}\Omega - L_S} (\bullet \otimes \rho_R^{\mathrm{eq}}) \Big\} + O\big(\hat{L}_V^4\big) \qquad (4.15) \\ &= \frac{i}{E + \hat{N}\Omega - L_S} + i\frac{1}{E + \hat{N}\Omega - L_S} [\hat{L}(E) - L_S] \frac{1}{E + \hat{N}\Omega - L_S} + O\big([\hat{L}(E) - L_S]^2\big). \qquad (4.16)\end{aligned}$$

By comparing terms of equal power in $1/(E + \hat{N}\Omega - L_S)$, we can see that the effective Liouvillian is $\hat{L}(E) = L_S + \hat{L}^{(2)}(E) + O\big(\hat{L}_V^4\big)$ with the leading correction

$$\hat{L}^{(2)}(E) = \operatorname*{tr}_R \Big\{ \hat{L}_V \frac{1}{E + \hat{N}\Omega - L_S - \hat{L}_R} \hat{L}_V (\bullet \otimes \rho_R^{\mathrm{eq}}) \Big\}. \tag{4.17}$$

Higher order contributions in $\hat{L}(E)$ can be constructed by continuing the expansion in $\hat{L}_V$ in Eq. (4.15).

To evaluate the trace over the reservoirs in Eq. (4.17), we now insert $\hat{L}_V$ [Eq. (4.14)] and use the commutation relation of K_1^p with the reservoir Liouvillian $\hat{L}_R$:

$$K_1^\pm \hat{L}_R = (\hat{L}_R - \eta\omega + \eta\hat{\mu}_\alpha) K_1^\pm. \tag{4.18}$$

This makes it possible to separate superoperators acting on the local system and on the reservoirs (summation over all indices implicit):

$$\hat{L}^{(2)}(E) = \frac{1}{4} \hat{G}^{(0)p_1p_2}_{12} \hat{R}^{(0)}_{12}(E) \hat{G}^{(0)p_3p_4}_{34} \operatorname*{tr}_R (p_2\ :K_1^{p_1} K_2^{p_2}:\ p_4\ :K_3^{p_3} K_4^{p_4}:\ \rho_R^{\mathrm{eq}}). \tag{4.19}$$

[4] For example, this is explicitly defined as $:K_1^p K_{1'}^{p'}:= K_1^p K_{1'}^{p'} - \operatorname{tr} K_1^p K_{1'}^{p'} \rho_R^{\mathrm{eq}}$.

Here we have defined the bare resolvent occurring between two coupling vertices:

$$\hat{R}^{(0)}_{12}(E) = \frac{1}{E + \hat{N}\Omega - L_S - \hat{\bar{\mu}}_{12} + \bar{\omega}_{12}} \tag{4.20}$$

with the shorthand notation $\bar{\omega}_{12\ldots} = \eta_1\omega_1 + \eta_2\omega_2 + \ldots$ and $\hat{\bar{\mu}}_{1\ldots} = \eta_1\hat{\mu}_1 + \ldots$

The trace over the reservoirs can now be computed using Wick's theorem for the superoperators K_1^p, which is proven in appendix B of Ref. [3]. This theorem lets us calculate expectation values of a set of fermion superoperators by summing up pair contractions:

$$\operatorname*{tr}_R p_2 K_1^{p_1} K_2^{p_2} \cdots p_n K_{n-1}^{p_{n-1}} K_n^{p_n} \rho_R^{\mathrm{eq}} = \sum_P (-1)^P p_{P_2} \left\langle K_{P_1}^{p_{P_1}} K_{P_2}^{p_{P_2}} \right\rangle \cdots p_{P_n} \left\langle K_{P_{n-1}}^{p_{P_{n-1}}} K_{P_n}^{p_{P_n}} \right\rangle. \tag{4.21}$$

The sum over P runs over all $n!2^{-n/2}$ ways of distributing the n indices $1, 2, \ldots, n$ to $n/2$ pairs. These pairs are (P_1, P_2), (P_3, P_4) and so on. Within each pair, the order of the indices is preserved, e.g., $P_2 > P_1$. The prefactor $(-1)^P$ is -1 if P contains an odd number of permutations and $+1$ otherwise. The individual contractions contain the reservoir Fermi function and the cutoff function $D(\omega)$:

$$\gamma_{12}^{p_1 p_2} := p_2 \left\langle K_1^{p_1} K_2^{p_2} \right\rangle = \delta_{1\bar{2}} \gamma^{p_2}(\bar{\omega}_1), \qquad \gamma^p(\omega) = p \frac{D(\omega)}{1 + e^{p\omega}}, \tag{4.22}$$

where β denotes inverse temperature and $\delta_{1\bar{2}} = \delta_{\alpha_1\alpha_2}\delta_{\sigma_1\sigma_2}\delta_{\eta_1\bar{\eta}_2}\delta(\omega_1 - \omega_2)$. In the zero temperature limit on which we focus, this simplifies to

$$\gamma^p(\omega) = p\Theta(-p\omega)D(\omega), \tag{4.23}$$

with Θ denoting the step function. In Eq. (4.19) where some contractions are eliminated due to normal ordering of the superoperators, Wick's theorem yields using the antisymmetry $\hat{G}^{(0)p_3p_4}_{34} = -\hat{G}^{(0)p_4p_3}_{43}$:

$$\hat{L}^{(2)}(E) = \frac{1}{4}\hat{G}^{(0)p_1p_2}_{12}\hat{R}^{(0)}_{12}(E)\hat{G}^{(0)p_3p_4}_{34}\left(\gamma^{p_1p_4}_{14}\gamma^{p_2p_3}_{23} - \gamma^{p_1p_3}_{13}\gamma^{p_2p_4}_{24}\right) \tag{4.24}$$

$$= \frac{1}{2}\hat{G}^{(0)p_1p_2}_{12}\hat{R}^{(0)}_{12}(E)\hat{G}^{(0)p_3p_4}_{34}\gamma^{p_1p_4}_{14}\gamma^{p_2p_3}_{23}. \tag{4.25}$$

From the above derivation of $\hat{L}^{(2)}(E)$, it is clear that higher-order terms in the expansion of $\hat{L}(E)$ in $\hat{L}_V$ will consist of the same building blocks $\hat{G}^{(0)pp'}_{11'}$, $\hat{R}^{(0)}_{12\ldots}(E)$, and $\gamma^{pp'}_{11'}$. To simplify their construction and the derivation of the RG equations, we will introduce a powerful diagrammatic language for expressions like Eq. (4.25).

4.2.4. Diagrammatic language (step 2)

The expression in Eq. (4.25) can be represented by a diagram:

$$\hat{L}^{(2)}(E) = \frac{1}{2}\gamma^{p_4}(\bar{\omega}_1)\gamma^{p_3}(\bar{\omega}_2)\,\hat{G}^{(0)p_1p_2}_{12}\,\hat{R}^{(0)}_{12}(E)\,\hat{G}^{(0)p_3p_4}_{\bar{2}\bar{1}} = \tag{4.26}$$

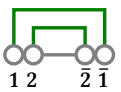

Here a pair of gray circles represent a bare vertex $\hat{G}^{(0)pp'}_{11'}$, which is connected to other vertices by green contraction lines representing $\gamma^{pp'}_{11'} = \delta_{1\bar{1}'}\gamma^{p'}(\bar{\omega})$. The indices which are indicated below the vertices are only restricted by the contraction lines, which always connect index 1 with $\bar{1}$ and so on. Between the vertices, the horizontal gray line represents the resolvent $\hat{R}^{(0)}_{12}(E)$. The indices 12 of the resolvent are always the indices standing on the left of the contraction lines above the resolvent. The prefactor $1/2$ in $\hat{L}^{(2)}(E)$ is a symmetry factor which must be included when translating this diagram because there are two contraction lines directly connecting the same pair of vertices. Having seen how a simple diagram can represent an already relatively complicated expression, we will now formalize the diagrammatic rules as well for more complicated diagrams.

Diagrammatic rules. One can show that the full series expansion of the effective Liouvillian can be obtained by including all possible diagrams which obey the following rules [76].

- All vertices are arranged on a single, horizontal line (here in gray).
- Each circle in each vertex has one index and is connected to a circle of another vertex by one contraction line. A vertex may not be connected to itself.
- A contraction line connects indices n and $\bar{n}$ and represents the scalar function $\gamma^p(\bar{\omega}_n)$, where p is the Keldysh index on the right-hand side of the contraction line. We usually write only those indices explicitly that are necessary to understand the diagram.
- Each crossing of two contraction lines contributes a minus sign.
- Neighboring vertices are connected by a resolvent $\hat{R}_X(E)$ represented by the horizontal, gray line. Here, X is the set of all indices of the contraction lines above the resolvent. By convention, the index of a contraction line is the index of the left circle to which it is connected.
- Each diagram is irreducible, i.e., it must stay connected by contraction lines and resolvents (green and gray lines) when removing a single resolvent anywhere in the diagram.[5]
- Vertices and resolvents do not commute.
- Equivalent diagrams should be accounted for only once. Two diagrams are considered equivalent if one diagram can be obtained from the other one by only permuting the circles with their attached contraction lines within individual vertices.
- Each time n contraction lines connect the same pair of vertices this adds a prefactor $1/n!$ to the diagram.[6] This explains the prefactor $1/2$ in Eq. (4.26). In contrast to Ref. [76], we

[5] Without this rule, we would obtain all diagrams for $\hat{\Pi}(E)$, not just those for $\hat{L}(E)$.

[6] The coupling Liouvillian is constructed such that every n-point vertex contains a prefactor $1/n!$. In a diagram where no pair of vertices is directly connected by more than one contraction line, this prefactor $1/n!$ is cancelled because there are $n!$ possible ways of connecting n contraction lines to n points of the vertex and each of these possible connections appears separately in the Wick contractions collected in the diagram. But if the same two vertices are connected by m lines, then these lines only represent $m!$ different Wick contractions in total, and not $m!$ per vertex. Thus, a correcting prefactor $1/m!$ is required.Similar combinatoric prefactors are known from Feynman [178] and Hugenholtz [179] diagrams.

do not explicitly write this symmetry factor in the diagrams.

Through these rules, the diagrammatic language faithfully represents the complete perturbation expansion of $\hat{L}(E)$, providing a very efficient way of collecting and manipulating terms of this expansion. When we discuss the Kondo model, we have the additional restriction to the diagrammatic language that in the bare series expansion only a two-point vertex appears. We do not explicitly write the Keldysh indices in the diagrams because we usually sum over all Keldysh indices, like in Eq. (4.26).

Effective resolvent. The diagrammatic language also suggests how to include whole classes of diagrams in individual diagrams by formulating the theory self-consistently. In the first step, we define an effective resolvent, in which we replace the bare system Liouvillian L_S with the effective Liouvillian $\hat{L}(E)$:

$$\hat{R}(E) = \frac{1}{E + \hat{N}\Omega - \hat{L}(E)}, \tag{4.27}$$

$$\hat{R}_X(E) = \hat{R}(E - \hat{\mu}_X + \bar{\omega}_X). \tag{4.28}$$

Again, X denotes a set of indices, e.g., $X = 12$ in a diagram like Eq. (4.26). By expanding the effective resolvent as a geometric series in $\hat{L}(E) - L_S$ one finds that it collects the diagrams

$\hat{R}(E) =$  (4.29)

Using effective resolvents instead of bare ones reduces the number of diagrams which we need to consider, provided we modify the diagrammatic rules:

- Vertices are connected by effective resolvents — represented by black horizontal lines — instead of bare (gray) resolvents.
- A diagram must stay connected by contraction lines and resolvents when removing two (or less) resolvents. Here we also call two parts of a diagram connected if the crossing of contraction lines from both parts cannot be avoided, even if there is no direct connection of these parts by contraction lines.

The last rule reduces the number of allowed diagrams, and guarantees that when inserting the diagrams for the effective resolvent into the diagrammatic series, we do not count any diagram multiple times.

With the usage of effective resolvents, the expansion must be solved self-consistently. The expansion of $\hat{L}(E)$ depends on the initially unknown $\hat{L}(E)$. This may seem impractical, but when deriving the RG equations this self-consistency presents no obstacle, while it improves the quality of the approximations made when truncating the diagrammatic expansion. Even when truncating the effective theory at a finite order, classes of infinitely many bare diagrams are taken into account. This strategy is well-known in field theoretical methods based on Green's functions, where one self-consistently calculates a self-energy [180].

Effective vertex. In the next step, we introduce an effective vertex, for which it is less obvious how to avoid double counting of diagrams. We cannot simply replace bare vertices with effective ones and discard some diagrams to avoid counting some bare diagram multiple times. Fortunately, when deriving the RG equations which are based on E-derivatives of diagrams, we will see that we can use effective vertices without risking double counting. The effective two-point vertex is defined as the sum of all connected diagrams with two fixed external contraction lines labeled 1 and 2 with fixed Keldysh indices p_1 and p_2:

$$\hat{G}^{p_1 p_2}_{12}(E) = \quad = \quad + \quad + \quad + O\left(G^3\right). \tag{4.30}$$

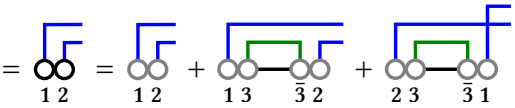

Effective vertices will be drawn in black to distinguish them from bare vertices. By $O(G^n)$ we indicate that terms containing n or more vertices are neglected.

For an effective n-point vertex including any number of internal lines (shown in green) the diagrammatic rules for $\hat{L}(E)$ apply with the modification that there are exactly n external lines (shown in blue). External lines are drawn towards the right and must be considered for the energy shift of the resolvents $\hat{R}_X(E)$. Here, X contains the indices of all external and internal contraction lines drawn above the resolvent. Thus, an effective vertex depends on the frequencies of the external contraction lines. We will see below how this complication can be overcome. Furthermore, unlike internal lines, external lines are distinguishable, and we need to consider diagrams separately which differ by permutations of external lines, except if these external lines are connected to the same vertex. For example, the last two diagrams in Eq. (4.30) must be distinguished. Finally, external lines are not translated to a contraction function $\gamma^p(\omega)$, for example:

$$= \gamma^{p_4}(\bar{\omega}_3)\hat{G}^{(0)p_1 p_3}_{13}\hat{R}_{13}(E)\hat{G}^{(0)p_4 p_2}_{\bar{3}2}. \tag{4.31}$$

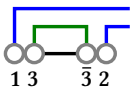

Since we can write down irreducible diagrams with many external lines, there also exist higher-order effective vertices like a four-point vertex, even if the bare theory only contains a two-point vertex. In general, infinitely many higher-order effective vertices are generated. Fortunately, such higher-order vertices only appear beyond the next-to-leading order in the perturbative expansion. Here we truncate the RG equations after the next-to-leading order, which turns out to be sufficient (see section 6.1.1 for a discussion of the truncation order). With the definition of the effective vertex, the basic diagrammatic language is complete, and we can start deriving the RG equations for the Kondo model.

4.3. Derivation of the RG equations

The diagrammatic expansion with effective resolvents and vertices poses several challenges. The expansion only yields a self-consistency equation for $\hat{L}(E)$, which could be solved iteratively from a suitable initial guess. When using the effective vertex, it is very difficult to avoid double counting of diagrams. This restricts the ability to systematically combine large classes of bare diagrams into only a few effective diagrams. Furthermore, for the Kondo model, the values of

individual diagrams diverge in the wideband limit $D \to \infty$. All these problems are avoided when we derive RG equations instead of just trying to sum up the diagrammatic expansion of $\hat{L}(E)$.

In the modern E-flow variant of the RTRG, the effective Liouvillian is not calculated directly, but one computes its second derivative and the derivative of the effective vertex. Truncating the series expansion for these objects, one can obtain a closed set of differential equations for the effective Liouvillian and vertex. As we will show, this provides a way to access these quantities without the above-mentioned issues. For the initial conditions of these differential equations, we will use some simplifications which occur at large Im E.

In this section, we derive the RG equations for models like the Kondo model with only a two-point vertex. These RG equations include the dynamics and transport observables like the current. The derivation presented in this section closely follows Ref. [76], where the Kondo model with a constant bias voltage and finite temperature was considered.

4.3.1. Energy derivatives (step 3)

One problem of the direct expansion of $\hat{L}(E) - L_S$ in terms of diagrams is the divergence for $D \to \infty$. This difficulty is typical for the Kondo-type models. The leading order diagram for $\hat{L}(E)$ contains a double integral over two frequencies in the reservoir contraction lines and can schematically be written in the form


$$= \int_0^\infty d\omega \int_0^\infty d\omega'\, D(\omega)D(\omega')\, O\left(\frac{1}{E \pm \omega \pm \omega' + i\Gamma}\right) = O(D), \tag{4.32}$$

where we included a value $\Gamma > 0$ from the effective Liouvillian[7] which ensures that there is no divergence at $\omega + \omega' = \mp E$. When considering the universal low-energy physics, which combines the weak coupling ($J \to 0$) and wideband ($D \to \infty$) limit, the double integral is divergent due to contributions of high energies (large ω and ω'). The key trick is to note that the diagram can be regularized by taking the second derivative with respect to the energy E occurring in the resolvent. In the limit $D \to \infty$ this yields a convergent double integral of the form $\int_0^\infty d\omega \int_0^\infty d\omega' (\omega + \omega' + \text{const.})^{-3}$.

In the diagrams, we denote a derivative with respect to E by a red slash through a resolvent:

$$\frac{\partial^2}{\partial E^2}\hat{L}(E) = \frac{\partial^2}{\partial E^2}\Big\{ + + O(G^4)\Big\} \tag{4.33}$$

$$= + + + 2 + O(G^4) \tag{4.34}$$

$$= + 2 + O(G^4). \tag{4.35}$$

In Eq. (4.34) we used that in a diagram with bare vertices (gray) the energy derivative only acts on the resolvents. The last diagram obtains a factor 2 because of the two possible orders of taking

[7] When evaluating similar integrals for the Kondo model, we will see in section 5.1.1 that the superoperator $\hat{L}(E)$ can indeed be replaced by a Floquet matrix $\hat{\Gamma}(E)$. The FRTRG results strongly suggest that all eigenvalues of this matrix have a positive real part.

the derivatives. In Eq. (4.35) we combined the first three diagrams of Eq. (4.34) by replacing bare vertices with effective vertices. These effective vertices also include of a large class of other higher-order bare diagrams which were not indicated in Eq. (4.34) and may improve the accuracy of the approximation involved in the truncation of the diagrammatic series. A tricky point is that to avoid double counting, it is essential that all effective vertices are separated by energy derivatives in the resolvents. Connecting two effective vertices directly by a resolvent without an energy derivative would lead to double counting of many bare diagrams. Thus, we can only use the effective vertices to rearrange the diagrams *after* taking the energy derivatives.

When translating the diagrams in Eq. (4.35) it is important to note that the shift in the energy argument of resolvents $\hat{R}(E)$ also applies to effective vertices:

$$= \gamma^{p_3}(\bar{\omega}_2)\gamma^{p_4}(\bar{\omega}_1)\hat{G}^{p_1p_2}_{12}(E)\frac{\partial^2\hat{R}_{12}(E)}{\partial E^2}\hat{G}^{p_3p_4}_{\bar{2}\bar{1}}(E-\hat{\tilde{\mu}}_{12}+\bar{\omega}_{12}). \tag{4.36}$$

To understand the shift in the energy argument of the right-most vertex, we remember that effective vertices depend on energy E because in their diagrammatic expansion they contain effective resolvents $\hat{R}(E)$. As for all resolvents [Eq. (4.20)], the energy argument of these resolvents is shifted by $-\hat{\tilde{\mu}}_X+\bar{\omega}_X$, where X denotes the set of indices of all contraction lines above the resolvent. Thus, every effective vertex has the same energy shift as the resolvent immediately left of it. Summarizing the rules for resolvents and vertices, we find that a vertex $\hat{G}^{p_1p_2}_{12}(E)$ shifts the energy argument of all functions of energy standing right of it by $-\hat{\tilde{\mu}}_{12}+\bar{\omega}_{12}$.

Using effective vertices to improve the accuracy of the diagrammatic expansion comes at the price of needing also RG equations for the vertices. The leading order diagrams for the effective vertex [Eq. (4.30)] contain one divergent frequency integral over one resolvent, so that convergence for $D\to\infty$ can be achieved by taking a single energy derivative. Up to third order in the effective vertices, we obtain

$\frac{\partial}{\partial E}\hat{G}^{p_1p_2}_{12}(E) =$

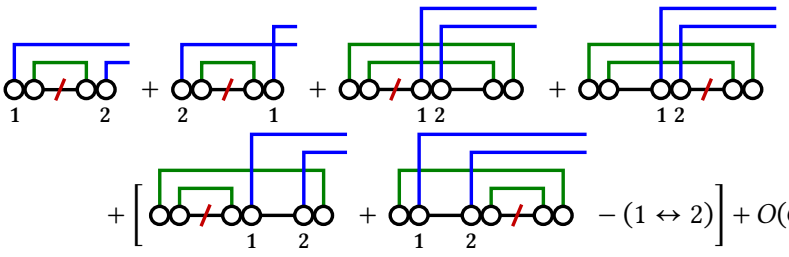

$+O(G^4).$ (4.37)

Like in the derivation of Eq. (4.35), we have first taken the energy derivative in the expansion (4.30) of $\hat{G}^{p_1p_2}_{12}(E)$ in bare vertices, and then grouped diagrams together by replacing bare vertices with effective vertices.

For the Kondo model, we have already seen in section 3.1.2 using Anderson's poor man's scaling approach that the renormalization of the coupling is essential to understand the low-energy physics. Thus, using effective vertices instead of bare vertices is not just a technical trick to include more bare diagrams in the effective diagrams, but it is necessary for analyzing models like the Kondo model. We will see in section 5.2.5 that the effective vertex indeed takes the role of the effective coupling in the Kondo model, with a scaling law that is very similar to the poor man's scaling result.

4.3.2. Derivatives of contraction lines (step 4)

In the next step, we want to use the energy derivatives to simplify the calculation of diagrams by removing integrals. The main idea is to replace energy derivatives by frequency derivatives in the resolvents, and to incorporate these frequency derivatives in the vertices and contraction lines. In the zero temperature limit, a frequency derivative of a contraction line leads to a Dirac-δ of the frequency and thereby removes the reservoir frequency integral.

So far, we are dealing with energy derivatives of the form $\partial_E \hat{R}_{12}(E) = \partial_E \hat{R}(E - \hat{\bar{\mu}}_{12} + \bar{\omega}_{12}) = \partial_{\bar{\omega}_1} \hat{R}_{12}(E)$, which can be turned into a reservoir frequency derivative. Using integration by parts, this frequency derivative can be shifted to the frequency dependence of the effective vertices and of the contraction lines. For example, denoting derivatives with respect to a frequency $\bar{\omega}_3$ by a red cross, we can write

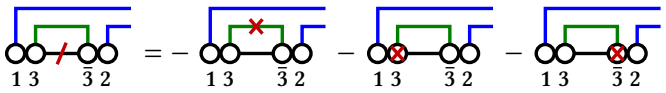

(4.38)

On the right-hand side we see derivatives of the form $\partial_{\bar{\omega}_3} \gamma^{p_4}(\bar{\omega}_3)$, $\partial_{\bar{\omega}_3} \hat{G}^{p_1 p_3}_{13}(E)$, and $\partial_{\bar{\omega}_3} \hat{G}^{p_4 p_2}_{32}(E - \hat{\bar{\mu}}_{13} + \bar{\omega}_{13})$. Since the derivative is taken with respect to a specific frequency $\bar{\omega}_3$, it is assigned to a circle (index) of a vertex. Starting from Eq. (4.38), we can derive an expression for $\partial_E \hat{G}^{p_1 p_2}_{12}(E)$, in which all derivatives are shifted to the contraction lines.

The ω-derivatives of effective vertices occurring in Eq. (4.38) can be calculated by inserting the definition (4.30) of the effective vertex in terms of bare diagrams. Taking frequency derivatives of Eq. (4.30) and using that the bare vertex is frequency-independent, one obtains[8]

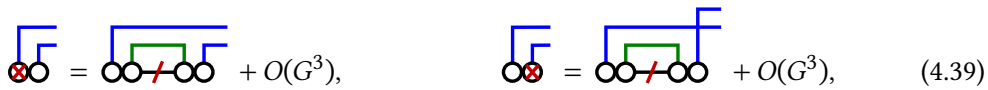

(4.39)

(4.40)

Inserting these vertex derivatives into Eq. (4.38) yields

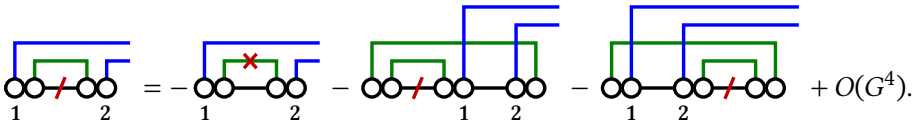

(4.41)

To complete our task of computing $\partial_E \hat{G}^{p_1 p_2}_{12}(E)$, we notice that when inserting Eq. (4.41) in the first term of Eq. (4.37), many terms cancel. By making use of the fact that the first two diagrams in Eq. (4.37) are equivalent up to a prefactor -1 and swapping indices 1 and 2, we can use Eq. (4.41)

[8] Here, one should remember that the two second-order diagrams on the right-hand side of Eq. (4.30) only depend either on $\bar{\omega}_1$ or on $\bar{\omega}_2$. When taking the derivatives with respect to $\bar{\omega}_1$ or $\bar{\omega}_2$, only one of these diagram will contribute.

to simplify Eq. (4.37) further and obtain our final result:

$$\frac{\partial}{\partial E}\hat{G}_{12}^{p_1 p_2}(E) = -$$ 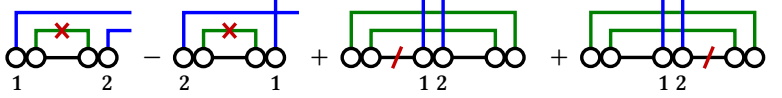 $$+ O(G^4) \tag{4.42}$$

$$= -$$ 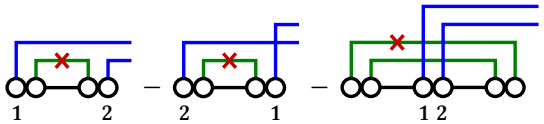 $$+ O(G^4). \tag{4.43}$$

In the last step, we have used integration by parts once again, which is especially simple because all vertex derivatives would be of higher order. This expression is much simpler than Eq. (4.37) since in the zero temperature limit the derivative of a contraction line sets its frequency to zero: $\partial_\omega \gamma^p(\omega) = -\delta(\omega)$. Thus, at zero temperature in Eq. (4.43), only one integral remains in the last term.

The same strategy can now be used for the RG equation for the effective Liouvillian, Eq. (4.35). Using integration by parts twice — once for each frequency $\bar{\omega}_1$ and $\bar{\omega}_2$ — we find

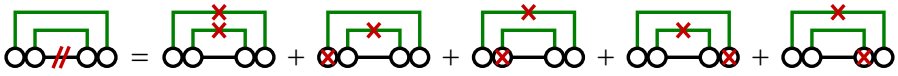 $$+ O(G^4). \tag{4.44}$$

The contribution of the last four diagrams can be simplified again by inserting the derivative of the effective vertex. Here it is important to remember that each diagram in Eq. (4.44) includes a combinatoric prefactor $\frac{1}{2}$ because two vertices are directly connected by two contraction lines. Using the antisymmetry of the vertices and inserting the vertex derivative, we obtain

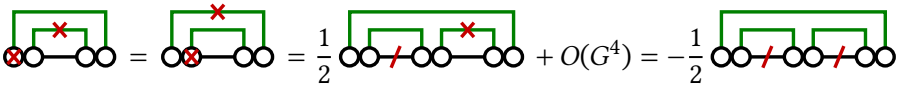 $$+ O(G^4). \tag{4.45}$$

A similar derivation leads to the same result for the last two diagrams in Eq. (4.44). When combining these results with Eq. (4.35), almost all terms cancel, and we obtain the simple RG equation

$$\frac{\partial^2}{\partial E^2}\hat{L}(E) =$$ 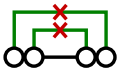 $$+ O(G^4), \tag{4.46}$$

in which no reservoir frequency integral remains at zero temperature.

Using integration by parts, we have simplified the RG equations such that at zero temperature only a single reservoir frequency integral remains in the RG equation for the effective vertex. At finite temperature, the RG equations become more complicated as more frequency integrals remain. These can be approximated based on an expansion around zero frequency, as discussed in Ref. [76]. Here we do not consider finite temperature, but note that there seem to be no fundamental obstacles to extending this approach to finite temperature in the presence of time-dependent driving. We stress, however, that the strength of the present method lies in the description of strongly correlated quantum systems at sufficiently low temperature such that interesting quantum effects — like the Kondo effect — are not suppressed by finite temperature.

4.3.3. Frequency dependence of the vertices (step 5)

We have already derived RG equations for the Liouvillian and the vertex. However, the effective vertex $\hat{G}^{p_1 p_2}_{12}$ is still a function of the frequencies $\bar{\omega}_1$ and $\bar{\omega}_2$. To obtain a numerically solvable set of ordinary differential equations, we need to remove this dependence on continuous variables. Fortunately, it suffices to include only the vertex at zero external frequencies in the RG equations, as we will see in the following.

It is beneficial that in the zero temperature limit of interest, the derivatives of the contraction lines already set many frequencies to zero. A vertex with external frequencies set to zero will be denoted by filled black circles. With this notation, the RG equations (4.43) and (4.46) become

$$\frac{\partial^2}{\partial E^2}\hat{L}(E) = \quad + O(G^4), \tag{4.47}$$

$$\frac{\partial}{\partial E}\hat{G}^{p_1 p_2}_{1_0 2_0}(E) = - \quad - \quad - \quad + O(G^4). \tag{4.48}$$

The indices $1_0, 2_0$ indicate that the external frequencies are set to zero. Thus, only the last diagram in the next-to-leading order in G in Eq. (4.48) still includes frequency-dependent vertices. Now we remember that the frequency-dependence of the effective vertex is a higher-order effect: In leading order, the effective vertex is given by the frequency-independent bare vertex [Eq. (4.30)]. We can thus write $=$ $+ O(G^2)$ and find that the frequency dependence in Eq. (4.48) only contributes to $O(G^4)$, which we neglect. This allows us to replace the two remaining frequency-dependent vertices in Eq. (4.48) with their zero-frequency values.

We have now completed our derivation of the RG equations: We have found a tractable set of ordinary differential equations (4.47) and (4.48) describing the energy dependence of the Liouvillian and the effective vertex. But to efficiently solve these RG equations numerically, we need to solve the integral in Eq. (4.48) analytically.

4.3.4. Frequency integral (step 6)

In Eq. (4.48), the last diagram includes an integral of the form

$$= \frac{1}{2}\hat{G}^{p_3 p_4}_{3_0 4_0}(E) \int_{-\infty}^{\infty} d\omega_4 \, \gamma^{p_5}(\bar{\omega}_4)\hat{R}_{34}(E)\hat{G}^{p_1 p_2}_{1_0 2_0}(\hat{E}_{34} + \bar{\omega}_4)\hat{R}_{1234}(E)\hat{G}^{p_5 p_6}_{4_0 \bar{3}_0}(\hat{E}_{1234} + \bar{\omega}_4), \tag{4.49}$$

where we used the shorthand notation $\hat{E}_X = E - \hat{\mu}_X$ and again X denotes a set of multi-indices, e.g., $X = 34$ or $X = 1234$. To simplify this integral, we first remember that the energy-dependence of the effective vertex is a higher-order effect, $\hat{G}^{p_1 p_2}_{1_0 2_0}(E + \omega) = \hat{G}^{p_1 p_2}_{1_0 2_0}(E) + O(G^2)$. This allows us to

neglect the shift by $\bar{\omega}_4$ in the energy arguments of the vertices:

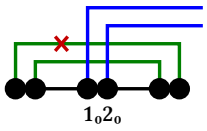

$$= -\frac{1}{2}\hat{G}^{p_3 p_4}_{3_0 4_0}(E)\,\mathcal{J}^{p_5}[\hat{G}^{p_1 p_2}_{1_0 2_0}](\hat{E}_{34})\,\hat{G}^{p_5 p_6}_{\bar{4}_0 \bar{3}_0}(\hat{E}_{1234}) + O(G^4), \tag{4.50}$$

$$\mathcal{J}^{p_5}[\hat{G}^{p_1 p_2}_{1_0 2_0}](\hat{E}_{34}) = -\int_{-\infty}^{\infty} d\omega_4\, \gamma^{p_5}(\bar{\omega}_4)\,\hat{R}_{34}(E)\,\hat{G}^{p_1 p_2}_{1_0 2_0}(\hat{E}_{34})\,\hat{R}_{1234}(E). \tag{4.51}$$

The integration variable ω_4 only remains in the contraction step function $\gamma^{p_5}(\bar{\omega}_4) = p_5\Theta(-p_5\bar{\omega}_4)$ and in the resolvents. Here we have already taken the wideband limit $D \to \infty$ because the integral is convergent in this limit. To solve it analytically, we approximate the frequency-dependence of the effective resolvent. To count the order in the vertices G, we used that $\partial_E^2 \hat{L}(E) = O(G^2)$. Aiming to bring Eq. (4.51) to the analytically solvable form $\int_0^\infty d\omega \frac{1}{\omega+A} B \frac{1}{\omega+C} D$, we expand $\hat{L}(\hat{E}_X + \bar{\omega}_X)$ around $\hat{E}_X$:

$$\hat{R}_X(E) = \frac{1}{\hat{E}_X + \bar{\omega}_X + \hat{N}\Omega - \hat{L}(\hat{E}_X + \bar{\omega}_X)} \tag{4.52}$$

$$= \frac{1}{\hat{E}_X + \bar{\omega}_X + \hat{N}\Omega - \hat{L}(\hat{E}_X) - \bar{\omega}_X \frac{\partial}{\partial E}\hat{L}(\hat{E}_X) + O(G^2)}. \tag{4.53}$$

This approximation of the resolvent can be written in the form

$$\hat{R}_X(E) = \frac{1}{\bar{\omega}_X + \hat{\chi}(\hat{E}_X)}\hat{Z}(\hat{E}_X) + O(G^2), \tag{4.54}$$

$$\hat{Z}(\hat{E}_X) = \frac{1}{1 - \frac{\partial}{\partial E}\hat{L}(\hat{E}_X)}, \tag{4.55}$$

$$\hat{\chi}(\hat{E}_X) = \hat{Z}(\hat{E}_X)[\hat{E}_X + \hat{N}\Omega - \hat{L}(\hat{E}_X)], \tag{4.56}$$

which allows us to bring Eq. (4.51) to the desired form:

$$\mathcal{J}^{p_5}[\hat{G}^{p_1 p_2}_{1_0 2_0}](\hat{E}_{34}) = -p_5 \int_0^\infty d\omega \frac{1}{\omega - p_5\hat{\chi}(\hat{E}_{34})}\hat{Z}(\hat{E}_{34})\hat{G}^{p_1 p_2}_{12}(\hat{E}_{34})\frac{1}{\omega - p_5\hat{\chi}(\hat{E}_{1234})}\hat{Z}(\hat{E}_{1234}) + O(G^2). \tag{4.57}$$

This can be solved exactly, assuming that the spectral decomposition of $\hat{\chi}$ is known. To state the solution of an integral of the present form, we consider three matrices A, B, C with spectral decomposition $A = \sum_a |a\rangle a\langle a|$ (analogous for C):

$$\int_0^\infty d\omega \frac{1}{\omega + A} B \frac{1}{\omega + C} = \sum_{ac} \frac{\log\left(\frac{a}{c}\right)}{a - c} |a\rangle\langle a|\, B\, |c\rangle\langle c| \tag{4.58}$$

$$= \frac{1}{2}\left(\frac{1}{A}B + B\frac{1}{C}\right) + O\left(\max_{ac} \frac{(a-c)^2\langle a|B|c\rangle}{(a+c)^3}\right). \tag{4.59}$$

An important consequence of the exact Eq. (4.58) is that the dependence on the Keldysh index p_5 drops out in $\mathcal{J}^{p_5}[\hat{G}^{p_1p_2}_{1_0 2_0}](E)$, and we will stop writing this index for the integral. This will allow us to completely remove the Keldysh indices in step 7.

Since the matrices A and C [$\hat{\chi}(\hat{E}_{34})$ and $\hat{\chi}(\hat{E}_{1234})$] can be diagonalized numerically, it is possible to use the exact solution (4.58) of the integral in the RG equations. But it is numerically beneficial to avoid the diagonalization of $\hat{\chi}$ and use the approximate representation of the integral in Eq. (4.59). A comparison of results with and without this approximation will be discussed in section 6.1.2, and shows that this approximation works very well. We can motivate this approximation using the structure of the involved Floquet matrices. First, it is important to remember that the integral which we want to approximate only appears in the next-to-leading order in the RG equations. In section 6.1.1, we verify that the contribution of the next-to-leading order is relevant, but the leading order is dominant. During most of the RG flow, $|E|$ is the largest energy scale and the far off-diagonal matrix elements of all Floquet matrices are strongly suppressed. The vertex that appears as matrix B in the integral only has significant entries on and near the diagonal, and in appendix J.3 we show explicitly that $\hat{G}_{12}(E)$ approximately commutes with the resolvent $\hat{R}(\hat{E}_X)$. Thus, the main approximation lies in the expansion of the logarithm in Eq. (4.58). This approximation is well justified as long as $|E|$ is large compared to $\hat{\tilde{\mu}}_X$, but it remains valid even at small $|E|$ as long as $\hat{\chi}(\hat{E}_X)$ does not become (approximately) singular. Therefore, the approximation of the integral only leads to negligible changes in the results, as we will see in section 6.1.2.

Another motivation for this approximation is the following. At vanishing driving, the approximation is exact because $\hat{\chi}(\hat{E}_{12}) = \hat{\chi}(\hat{E}_{1234})$ and all Floquet matrices are diagonal. Thus, the deviation due to approximating the integral must be of the order $O(G\Delta/\tilde{E})$ (or higher) where $\Delta = \|\hat{\mu}_{LR}\|$ is the energy scale of the bias voltage and $\tilde{E}$ is a renormalized energy scale $\tilde{E} \sim E$ that remains finite for $E \to 0$. Inserting this in Eq. (4.59) yields

$$\mathcal{J}[\hat{G}^{p_1p_2}_{1_0 2_0}](\hat{E}_{34}) = \frac{1}{2}\left[\hat{R}(\hat{E}_{34})\hat{G}^{p_1p_2}_{12}(\hat{E}_{34})\hat{Z}(\hat{E}_{1234}) + \hat{Z}(\hat{E}_{34})\hat{G}^{p_1p_2}_{12}(\hat{E}_{34})\hat{R}(\hat{E}_{1234})\right] + O(\Delta G\tilde{E}^{-2}). \quad (4.60)$$

As long as $\tilde{E}$ is larger than Δ, we can treat the omitted terms as higher-order correction [76].

Now that we know how the integral can be solved, we can summarize the general RG equations for a model with only a two-point vertex:

$$\frac{\partial^2}{\partial E^2}\hat{L}(E) = \frac{1}{2}\hat{G}^{p_1p_2}_{12}(E)\,\hat{R}(\hat{E}_{12})\,\hat{G}^{p_3p_4}_{\bar{2}\bar{1}}(\hat{E}_{12}) + O(G^4), \quad (4.61)$$

$$\frac{\partial}{\partial E}\hat{G}^{p_1p_2}_{12}(E) = \hat{G}^{p_1p_3}_{13}(E)\,\hat{R}(\hat{E}_{13})\,\hat{G}^{p_4p_2}_{\bar{3}2}(\hat{E}_{13}) - (1 \leftrightarrow 2) - \frac{1}{2}\hat{G}^{p_3p_4}_{34}(E)\,\mathcal{J}[\hat{G}^{p_1p_2}_{12}](\hat{E}_{34})\,\hat{G}^{p_5p_6}_{\bar{4}\bar{3}}(\hat{E}_{34}) + O(G^4). \quad (4.62)$$

In these equations, all frequencies are set to zero, although this is not explicitly denoted. As before, we implicitly sum over all indices which appear only on one side of the equation.

4.3.5. Summing over p and η indices (step 7)

The RG equations can be simplified further by removing the Keldysh indices p and the particle-hole indices η in the multi-indices $1, 2, 3, 4$. We begin by defining the vertex summed over the

Keldysh indices as $\breve{G}_{12}(E) \coloneqq \sum_{p_1 p_2} \hat{G}_{12}^{p_1 p_2}(E)$, and sum over all Keldysh indices in Eq. (4.62). Then only Keldysh-summed indices remain and we can completely drop the Keldysh indices.

In the next step, we assume that the vertex is particle number conserving as it is in the Kondo model of interest. This is expressed as $\breve{G}_{11'} \propto \delta_{\eta\bar{\eta}'}$ and allows us to remove the η indices. We only need vertices $\breve{G}_{11'}$ with $\eta = -\eta' = +$ in the RG equations, and can use the general property $\breve{G}_{1'1} = -\breve{G}_{11'}$ [Eq. (4.14)] to obtain a vertex with the opposite order of η indices if necessary. A vertex without η indices will be denoted $\bar{G}$. Following the convention that the first multi-index has $\eta = +$ and the second one has $\eta = -$, we redefine $\hat{\tilde{\mu}}_{12} = \hat{\mu}_1 - \hat{\mu}_2$. As an example of this notation, we consider the RG equation (4.61) for $L(E)$ and write the index η explicitly:

$$\begin{aligned}
&\sum_{\eta_1\eta_2} \breve{G}_{12}(E) R(\hat{E}_{12}) \breve{G}_{\bar{2}\bar{1}}(\hat{E}_{12}) \\
&\quad = \breve{G}_{1+,2-}(E) \hat{R}(\hat{E}_{1+,2-}) \breve{G}_{2+,1-}(\hat{E}_{1+,2-}) + \breve{G}_{1-,2+}(E) \hat{R}(\hat{E}_{1-,2+}) \breve{G}_{2-,1+}(\hat{E}_{1-,2+}) && (4.63)\\
&\quad = \breve{G}_{1+,2-}(E) \hat{R}(\hat{E}_{1+,2-}) \breve{G}_{2+,1-}(\hat{E}_{1+,2-}) + [-\breve{G}_{2+,1-}(E)] \hat{R}(\hat{E}_{2+,1-}) [-\breve{G}_{1+,2-}(\hat{E}_{2+,1-})] && (4.64)\\
&\quad = 2\bar{G}_{12}(E) \hat{R}(\hat{E}_{12}) \bar{G}_{21}(\hat{E}_{12}). && (4.65)
\end{aligned}$$

A similar calculation leads to the RG equation for the vertex and lets us obtain the final form of the general RG equations:

$$\frac{\partial^2}{\partial E^2} \hat{L}(E) = \bar{G}_{12}(E)\, \hat{R}(\hat{E}_{12})\, \bar{G}_{21}(\hat{E}_{12}) + O(G^4), \tag{4.66}$$

$$\begin{aligned}
\frac{\partial}{\partial E} \bar{G}_{12}(E) = {} & \bar{G}_{13}(E)\, \hat{R}(\hat{E}_{13})\, \bar{G}_{32}(\hat{E}_{13}) - \bar{G}_{32}(E)\, \hat{R}(\hat{E}_{32})\, \bar{G}_{13}(\hat{E}_{32}) \\
& - \bar{G}_{34}(E)\, \mathcal{J}[\bar{G}_{12}](\hat{E}_{34})\, \bar{G}_{43}(\hat{E}_{34}) + O(G^4).
\end{aligned} \tag{4.67}$$

From here on, we will only work with the vertex $\bar{G}_{12}$ without Keldysh (p) and η indices.

With the effective Liouvillian and the effective vertex, we can describe the dynamics of the local quantum system. But for the single channel Kondo model which has our interest, this local quantum system consists only of a single spin 1/2. Since we consider the isotropic case with no magnetic field, the time evolution can only be the relaxation of a spin to the completely mixed state $\rho = \mathbb{1}/2$. Thus, the RG equations for the Liouvillian and the effective vertex cannot be our final result, but they will be the basis for calculating the current and the differential conductance through the quantum dot. We will see below that both $\hat{L}(E)$ and $\bar{G}_{12}(E)$ are not only required for calculating transport properties, but we can also use the already derived and simplified diagrams to compute the current.

4.3.6. Transport current (step 8)

To include a nonlocal observable in the RG equations, we need to express it as a superoperator and derive its representation in the diagrammatic language. Let us consider a general observable represented by a Hermitian operator A which acts on the full system including local system and reservoirs, and define $\langle A \rangle(t) = \mathrm{tr}[A\rho^{\mathrm{tot}}(t)]$ as the expectation value of A at time t. As discussed in section 1.2, an observable can be expressed in Liouville space by a kernel $\Sigma_A(t, t')$ — a

superoperator which considers the memory of the system — through

$$\langle A\rangle(t) = -i\int_{t_0}^{t} ds\ \mathrm{tr}\,\Sigma_A(t,s)\,\rho(s). \tag{4.68}$$

Fortunately, when expanding $\Sigma_A(t,s)$ and $L(t,s)$ in the coupling, the two series differ only by the left-most superoperator in each term, which is $\hat{L}_V$ for $L(t,s)$ and $iA\bullet$ or $\frac{i}{2}\{A,\bullet\}$ for $\Sigma_A(t,s)$. To use this similarity also in the diagrammatic language, we need to write the observable superoperator $\frac{i}{2}\{A,\bullet\}$ in the form of a vertex analogous to $\hat{L}_V$. For the charge current in reservoir γ, we need the following two-point vertex:

$$\frac{i}{2}\{A,\bullet\} = \frac{1}{2}\{[H_V,N_\gamma],\bullet\} = \frac{1}{2}p'\,\mathrm{tr}\,I^{\gamma pp'}_{11'}\ :K^{p}_{1}K^{p'}_{1'}:, \tag{4.69}$$

where again the vertex is restricted by the antisymmetry $I^{\gamma p'p}_{1'1} = -I^{\gamma pp'}_{11'}$. Now we can obtain diagrams for the current kernel $\hat{\Sigma}_\gamma(E)$ simply by replacing the left-most coupling vertex in a diagram for $\hat{L}(E)$ by a current vertex $\hat{I}^{\gamma pp'}_{11'}(E)$. This replacement works both for bare and for effective vertices, and all steps 3–7 apply likewise. The effective current vertex is given by the same diagrams and RG equations as the effective coupling vertex when replacing the left-most coupling vertex in each diagram and in each term of the final RG equations (4.66)–(4.67) with the current vertex:

$$\frac{\partial^2}{\partial E^2}\hat{\Sigma}_\gamma(E) = \bar{I}^{\gamma}_{12}(E)\,\hat{R}(\hat{E}_{12})\,\bar{G}_{21}(\hat{E}_{12}) + O(G^4), \tag{4.70}$$

$$\begin{aligned}\frac{\partial}{\partial E}\bar{I}^{\gamma}_{12}(E) = {}& \bar{I}^{\gamma}_{13}(E)\,\hat{R}(\hat{E}_{13})\,\bar{G}_{32}(\hat{E}_{13}) - \bar{I}^{\gamma}_{32}(E)\,\hat{R}(\hat{E}_{32})\,\bar{G}_{13}(\hat{E}_{32})\\ & - \bar{I}^{\gamma}_{34}(E)\,\mathcal{J}[\bar{G}_{12}](\hat{E}_{34})\,\bar{G}_{43}(\hat{E}_{34}) + O(G^4).\end{aligned} \tag{4.71}$$

To simplify the notation, we use that $\bar{I}^{\gamma}_{12}(E) = O(G)$ is of the same order as the coupling vertex, as we will prove explicitly in section 5.2.3. Here $\bar{I}^{\gamma}_{12}(E)$ is defined analogous to $\bar{G}_{12}(E)$ by summing over the Keldysh indices and fixing $\eta_1 = +, \eta_2 = -$ in $\hat{I}^{\gamma pp'}_{12}(E)$.

4.3.7. Differential conductance (step 9)

In the RG equations, we will include not only the current, but also the differential conductance. In principle, this information is redundant since the differential conductance can also be computed by numerically differentiating the current. But we will see in section 6.2 that calculating the differential conductance directly in the RG equations leads to slightly more accurate and better converged results.[9] Furthermore, the comparison of current and separately computed differential conductance provides a consistency check for our method.

To directly include the differential conductance in the RG equations, we need a diagrammatic representation for the variation of the current under an infinitesimal variation of the chemical

[9] The difference between a numerical derivative of the current and a direct calculation of the differential conductance is not large compared to the expected precision of the method. But calculating the differential conductance directly has numerical advantages and will simplify the derivation of initial conditions for the RG flow in section 5.2.6.

potential. Let us consider a time-constant, infinitesimal variation $\delta\bar{\mu}_{12} = (\delta_{\alpha_1 L} - \delta_{\alpha_2 L})\delta V_{\text{avg}}$ of the chemical potentials represented by a scalar in Floquet space. In the diagrams, the variation of $\hat{\bar{\mu}}_X$ only affects the resolvents:

$$\delta\hat{R}_X(E) = \delta\bar{\mu}_X \frac{\partial}{\partial E}\hat{R}_X(E) + \hat{R}_X(E)\,\delta\hat{L}(\hat{E}_X + \bar{\omega}_X)\hat{R}_X(E), \tag{4.72}$$

$$\delta\hat{L}(E) = \hat{L}(E)|_{\hat{\bar{\mu}}+\delta\bar{\mu}} - \hat{L}(E)|_{\hat{\bar{\mu}}}. \tag{4.73}$$

Here we have split the variation of $\hat{R}_X(E)$ into two contributions. The first term captures that $\hat{R}_X(E) = \hat{R}(E - \hat{\bar{\mu}}_X + \bar{\omega}_X)$ directly depends on $\delta\bar{\mu}_X$ through the shift in the energy argument. The second part in Eq. (4.72) takes into account that the chemical potentials influence the function $\hat{L}(E)$ at constant energy argument. This is reflected by the variation $\delta\hat{L}(E)$, which will be denoted δ in the diagrams. As we have discussed before, the diagrams for $\hat{L}(E)$ and for $\hat{\Sigma}_\gamma(E)$ are the same, except that the left-most vertex is either a coupling vertex (in $\hat{L}$) or a current vertex (in $\hat{\Sigma}_\gamma$). This general observation remains correct for the variation of these quantities, such that by deriving diagrams for $\delta\hat{L}$ we also find a way to include $\delta\hat{\Sigma}_\gamma(E)$ in the RG equations, which will eventually allow us to directly compute the differential conductance from the RG flow.

Using Eq. (4.72) and the diagrammatic expansion of $\hat{L}(E)$ in bare vertices, we can derive the diagrammatic series for $\delta\hat{L}(E)$:

$\delta\hat{L}(E) = \delta\bar{\mu}_{12}$ 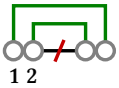 $+\,\delta\bar{\mu}_{12}$ 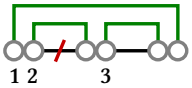 $+\,\delta\bar{\mu}_{13}$ 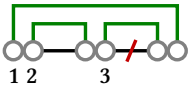 $+$ 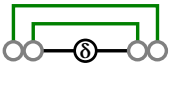 $+\,O(G^4).$ (4.74)

Here we have neglected a term of the order $O(G^3\delta\hat{L})$ because we can argue that $\delta\hat{L}(E) = O(G)$ is of the same order as a coupling vertex. The leading order in Eq. (4.74) shows us that $\partial_E\delta\hat{L}(E) = O(G^2/E)$ is of the same order as $\partial_E\bar{G}_{12}(E)$. In the discussion of the initial condition of the RG flow in section 5.2, we will furthermore see that $\delta\hat{L}(E)$ vanishes at the beginning of the RG flow because it vanishes in equilibrium.[10] Thus, $\delta\hat{L}(E)$ is of the order $O(G)$ or higher order and terms of the order $O(G^3\delta\hat{L})$ are negligible.

After taking an energy derivative of Eq. (4.74) to obtain the RG equation, we can again use effective vertices to reduce the number of diagrams and improve the accuracy. Like in the diagrams for $\hat{L}(E)$, we use integration by parts to take derivatives of contraction functions and thereby remove frequency integrals. Following the same steps 3–5 as in the derivation of Eq. (4.46), we obtain

$\frac{\partial}{\partial E}\delta\hat{L}(E) = \delta\bar{\mu}_{12}$ 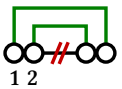 $+\,(\delta\bar{\mu}_{12} + \delta\bar{\mu}_{13})$ 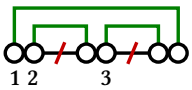

$+$  $+$ 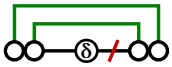 $+\,O(G^4)$ (4.75)

$= \delta\bar{\mu}_{12}$ 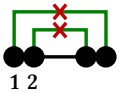 $-$ 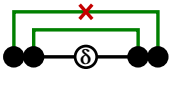 $+\,O(G^4).$ (4.76)

[10] In equilibrium, $\delta\hat{L}(E)$ must be independent of the sign of the variation $\delta\bar{\mu}_X$ of the chemical potentials. Thus, it cannot contain any terms linear in $\delta\bar{\mu}_X$.

In the last diagram we have again neglected the frequency-dependence of the effective vertex because it is a higher-order contribution (see step 5). The integral appearing in the last diagram is of the same form as the integral in the RG equation for the effective vertex. Following the same strategy as in step 7, we sum over the Keldysh and η indices to obtain

$$\frac{\partial}{\partial E}\delta\hat{L}(E) = \frac{1}{2}\delta\bar{\mu}_{12}\,\hat{G}_{12}^{p_1p_2}(E)\,\hat{R}(\hat{E}_{12})\,\hat{G}_{\bar{2}\bar{1}}^{p_3p_4}(\hat{E}_{12}) - \frac{1}{2}\hat{G}_{12}^{p_1p_2}(E)\,\mathcal{J}[\delta\hat{L}](\hat{E}_{12})\,\hat{G}_{\bar{2}\bar{1}}^{p_3p_4}(\hat{E}_{12}) + O(G^4) \quad (4.77)$$

$$= \delta\bar{\mu}_{12}\,\bar{G}_{12}(E)\,\hat{R}(\hat{E}_{12})\,\bar{G}_{21}(\hat{E}_{12}) - \bar{G}_{12}(E)\,\mathcal{J}[\delta\hat{L}](\hat{E}_{12})\,\bar{G}_{21}(\hat{E}_{12}) + O(G^4). \quad (4.78)$$

The RG equation for $\delta\hat{\Sigma}_\gamma(E)$ can be obtained by replacing the left-most vertex in both terms in Eq. (4.78) with the current vertex, as we did with the RG equation for $\hat{L}(E)$ in Eq. (4.70).

4.4. Initial condition of the RG flow

Now that we know the RG equations, we still need an initial condition to solve them. Different strategies exist for finding initial conditions for the E-flow RTRG [74–76]. Here we follow the idea put forward in Refs. [74, 76], which has been applied to the Kondo model before and which can be extended to include Floquet matrices. What all these strategies have in common is that one starts the RG flow from $E = i\Lambda_0$ for some large $\Lambda_0 \gg T_K$ and uses that for this value of the flow parameter the system can be approximated by weak coupling or equilibrium results. The full details of the initial conditions will be presented in chapter 5, since they depend on details of the Kondo model. The key points to note here are the following.

At large imaginary part $\mathrm{Im}\,E$ of the Laplace variable, the Laplace transform — or Floquet matrix — only captures the physics on very short timescales. On these short timescales, low-energy processes which lead to the strong effective coupling in the Kondo model do not play a significant role. There is simply not enough time to form a Kondo state with strong effective coupling. Thus, at large $\mathrm{Im}\,E$ the coupling between the system and the reservoirs is weak, bare perturbation theory converges, and effective quantities resemble the bare ones. We will use results from bare perturbation theory at large $\mathrm{Im}\,E$ and some properties of the model, to first construct an initial condition for the RG flow in equilibrium. In the equilibrium RG flow, we can then reach $E = i\Lambda_0$, where we start including nonequilibrium and driving effects. Again, we use that at large $\mathrm{Im}\,E$ low energy scales such as the bias voltage do not play a significant role, such that we can approximate all quantities appearing in the RG equations by their equilibrium values. Eventually, the nonequilibrium RG equations are solved numerically starting from $E = i\Lambda_0$ until $E = 0$, where we obtain observables like the current.

4.5. Summary

In this first technical chapter, we introduced a diagrammatic language for periodically driven open quantum systems and showed how it allows for an elegant derivation of RG equations for the FRTRG in close analogy to Ref. [76]. By taking energy derivatives of the diagrammatic expansion, we could use effective vertices to sum up large classes of diagrams in just a few effective diagrams. The diagrammatic derivation allowed us to bring the RG equations to a

compact and comparably simple form while avoiding cumbersome algebra. Here we restricted the discussion to models with only a two-point vertex such as the Kondo model and derived the general RG equations (4.66), (4.67), (4.70), (4.71) and (4.78) for such models in next-to-leading order in the coupling. The general concepts explained in this chapter can also be applied to other models. For example, for models including a one-point vertex, other RG equations can be derived.

5. Application of the FRTRG to the Kondo model

Knowing the RG equations for general two-point vertex models from chapter 4, we can now proceed to the concrete application to the Kondo model. First, the symmetries of the model are used to derive parametrizations for all superoperators appearing in the RG equations such that only Floquet matrices but no superoperators remain in the RG equations (steps 10 and 11). This leads to the final RG equations (5.19)–(5.27) which conclude the lengthy derivation in steps 1–11.

To make use of these RG equations, an initial condition is required. First, the equilibrium case is analyzed to construct the equilibrium RG flow (steps 12–14). Then an initial condition for the RG flow in nonequilibrium is derived (step 15). Exception for this last step, we closely follow Ref. [76]. This derivation has been published in Ref. [3], but here we extend it by discussing different possible approximations and two possible initial conditions of the RG flow.

5.1. RG equations

The RG equations derived in chapter 4 involve Floquet-matrices, in which each matrix element is a superoperator acting on the Liouville space of the Kondo model. In the isotropic Kondo model, these superoperators are strongly restricted by symmetries such that they can be parametrized using a simple algebra of only five superoperator elements, as we will see below. Using the Floquet-matrix valued coefficients of these elements to parametrize the superoperators significantly reduces the numerical effort for solving the RG equations. Furthermore, for the vertex superoperator $\bar{G}_{12}$ this parametrization allows us to distinguish different contributions which are of different order in the coupling. This will lead to a much clearer picture showing which order is relevant and which parts can be neglected in the final RG equations.

5.1.1. Parametrization of superoperators (step 10)

To parametrize the superoperators, we need to know the Liouville space of the system and the symmetries obeyed by the dynamics. In the single-channel Kondo model of interest, the local system is a single spin $\frac{1}{2}$, represented by the Liouville space of 2×2 density matrices. In the isotropic case, on which we focus here, the evolution must be invariant under a rotation of the local spin state: If a state ρ_0 evolves to $\rho(t)$, then a rotated state $\mathcal{U}\rho_0$ must evolve to $\mathcal{U}\rho(t)$ where the superoperator $\mathcal{U}\rho = U\rho U^\dagger$ denotes a rotation of the spin and $U \in \mathrm{SU}(2)$. Similar symmetries for open quantum systems have been discussed in section 2.3.1 with the aim of simplifying the description of the dynamics. But here we consider a slightly different situation than in section 2.3.1. We restrict the evolution to obey the symmetry, but we do not pose any

restrictions on the initial states. Thus, we also describe the evolution of polarized spin states, but we do not consider evolutions that could cause such a polarization.

For the effective Liouvillian, the rotational invariance implies that it must commute with the rotation superoperator, $[L(E), \mathcal{U}] = 0$. In the parametrization of $L(E)$, we can furthermore use that every Liouvillian must be trace destroying, $(\mathbb{1}|L(E) = 0$. Here we use the Dirac notation in Liouville space introduced in section 2.1.2, in which $(\mathbb{1}|$ denotes the trace: $(\mathbb{1}|L(E)|\rho) = \mathrm{tr}[L(E)\rho]$. The trace-destroying property of the Liouvillian makes sure that density operators remain trace-normalized during the evolution. Using these restrictions, one finds that the superoperator $\hat{L}(E)$ can be described by a single Floquet matrix $\hat{\Gamma}(E)$:

$$\hat{L}(E) = -i\hat{\Gamma}(E)\bar{L}^a, \qquad \bar{L}^a = \frac{1}{2}\sum_{i=1}^{3} |\sigma_i)(\sigma_i| = \mathbb{I} - \frac{1}{2}|\mathbb{1})(\mathbb{1}| = \mathbb{I} - \frac{1}{2}\mathbb{1}\,\mathrm{tr}\,. \tag{5.1}$$

The Floquet matrix $\hat{\Gamma}(E)$ takes the role of the spin relaxation rate at energy E, and $\bar{L}^a$ is the isotropic trace-destroying superoperator.

Importantly, $\hat{L}(E)$ acts like $-i\hat{\Gamma}(E)\mathbb{I}$ on traceless operators. To make use of this property, we remember that the coupling vertex was defined originally to express the coupling Liouvillian L_V [Eq. (4.14)]. To ensure that L_V is trace-destroying, also the coupling vertex must be trace-destroying, $(\mathbb{1}|\bar{G}_{12}(E) = 0$. In the RG equations the superoperators $\hat{R}(E)$, $\hat{Z}(E)$ and $\hat{\chi}(E)$ [defined in step 6, Eqs. (4.54)–(4.56)] always stand on the left of a coupling vertex and therefore only act on traceless operators. Thus, in these superoperators we can simply replace $\hat{L}(E)$ by $-i\hat{\Gamma}(E)$ such that they become scalars in superoperator space while remaining matrices in Floquet space.

Likewise, the current kernel $\hat{\Sigma}_\gamma$ and its voltage-variation can be described by a single parameter. By construction of the current kernel, we are only interested in $(\mathbb{1}|\hat{\Sigma}_\gamma$, the part that occurs in the calculation of the current. Since also $\hat{\Sigma}_\gamma$ has to preserve the rotational symmetry, the only remaining term in $\hat{\Sigma}_\gamma$ with a nonzero contribution to $(\mathbb{1}|\hat{\Sigma}_\gamma$ is

$$\hat{\Sigma}_\gamma(E) = i\hat{\Gamma}^\gamma(E)\bar{L}^b, \qquad \bar{L}^b = \frac{1}{2}|\mathbb{1})(\mathbb{1}| = \mathbb{I} - \bar{L}^a. \tag{5.2}$$

In step 16, we will see that the Floquet matrix $\hat{\Gamma}^\gamma(E = 0)$ contains the Fourier modes of the current.

The parametrization of the vertices is more complicated due to the coupling to the reservoirs. The current vertex $\bar{I}^\gamma_{12}$ and the coupling vertex $\bar{G}_{12}$ are not only superoperators, but also matrices in reservoir spin space with indices σ_1, σ_2 contained in the multi-indices $1, 2$, which couple the vertex to fermion creation and annihilation operators $c^\dagger_{\alpha_1\sigma_1\omega_1}$ and $c_{\alpha_2\sigma_2\omega_2}$. The rotational symmetry of the model implies that the rotated vertex $\mathcal{U}^\dagger\bar{G}_{12}\mathcal{U}$ coupled to rotated reservoirs must be equal to the non-rotated vertex coupled to non-rotated reservoirs. When rotating the local state ρ to $U\rho U^\dagger$, the reservoir field operators must transform as[1] $c^\dagger_{\sigma_1} \mapsto \sum_{\sigma_2} U_{\sigma_2\sigma_1}c^\dagger_{\sigma_2}$. Thus, invariance of a vertex under rotational symmetry means, writing only spin indices for simplicity,

$$\sum_{\sigma_1\sigma_2\sigma_3\sigma_4} (\mathcal{U}^\dagger\bar{G}_{\sigma_1\sigma_2}\mathcal{U}) \otimes (U_{\sigma_3\sigma_1}c^\dagger_{\sigma_3}c_{\sigma_4}U^\dagger_{\sigma_2\sigma_4}) = \sum_{\sigma_1\sigma_2} \bar{G}_{\sigma_1\sigma_2} \otimes (c^\dagger_{\sigma_1}c_{\sigma_2}), \tag{5.3}$$

[1] When ρ is transformed to $U\rho U^\dagger$, pure basis states transform as $|\sigma\rangle \mapsto U|\sigma\rangle = \sum_{\sigma'}|\sigma'\rangle U_{\sigma'\sigma}$ with $U_{\sigma'\sigma} = \langle\sigma'|U|\sigma\rangle$. Creation operators must transform analogously: $c^\dagger_\sigma \mapsto Uc^\dagger_\sigma U^\dagger = \sum_{\sigma'} c^\dagger_{\sigma'}U_{\sigma'\sigma}$.

	L^a	L^b	L^1	L^2	L^3
L^a	L^a	0	0	L^2	L^3
L^b	0	L^b	L^1	0	0
L^1	L^1	0	0	$\pm L^1$	$3L^b$
L^2	L^2	0	0	$\frac{1}{2}(L^a \pm L^2)$	$\pm L^3$
L^3	0	L^3	$L^a \pm 2L^2$	0	0

Table 5.1.: Products $L^i L^j$ (upper sign) and $(L^{i\top} L^{j\top})^\top$ (lower sign), where the transpose is only taken in reservoir spin space, $L^{i\top}_{\sigma\sigma'} \coloneqq L^i_{\sigma'\sigma}$. L^i and L^j label the rows and columns, respectively. See tables I and II in Ref. [76].

which can be simplified to

$$\sum_{\sigma_3\sigma_4} \mathcal{U}^\dagger (U_{\sigma_1\sigma_3} \bar{G}_{\sigma_3\sigma_4} U^\dagger_{\sigma_4\sigma_2}) \mathcal{U} = \bar{G}_{\sigma_1\sigma_2}. \tag{5.4}$$

This symmetry relation must be obeyed by both the current vertex and the coupling vertex with which we will continue next.

Using Eq. (5.4), one can prove that the most general form of a vertex consistent with rotational symmetry has five Floquet-matrix coefficients $\hat{G}^\xi$ (see appendix H):

$$\bar{G}_{11'} = \sum_{\xi=a,b,1,2,3} \hat{G}^\xi_{\alpha\alpha'} L^\xi_{\sigma\sigma'} \tag{5.5}$$

with the superoperators

$$L^a_{\sigma\sigma'} = \delta_{\sigma\sigma'} \bar{L}^a = \delta_{\sigma\sigma'} \frac{1}{2} \sum_{i=1}^{3} |\sigma_i)(\sigma_i|, \qquad L^b_{\sigma\sigma'} = \delta_{\sigma\sigma'} \bar{L}^b = \frac{1}{2} \delta_{\sigma\sigma'} |\mathbb{1})(\mathbb{1}|, \tag{5.6}$$

$$L^1_{\sigma\sigma'} = \frac{1}{2} \sum_{i=1}^{3} \sigma^i_{\sigma\sigma'} |\mathbb{1})(\sigma_i|, \qquad L^2_{\sigma\sigma'} = \frac{i}{4} \sum_{i,j,k=1}^{3} \varepsilon_{ijk} \sigma^k_{\sigma\sigma'} |\sigma_i)(\sigma_j|, \qquad L^3_{\sigma\sigma'} = \frac{1}{2} \sum_{i=1}^{3} \sigma^i_{\sigma\sigma'} |\sigma_i)(\mathbb{1}|. \tag{5.7}$$

These superoperators form an algebra with the multiplication table given in table 5.1, which will be used to further simplify the RG equations. The prefactors of these superoperators are chosen such that the notation is consistent with Ref. [76]. For the coupling vertex, we can use that it is trace-destroying, which implies that $\hat{G}^b = \hat{G}^1 = 0$ and only three finite coefficients remain.

The same symmetry relation (5.4) holds for the current vertex $\bar{I}^\gamma_{11'}$ with coefficients denoted $\hat{I}^{\gamma\xi}_{\alpha\alpha'}$. Since we only need the trace $(\mathbb{1}|\Sigma_\gamma$ of the current kernel to compute the current, we can ignore all components of the current vertex which do not contribute to $(\mathbb{1}|\bar{I}^\gamma_{11'}$, setting $\hat{I}^{\gamma a}_{\alpha\alpha'} = \hat{I}^{\gamma 2}_{\alpha\alpha'} = \hat{I}^{\gamma 3}_{\alpha\alpha'} = 0$. Furthermore, the current vertex only acts on traceless operators such that we can also set $\hat{I}^{\gamma b}_{\alpha\alpha'} = 0$, leaving only one component for which we define $\hat{I}^\gamma_{12} = -4\hat{I}^{\gamma 1}_{12}$ to keep the notation consistent with Ref. [76]:

$$\bar{I}^\gamma_{11'} = -\frac{1}{4} \hat{I}^\gamma_{\alpha\alpha'} L^1_{\sigma\sigma'}. \tag{5.8}$$

By exploiting the spin-symmetry, we have, in fact, also removed the reservoir spin indices from the vertex parametrization. But we will still use digits as indices which then only label a reservoir, $1 = \alpha_1$, when working with $\hat{G}^{\xi}_{12}$ and $\hat{I}^{\gamma}_{12}$.

For the RG equations, it will be important which parameter of the vertex is dominant and which parameters only lead to higher-order corrections. This can be understood by comparison to the bare vertex. Since the bare vertex describes a commutator with the bare coupling Hamiltonian, it vanishes when acting on the identity matrix $\mathbb{1}$ on the local system. Thus, $\hat{G}^3 = 0$ in the bare vertex. We furthermore remember that the coupling Hamiltonian [Eq. (3.2)] is of the form $H_V = \sum_{\sigma\sigma'} h_{\sigma\sigma'} c^\dagger_\sigma c_{\sigma'}$, where $\sum_\sigma h_{\sigma\sigma} = 0$. This motivates that $\hat{G}^a$ must vanish as well in the bare vertex. We will see in section 5.2.3 by explicit calculation that this assumption is indeed correct.

Knowing that only $\hat{G}^2$ is contained in the bare coupling, we can identify this as the leading contribution of the coupling, and define the effective coupling by some norm of the Floquet matrix $\hat{G}^2$: $J = \|\hat{G}^2\|$. This allows us to count orders in the effective coupling J. The other components of the coupling vertex, $\hat{G}^3$ and $\hat{G}^a$, can only arise from terms of the order J^2 in the effective vertex. The current vertex also describes a coupling between the system and the reservoirs, and must therefore be of the order J (or higher). With this information in hand, we can write down the RG equations for the Floquet-matrix valued parameters, keeping only leading and next-to-leading order in J.

5.1.2. RG equations for parametrization (step 11)

The RG equations for the Kondo model can now be derived by inserting the parametrization in the RG equations derived in chapter 4. For the Liouvillian, inserting Eqs. (5.1) and (5.5) in Eq. (4.66) yields

$$-i\bar{L}^a \frac{\partial^2}{\partial E^2} \hat{\Gamma}(E) = \operatorname*{tr}_\sigma (L^2 L^2)\, \hat{G}^2_{12}(E)\, \hat{R}(\hat{E}_{12})\, \hat{G}^2_{21}(\hat{E}_{12}) + O(J^4/\tilde{E}). \tag{5.9}$$

Here tr_σ denotes the trace over the reservoir spin components, i.e., $\mathrm{tr}_\sigma L^i = \sum_\sigma L^i_{\sigma\sigma}$, and the indices $1, 2$ only contain the reservoir indices α_1, α_2. In the resolvent we have replaced $\hat{L}(E)$ by $-i\hat{\Gamma}(E)$ such that $\hat{R}(E)$ is not a superoperator anymore, and the energy scale $\tilde{E} = E + i\Gamma(E)$ indicates the order of an inverse resolvent.[2] There is no contribution from $\hat{G}^3$ in Eq. (5.9) because $\mathrm{tr}_\sigma L^3 L^\xi = \mathrm{tr}_\sigma L^\xi L^3 = 0$ for $\xi = a, 2, 3$. $\hat{G}^a$ does not appear because $\mathrm{tr}_\sigma L^2 L^a = \mathrm{tr}_\sigma L^a L^2 = 0$, such that contributions of the form $\hat{G}^a \hat{R} \hat{G}^2$ or $\hat{G}^2 \hat{R} \hat{G}^a$ do not occur. A term of the form $\hat{G}^a \hat{R} \hat{G}^a$ that could occur in Eq. (5.9) is beyond next-to-leading order since $\hat{G}^a = O(J^2)$. Thus, the RG equation for the Floquet matrix $\hat{\Gamma}$ describing spin relaxation is

$$\frac{\partial^2}{\partial E^2} \hat{\Gamma}(E) = i\hat{G}^2_{12}(E)\, \hat{R}(\hat{E}_{12})\, \hat{G}^2_{21}(\hat{E}_{12}) + O(J^4/\tilde{E}). \tag{5.10}$$

Similarly, one can derive the RG equation for the current kernel parameter $\hat{\Gamma}^\gamma$. Inserting the parametrization in the RG equation (4.70) for $\hat{\Sigma}_\gamma(E)$ yields

$$\frac{\partial^2}{\partial E^2} \hat{\Gamma}^\gamma(E) = i\frac{3}{2} \hat{I}^\gamma_{12}(E)\, \hat{R}(\hat{E}_{12})\, \hat{G}^3_{21}(\hat{E}_{12}) + O(J^5/\tilde{E}). \tag{5.11}$$

[2] Here, one can define $\Gamma(E)$ as the (by absolute value) smallest eigenvalue of $\hat{\Gamma}(E)$.

Here the leading order is already $O(J^3/\tilde{E})$ because $\hat{I}^\gamma = O(J)$ and $\hat{G}^3 = O(J^2)$.

Likewise, the RG equations for the voltage variations of $\hat{\Gamma}$ and $\hat{\Gamma}^\gamma$, which allow computing the differential conductance directly from the RG equations, can be computed. From the RG equation (4.78) for $\delta\hat{L}(E)$, we can compute the leading order RG equation for $\delta\hat{\Gamma}(E)$:

$$\frac{\partial}{\partial E}\delta\hat{\Gamma}(E) = i\delta\mu_{12}\,\hat{G}^2_{12}(E)\,\hat{R}(\hat{E}_{12})\,\hat{G}^2_{21}(\hat{E}_{12}) + O(\delta\mu\, J^3/\tilde{E}). \tag{5.12}$$

Here it is sufficient to consider only the leading order because $\delta\hat{\Gamma}(E)$ only enters other RG equations in next-to-leading order corrections.[3] This contrasts with $\delta\hat{\Gamma}^\gamma(E)$, for which we need the leading and next-to-leading order. Its RG equation is obtained from Eq. (4.78) by replacing the left-most coupling vertex by a current vertex and inserting the parametrization:

$$i\frac{\partial}{\partial E}\delta\hat{\Gamma}^\gamma(E) = -\frac{3}{2}\delta\hat{\tilde{\mu}}_{12}\,\hat{I}^\gamma_{12}(E)\,\hat{R}(\hat{E}_{12})\,\hat{G}^3_{21} - i\frac{3}{2}\hat{I}^\gamma_{12}(E)\,\mathcal{J}[\delta\hat{\Gamma}](\hat{E}_{12})\,\hat{G}^3_{21}(\hat{E}_{12}) + O(\delta\mu\, J^5/\tilde{E}). \tag{5.13}$$

Here we used for the second term that $\sum_{\sigma_1\sigma_2} L^1_{\sigma_1\sigma_2}\bar{L}^a L^\xi_{\sigma_2\sigma_1} = \mathrm{tr}_\sigma\, L^1 L^a L^\xi = 6\delta_{\xi 3}\bar{L}^b$.

The RG equations for the vertex Floquet matrix coefficients $\hat{G}^{a,2,3}$ are more involved. The final RG equations (5.21)–(5.24) will show that $\hat{G}^a$ only enters in next-to-leading order corrections to the other RG equations. It is therefore sufficient to consider only the leading order in the RG equation for $\hat{G}^a$, as we also did for $\delta\hat{\Gamma}$. Taking the L^a component of the leading order term in the RG equation (4.67) we find that[4]

$$\frac{\partial}{\partial E}\hat{G}^a_{12}(E) = \frac{1}{2}\hat{G}^2_{13}(E)\,\hat{R}(\hat{E}_{13})\,\hat{G}^2_{32}(\hat{E}_{13}) - \frac{1}{2}\hat{G}^2_{32}(E)\,\hat{R}(\hat{E}_{32})\,\hat{G}^2_{13}(\hat{E}_{32}) + O(J^4/\tilde{E}). \tag{5.14}$$

In equilibrium, $\hat{\mu}_L = \hat{\mu}_R$, all Floquet matrices are diagonal and the two terms cancel. Thus, the right-hand side of Eq. (5.14) is of the order $O(\Delta J^2/\tilde{E}^2)$, where Δ denotes again the energy scale of the bias voltage. The RG equation (4.67) for the vertex shows in the leading order that $\partial_E J = O(J^2/\tilde{E})$. The comparison leads to the conclusion that $\hat{G}^a = O(J^2\Delta/\tilde{E})$. Since $\tilde{E}$ is typically large, one can neglect $\hat{G}^a$ entirely with only small deviations from the result including $\hat{G}^a$ which we derive here (see section 6.1.3 and appendix J for a discussion of this approximation).

The RG equations for $\hat{G}^2$, $\hat{G}^3$, and I^γ are derived from the RG equations (4.67) for the coupling vertex and (4.71) for the current vertex. To distinguish which coefficients $(\hat{G}^a, \hat{G}^2, \hat{G}^3)$ must be taken into account in which vertex in Eq. (4.67), we remember that L^3 vanishes when acting on traceless operators, while the vertex $\bar{G}$ maps every operator to a traceless operator. Thus, $\hat{G}^3$ can appear only as the right-most vertex in the RG equations. Using this and the multiplication table for L^ξ, one can derive the leading order of the RG equations for $\hat{G}^2$, $\hat{G}^3$ and $\hat{I}^\gamma$ in close analogy to the previously steps. The only new point is that the next-to-leading order term in Eq. (4.67)

[3] Note the difference to Eqs. (5.10) and (5.11): In those RG equations the next-to-leading order is zero, whereas in Eq. (5.12) we neglect it because the result itself will only be used in a next-to-leading order correction.

[4] By writing $O(J^4/\tilde{E})$ for the next correction, we anticipate that the next-to-leading order in this RG equation vanishes. This follows from the multiplication rules for L^a and L^2, and from Eq. (5.15), but is unimportant since $O(J^3/\tilde{E})$ would also be negligible here.

involves a combination of superoperators, for which we need some additional relations:[5]

$$\sum_{\sigma_3\sigma_4} L^2_{\sigma_3\sigma_4} L^2_{\sigma_1\sigma_2} L^2_{\sigma_4\sigma_3} = \frac{1}{2} L^2_{\sigma_1\sigma_2}, \qquad \sum_{\sigma_3\sigma_4} L^2_{\sigma_3\sigma_4} L^2_{\sigma_1\sigma_2} L^3_{\sigma_4\sigma_3} = -L^3_{\sigma_1\sigma_2}, \qquad \sum_{\sigma_3\sigma_4} L^1_{\sigma_3\sigma_4} L^2_{\sigma_1\sigma_2} L^2_{\sigma_4\sigma_3} = -L^1_{\sigma_1\sigma_2}. \tag{5.15}$$

Using these relations, we find the RG equations for the Floquet-matrix coefficients of the vertices:

$$\begin{aligned}\frac{\partial}{\partial E}\hat{G}^2_{12}(E) = {} & \frac{1}{2}\hat{G}^2_{13}(E)\,\hat{R}(\hat{E}_{13})\,\hat{G}^2_{32}(\hat{E}_{13}) + \frac{1}{2}\hat{G}^2_{32}(E)\,\hat{R}(\hat{E}_{32})\,\hat{G}^2_{13}(\hat{E}_{32}) + \hat{G}^a_{13}(E)\,\hat{R}(\hat{E}_{13})\,\hat{G}^2_{32}(\hat{E}_{13}) \\ & + \hat{G}^2_{13}(E)\,\hat{R}(\hat{E}_{13})\,\hat{G}^a_{32}(\hat{E}_{13}) - \hat{G}^a_{32}(E)\,\hat{R}(\hat{E}_{32})\,\hat{G}^2_{13}(\hat{E}_{32}) - \hat{G}^2_{32}(E)\,\hat{R}(\hat{E}_{32})\,\hat{G}^a_{13}(\hat{E}_{32}) \\ & - \frac{1}{2}\hat{G}^2_{34}(E)\,\mathcal{J}[\hat{G}^2_{12}](\hat{E}_{34})\,\hat{G}^2_{43}(\hat{E}_{1234}) + O(J^4/\tilde{E}),\end{aligned} \tag{5.16}$$

$$\begin{aligned}\frac{\partial}{\partial E}\hat{G}^3_{12}(E) = {} & \hat{G}^2_{13}(E)\,\hat{R}(\hat{E}_{13})\,\hat{G}^3_{32}(\hat{E}_{13}) + \hat{G}^2_{32}(E)\,\hat{R}(\hat{E}_{32})\,\hat{G}^3_{13}(\hat{E}_{32}) + \hat{G}^a_{13}(E)\,\hat{R}(\hat{E}_{13})\,\hat{G}^3_{32}(\hat{E}_{13}) \\ & - \hat{G}^a_{32}(E)\,\hat{R}(\hat{E}_{32})\,\hat{G}^3_{13}(\hat{E}_{32}) + \hat{G}^2_{34}(E)\,\mathcal{J}[\hat{G}^2_{12}](\hat{E}_{34})\,\hat{G}^3_{43}(\hat{E}_{1234}) + O(J^5/\tilde{E}),\end{aligned} \tag{5.17}$$

$$\begin{aligned}\frac{\partial}{\partial E}\hat{I}^\gamma_{12}(E) = {} & \hat{I}^\gamma_{13}(E)\,\hat{R}(\hat{E}_{13})\,\hat{G}^2_{32}(\hat{E}_{13}) + \hat{I}^\gamma_{32}(E)\,\hat{R}(\hat{E}_{32})\,\hat{G}^2_{13}(\hat{E}_{32}) + \hat{I}^\gamma_{13}(E)\,\hat{R}(\hat{E}_{13})\,\hat{G}^a_{32}(\hat{E}_{13}) \\ & - \hat{I}^\gamma_{32}(E)\,\hat{R}(\hat{E}_{32})\,\hat{G}^a_{13}(\hat{E}_{32}) + \hat{I}^\gamma_{34}(E)\,\mathcal{J}[\hat{G}^2_{12}](\hat{E}_{34})\,\hat{G}^2_{43}(\hat{E}_{1234}) + O(J^4/\tilde{E}).\end{aligned} \tag{5.18}$$

5.1.3. Summary of the final RG equations

The RG equations can be written as a set of ordinary differential equations by using the auxiliary variable $\hat{Z}(E)^{-1} = 1 + i\partial_E\hat{\Gamma}(E)$ [see Eq. (4.55)]. We shorten the notation by omitting the energy arguments and remembering that for any function of energy $f(E)$ the energy argument E is replaced by $\hat{E}_X$ if there are open indices X standing to the left of f, e.g., $\hat{G}^2_{34}\hat{G}^2_{12}\hat{G}^2_{43} = \hat{G}^2_{34}(E)\hat{G}^2_{12}(\hat{E}_{34})\hat{G}^2_{43}(\hat{E}_{1234})$.

$$\partial_E\hat{\Gamma} = -i\left(\hat{Z}^{-1} - 1\right) \tag{5.19}$$

$$\partial_E\hat{Z} = \hat{Z}\,\hat{G}^2_{12}\,\hat{R}\,\hat{G}^2_{21}\,\hat{Z} + 0 + O(\tilde{E}^{-1}J^4) \tag{5.20}$$

$$\begin{aligned}\partial_E\hat{G}^2_{12} = {} & \frac{1}{2}\hat{G}^2_{13}\,\hat{R}\,\hat{G}^2_{32} + \frac{1}{2}\hat{G}^2_{32}\,\hat{R}\,\hat{G}^2_{13} - \frac{1}{2}\hat{G}^2_{34}\,\mathcal{J}[\hat{G}^2_{12}]\,\hat{G}^2_{43} \\ & + \hat{G}^2_{13}\,\hat{R}\,\hat{G}^a_{32} + \hat{G}^a_{13}\,\hat{R}\,\hat{G}^2_{32} - \hat{G}^2_{32}\,\hat{R}\,\hat{G}^a_{13} - \hat{G}^a_{32}\,\hat{R}\,\hat{G}^2_{13} + O(\tilde{E}^{-1}J^4)\end{aligned} \tag{5.21}$$

$$\partial_E\hat{G}^3_{12} = \hat{G}^2_{13}\,\hat{R}\,\hat{G}^3_{32} + \hat{G}^2_{32}\,\hat{R}\,\hat{G}^3_{13} + \hat{G}^2_{34}\,\mathcal{J}[\hat{G}^2_{12}]\,\hat{G}^3_{43} + \hat{G}^a_{13}\,\hat{R}\,\hat{G}^3_{32} - \hat{G}^a_{32}\,\hat{R}\,\hat{G}^3_{13} + O(\tilde{E}^{-1}J^5) \tag{5.22}$$

$$\partial_E\hat{G}^a_{12} = \frac{1}{2}\hat{G}^2_{13}\,\hat{R}\,\hat{G}^2_{32} - \frac{1}{2}\hat{G}^2_{32}\,\hat{R}\,\hat{G}^2_{13} + O(\tilde{E}^{-1}J^4) \tag{5.23}$$

$$\partial_E\hat{I}^\gamma_{12} = \hat{I}^\gamma_{13}\,\hat{R}\,\hat{G}^2_{32} + \hat{I}^\gamma_{32}\,\hat{R}\,\hat{G}^2_{13} + \hat{I}^\gamma_{34}\,\mathcal{J}[\hat{G}^2_{12}]\,\hat{G}^2_{43} + \hat{I}^\gamma_{13}\,\hat{R}\,\hat{G}^a_{32} - \hat{I}^\gamma_{32}\,\hat{R}\,\hat{G}^a_{13} + O(\tilde{E}^{-1}J^4) \tag{5.24}$$

$$\partial_E\delta\hat{\Gamma} = i\delta\bar{\mu}_{12}\,\hat{G}^2_{12}\,\hat{R}\,\hat{G}^2_{21} + O(\delta\mu\,\tilde{E}^{-1}J^3) \tag{5.25}$$

$$\partial_E\delta\hat{\Gamma}^\gamma = i\frac{3}{2}\delta\bar{\mu}_{12}\,\hat{I}^\gamma_{12}\,\hat{R}\,\hat{G}^3_{21} - \frac{3}{2}\hat{I}^\gamma_{12}\,\mathcal{J}[\delta\hat{\Gamma}]\,\hat{G}^3_{21} + O(\delta\mu\,\tilde{E}^{-1}J^5) \tag{5.26}$$

$$\partial_E^2\hat{\Gamma}^\gamma = i\frac{3}{2}\hat{I}^\gamma_{12}\,\hat{R}\,\hat{G}^3_{21} + 0 + O(\tilde{E}^{-1}J^4) \tag{5.27}$$

To facilitate later discussion of various possible truncation schemes, we mark the leading order terms in blue, the next-to-leading order in violet, and the next higher order in green. In red, we

[5] The calculation is given in appendix F of Ref. [3].

indicate terms that are of next-to-leading order in J and in $\Delta/\tilde{E}$, which are precisely the terms involving $\hat{G}^a_{12}$. In these RG equations the indices $1, \dots$ only indicate reservoirs, $1 = \alpha = L, R$, and we implicitly sum over these indices. The voltage variation $\delta\bar{\mu}_{12}$ is a scalar in Floquet space, whereas all other objects are Floquet matrices. We remind of the following definitions:

$$\hat{R}(E) = \frac{1}{E + \hat{N}\Omega - \hat{L}(E)}, \qquad \text{[see Eq. (4.27)]} \tag{5.28}$$

$$\hat{\chi}(E) = \hat{Z}(E)\left[E + \hat{N}\Omega + i\hat{\Gamma}(E)\right], \qquad \text{[see Eq. (4.56)]} \tag{5.29}$$

$$\mathcal{I}[\hat{G}^2_{12}](E) = \int_0^\infty d\omega \, \frac{1}{\omega + \hat{\chi}(E)} \hat{Z}(E)\, \hat{G}^2_{12}(E) \frac{1}{\omega + \hat{\chi}(\hat{E}_{12})} \hat{Z}(\hat{E}_{12}), \qquad \text{[see Eq. (4.57)]} \tag{5.30}$$

$$\mathcal{I}[\delta\hat{\Gamma}](E) = \int_0^\infty d\omega \, \frac{1}{\omega + \hat{\chi}(E)} \hat{Z}(E)\, \delta\hat{\Gamma}(E) \frac{1}{\omega + \hat{\chi}(E)} \hat{Z}(E). \tag{5.31}$$

The integrals $\mathcal{I}[\cdots]$ are solved or approximated as discussed in section 4.3.4. These RG equations are suitable for a numerical implementation. However, they can still be solved using different truncation schemes and further, more subtle approximations. A comparison of these results in section 6.1 indicates that the underlying expansion in J indeed converges.

The RG equations include shifts in the energy arguments by multiples of $\hat{\bar{\mu}}_{LR}$. For example, $\partial_E \hat{G}^2_{12}(E)$ depends on $\hat{G}^2_{12}(E + n\hat{\bar{\mu}}_{LR})$, $n \in \{-2, -1, \dots, 2\}$, such that in principle we obtain an infinite set of coupled differential equations. To solve these equations numerically, we need to keep a finite number of such voltage-shifted copies and check for convergence with an increasing number of such copies. In the final RG equations we find such energy shifts in $\hat{\Gamma}$, $\hat{Z}$, $\hat{G}^2$ and $\hat{G}^3$. For $\hat{Z}$ we can estimate the effect of an energy shift from the energy derivative: $\hat{Z}(E \pm \Delta) - \hat{Z}(E) \sim \Delta \partial_E \hat{Z}(E) = O(\Delta J^2/\tilde{E})$ and analogous for $\hat{G}^2$ and $\hat{G}^3$. Inserting this in the RG equations shows that the mistake made by neglecting the energy shift is of next-to-leading order in all RG equations. Thus, the energy shifts are not negligible, but even when neglecting them, the leading order remains correct. This allows us to restrict the energy arguments included in the numerical solution to $E + n\hat{\bar{\mu}}_{LR}$ with $|n| \leq n_{\max}$ for some positive integer $n_{\max}$. Energy shifts beyond $\pm n_{\max}$ can be approximated, e.g., by using $\hat{\Gamma}(E + [n_{\max} + 1]\hat{\bar{\mu}}_{LR}) \approx \hat{\Gamma}(E + n_{\max}\hat{\bar{\mu}}_{LR})$ in the numerical evaluation. A quantitative discussion of the effect of $n_{\max}$ on the results of the FRTRG in section 6.5 will show that for $n_{\max} = 4$ the results are almost perfectly converged, such that the finite $n_{\max}$ does not limit the accuracy of the method.

5.2. Equilibrium initial condition

To solve the RG equations, we need an initial condition of the RG flow. Eventually, we want to describe a system driven out of equilibrium, but it is simpler to first construct the RG flow in equilibrium, where the RG equations simplify significantly and many properties of the model are known exactly. We will see below that the RG flow in equilibrium can be used to find an initial condition in nonequilibrium. An overview of the steps leading to the initial condition is given in figure 5.1. But before we try to understand the equilibrium RG flow, we need to understand why the model simplifies at the beginning of the RG flow at large $\mathrm{Im}\, E$ and what exactly we want to describe with the RG flow — what is universal.

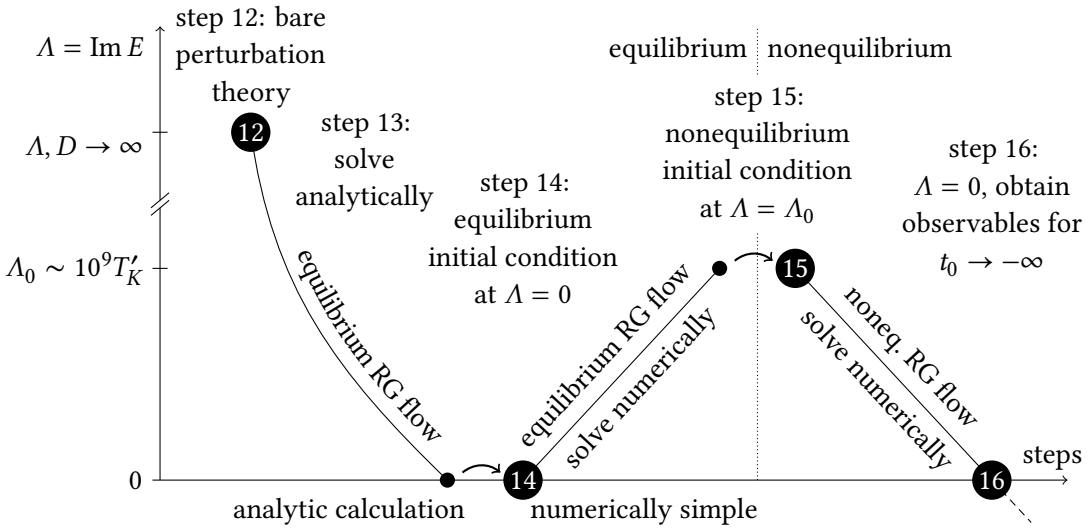

Figure 5.1.: Schematic overview of the steps involved in the derivation of the initial condition for the RG flow. In steps 1–11 the RG equations for the Kondo model were derived. At large Λ, the system is approximately in equilibrium, as discussed in section 5.2.1. The RG flow is first constructed in equilibrium using properties at large Λ (step 12) and at $\Lambda = 0$ (step 14). To understand the flow at large Λ, we need to distinguish universal and nonuniversal contributions (section 5.2.2). Once the equilibrium initial conditions at $\Lambda = 0$ are known, the equilibrium RG equations can be integrated numerically to reach $\Lambda = \Lambda_0 \gg T_K$. At Λ_0, the system is approximately in equilibrium and the result of the equilibrium RG flow is used as initial condition for the nonequilibrium RG flow (step 15). Eventually, the nonequilibrium RG flow is solved numerically from $E = i\Lambda_0$ to $E = 0$. In the numerical implementation, only this last step has a significant runtime.

5.2.1. Properties of the model at large Λ

To determine initial conditions in equilibrium and in nonequilibrium we will make use of the fact that the model simplifies at large $\Lambda \coloneqq \mathrm{Im}\, E$ in two ways. Firstly, the effective coupling J is weak at large Λ. Indeed, Λ takes a role similar to the cutoff energy D in Anderson's poor man's scaling (see section 3.1.2), as an analysis of the equilibrium RG equations will show [see Eqs. (5.58) and (5.63)]. In the poor man's scaling approach, we only included the effect of reservoir energies above a cutoff D in the calculation of the effective coupling. Here in the diagrammatic language the contribution of reservoir energies below Λ is suppressed by resolvents of the form $\hat{R}(E) \sim 1/(\omega + E)$, while reservoir energies far above Λ are hardly affected. Thus, Λ serves as a smooth cutoff that defines which reservoir energies are included in the renormalization of the coupling. The effective coupling is of the order $1/\log(\Lambda)$ as long as Λ remains small compared to the bandwidth D in the cutoff function $D(\omega)$.

The second simplification is the suppression of nonequilibrium effects. A crucial property of the model at large Λ is that the Kondo temperature does not emerge as a low-energy scale. We remember from the poor man's scaling that the Kondo temperature T_K emerges at the end of the RG flow as the energy scale where the system reaches a strong coupling regime. But when we stop the RG flow earlier at Λ and the system does not reach the strong coupling regime, the only

remaining inherent energy scales in equilibrium are the bandwidth D and the energy Λ. Thus, by simple comparison of energy scales, we can see that a bias voltage is negligibly small compared to all other energy scales at sufficiently large Λ.[6] This implies that the system is approximately in equilibrium. Making use of these results, we will construct the RG flow in equilibrium and start in the weak coupling regime at large Λ.

5.2.2. Universality in the RG flow

Constructing the initial condition is closely connected to the question of universality. In the poor man's scaling approach, we already motivated that different combinations of bare coupling and bandwidth or even different cutoff functions $D(\omega)$ will lead to the same universal low-energy physics. This is illustrated by considering different energy scales [124, 138, 139]. At high energies of the order of D, the density of states in the reservoirs may be a complicated function. The renormalization of the coupling already starts at such high energies. When zooming in to energy scales lower than D, the density of states becomes smooth and slowly varying. Various physical realizations of a system experiencing the Kondo effect start looking similar as one discards all higher energies and only considers their effect on the renormalization of the coupling. As the energy scale is lowered further, the renormalization of the coupling continues and the density of states is approximately constant, such that different realizations of the (single channel) Kondo model now only differ by the energy scale at which they reach the strong effective coupling regime. This is the situation described by our RG equations. All details of the density of states now only affect the Kondo temperature. Thus, the RG equations capture only the universal part of the Kondo model, and we need to find a universal initial condition for this RG flow.

This universality is reflected in an approximation which we made when deriving the RG equations: We have taken the limit $D \to \infty$ in all diagrams contributing to the RG equations. This makes sure that we really capture only the universal properties of the model that are independent of the cutoff D. But when constructing the initial condition for the RG flow, this leads to the complication that the connection to bare perturbation theory is less obvious. In bare perturbation theory we need a finite reservoir bandwidth D, but we aim to describe an RG flow that is independent of D. To find the initial condition of the RG flow, we will therefore combine general properties of the model like the unitary conductance with properties which we will obtain from bare perturbation theory by carefully selecting only universal terms. Keeping in mind that results from bare perturbation theory will require a careful interpretation in the view of universality, we start by expressing the Kondo model in Liouville space.

5.2.3. Liouville-space Kondo model

Having noticed that the coupling is weak at large $\mathrm{Im}\, E$, we can now derive the leading order contributions to $\hat{G}^2_{12}$, $\hat{G}^3_{12}$, and $\hat{I}^\gamma_{12}$ in bare perturbation theory. We start by computing the bare

[6] This is directly visible in the RG equations: The voltage only appears in energy shifts $\hat{E}_X = E + n\hat{\mu}_{LR}$ for some integer n. At large Λ, the voltage described by the Floquet matrix $\hat{\mu}_{LR}$ becomes negligible compared to E.

vertex for the Kondo model. The coupling Hamiltonian [see Eq. (3.2)]

$$H_V(t) = \frac{1}{2} \sum_{\alpha\alpha'\sigma\sigma'} \bar{J}^{(0)}(t)_{\alpha\alpha'} \mathbf{S} \cdot \boldsymbol{\sigma}_{\sigma\sigma'} \iint d\omega\, d\omega'\, c^\dagger_{\alpha\sigma\omega} c_{\alpha'\sigma'\omega'} \tag{5.32}$$

defines the coupling Liouvillian $L_V = [H_V, \bullet]$, which we express using the coupling vertex and the fermion superoperators $K_1^+ = c_1 \bullet$ and $K_1^- = \bullet c_1$:

$$L_V = \frac{1}{4} \bar{J}^{(0)}_{\alpha\alpha'} \eta \delta_{\eta\bar{\eta}'} \boldsymbol{\sigma}_{\sigma\sigma'} \cdot (\mathbf{S} :c_1 c_{1'}: \bullet + \bullet \mathbf{S} :c_{1'} c_1:) = \frac{1}{2} p' G^{(0)pp'}_{11'} :K_1^p K_{1'}^{p'}: . \tag{5.33}$$

This leads to the result for the bare vertex[7]

$$G^{(0)pp'}_{11'} = \delta_{pp'} \begin{cases} g_{11'} \bullet & \text{for } p = + \\ - \bullet g_{11'} & \text{for } p = -, \end{cases} \tag{5.34}$$

which fulfills $G^{(0)p'p}_{1'1} = -G^{(0)pp'}_{11'}$ as required by the diagrammatic language [Eq. (4.14)]. Here, $g_{11'}$ is an operator defined by

$$g_{11'} = \frac{1}{2} \delta_{\eta\bar{\eta}'} \begin{cases} \bar{J}^{(0)}_{\alpha\alpha'} \mathbf{S} \cdot \boldsymbol{\sigma}_{\sigma\sigma'} & \text{for } \eta = + \\ -\bar{J}^{(0)}_{\alpha'\alpha} \mathbf{S} \cdot \boldsymbol{\sigma}_{\sigma'\sigma} & \text{for } \eta = -. \end{cases} \tag{5.35}$$

Summing over the Keldysh indices and setting $\eta = -\eta' = +$ we obtain the vertex $\bar{G}_{11'}$ for which we defined the parametrization in Eq. (5.5):[8]

$$\bar{G}^{(0)}_{11'} = [g_{11'}, \bullet] = \frac{1}{4} \bar{J}^{(0)}_{\alpha\alpha'} \sum_{i=1}^{3} \sigma^i_{\sigma\sigma'} [\sigma^i, \bullet] = -\bar{J}^{(0)}_{\alpha\alpha'} L^2_{\sigma\sigma'}. \tag{5.36}$$

Thus, in the bare vertex only the component $\hat{G}^2$ is present while $\hat{G}^a$ and $\hat{G}^3$ vanish, as we have used when counting orders in the coupling J in step 11.

Analogously, we compute the current vertex using the charge current operator

$$I_\gamma = -i[H_V, N_\gamma] = i \frac{1}{2} \bar{J}^{(0)}_{\alpha\alpha'} (\delta_{\alpha\gamma} - \delta_{\alpha'\gamma}) \mathbf{S} \cdot \boldsymbol{\sigma}_{\sigma\sigma'} c^\dagger_{\alpha\sigma\omega} c_{\alpha'\sigma'\omega'}. \tag{5.37}$$

In the diagrammatic language, this current operator enters via the current vertex, which we defined in Eq. (4.69) by

$$\frac{i}{2}\{I_\gamma, \bullet\} = \frac{1}{2}\{[H_V, N_\gamma], \bullet\} = \frac{1}{2} p' I^{\gamma(0)pp'}_{11'} :K_1^p K_{1'}^{p'}:, \tag{5.38}$$

such that we find for the Kondo model:

$$I^{\gamma(0)pp'}_{11'} = -\frac{1}{2} p' \big(\eta \delta_{\alpha\gamma} + \eta' \delta_{\alpha'\gamma}\big) G^{(0)pp'}_{11'}. \tag{5.39}$$

[7] Here we do not mark the bare coupling vertex as a Floquet matrix because we focus on the simpler case of time-independent coupling, but in section 5.3.2 we will see that $\bar{J}_{\alpha\alpha'}$ can be time-dependent such that the bare coupling becomes a Floquet matrix.

[8] One can show that $L^2_{\sigma\sigma'} = -\frac{1}{4} \sum_{i=1}^3 \sigma^i_{\sigma\sigma'} [\sigma^i, \bullet]$ by acting on the complete basis $\{\mathbb{1}, \sigma^1, \sigma^2, \sigma^3\}$ of the Liouville space. For $\mathbb{1}$ the relation is trivial and for σ^j we find that $\frac{1}{4} \sum_{k=1}^3 \sigma^k_{\sigma\sigma'} [\sigma^k, \sigma^j] = \frac{i}{2} \sum_{i,k=1}^3 \varepsilon_{kji} \sigma^k_{\sigma\sigma'} \sigma^i = -L^2_{\sigma\sigma'} \sigma^j$.

Like for the current vertex, we sum over the Keldysh indices and set $\eta = -\eta' = +$ to obtain

$$\bar{I}^{\gamma(0)}_{11'} = -\frac{1}{2}(\delta_{\alpha\gamma} - \delta_{\alpha'\gamma})\{g_{11'}, \bullet\} = -\frac{1}{8}(\delta_{\alpha\gamma} - \delta_{\alpha'\gamma})\bar{J}^{(0)}_{\alpha\alpha'} \sum_{i=1}^{3} \sigma^i_{\sigma\sigma'}\{\sigma^i, \bullet\} \tag{5.40}$$

$$= -\frac{1}{4}(\delta_{\alpha\gamma} - \delta_{\alpha'\gamma})\bar{J}^{(0)}_{\alpha\alpha'}(L^1_{\sigma\sigma'} + L^3_{\sigma\sigma'}). \tag{5.41}$$

As discussed in section 5.1.1, the contribution of L^3 can be omitted since it vanishes under the trace and therefore does not contribute to the current. For the parametrization defined in Eq. (5.8), this yields $I^{\gamma(0)}_{11'} = (\delta_{\alpha\gamma} - \delta_{\alpha'\gamma})\bar{J}^{(0)}_{\alpha\alpha'}$.

5.2.4. Bare perturbation theory and universality

While $\hat{G}^2_{12}$ and $\hat{I}^{\gamma}_{12}$ appear naturally when expressing the Kondo model in Liouville space, the vertex $\hat{G}^3_{12}$ only occurs in the effective vertex. Here we calculate the leading order diagrams of this effective vertex in bare perturbation theory to obtain $\hat{G}^3_{12}$ in the weak coupling regime with a finite bandwidth D.

$$\hat{G}^{p_1p_2}_{12}(E) - G^{(0)p_1p_2}_{12} = \quad + \quad + O(J^3) \tag{5.42}$$

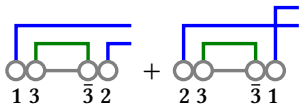

$$= \int d\omega\, \gamma^{p_4}(\eta_3\omega) G^{(0)p_1p_3}_{13} \frac{1}{E + \eta_3\omega - \hat{\bar{\mu}}_{13}} G^{(0)p_4p_2}_{\bar{3}2} - (1 \leftrightarrow 2) + O(J^3) \tag{5.43}$$

$$= G^{(0)p_1p_3}_{13} \int_0^\infty d\omega\, \frac{D(\omega)}{p_4\hat{E}_{13} - \omega} G^{(0)p_4p_2}_{\bar{3}2} - (1 \leftrightarrow 2) + O(J^3). \tag{5.44}$$

Here $(1 \leftrightarrow 2)$ denotes the same term with multi-indices $1, 2$ and Keldysh indices p_1, p_2 interchanged. As explained in section 5.2.1, for the initial conditions we will only need the effective vertex in equilibrium, which for $E = i\Lambda$ simplifies to[9]

$$\bar{G}_{12}(i\Lambda) - \bar{G}^{(0)}_{12} = \int_0^\infty d\omega\, \frac{D(\omega)}{pi\Lambda - \omega}\left(G^{(0)p'p'}_{13} G^{(0)pp}_{\bar{3}2} - G^{(0)p'p'}_{23} G^{(0)pp}_{\bar{3}1}\right) + O(J^3) \tag{5.45}$$

$$= -\frac{1}{2}\int_{-\infty}^\infty d\omega\, \frac{D(\omega)}{i\Lambda - \omega} \bar{J}^{(0)}_{13} \bar{J}^{(0)}_{32} L^3_{\sigma_1\sigma_2} - \int_0^\infty d\omega\, \frac{\omega D(\omega)}{\Lambda^2 + \omega^2} \bar{J}^{(0)}_{13} \bar{J}^{(0)}_{32} L^2_{\sigma_1\sigma_2} + O(J^3) \tag{5.46}$$

$$= i\frac{\pi}{2}\frac{D}{D+\Lambda} \bar{J}^{(0)}_{13} \bar{J}^{(0)}_{32} L^3_{\sigma_1\sigma_2} + \left[\frac{\pi}{2}\frac{D}{D+\Lambda} - \log\left(\frac{D}{\Lambda}\right)\frac{D^2}{D^2 - \Lambda^2}\right] \bar{J}^{(0)}_{13} \bar{J}^{(0)}_{32} L^2_{\sigma_1\sigma_2} + O(J^3). \tag{5.47}$$

[9] In Eq. (5.45), we use that for the bare vertex $G^{(0)pp'}_{11'} \propto \delta_{pp'}$. In the first term in Eq. (5.45) we have $\eta_1 = \bar{\eta}_2 = \bar{\eta}_3 = +$, and in the second term $\eta_2 = \bar{\eta}_3 = \bar{\eta}_1 = +$. In the step from Eq. (5.45) to (5.46), we use $\sum_p pG^{(0)pp}_{11'} = \frac{1}{4}\bar{J}^{(0)}_{\alpha\alpha'} \sum_i \sigma^i_{\sigma\sigma'}\{\sigma^i, \bullet\} = \frac{1}{2}\bar{J}^{(0)}_{\alpha\alpha'}(L^1 + L^3)_{\sigma\sigma'}$ and $\sum_p G^{(0)pp}_{11'} = -\bar{J}^{(0)}_{\alpha\alpha'} L^2_{\sigma\sigma'}$ to express the bare vertex with $\eta = -\eta' = +$ as $G^{(0)pp}_{11'} = \frac{1}{2}\bar{J}^{(0)}_{\alpha\alpha'}[-L^2 + \frac{p}{2}(L^1 + pL^3)]$. This allows us to identify even and odd contributions in p: $\sum_{p'}\left(G^{(0)p'p'}_{13} G^{(0)pp}_{\bar{3}2} - G^{(0)p'p'}_{23} G^{(0)pp}_{\bar{3}1}\right) = \frac{1}{2}\bar{J}^{(0)}_{13}\bar{J}^{(0)}_{32}\left\{L^2L^2 - \frac{p}{2}L^2(L^1 + L^3) - \left(L^{2\top}L^{2\top}\right)^\top + \frac{p}{2}\left[L^{2\top}(L^1 + L^3)^\top\right]^\top\right\}_{\sigma\sigma'} = \frac{1}{2}\bar{J}^{(0)}_{13}\bar{J}^{(0)}_{32}(L^2 - pL^3)_{\sigma\sigma'}$.

The first term in Eq. (5.47) is the leading order contribution to G^3_{12} in bare perturbation theory, whereas the second term is a next-to-leading order contribution to G^2_{12}. Since we consider the equilibrium case, these vertices are not Floquet matrices here. We notice that this result shows explicitly that G^a_{12} vanishes in equilibrium when neglecting terms of the order $O(J^3)$.

The result in Eq. (5.47) clearly shows the problem of using bare perturbation theory when aiming to find a universal initial condition. For the term contributing to G^3_{12}, one can distinguish a high-energy cutoff function $D/(D+\Lambda)$ from the universal part $i\frac{\pi}{2}(\bar{J}^{(0)})^2_{12}$. But the term for G^2_{12} shows that bare perturbation theory only converges if $\log(D/\Lambda)$ does not become too large. Only if $J^{(0)}\log(D/\Lambda) \sim \frac{\log(D/\Lambda)}{\log(D/T_K)} \ll 1$, all higher-order terms are strongly suppressed.[10] This illustrates that the bare perturbation theory only resembles the universal RG flow in a certain parameter regime. If Λ is too large, nonuniversal terms depending on D become relevant. If Λ is too small, higher orders of the bare perturbation theory become relevant. Fortunately, the simple structure of the term for G^3_{12} allowed us to identify the universal leading order initial condition in a regime where perturbation theory converges:

$$G^3_{12}(E) = i\frac{\pi}{2}\bar{J}^{(0)}_{13}\bar{J}^{(0)}_{32} = i\pi 2\sqrt{x_1x_2}(J^{(0)})^2. \tag{5.48}$$

However, due to the mentioned difficulties of using bare perturbation theory to predict universal initial conditions, we will not determine an initial condition for $\Gamma(E)$ using this method. Instead, we will now solve the equilibrium RG flow such that we can use $\Gamma(E=0)$ as a reference energy and initial condition of the RG flow.

5.2.5. Equilibrium RG flow (step 13)

The analytic solution of the RG flow in equilibrium will make it possible to combine different properties of the model to find the initial condition of the flow. We will use properties of the model like the universal conductance and the Kondo temperature, which emerge at strong coupling, and bare perturbation theory at large Λ and weak coupling. This requires that we understand the equilibrium RG flow which connects these regimes.

In equilibrium, when the time-dependent driving vanishes, all Floquet matrices become diagonal and can be replaced by scalars, which are Laplace transforms of the corresponding functions of time-differences [see discussion of Eq. (4.3)]. To simplify the RG equations, we can use that in equilibrium there is no current, $\Gamma^\gamma = 0$, and also $\delta\Gamma = 0$ because the spin relaxation rate $\Gamma(E)$ must be a symmetric function of the bias voltage $\hat{\mu}_{LR}$ such that $\partial_{V_{\text{avg}}}\Gamma(E) = 0$. Furthermore, we have seen in the RG equation (5.14) for $\hat{G}^a$ that G^a is not renormalized in equilibrium, $\partial_E G^a = 0$, and in section 5.1.1 that G^a is not contained in the bare vertex. Thus, also G^a vanishes in equilibrium.

To solve the RG equations, we use that the vertices G^2_{12} and G^3_{12} in the Kondo model describe a coupling between reservoirs α_1 and α_2, which comes with the asymmetry prefactor $2\sqrt{x_1x_2}$ as defined below Eq. (3.3). We have seen in Eqs. (5.36), (5.41) and (5.48) that this asymmetry

[10] To estimate $J^{(0)} \sim 1/\log(D/T_K)$, one can use the poor man's scaling result Eq. (3.13) or the result of the equilibrium RG flow in Eq. (5.63).

prefactor indeed appears in the bare vertices. From the results of bare perturbation theory we take the ansatz

$$G^2_{12} = -2\sqrt{x_1 x_2}J, \tag{5.49}$$
$$G^3_{12} = 2\sqrt{x_1 x_2}K, \tag{5.50}$$
$$I^\gamma_{12} = (\delta_{1\gamma} - \delta_{2\gamma})2\sqrt{x_1 x_2}M, \tag{5.51}$$

which can be used to solve the RG equations in equilibrium, as we will see next. Here, J is the exchange coupling and M is the transport exchange rate. From the results in bare perturbation theory (step 12) we know that $J > 0$ and M are real numbers, whereas K should be purely imaginary at weak coupling. The only remaining nonzero integral in the RG equations simplifies to $\mathcal{J}[G^2_{12}] = RG^2_{12}Z$ because the approximation in Eq. (4.60) becomes exact. For $E = i\Lambda$ and $\Lambda \geq 0$, the equilibrium RG equations read [76]

$$\frac{d}{d\Lambda}\Gamma(\Lambda) = \frac{1}{Z} - 1, \tag{5.52}$$
$$\frac{d}{d\Lambda}Z(\Lambda) = 4\frac{Z^2J^2}{\Lambda+\Gamma}, \tag{5.53}$$
$$\frac{d}{d\Lambda}J(\Lambda) = -2\frac{J^2(1+ZJ)}{\Lambda+\Gamma}, \tag{5.54}$$
$$\frac{d}{d\Lambda}K(\Lambda) = -4\frac{JK(1-ZJ)}{\Lambda+\Gamma}, \tag{5.55}$$
$$\frac{d}{d\Lambda}M(\Lambda) = -2\frac{JM}{\Lambda+\Gamma}, \tag{5.56}$$
$$\frac{d}{d\Lambda}\delta\Gamma^\gamma(\Lambda) = i12x_Lx_R\frac{MK}{\Lambda+\Gamma}\delta V_{\text{avg}}. \tag{5.57}$$

In the last equation for $\delta\Gamma^\gamma$, we have fixed $\gamma = L$ to insert $\delta\bar{\mu}_{LR} = \delta V_{\text{avg}}$.[11] When neglecting next-to-leading order terms and assuming that $\Lambda \gg \Gamma$, Eq. (5.54) resembles the poor man's scaling equation (3.11). This equation shows that the coupling which is weak at large Λ will increase as Λ is lowered. But in contrast to the poor man's scaling, the RG flow does not diverge as $\Lambda \to 0$ because of the spin relaxation rate $\Gamma > 0$ in the denominator of the RG equations. Thus, the divergence in poor man's scaling is avoided by including the effective Liouvillian in the resolvent.

We proceed solving the equilibrium RG equations. With the change of variables $\lambda = \Lambda + \Gamma$, $J' = JZ$, and $M' = ZM$, and after multiplying by $\frac{d\Lambda}{d\lambda} = Z$, we obtain

$$\frac{d}{d\lambda}J' = -2\frac{J'^2(1-J')}{\lambda} \tag{5.58}$$
$$\frac{d}{d\lambda}Z = 4\frac{ZJ'^2}{\lambda} \tag{5.59}$$
$$\frac{d}{d\lambda}K = -4\frac{J'K(1-J')}{\lambda} \tag{5.60}$$
$$\frac{d}{d\lambda}M' = -2\frac{J'M'(1-2J')}{\lambda} \tag{5.61}$$
$$\frac{d}{d\lambda}\delta\Gamma^L = i12x_Lx_R\frac{M'K}{\lambda}\delta V_{\text{avg}}. \tag{5.62}$$

[11] Differential conductance and current are the same in both reservoirs. The reservoir label γ only affects the sign due to the definition of the current. We can thus fix $\gamma = L$ in the RG equations and only derive initial conditions for I^L_{12}, Γ^L, and $\delta\Gamma^L$ for the current in the left reservoir.

The independent equation (5.58) for J' can be integrated, defining the integration constant

$$T_K' = \lambda \sqrt{\frac{J'}{1-J'}} e^{-\frac{1}{2J'}}, \tag{5.63}$$

which is a reference energy scale for the low-energy physics similar to the Kondo temperature in poor man's scaling [Eq. (3.13)]. Since we are working in equilibrium, where the Kondo temperature T_K is the universal low-energy reference scale, the integration constant T_K' must be related to T_K by some constant number. Using the FRTRG to compute the differential conductance $G(V_{\text{avg}}, V_{\text{osc}} = 0)$, we will find that $T_K \approx 3.44 T_K'$ for T_K defined in Eq. (3.15). In the initial condition for the RG flow, we will choose T_K' as a reference energy and define all energies relative to T_K'.

By multiplying the RG equations with $\frac{d\lambda}{dJ'}$, we can eliminate the flow parameter and obtain integrable differential equations:

$$\frac{d}{dJ'} Z = -2 \frac{Z}{1-J'} \qquad \Longrightarrow \qquad Z = Z_0 (1-J')^2, \tag{5.64}$$

$$\frac{d}{dJ'} K = 2 \frac{K}{J'} \qquad \Longrightarrow \qquad K = K_0 J'^2, \tag{5.65}$$

$$\frac{d}{dJ'} M' = \frac{M'}{J'} - \frac{M'}{1-J'} \qquad \Longrightarrow \qquad M' = M_0 J' (1-J'), \tag{5.66}$$

$$\frac{d}{dJ'} \delta\Gamma^L = -i6 x_L x_R \frac{M' K}{J'^2 (1-J')} \delta V_{\text{avg}} \qquad \Longrightarrow \qquad \delta\Gamma^L = -i3 x_L x_R M_0 K_0 J'^2 \delta V_{\text{avg}}. \tag{5.67}$$

In solving Eq. (5.67), we have set an additive integration constant to zero because the differential conductance must vanish for vanishing effective coupling J. In the next step, we will determine the remaining integration constants and initial values for this RG flow.

5.2.6. Initial condition of equilibrium RG flow (step 14)

To obtain the equilibrium RG flow will now combine the results from bare perturbation theory and properties of the model to determine initial values for J' and Γ, and the integration constants Z_0, K_0, and M_0. First, we want to argue using the poor man's scaling equation that $Z_0 = 1$ in Eq. (5.64) or — equivalently — $\partial_\Lambda \Gamma(\Lambda) \to 0$ for $\Lambda \to \infty$. For $\Lambda \to \infty$ we know that the coupling J should scale like $\partial_\Lambda J = -2J^2/\Lambda$ where Λ is the high-energy cutoff. But this is only reflected in the RG equation (5.54) if asymptotically $\Lambda + \Gamma \approx \Lambda$, or, formulated differently, if Γ grows only sublinearly in Λ. Thus, $\partial_\Lambda \Gamma \to 0$ for $\Lambda \to \infty$ and $Z_0 = 1$. The same result can be found by calculating the leading diagram  for Γ and noticing that all terms that could contribute to Z_0 are nonuniversal [76].

The integration constants M_0 and K_0 can be obtained by comparison to bare perturbation theory in the weak coupling regime. We know from the bare coupling and current vertices in Eqs. (5.36) and (5.41) that $I^{\gamma}_{11'} = -(\delta_{\alpha\gamma} - \delta_{\alpha'\gamma}) G^2_{11'}$ such that $M = J$ in the limit $J \to 0$. This implies that $M_0 = 1$. Likewise, K_0 can be fixed using the weak coupling limit $J \to 0$. From bare perturbation theory we know that in this limit $K = i\pi J^2$ [Eq. (5.48)], such that $K_0 = i\pi$.

Now we still need initial conditions for $\Gamma(\Lambda)$ and $J'(\Lambda)$, which we will find at $\Lambda = 0$. Here we can use the universal differential conductance of the Kondo model, which implies that the

current between the reservoirs for an infinitesimal voltage is $\delta I = 4x_L x_R(2e^2/h)\delta V_{\text{avg}}$. Using the parametrization of the current kernel Σ_γ [Eq. (5.2)] we find that the current between the reservoirs at constant, infinitesimal bias voltage is just $\delta\Gamma^L$ (see section 5.4 for a more detailed derivation). Thus, at $\Lambda = 0$ we find that $4x_L x_R/\pi = \delta\Gamma^L/\delta V_{\text{avg}} = 3\pi x_L x_R J'^2$ where we have inserted Eq. (5.67) and used that $e = \hbar = 1$. This yields the initial condition for the coupling:

$$J'(\Lambda = 0) = \frac{2}{\sqrt{3}\pi}. \tag{5.68}$$

The only remaining unknown initial condition for $\Gamma(\Lambda = 0)$ can be fixed by simply defining it as a reference energy scale. From Eq. (5.63) it follows that $\Gamma(\Lambda = 0) = e^{\sqrt{3}\pi/4}\left[(\sqrt{3}\pi/2) - 1\right]^{1/2} T'_K$ such that we can equivalently use T'_K or $\Gamma(0)$ as a reference energy scale. This completes the derivation of initial conditions of the equilibrium RG equations at $\Lambda = 0$.

5.2.7. Summary of the equilibrium RG flow

Using the initial conditions

$$J'(0) = \frac{2}{\sqrt{3}\pi}, \qquad \Gamma(0) = e^{\frac{\sqrt{3}\pi}{4}} \sqrt{\frac{\sqrt{3}\pi}{2} - 1}\, T'_K, \qquad Z(0) = \left[1 - J'(0)\right]^2 \tag{5.69}$$

the equilibrium RG equations (5.52)–(5.54) can be solved numerically[12] for $J'(\Lambda) = J(\Lambda)Z(\Lambda)$, $\Gamma(\Lambda)$, and $Z(\Lambda)$. All other quantities are given by

$$G^2_{12} = -2\sqrt{x_1 x_2}J, \tag{5.70}$$
$$G^3_{12} = i\pi 2\sqrt{x_1 x_2}J'^2, \tag{5.71}$$
$$I^\gamma_{12} = (\delta_{1\gamma} - \delta_{2\gamma})2\sqrt{x_1 x_2}J(1 - J'), \tag{5.72}$$
$$\delta\Gamma^L = 3\pi x_L x_R \delta V_{\text{avg}}\, J'^2, \tag{5.73}$$

or vanish in equilibrium. The corresponding results for RG equations truncated after the leading order are given in appendix I.

5.3. Nonequilibrium initial conditions

Now that we know the universal RG flow in equilibrium, we can construct initial conditions for the nonequilibrium RG equations at $E = i\Lambda_0$. From the discussion in section 5.2.1, we recall that at large $\text{Im}\, E$ the system is approximately in equilibrium, such that we can use the results of the equilibrium RG flow as an initial condition for the nonequilibrium RG flow. Here we show how to find the Floquet matrices for the nonequilibrium RG flow from the equilibrium results. We will see that the bias voltage pushing the system out of equilibrium can be described in two different ways. It can either be described directly through the chemical potentials $\hat{\tilde{\mu}}_{LR}$ which

[12] We have analytically solved the equilibrium RG equations as a function of J', but to obtain $J'(E)$ at a fixed E we solve these equations numerically.

appear in the RG equations, or it can be included in the coupling $\bar{J}_{LR}$ by a unitary transformation of the Hamiltonian. For both ways, we will derive the nonequilibrium initial condition such that we can compare the results in chapter 6, where we will also discuss the numerical benefits and difficulties of both approaches.

5.3.1. Initial conditions without unitary transformation (step 15a)

We first consider the simpler case starting from the untransformed Kondo Hamiltonian [Eq. (3.2)] and describe the time-dependent electrochemical potentials by Floquet matrices which appear in the resolvents. This is the method which we used in the whole derivation of the RG equations, and the same method that was also used in Ref. [3]. As discussed in section 5.2.1, the bias voltage is negligible at $E = i\Lambda_0$, such that we only need to form Floquet matrices from the results of the equilibrium RG flow. We start by identifying from the equilibrium RG flow that some terms vanish in equilibrium:

$$\hat{G}^a_{12}(i\Lambda_0) = 0, \qquad \delta\hat{\Gamma}(i\Lambda_0) = 0. \tag{5.74}$$

The current $\hat{I}^\gamma(E)$ will be discussed separately. Next we turn to the nonvanishing terms.

From the equilibrium RG flow, we know $\Gamma(E)$ and all other quantities appearing in the RG equations as scalar functions of E, where E can take any value with $\operatorname{Im} E \geq 0$. But in the nonequilibrium RG equations we need the Floquet matrices $\hat{\Gamma}(E)$ and $\hat{\Gamma}(E + n\hat{\tilde{\mu}}_{LR})$, including shifts by integer multiples of the voltage Floquet matrix $\hat{\tilde{\mu}}_{LR}$. To obtain Floquet matrices, we first remember that in equilibrium functions like $\Gamma(t, t')$ in the time domain cannot depend on absolute time because the system is time-translation invariant. The Floquet matrix representing such a function is given by $\hat{\Gamma}(E) = \Gamma(E + \hat{N}\Omega)$, where $\Gamma(E)$ is the Laplace transform of $\Gamma(s) = \Gamma(t, t - s)$ and $\hat{N}$ is a diagonal Floquet matrix [see Eq. (4.2)]. Since $\hat{N}$ is diagonal, $\hat{\Gamma}(E)$ is also diagonal and the function $\Gamma(E)$ is evaluated element-wise for the diagonal elements of $E + \hat{N}\Omega$. When we include a shift of the energy argument by a non-diagonal Floquet matrix $\hat{\tilde{\mu}}_{LR}$, we define

$$\hat{\Gamma}(E + n\hat{\tilde{\mu}}_{LR}) = \Gamma(E + n\hat{\tilde{\mu}}_{LR} + \hat{N}\Omega) \tag{5.75}$$

in the eigenbasis of the argument $E + n\hat{\tilde{\mu}}_{LR} + \hat{N}\Omega$ on the right-hand side. By numerically diagonalizing this Floquet matrix, we can thus find initial conditions for $\hat{\Gamma}(E + n\hat{\tilde{\mu}}_{LR})$ at $E = i\Lambda_0$, which we transform back to the standard Floquet basis. Using Eqs. (5.70) and (5.71), we analogously obtain the initial conditions

$$\hat{Z}(E + n\hat{\tilde{\mu}}_{LR}) = Z(E + n\hat{\tilde{\mu}}_{LR} + \hat{N}\Omega), \tag{5.76}$$

$$\hat{G}^2_{12}(E + n\hat{\tilde{\mu}}_{LR}) = -2\sqrt{x_1 x_2}J(E + n\hat{\tilde{\mu}}_{LR} + \hat{N}\Omega), \tag{5.77}$$

$$\hat{G}^3_{12}(E + n\hat{\tilde{\mu}}_{LR}) = i\pi 2\sqrt{x_1 x_2}J'^2(E + n\hat{\tilde{\mu}}_{LR} + \hat{N}\Omega). \tag{5.78}$$

For I^γ_{12} and $\delta\Gamma^\gamma$, we do not need to include any shifts by $\hat{\tilde{\mu}}_{LR}$ because no shifted terms appear in the RG equations (5.19)–(5.27). For these Floquet matrices, it is sufficient to consider [see Eqs. (5.72) and (5.73)]

$$\hat{I}^\gamma_{12}(E) = (\delta_{1\gamma} - \delta_{2\gamma})2\sqrt{x_1 x_2}J(E + \hat{N}\Omega)\left[1 - J'(E + \hat{N}\Omega)\right], \tag{5.79}$$

$$\delta\hat{\Gamma}^L(E) = 3\pi x_L x_R \delta V_{\text{avg}}\, J'^2(E + \hat{N}\Omega). \tag{5.80}$$

The current rate $\Gamma^\gamma(E)$ is treated specially in the initial conditions. We could start from the equilibrium value $\Gamma^\gamma(i\Lambda_0) = 0$, but we can use $\delta\Gamma^L$ to find a better estimate. At large $\operatorname{Im} E$ we can assume that the system responds linearly to the bias voltage such that for a constant bias voltage $\Gamma^\gamma(\Lambda_0) = \bar{\mu}_{LR}\,\delta\Gamma^\gamma(\Lambda_0)/\delta\bar{\mu}_{LR}$. For Floquet matrices, we use[13]

$$\hat{\Gamma}^L(E) = \frac{\hat{\bar{\mu}}_{LR}}{\delta\bar{\mu}_{LR}}\delta\Gamma^L(E + \hat{N}\Omega), \qquad \partial_E\hat{\Gamma}^L(E) = \frac{\hat{\bar{\mu}}_{LR}}{\delta\bar{\mu}_{LR}}\partial_E\delta\Gamma^L(E + \hat{N}\Omega). \tag{5.81}$$

Compared to the simpler equilibrium initial condition $\hat{\Gamma}^\gamma = 0$, this significantly improves the convergence of the current as a function of the numerical parameter Λ_0 as we will quantitatively discuss in section 6.2. In Eq. (5.81), the Floquet matrices are ordered such that in the time domain $\hat{\Gamma}^L(t,s) = \bar{\mu}_{LR}(t)\,\delta\Gamma^L(t,s)/\delta\bar{\mu}_{LR}$, assuming that the current measured at time t is proportional to the voltage at time t. With these initial conditions, we assume a linear and adiabatic response, which is justified since the voltage and the driving frequency Ω are small compared to the huge energy scale Λ_0.

This completes the simpler set of initial conditions for the nonequilibrium RG flow, which we used to generate the data presented in sections 3.2 and 3.3. We will continue with the derivation of a different initial condition for the RG flow which is advantageous when $V_{\text{avg}} = 0$ (see section 6.4 for a comparison).

5.3.2. Unitary transformation

By a unitary transformation, we can shift the time-dependence from the reservoir Hamiltonian to the coupling. This will have the advantage that $\hat{\bar{\mu}}_{LR}$ becomes a scalar and even vanishes in some cases. This is particularly useful because for $V_{\text{avg}} = 0$ it can significantly reduce the numerical effort of solving the RG equations. If all calculations were exact, the initial condition for the transformed system would be equivalent to the approach described above. But since we have made various approximations and need to work with truncated Floquet matrices in the numerical implementation, this is no longer guaranteed. In chapter 6 we will compare the results from the different initial conditions and see that while both methods show very good agreement, the simpler approach described above avoids some numerical complications.

The aim of the unitary transformation is to change the chemical potentials $\mu_\alpha(t)$. More precisely, we split $\mu_\alpha(t) = \mu^j_\alpha(t) + \mu^r_\alpha(t)$ where $\mu^j_\alpha(t)$ will be removed by the transformation. The previously discussed case without unitary transformation corresponds to $\mu^j_\alpha(t) = 0$. A general unitary transformation maps the Hamiltonian to

$$\tilde{H}(t) = U(t)H(t)U(t)^\dagger - iU(t)\frac{\partial U(t)^\dagger}{\partial t}, \tag{5.82}$$

such that for any state $|\psi(t)\rangle$ that fulfills the Schrödinger equation with Hamiltonian $H(t)$, the transformed state $U(t)|\psi(t)\rangle$ fulfills the Schrödinger equation with the transformed Hamiltonian

[13] This initial condition for $\partial_E\hat{\Gamma}^L(E)$ was only found at a late stage of this work. The results presented in figure 3.7 and figure 3.8 were computed with the simpler initial condition $\partial_E\hat{\Gamma}^L(i\Lambda_0) = 0$ taken from equilibrium, which leads to slower convergence of the current as a function of Λ_0. We have checked for some representative data points that this does not lead to any visible deviations.

$\tilde{H}(t)$. To partially remove the chemical potentials in the reservoir Hamiltonian, we choose the unitary operator

$$U(t) = e^{i\int_0^t ds \sum_\alpha \mu_\alpha^j(s) N_\alpha} \tag{5.83}$$

involving the particle number operator N_α for reservoir α, such that

$$iU(t)\frac{\partial U(t)^\dagger}{\partial t} = \sum_\alpha \mu_\alpha^j(t) N_\alpha. \tag{5.84}$$

Thus, the second term in Eq. (5.82) removes the part $\mu_\alpha^j(t)$ of the chemical potential as intended, but the similarity transform with $U(t)$ makes the transformed total system Hamiltonian more complicated, giving the creation and annihilation operators a time-varying phase:

$$U(t)c_1 U(t)^\dagger = e^{\eta i \int_0^t ds\, \mu_1^j(s)} c_1. \tag{5.85}$$

In the Kondo Hamiltonian (3.2), this only affects the coupling part H_V and is equivalent to replacing the coupling $\bar{J}^{(0)}_{\alpha\alpha'}$ with

$$\bar{J}^{(0)}_{\alpha\alpha'}(t) = e^{i\int_0^t ds[\mu_\alpha^j(s) - \mu_{\alpha'}^j(s)]} \bar{J}^{(0)}_{\alpha\alpha'}, \tag{5.86}$$

such that the transformed total system Hamiltonian is

$$\tilde{H}(t) = \sum_{\alpha\alpha'\sigma\sigma'} \bar{J}^{(0)}_{\alpha\alpha'}(t)\, \mathrm{S}\cdot\boldsymbol{\sigma}_{\sigma\sigma'} \iint d\omega\, d\omega'\, c^\dagger_{\omega\sigma\alpha} c_{\omega'\sigma'\alpha'} + \sum_{\alpha\sigma}\int d\omega \left[\omega + \mu_\alpha^r(t)\right] c^\dagger_{\alpha\sigma\omega} c_{\alpha\sigma\omega}. \tag{5.87}$$

It is important to notice that only the phase of the coupling $\bar{J}^{(0)}_{\alpha\alpha'}$ for $\alpha \neq \alpha'$ is altered by the transformation.

In general, this unitary transformation allows us to split the bias voltage in an arbitrary way such that one part is included in the coupling. But when using the Floquet formalism this freedom gets restricted because $H(t)$ must be periodic in time, and to avoid huge Floquet matrices, it is feasible to have a short time period T such that $H(t+T) = H(t)$. This leads to the constraint that $\bar{J}^{(0)}_{\alpha\alpha'}(t)$ should have the same periodicity as the physical bias voltage. This is always the case if the time-averaged bias voltage vanishes, $\int_0^T dt V(t) = 0$. But for a finite average bias voltage V_{avg} which is not an integer multiple of the frequency Ω, we need to partially include the bias voltage in $\mu_\alpha^r(t)$. However, we can always choose $\mu_\alpha^r(t)$ to be constant and include the time-dependent part in $\mu_\alpha^j(t)$. In the following, we will only consider this case of constant μ_α^r, such that the Floquet matrix $\hat{\tilde{\mu}}^r_{LR} = (\mu_L^r - \mu_R^r)\mathbb{1}$ can be replaced by a scalar.

5.3.3. Initial conditions bias transformed into coupling (step 15b)

When using the transformed Hamiltonian (5.87), the time dependence of the coupling must be included in the nonequilibrium initial condition of the RG flow. To properly treat this time dependence, we remind that at $E = i\Lambda_0$ the system responds adiabatically to the bias voltage since low-energy effects are suppressed (see section 5.2.1). We can thus construct initial conditions for the nonequilibrium system by using the equilibrium RG flow and an adiabatic approximation.

In Floquet space, the coupling becomes a Floquet matrix:

$$\hat{J}^{(0)}_{\alpha\alpha'} = \bar{J}^{(0)}_{\alpha\alpha'}\hat{F}^{\alpha\alpha'}, \qquad \hat{F}^{\alpha\alpha'}_{nm} = \frac{1}{T}\int_0^T dt\, e^{i(n-m)\Omega t + i\int_0^t ds\,[\mu^j_\alpha(s) - \mu^j_{\alpha'}(s)]}. \tag{5.88}$$

This definition follows from Eq. (4.5) analogous to the Floquet matrix $\hat{\mu}^r_\alpha$ for the chemical potentials and fulfills the important relation[14]

$$\hat{F}^{\alpha\alpha'}\hat{F}^{\alpha'\alpha''} = \hat{F}^{\alpha\alpha''} \qquad \text{for each } \alpha' \text{ (no sum)}. \tag{5.89}$$

By way of exception, we do not sum over α' in Eq. (5.89). This property shows that terms of the form $\hat{J}^{(0)}_{\alpha\alpha'}\hat{J}^{(0)}_{\alpha'\alpha} = (\bar{J}^{(0)}_{\alpha\alpha'})^2\mathbb{1}$ are completely unaffected by the unitary transformation. Consequently, $\hat{\Gamma}(E)$, $\hat{Z}(E)$, $\delta\hat{\Gamma}^\gamma(E)$, and $\hat{\Gamma}^\gamma(E)$ should not be affected by the transformation, and we can use the same initial conditions for these Floquet matrices as in the case without unitary transformation by only replacing $\hat{\mu}_{12}$ with $\bar{\mu}^r_{12}$.

Finally, we need initial conditions for the vertices. Since the system responds adiabatically to the time-dependent coupling at high $\operatorname{Im} E$, the vertices are given by multiplication of the equilibrium results with $\hat{F}^{12} \equiv \hat{F}^{\alpha_1\alpha_2}$: $\hat{G}^2_{12} = G^2_{12}\hat{F}^{12}$. With the product rule (5.89), we know that no other Floquet matrices than $\hat{F}^{12}$ can arise due to combinations of vertices. We therefore define the effective coupling Floquet matrix

$$\hat{J}_{\alpha\alpha'}(E) \coloneqq 2\sqrt{x_\alpha x_{\alpha'}}\hat{F}^{\alpha\alpha'}J(E + \hat{N}\Omega), \tag{5.90}$$

where $J(E)$ is taken from the equilibrium RG flow. Here the Floquet matrices are ordered like in Eq. (5.81) such that $\hat{J}_{\alpha\alpha'}(E)$ describes an adiabatic response to the time-dependent phase in the bare coupling. Using Eq. (5.90), we can take the initial conditions for the vertices from the results of the equilibrium RG flow in Eqs. (5.70)–(5.73) and from the adiabatic response:

$$\hat{G}^2_{12}(E) = -\hat{J}_{12}(E), \tag{5.91}$$

$$\hat{G}^3_{12}(E) = i\pi\hat{J}_{12}(E)J(E + \hat{N}\Omega)[Z(E + \hat{N}\Omega)]^2, \tag{5.92}$$

$$\hat{I}^\gamma_{12}(E) = (\delta_{1\gamma} - \delta_{2\gamma})\hat{J}_{12}(E)\left[1 - Z(E + \hat{N}\Omega)J(E + \hat{N}\Omega)\right]. \tag{5.93}$$

The energy shifts by multiples of the voltage $\bar{\mu}^r_{LR}$ appearing in the nonequilibrium RG equations can easily be calculated since $\bar{\mu}^r_{LR}$ is not a Floquet matrix. This completes the derivation of an initial condition to solve the nonequilibrium RG equations.

5.3.4. Special case: harmonic driving

In chapter 3, we discussed in detail the results obtained for a bias voltage of the form $V(t) = V_{\text{avg}} + V_{\text{osc}}\cos(\Omega t)$. In this case, we can split $V_{\text{avg}} = V^r_{\text{avg}} + n_j\Omega$ such that V^r_{avg} is included in μ^r_α,

[14] Using the definition of $\hat{F}^{12}$ and no sum convention: $(\hat{F}^{12}\hat{F}^{23})_{nm} = (2\pi)^{-2}\sum_k\iint_0^{2\pi} dx\,dy\,e^{i(n-k)x + i(k-m)y}e^{iA_{12}(x)+iA_{23}(y)}$, where $A_{12}(\Omega t) = \int_0^t ds[\mu^j_1(s) - \mu^j_2(s)]$ is a real-valued function such that $A_{12}(x) + A_{23}(x) = A_{13}(x)$. The terms involving k yield $2\pi\delta(x-y)$ such that $(\hat{F}^{12}\hat{F}^{23})_{nm} = (2\pi)^{-1}\int_0^{2\pi} dx\,e^{i(n-m)x}e^{iA_{12}(x)+iA_{23}(x)} = \hat{F}^{13}_{nm}$ independent of the index 2.

whereas the shift by $n_j\Omega$ for an integer n_j can be included in μ_α^j and enters the coupling via $\hat{F}^{12}$. The Floquet matrix structure in the initial conditions is then

$$\hat{F}^{LR}_{nm} = \frac{1}{T}\int_0^T dt\, e^{i(n-m+n_j)\Omega t - i\frac{V_{\rm osc}}{\Omega}\sin(\Omega t)} = \mathcal{J}_{n-m+n_j}\left(\frac{V_{\rm osc}}{\Omega}\right). \tag{5.94}$$

The Bessel functions $\mathcal{J}_n(x)$ are strongly suppressed for $|n| \gg x$. Thus, all Floquet matrix elements that are sufficiently far away from the diagonal are small.

5.3.5. Summary of nonequilibrium initial conditions

The initial conditions for the nonequilibrium RG equations (5.19)–(5.27) for $E = i\Lambda_0$, $\Lambda_0 \gg T_K$ can be summarized as follows:

$$\hat{\Gamma}(E) = \Gamma(E + \hat{N}\Omega), \tag{5.95}$$
$$\hat{Z}(E) = Z(E + \hat{N}\Omega), \tag{5.96}$$
$$\hat{G}^2_{12}(E) = -2\sqrt{x_1x_2}\hat{F}^{12}J(E + \hat{N}\Omega), \tag{5.97}$$
$$\hat{G}^3_{12}(E) = i\pi 2\sqrt{x_1x_2}\hat{F}^{12}[J(E + \hat{N}\Omega)\,Z(E + \hat{N}\Omega)]^2, \tag{5.98}$$
$$\hat{G}^a_{12}(E) = 0, \tag{5.99}$$
$$\hat{I}^\gamma_{12}(E) = (\delta_{1\gamma} - \delta_{2\gamma})2\sqrt{x_1x_2}\hat{F}^{12}J(E + \hat{N}\Omega)\left[1 - Z(E + \hat{N}\Omega)\,J(E + \hat{N}\Omega)\right], \tag{5.100}$$
$$\delta\hat{\Gamma}(E) = 0, \tag{5.101}$$
$$\delta\hat{\Gamma}^L(E) = 3\pi x_L x_R \delta V_{\rm avg}\,[J(E + \hat{N}\Omega)\,Z(E + \hat{N}\Omega)]^2, \tag{5.102}$$
$$\hat{\Gamma}^L(E) = 3\pi x_L x_R \hat{\tilde{\mu}}_{LR}[J(E + \hat{N}\Omega)\,Z(E + \hat{N}\Omega)]^2, \tag{5.103}$$
$$\partial_E\hat{\Gamma}^L(E) = -12\pi x_L x_R \hat{\tilde{\mu}}_{LR}\frac{J(E + \hat{N}\Omega)^3 Z(E + \hat{N}\Omega)^2\left[1 - Z(E + \hat{N}\Omega)J(E + \hat{N}\Omega)\right]}{E + i\Gamma(E + \hat{N}\Omega)}. \tag{5.104}$$

The RG equations also include a shift of the energy arguments by integer multiples of the voltage Floquet matrix $\hat{\tilde{\mu}}^r_{LR}$. When using the unitary transformation, we restrict this shift to be a scalar, $\hat{\tilde{\mu}}^r_{LR} \propto \mathbb{1}$. In the case without unitary transformation this voltage shift is a Floquet matrix, but $\hat{F}^{12} = \mathbb{1}$ such that one can work in the eigenbasis of $E + \hat{N}\Omega + n\hat{\tilde{\mu}}^r_{LR}$ to include this shift. The corresponding results for the leading order RG equations are given in appendix I.

5.4. Calculating transport observables (step 16)

In this final step, we show how to calculate the current and the differential conductance after solving the nonequilibrium RG equations numerically. We focus on the situation long after the voltage has been switched on ($t_0 \to -\infty$) and do not try to calculate the transient dynamics.[15]

[15] In principle, it is possible to compute the transient dynamics. The RG equations allow us to compute, e.g., the current kernel Γ^γ and the spin relaxation rate Γ as a function of E, and one can numerically do an inverse Laplace transform of these functions. But this is beyond the scope of this thesis and would require additional checks of the validity of the RG equations for $\mathrm{Im}\,E < 0$.

In the Floquet formalism, this implies that only Floquet matrices at energy argument $E = 0$ are needed. As the following calculation will show, we can directly read off the Fourier modes of the current and the differential conductance from the Floquet matrices Γ^γ and $\delta\Gamma^\gamma$ when the RG flow reaches $E = 0$.

By the definition of the current kernel Σ_γ in the time domain in Eq. (1.2) and its parametrization in Eq. (5.2), the expectation value of the current in reservoir γ for $t_0 \to -\infty$ is

$$I_\gamma(t) = \int_{-\infty}^{t} ds\, \Gamma^\gamma(t,s)\ \mathrm{tr}\,\rho(s) = \sum_n e^{-in\Omega t}\hat{\Gamma}^\gamma(E=0)_{n0}. \tag{5.105}$$

In the last step we have used the normalization of states, $\mathrm{tr}\,\rho(s) = 1$, and the definition of the Floquet matrix [Eq. (4.2)]. Thus, the central column of the Floquet matrix $\Gamma^\gamma(E = 0)$ contains the Fourier modes of the current. A similar relation follows for the differential conductance from the variation of the voltage. When using $\delta\bar{\mu}_{12} = (\delta_{1L} - \delta_{2L})\delta V_{\mathrm{avg}}$ for the variation of the time-averaged bias voltage (see section 4.3.7), the central column of the Floquet matrix $\delta\hat{\Gamma}^L(E = 0)/\delta V_{\mathrm{avg}}$ contains the Fourier modes of the differential conductance:

$$G(t) = \frac{dI_L(t)}{dV_{\mathrm{avg}}} = \sum_n e^{-in\Omega t}\frac{\delta\hat{\Gamma}^L(E=0)_{n0}}{\delta V_{\mathrm{avg}}}. \tag{5.106}$$

5.5. Summary

Starting from the RG equations for two-point vertex models, we used the specific properties of the isotropic Kondo model to parametrize the superoperators appearing in the RG equations. We derived RG equations for these parametrizations including the leading and next-to-leading order in the coupling. The resulting ordinary differential equations with the energy flow parameter E can be solved numerically given an initial condition at flow parameter $E = i\Lambda_0$, where $\Lambda_0 \sim 10^9 T_K'$ is much larger than all energy scales in the system. To derive this initial condition, we first analytically determined the universal contributions to the equilibrium RG flow at flow parameter $\Lambda = \mathrm{Im}\, E \to \infty$ using bare perturbation theory. Using these results and known properties of the Kondo model in equilibrium, we derived the exact initial condition for the RG equations at $E = 0$ in equilibrium. We then provided two initial conditions for the nonequilibrium RG flow at $E = i\Lambda_0$ that can be obtained from a numerical solution of the equilibrium RG flow. Once the initial conditions are known, the nonequilibrium RG equations are solved numerically from $E = i\Lambda_0$ to $E = 0$. At the end of the RG flow, we directly obtain the Fourier modes of the current and the differential conductance. An overview of all derivation steps of the FRTRG for the Kondo model is provided in table 5.2.

We provided two possible initial conditions for the nonequilibrium RG flow, one of which is based on a unitary transformation of the original Hamiltonian. In section 6.4, we will show that these lead to the same results, and that both have numerical advantages and disadvantages. In the RG equations, we have identified different orders in J and different approximations that may simplify the analytic derivation or the numerical solution. These will be compared in section 6.1, where we will find indications that the underlying expansion in the coupling converges.

Step	Description	Result
1	Expansion in the coupling	Formal expansion for $\hat{\Pi}(E)$ and $\hat{L}(E)$
2	Diagrammatic language	Diagrams for $\hat{L}(E)$ and $\hat{G}_{12}^{p_1 p_2}(E)$
3	Energy derivatives	Diagrams for $\partial_E^2 \hat{L}(E)$ and $\partial_E \hat{G}_{12}^{p_1 p_2}(E)$
4	Derivatives of contraction lines	Eliminate almost all integrals in diagrams for $\partial_E^2 \hat{L}(E)$ and $\partial_E \hat{G}_{12}^{p_1 p_2}(E)$
5	Frequency dependence of vertices	Frequencies in vertex indices are negligible
6	Frequency integral in RG equation for $\partial_E \hat{G}_{1_0 2_0}^{p_1 p_2}(E)$	We can calculate the integral using numerical diagonalization or an approximation
7	Sum over p and η indices	Only $\bar{G}_{12}(E)$ with fixed $\eta_1 = +, \eta_2 = -$ appears in RG equations, instead of $\hat{G}_{12}^{p_1 p_2}(E)$
8	RG equations for transport current	RG equations for current vertex $\hat{I}_{12}^{\gamma p_1 p_2}(E)$ and kernel $\hat{\Sigma}_\gamma(E)$ by analogy to $\hat{G}_{12}^{p_1 p_2}$ and $\hat{L}(E)$
9	RG equations for differential conductance using voltage variation	RG equations for $\delta\hat{\Sigma}_\gamma(E)$ and $\delta\hat{\Gamma}(E)$
10	Parametrization of superoperators	Superoperator algebra and Floquet matrices parametrizing the superoperators
11	Parametrization in RG equations	Final nonequilibrium RG equations
12	Liouville space formulation of the Kondo model	Leading order bare perturbation theory results for vertices that can be used at large Im E
13	Equilibrium RG flow	Connection of results for large Im E from bare perturbation theory to $E = 0$
14	Equilibrium initial conditions	Initial conditions at $E = 0$ in equilibrium
15	Nonequilibrium initial conditions	Final initial conditions at $E = i\Lambda_0$
15(a)	...with untransformed Hamiltonian	
15(b)	...with transformed Hamiltonian	
16	Calculating observables	RG flow results contain Fourier modes of current and differential conductance

Table 5.2.: Overview of the steps in the derivation of the FRTRG for the Kondo model. A horizontal line marks the separation between chapter 4 (general model with only a two-point vertex) and chapter 5 (Kondo model).

6. Numerical implementation and convergence

We have derived the RG flow as a set of ordinary differential equations (ODEs) with known initial condition, which can be solved numerically. However, we assumed that we can start the RG flow at sufficiently large Λ_0 and work with Floquet matrices of infinite size. In this chapter, we will discuss those aspects of the method which are best understood by looking at the numerical results. We will compare different truncation orders of the RG equations to verify that the expansion in the coupling J that underlies the whole method indeed converges. We will see that the truncation of Floquet matrices to finite size leads to subtle issues when including the time-dependence in the coupling (see step 15b). Various checks will confirm that the FRTRG results for harmonic driving are robust and converged. The numerical implementation of the FRTRG for the Kondo model is publicly available.[1] Some main outcomes of this chapter have been mentioned in Ref. [3].

6.1. RG equations in different truncation schemes

In the derivation of the RG equations, we have seen that different approximations and truncation orders of these equations can be used. These include the approximation of a frequency integral in section 4.3.4, neglecting the vertex component $\hat{G}^a$, and neglecting all next-to-leading order terms in the RG equations. Here we discuss the effect of these approximations and implications for the general accuracy of the method. An overview of different approximations is shown in figure 6.1.

6.1.1. Convergence of the expansion in the coupling

First, we focus on the convergence of the expansion in J that underlies the whole derivation of the FRTRG. In the general derivation of the effective Liouvillian and the effective coupling vertex, we expanded up to third order in the coupling J (steps 3–9). In the parametrization for the Kondo model, we then kept terms up to next-to-leading order in J (steps 10–11). To verify that this approximation is valid, we compare to a truncation of the final RG equations in leading order in J. The leading order terms are marked in blue in Eqs. (5.20)–(5.27) and the initial condition for the RG flow is given in appendix I. A small deviation of the next-to-leading order results from the leading order indicates the convergence of the expansion in J.

In figure 6.2, we can see that the leading order RG equations overestimate the peaks in the differential conductance at $V_{\text{avg}} = n\Omega, n \in \mathbb{Z}$. But we also find that the overall difference between

[1] `https://github.com/stiglers-eponym/frtrg`

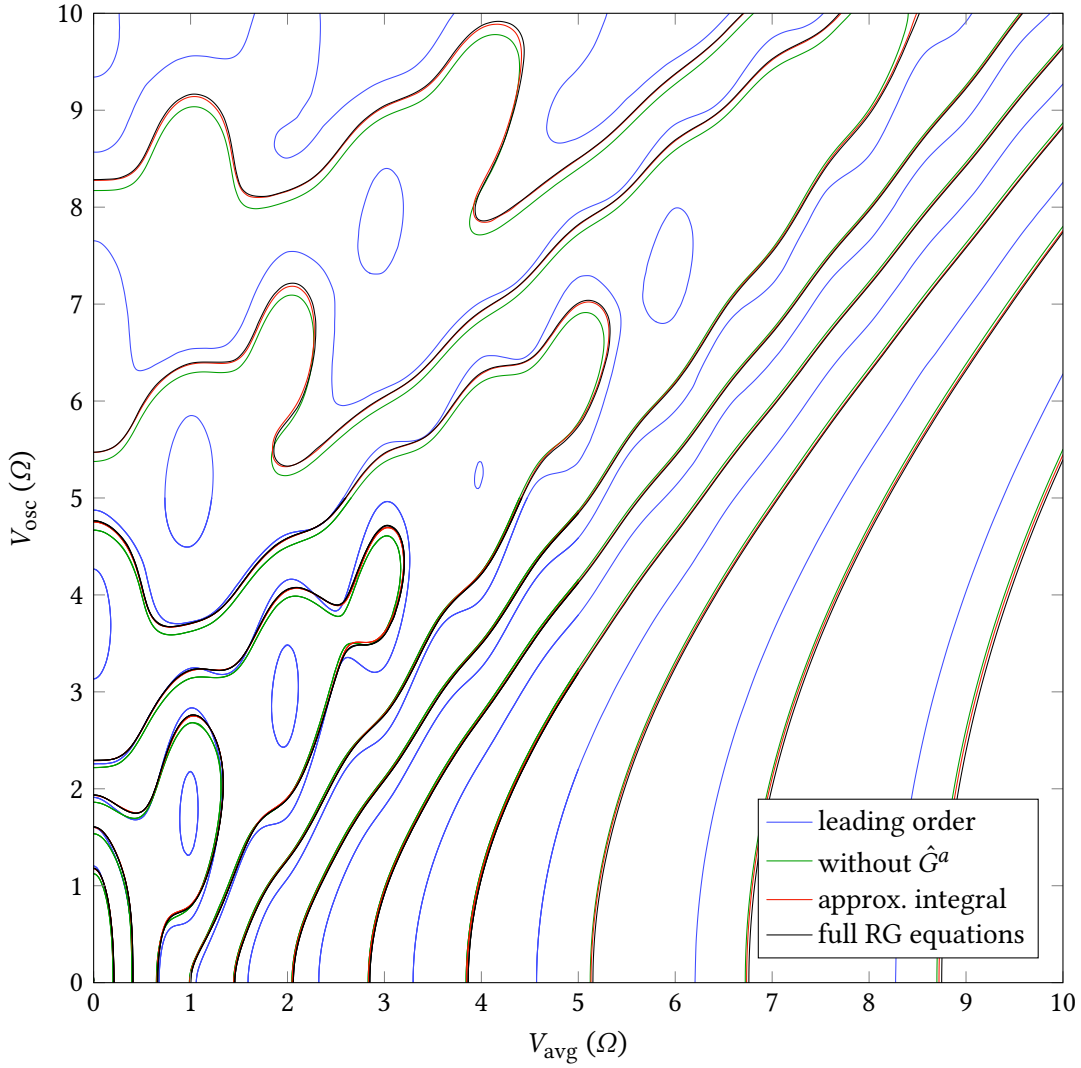

Figure 6.1.: Contour plot of the differential conductance for $\Omega = 4.8T_K$ calculated using RG equations in different truncation orders and approximations. The curves indicate $G = (2e^2/h)/n$, $n = 2, 3, \ldots$ Results from next-to-leading order RG equations with approximated frequency integral (red) show good agreement with the exact solution of the integral (black), whereas additionally neglecting $\hat{G}^a$ (green, same approximation as used in Ref. [3]) leads to slightly larger deviations. Keeping only the leading order (blue) causes significant deviations. The unitary transformation in the initial conditions and the Floquet matrix truncation and mitigation to truncation effects discussed in section 6.4 to no lead to relevant deviations. For $V_{\mathrm{avg}}, V_{\mathrm{osc}} < 5\Omega$, we the figure shows results with and without the unitary transformation, but one can hardly see a difference because the curves lie almost perfectly on top of each other. Thus, these implementation details do not have any significant effect on the results. Subtleties of the comparison of different approximations are discussed in appendix J.1.

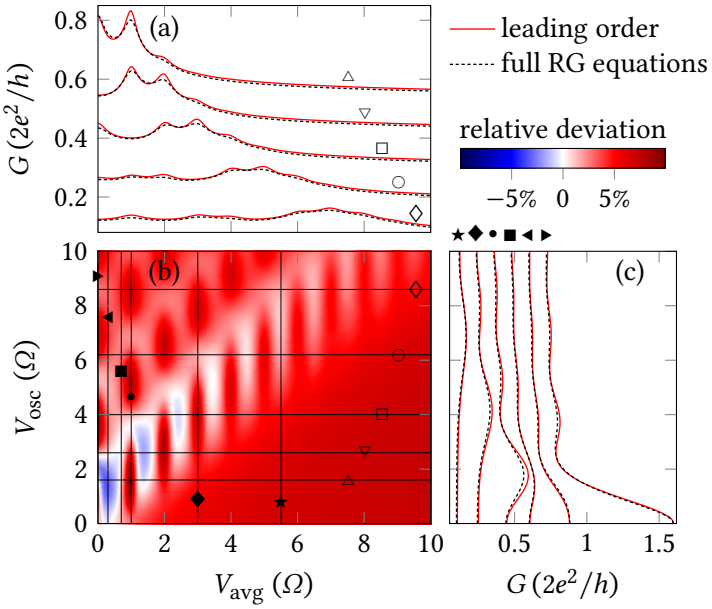

Figure 6.2.: (a), (c) Comparison of differential conductance G calculated using RG equations truncated in leading (red curve) or next-to-leading order (black dashed curve) for $\Omega = 4.8T_K$. The scales refer to the lowest curve, and all subsequent curves are separated by $0.12(2e^2/h)$ for clarity. (b) Relative deviation of G in leading order from next-to-leading order results. Horizontal (vertical) black lines show cuts at fixed V_{osc} (V_{avg}) which are shown in panel (a) [(c)]. The leading order RG equations lead to more pronounced side peaks because some processes contributing to decoherence due to the driving are neglected.

results from RG equations truncated in leading and next-to-leading order is mostly around 5%, reaching at most 10% for the shown parameter range. This indicates that the expansion in J converges and that the deviation of roughly 5% may be a good estimate for the accuracy of the FRTRG for the Kondo model in next-to-leading order.[2]

The sharper peaks due to photon-assisted tunneling in the leading order RG results can be understood as a result of underestimated decoherence. The next-to-leading order terms in the RG equations include many processes that contribute to the decoherence due to the periodic driving. As these processes are neglected, the peaks become sharper.[3] However, the predictions from leading order FRTRG already include decoherence processes and provide a better quantitative description than the phenomenological description with only photon-assisted tunneling, which we discussed in section 3.2.2 [see Eq. (3.18)].

6.1.2. Approximation of the frequency integral in next-to-leading order

Taking the comparison of leading and next-to-leading order truncation as a reference for the reliability of our results, we can now analyze the effect of other approximations. The numerical

[2]The uncertainty can also be estimated based on the expansion parameter J or $J' = ZJ$. The RG equations and their derivation indicate that terms involving higher orders in J are also of higher order in Z, such that we can combine J and Z in J' to estimate the expansion parameter. For the parameters shown in figure 6.2, the coupling lies in the range $0.16 \lesssim J' < 0.37$ or $0.23 \lesssim J < 0.92$. In the expansion up to next-to-leading order in J', a precision of a few percent seems optimistic. But the clever resummation of different terms using effective vertices and the effective Liouvillian makes a fast convergence even for relatively large J' possible.

[3]One can also argue using the RG equations: In the leading order renormalization of the vertices in the final RG equations (5.19)–(5.27), the resonances at $V_{\mathrm{avg}} = n\Omega$, $n \in \mathbb{Z}$ can be attributed to resonances in the energy-shifted resolvent $\hat{R}(\hat{E}_{12}) = 1/[E + \hat{\mu}_{12} + \hat{N}\Omega + \hat{\Gamma}(\hat{E}_{12})]$. These are largest for $\alpha_1 \neq \alpha_2$ when $\hat{\mu}_{12} + \hat{N}\Omega$ has an approximately vanishing eigenvalue. Thus, the leading order terms in the RG flow produce the resonances due to photon-assisted driving.

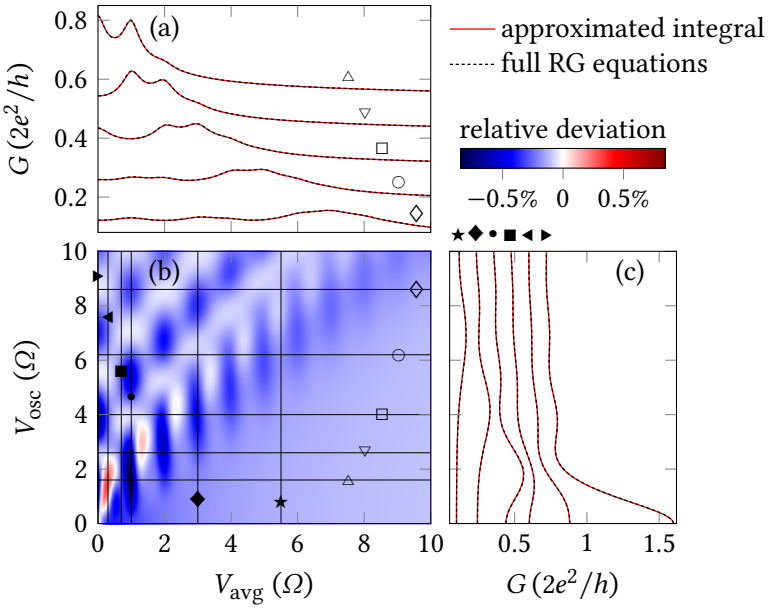

Figure 6.3.: Deviation of the differential conductance calculated using the approximated frequency integral (red curves, see section 4.3.4) from the full next-to-leading order RG equations (black dashed curves) for $\Omega = 4.8T_K$. The deviation is clearly much smaller than when comparing to the leading order RG equations in figure 6.2 (note the different color scales). The present figure is structured like figure 6.2.

solution of the RG equations can be simplified by approximating the frequency integral $\mathcal{I}[\cdots]$. As derived in section 4.3.4, $\mathcal{I}[\cdots]$ can be solved exactly by diagonalizing the Floquet matrix $\hat{\chi}(\hat{E}_X)$ for different energy shifts $\hat{E}_X$. An approximation of the form $\mathcal{I}[\hat{A}] \approx \frac{1}{2}\left(\hat{R}\hat{A}\hat{Z} + \hat{Z}\hat{A}\hat{R}\right)$ avoids the diagonalization and speeds up the numerical integration of the RG equations. In figure 6.3, we compare the differential conductance computed with and without this approximation of the integral and find that the deviation is less than 1%. We consider this deviation to be negligibly small and used the approximation of the frequency integral for all FRTRG results presented in chapter 3. A technical argument why this approximation works so well is presented in appendix J.2.

6.1.3. Relevance of $\hat{G}^a$

Another possible simplification of the next-to-leading order in the RG equations lies in neglecting the vertex component $\hat{G}^a_{12}$ [red terms in Eqs. (5.19)–(5.27)]. In figure 6.4, we compare the results without $\hat{G}^a_{12}$ and with the approximated frequency integral to results obtained using the full RG equations. This comparison shows that neglecting $\hat{G}^a_{12}$ causes only a deviation that is at most of the same order as the estimated accuracy of the method, which we take from the comparison between leading and next-to-leading order truncation. Thus, $\hat{G}^a_{12}$ remains small during the RG flow and its effect on the results is very limited, legitimating the usage of this approximating in Ref. [3]. But since this deviation is not much smaller than our rough estimate of the accuracy and since neglecting $\hat{G}^a_{12}$ does not significantly simplify the numerical solution of the RG equations, we do not use this approximation here. In appendix J.3, we show explicitly that $\hat{G}^a_{12}$ indeed remains small, but not completely negligible.

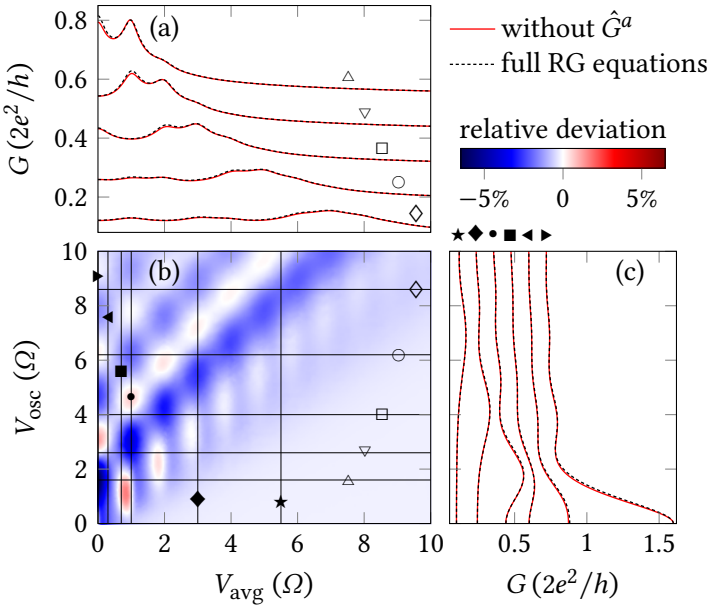

Figure 6.4.: Deviation of the differential conductance due to approximations in the next-to-leading order RG equations for $\Omega = 4.8T_K$. The approximations include neglecting the vertex component $\hat{G}^a_{12}$ and approximating the frequency integral as explained in section 4.3.4. A significant deviation is visible for $V_{\mathrm{avg}} \approx 0$, $V_{\mathrm{osc}} \lesssim 2\Omega$. Overall, the deviation is considerably smaller than the difference between results from leading and next-to-leading order truncation of the RG equations (see figure 6.2).

6.2. High energy cutoff Λ_0

When deriving the initial conditions for the nonequilibrium RG flow in section 5.3, we assumed that the numerical RG flow can be started at $E = i\Lambda_0$ where Λ_0 is a sufficiently large energy scale. Here we discuss the convergence of the results as a function of Λ_0. Most importantly, we have checked that the differential conductance calculated via $\delta\hat{\Gamma}^\gamma$ in the RG equations is already well converged for $\Lambda_0 = 10^6 T_K'$, whereas the current ($\hat{\Gamma}^\gamma$ in the RG equations) converges slower. The results in chapter 3 are obtained using $\Lambda_0 = 10^9 T_K'$ such that also the current is approximately converged, as we will see in the following.

The convergence of the current as a function of Λ_0 is illustrated in figure 6.5, which shows the average current I_{avg} and the alternating current I_{osc} (first harmonic) in the limit $\Lambda_0 \to \infty$. To obtain this limit, the RG equations are solved for $10^5 T_K' \leq \Lambda_0 \leq 10^9 T_K'$ and a curve of the form $I(\Lambda_0) = I_0 + \alpha J(\Lambda_0)^n$ is fitted to the result for I_{avg} and I_{osc}, with $J(\Lambda_0)$ denoting the equilibrium coupling strength used in the initial conditions. The exponent n is not a fit parameter, but an integer, depending on the initial condition for the current. With the initial conditions in Eq. (5.81) taken from adiabatic linear response, we find the best agreement with the FRTRG results for $n = 4$. When using $\partial_E \hat{\Gamma}^\gamma(i\Lambda_0) = 0$ in the initial conditions as in Ref. [3] we know that better initial conditions would lead to a correction to $\hat{\Gamma}^\gamma(i\Lambda_0)$ of the order $E\partial_E \delta\Gamma^\gamma(E)/\delta V_{\mathrm{avg}} = O(J^3)$ such that $n = 3$. With the simplest initial condition $\hat{\Gamma}^\gamma(i\Lambda_0) = 0$, the leading correction is of the order $\delta\Gamma^\gamma(E)/\delta V_{\mathrm{avg}} = O(J^2)$ such that $n = 2$. We checked that these exponents lead to good agreement with the FRTRG results for $I_{\mathrm{avg}}(\Lambda_0)$ and $I_{\mathrm{osc}}(\Lambda_0)$, confirming that the initial conditions for $\hat{\Gamma}^\gamma(i\Lambda_0)$ and $\partial_E \hat{\Gamma}^\gamma(i\Lambda_0)$ in Eq. (5.81) correctly describe the leading and next-to-leading order correction to the equilibrium value $\hat{\Gamma}^\gamma(i\Lambda_0) = 0$ in the universal RG flow.

Figure 6.5 shows based on this fit that at $\Lambda_0 = 10^9 T_K'$ the deviation from the limit $\Lambda_0 \to \infty$ remains well below 0.05% for I_{osc} and I_{avg} and thereby well below the estimated uncertainty of

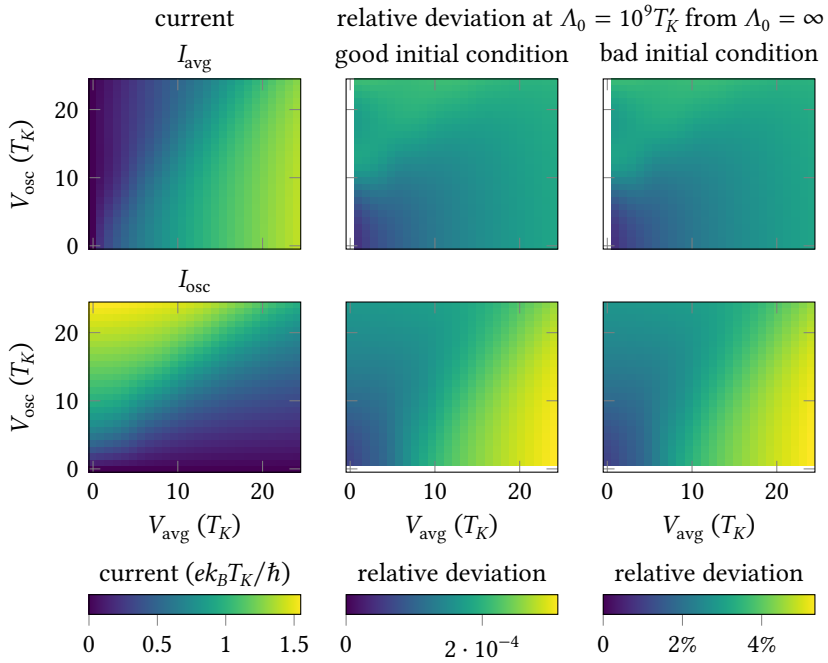

Figure 6.5.: Convergence of the direct (upper row) and alternating current (lower row) as a function of Λ_0 at fixed frequency $\Omega = 4.8T_K$ for different initial conditions. The middle and right column show relative deviations of the current I_{avg} or I_{osc} for $\Lambda_0 = 10^9 T_K'$ from an extrapolated value for $\Lambda_0 = \infty$. With the initial conditions for $\hat{\Gamma}^\gamma(E)$ and $\partial_E\hat{\Gamma}^\gamma(E)$ based on linear response as explained in section 5.3.1 (middle column) the current converges roughly like J^4 and relative deviations at $\Lambda_0 = 10^9 T_K'$ are of the order 10^{-4}. With the simpler initial conditions $\hat{\Gamma}^\gamma(E) = \partial_E\hat{\Gamma}^\gamma(E) = 0$ from equilibrium (right column) the current converges roughly like J^2 and deviations at $\Lambda_0 = 10^9 T_K'$ from the limit $\Lambda_0 = \infty$ are of the order 10^{-2}. The differential conductance G is not shown because for $\Lambda_0 \gtrsim 10^6 T_K'$ it mainly depends on the precision of the ODE solver and not on Λ_0.

the method when using good initial conditions.[4] Thus, the convergence as a function of Λ_0 is fast enough such that for $\Lambda_0 \sim 10^9 T_K'$ all results are sufficiently converged and an extrapolation to higher Λ_0 is not necessary. But figure 6.5 also highlights the importance of good initial conditions for the universal RG flow. Simply taking the equilibrium value $\Gamma^\gamma(i\Lambda_0) = 0$ as initial condition would lead to significant deviations of up to 5% in the current for $\Lambda_0 = 10^9 T_K'$ and to much slower convergence as a function of Λ_0.

For the differential conductance computed via $\delta\hat{\Gamma}^\gamma(E)$, convergence as a function of Λ_0 is not an issue because its equilibrium value provides a good initial condition. The numerical precision of G is mainly connected to the precision of the ODE solver, which leads to the highest numerical uncertainty near equilibrium. However, we can estimate this uncertainty to reach at most 0.1% for the parameters used for harmonic driving. Since this uncertainty increases with Λ_0, it is important to have good initial conditions such that Λ_0 does not need to be too large.

[4]This suggests that $\Lambda_0 = 10^9 T_K'$ is more than enough to reach good convergence. It would be sufficient to use $\Lambda_0 = 10^7 T_K'$ to obtain reliable results for the current. Here we use $\Lambda_0 = 10^9 T_K'$ because the optimal initial condition for $\partial_E\hat{\Gamma}^\gamma(i\Lambda_0)$ was found at a late stage of this work.

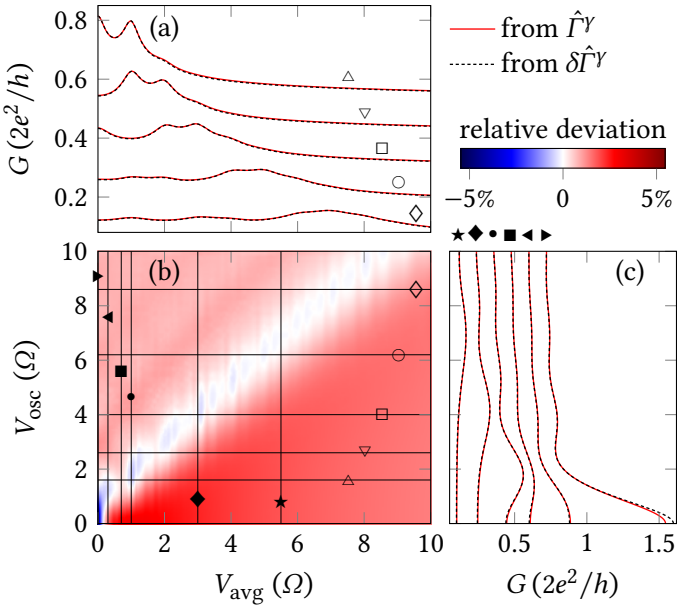

Figure 6.6.: Comparison of the differential conductance G computed directly via $\delta\hat{\Gamma}^\gamma$ (dashed black curves), and as numerical derivative of the current calculated via $\hat{\Gamma}^\gamma$ (red curves) for $\Omega = 4.8T_K$. The deviation reaches 5% near equilibrium, but remains below 2% for other parameters. This supports an optimistic estimate of the uncertainty of the method of only a few percent in the differential conductance. Small fluctuations are due to numerical effects in the differentiation of the current.

6.3. Consistency of current and differential conductance

In the RG equations we explicitly include the differential conductance (via $\delta\hat{\Gamma}^\gamma$) and the current (via $\hat{\Gamma}^\gamma$) such that both can be computed independently. The comparison of the differential conductance G calculated directly via $\delta\hat{\Gamma}^\gamma$ to the numerical derivative of the current provides a self-consistency check of the method. In figure 6.6, we see this comparison, which shows deviations of a few percent. We note that the RG equations for $\delta\hat{\Gamma}^\gamma$ and $\hat{\Gamma}^\gamma$ rely on separate expansions in the coupling J and separate initial conditions, such that we expect deviations due to higher-order corrections. For example, the initial condition for the RG flow guarantees that the differential conductance computed via $\delta\hat{\Gamma}^\gamma$ correctly reproduces the equilibrium value $2e^2/h$ — assuming the ODE solver works perfectly. In contrast, when calculating G via $\hat{\Gamma}^\gamma$, we find a deviation of 5.5% from the unitary conductance near equilibrium. This relatively large deviation near equilibrium is not surprising, since in equilibrium our expansion parameter J — the effective coupling — reaches its largest value of $2/(\sqrt{3}\pi)$. As discussed in section 6.1.1, the overall uncertainty of a few percent is in agreement with the estimated accuracy of the method.

6.4. Floquet matrix truncation and unitary transformation

An important parameter for the numerical solution is the size of the Floquet matrices. In the derivation, we assumed that all Floquet matrices have infinitely many matrix elements. For the numerical solution, we need to make sure that the truncation to finite size does not affect the results. As we will see below, this strongly depends on the choice of initial conditions and the unitary transformation of the Hamiltonian discussed in section 5.3.2.

To understand the effect of the truncation of the Floquet matrices, we first analyze the generic structure of Floquet matrices based on their definition. From section 4.2.1, we remember that for

a function $f(t, t_0)$ of two time arguments

$$\hat{f}(E)_{nm} = \tilde{f}_{n-m}(E + m\Omega), \qquad \tilde{f}_n(E) = \frac{1}{T}\int_0^\infty ds\, e^{iEs} \int_0^T dt\, e^{in\Omega t} f(t, t-s). \tag{6.1}$$

The Floquet matrix $\hat{f}(E)_{nm}$ representing f is defined such that $n - m$ is the Fourier index of the time-periodic function $f_s(t) \coloneqq f(t, t-s)$. Assuming that all functions are smooth in the time domain on some timescale τ, we know that matrix elements $\hat{f}(E)_{nm}$ far away from the diagonal must become small: $\hat{f}(E)_{nm}$ is suppressed for $|n-m| \gtrsim 1/(\Omega\tau)$.

The further structure of $\hat{f}(E)_{nm}$ depends on the structure and smoothness of the Laplace transform $\tilde{f}_n(E)$. In the RG flow, we have $\operatorname{Im} E \geq 0$ such that E is far away from all nonanalytic features that only lie in the lower half of the complex plane. It will therefore generally be a smooth function of E. During most of the RG flow, for $\operatorname{Im} E \gg \Omega$, we expect $\tilde{f}_n(E)$ to be smooth on a scale larger than Ω, such that $\hat{f}(E)_{n+1,m+1} = \hat{f}(E+\Omega)_{nm} \approx \hat{f}(E)_{nm}$. Examples of such Floquet matrices are the matrices which we use in the initial conditions. Both $\hat{\tilde{\mu}}_{LR}$ and $\hat{F}^{LR}_{nm}$ [defined in Eqs. (4.5) and (5.88)] even fulfill $\hat{f}_{n+1,m+1} = \hat{f}_{nm}$ exactly. But unfortunately, this general Floquet matrix structure can lead to strong truncation effects when reducing the infinite Floquet matrices to finite size.

This truncation is unproblematic if all discarded off-diagonal matrix elements are negligibly small. In this case, the product of two truncated Floquet matrices equals the truncated product of two infinite Floquet matrices. But this structure is not guaranteed by general principles for the Floquet matrices, such that it must be checked explicitly during and after the RG flow. This check yields different results depending on how the driving is treated in the initial conditions. To illustrate this difference, figure 6.7 shows Floquet matrices at the end of the RG flow. With the untransformed Kondo Hamiltonian and the initial conditions explained in section 5.3.1, the truncation has hardly any effect if the matrix size is chosen sufficiently large. In this case, all Floquet matrices are approximately diagonal sufficiently far away from the center of the matrix, as shown in the left column of figure 6.7.

But when using a unitary transformation of the Hamiltonian to include the time-dependent voltage in the coupling (see section 5.3.2), the initial Floquet matrix $\hat{F}^{LR}_{12}$ that appears in the coupling at $E = i\Lambda_0$ can have many relevant off-diagonal matrix elements. In the third and fourth column of figure 6.7 we see Floquet matrices at the end of the RG flow with the time-dependence included in the coupling, and we find that the matrix for the coupling $\hat{G}^2_{LR}$ has many relevant off-diagonal matrix elements. Thus, for matrices like $\hat{G}^2_{LR}$ the product of truncated matrices will not be the same as the truncated product of two infinite Floquet matrices, and we need to find a way to mitigate the truncation effects.

To reduce the truncation effects, we use the generic structure of the Floquet matrices and that $\hat{f}(E)_{n+1,m+1} \approx \hat{f}(E)_{nm}$. Since we want to simulate infinite size Floquet matrices, we aim to estimate the truncated product of two infinite Floquet matrices, although we only know the truncated matrices. We use that a truncated Floquet matrix can be linearly extrapolated along its diagonals to find an estimate for a larger matrix: We assume that near the edge of the truncated matrix $\hat{f}_{n+k,m+k}(E)$ can be approximated by a linear function of k that can be extrapolated beyond the truncated matrix. To compute the product of two truncated Floquet

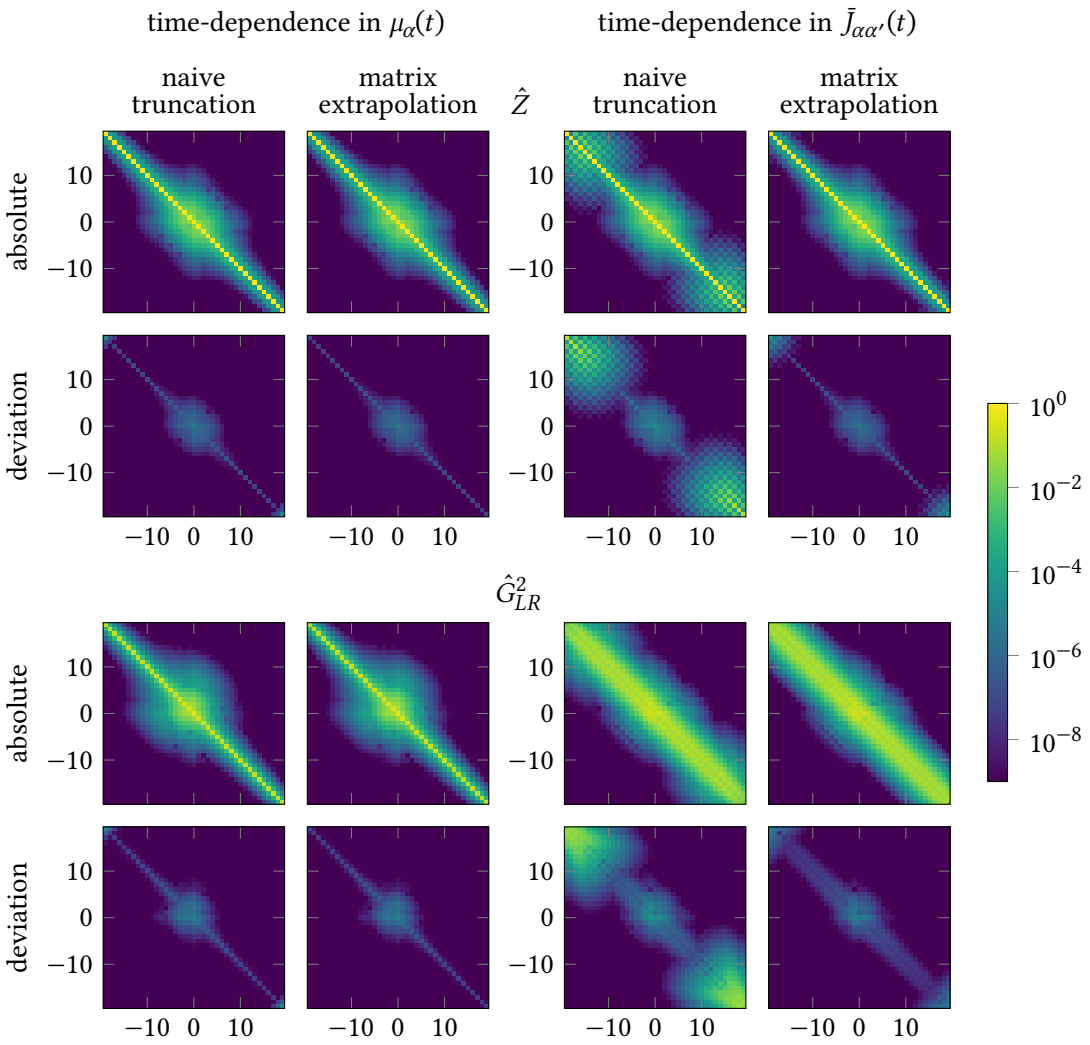

Figure 6.7.: Floquet matrices (absolute values of matrix elements) $\hat{Z}(E)$ (upper panels) and $\hat{G}^2_{LR}(E)$ (lower panels) at the end of the RG flow at $E = 0$ with different initial conditions and Floquet matrix truncation strategies for $\Omega = 4.8T_K$, $V_{\text{avg}} = 1.2\Omega$, and $V_{\text{osc}} = 1.8\Omega$. The second and fourth row show the deviation from an RG flow with larger Floquet matrices. For sufficiently large Floquet matrices, one expects that using even larger matrices will not make any difference. The left plots show RG flow results without the unitary transformation in the Hamiltonian, while the right panels show results with the unitary transformation, which shifts the time dependence from $\mu_\alpha(t)$ to $\bar{J}_{\alpha\alpha'}(t)$. The second and fourth column show the results of an RG flow, in which Floquet matrices were extrapolated to larger size in each matrix product to mitigate truncation effects, as explained in the text. One can see that when including the periodic driving in the coupling by the unitary transformation, strong truncation effects appear, which can be reduced significantly using matrix extrapolation. Without the unitary transformation, this extrapolation is not necessary. Only with the unitary transformation, the Floquet matrix $\hat{G}^2_{LR}$ has relevant off-diagonal matrix elements far away from the center of the matrix.

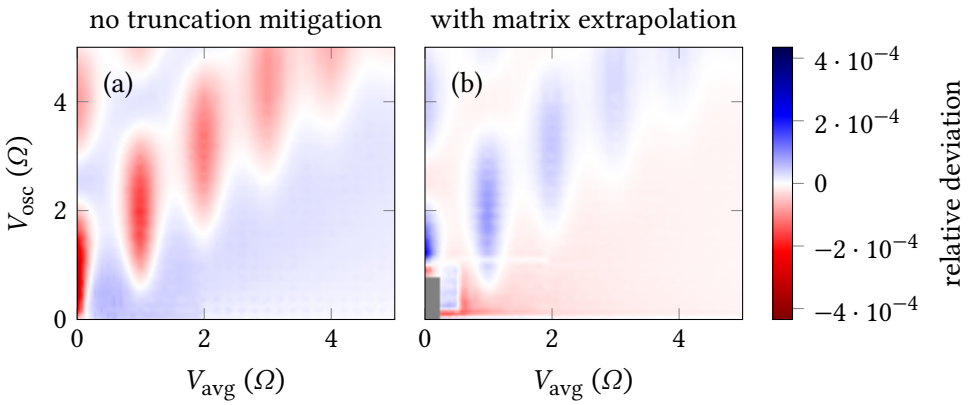

Figure 6.8.: Relative deviation of the differential conductance G calculated with the unitary transformation in the Hamiltonian from a calculation without this transformation for $\Omega = 4.8T_K$. (a) Results with naive Floquet matrix truncation, see third column in figure 6.7. (b) Results with matrix extrapolation to mitigate truncation effects as explained in the text, see fourth column in figure 6.7. Near equilibrium, where the ODE solver precision limits the accuracy, this method should not be used (gray area). On the scale shown here with relative deviations of the order 10^{-4}, the result is sensitive to details of the matrix extrapolation such that numerical effects are visible in (b). In general, the deviation from results without unitary transformation is slightly smaller when using the matrix extrapolation to reduce truncation effects.

matrices, we first extrapolate both to a larger size, then compute the matrix product, and finally truncate the matrix product to the original size.[5] This modified matrix product allows us to simulate infinite Floquet matrices, although we use matrices of finite size.

Using this mitigation strategy, we can improve the convergence of the RG flow and limit the truncation effects visible in the matrices at the end of the RG flow. As an example, the fourth column of figure 6.7 shows Floquet matrices after an RG flow with the modified matrix product. It clearly shows significantly less truncation effects than the third column, in which truncation effects were ignored. One can also see in the first two columns of figure 6.7 that the same strategy could be applied to the RG flow with the untransformed Hamiltonian, but that it is not needed there because truncation effects are already negligible.

Interestingly, for harmonic driving and sufficiently large Floquet matrices the observables computed at the end of the RG flow are hardly affected by the strong truncation effects. In figure 6.8 we compare the differential conductance computed with and without the unitary transformation which shifts the time-dependence to the coupling. Independent of whether we simply ignore the truncation effects in figure 6.8(a) or reduce the truncation effects with the previously explained strategy in figure 6.8(b), we find excellent agreement with the results obtained using the untransformed Hamiltonian. Thus, for harmonic driving, we can consider the unitary transformation and matrix truncation strategy to be implementation details with negligible influence on the final results. However, reducing the truncation effects allows us to apply this method also in situations with many relevant Fourier modes in the driving, such as

[5] When implementing this, we use an equivalent but more efficient algorithm to compute this modified matrix product. The implementation can be found in `https://github.com/stiglers-eponym/frtrg`.

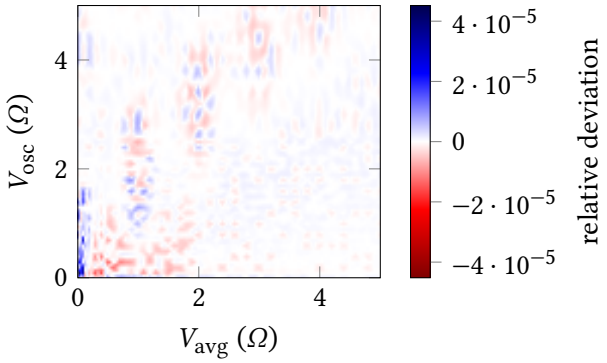

Figure 6.9.: Relative deviation of the differential conductance G calculated with 9 voltage-shifted copies at $E + n\hat{\tilde{\mu}}_{LR}$ in the RG equations from results with 15 such copies for $\Omega = 4.8T_K$. The deviation is so small that other numerical effects, e.g., the finite precision of the ODE solver, become relevant and lead to visible fluctuations. This comparison shows that the truncation of the set of voltage-shifted copies to a finite number has no relevant effect on the results.

the short voltage pulse discussed in section 3.4, which require much larger Floquet matrices.

6.5. Number of energy-shifted replicas

The nonequilibrium RG equations (5.19)–(5.27) couple functions of energy at arguments E and $E + n\hat{\tilde{\mu}}_{LR}$ where $n \in \{-2, -1, \ldots, 2\}$ (see section 5.1.3). In the numerical solution we usually include 9 copies of these functions at energy arguments $E + n\hat{\tilde{\mu}}_{LR}$, $|n| \leq 4$ and approximate, e.g., $\hat{\Gamma}(E + 5\hat{\tilde{\mu}}_{LR}) \approx \hat{\Gamma}(E + 4\hat{\tilde{\mu}}_{LR})$. A comparison to results with 15 such voltage-shifted copies ($|n| \leq 7$) in figure 6.9 shows only negligible differences well below 10^{-4} (relative deviation) except near equilibrium where the ODE solver precision and numerical effects limit the numerical precision. To verify that the finite number of copies does not affect the numerical results, we furthermore checked that different choices of splitting the chemical potential into $\mu_\alpha(t) = \mu_\alpha^j(t) + \mu_\alpha^r(t)$ (see section 5.3.2) also agree with relative deviations of at most 10^{-4}. At resonant voltages $V_{\mathrm{avg}} = n\Omega$ where n is an integer, the unitary transformation makes the voltage-shifted copies unnecessary because we can set $\mu_\alpha^r = 0$, and we find again excellent agreement with the untransformed Hamiltonian (relative deviations well below 10^{-4}). Thus, the finite number of voltage-shifted copies does not limit the precision of the results.

6.6. Symmetries

The FRTRG for the Kondo model presented here does not require large numerical resources. For typical parameters, the RG flow can be solved within seconds or at most a few minutes on a modern laptop. However, this advantage relies on the parametrization of all superoperators by scalars, which leads to the lengthy form of the RG equations (5.19)–(5.27). For many systems, the FRTRG may be applicable, but the matrix elements of the Floquet matrices will be superoperators in Liouville space instead of scalars. This increases the numerical effort significantly and makes an efficient implementation more important. It is therefore helpful to consider the generic symmetries appearing in the Floquet matrix formalism.

A useful general symmetry is based on the Hermiticity of quantum states. To ensure that density operators remain Hermitian, every superoperator should preserve the Hermiticity of the operators on which it acts. A superoperator-valued function of time $\mathcal{S}(t, s)$ is Hermiticity-

	$\mathcal{C}$-symmetry	if $x_L = x_R$	matrix structure for $V(t) = -V(-t)$
$\hat{\Gamma}$	+		even
$\hat{Z}$	+		even
$\hat{\Gamma}^\gamma$	+		odd
$\partial_E \hat{\Gamma}^\gamma$	−		odd
$\delta\hat{\Gamma}$	+		odd
$\delta\hat{\Gamma}^\gamma$	+		even
$\hat{G}^2_{12}$	+	$\hat{G}^2_{LL} = \hat{G}^2_{RR}$	even (only for $\alpha_1 = \alpha_2$)
$\hat{G}^a_{12}$	−	$\hat{G}^a_{12} = (\delta_{1L} - \delta_{2R})\hat{G}^a_{LL}$	odd (only for $\alpha_1 = \alpha_2$)
$\hat{G}^3_{12}$	−	$\hat{G}^3_{LL} = \hat{G}^3_{RR}$	even (only for $\alpha_1 = \alpha_2$)
$\hat{I}^\gamma_{12}$	−	$\hat{I}^\gamma_{LL} = \hat{I}^\gamma_{RR}$	odd (only for $\alpha_1 = \alpha_2$)

Table 6.1.: Symmetries of Floquet matrices appearing in the RG equations. The second column shows the sign in $\hat{X}(-E^*)^*_{-n,-m} = \pm\hat{X}(E)_{n,m}$ or $\hat{X}_{12}(-E^*)^*_{-n,-m} = \pm\hat{X}_{21}(E)_{n,m}$ for vertices, where $\hat{X}$ or $\hat{X}_{12}$ denotes the Floquet matrix. The third column shows identities that simplify the vertices in the case of symmetric coupling, $x_L = x_R$. The last column shows which Floquet matrix elements remain finite for $\mathrm{Re}\, E = 0$ when a voltage of the form $V(t) = -V(-t)$ is included in the coupling by the unitary transformation of the Hamiltonian. Matrix elements X_{nm} remain finite only if $n + m$ is even or odd as indicated in the last column, other matrix elements vanish. In the reservoir matrices ($\hat{G}^2$, $\hat{G}^a$, $\hat{G}^3$, and $\hat{I}^\gamma$) this only applies to diagonal elements in reservoir space, e.g., for $\hat{G}^2_{LL}$.

preserving if

$$\mathcal{C}\mathcal{S}(t,s)\mathcal{C} = \mathcal{S}(t,s) \tag{6.2}$$

where $\mathcal{C}a = a^\dagger$ is the antilinear map of Hermitian conjugation acting on operators. In Floquet space, this relation transforms to [see Eq. (6.1)] [55, 76]

$$\mathcal{C}\hat{\mathcal{S}}(E)_{n,m}\mathcal{C} = \hat{\mathcal{S}}(-E^*)_{-n,-m}. \tag{6.3}$$

In the RG equations, we can use this relation for all Floquet matrices with two important modifications. Firstly, some Floquet matrices include a complex prefactor, which can change the sign in Eq. (6.3). The sign for each matrix is given in table 6.1. Secondly, in the vertices, this symmetry cross-connects reservoir matrix elements $\hat{X}_{12}$ and $\hat{X}_{21}$. Indeed, one can show[6] that $\mathcal{C}\bar{G}_{12}(E)\mathcal{C} = -\bar{G}_{21}(-E^*)$ such that $\bar{G}_{LR}$ is connected to $\bar{G}_{RL}$. This symmetry provides a check for the initial conditions and for the RG flow, which is indeed exactly fulfilled during the whole RG flow.

This $\mathcal{C}$-symmetry is especially helpful when the voltage can be completely included in the coupling by a unitary transformation such that $\mu^r_\alpha = 0$. In this case, we do not need any copies of

[6] From the definition of the coupling vertex [Eq. (4.14)] we remember that it appears in a coupling Liouvillian of the form $2\hat{L}_V = \sum_{pp'} p'\hat{G}^{pp'}_{11'} :K^p_1 K^{p'}_{1'}:$, which maps Hermitian to anti-Hermitian operators. Using this property and $\mathcal{C}K^\pm_{\bar{1}}\mathcal{C} = K^\mp_{\bar{1}}$, we find that the vertex with Keldysh indices fulfills $\mathcal{C}\hat{G}^{p_1p_2}_{12}\mathcal{C} = \hat{G}^{\bar{p}_1\bar{p}_2}_{\bar{1}\bar{2}}$. Summing over the Keldysh indices and fixing $\eta = -\eta' = +$ leads to the relation $\mathcal{C}\bar{G}_{12}\mathcal{C} = -\bar{G}_{21}$. For the effective vertices we need to add energy arguments as in Eq. (6.3). The relations for $\hat{G}^{2,3,a}_{12}$ in table 6.1 are obtained using properties of the superoperator algebra defined in Eqs. (5.6)–(5.7): $\mathcal{C}L^2\mathcal{C} = -(L^2)^\top$, $\mathcal{C}L^3\mathcal{C} = (L^3)^\top$ and $\mathcal{C}L^a\mathcal{C} = L^a = (L^a)^\top$.

the Floquet matrices at energy arguments $E + n\hat{\mu}_{LR}$, such that we can work with Re $E = 0$ during the whole RG flow. Only for Re $E = 0$, the $\mathcal{C}$-symmetry is a symmetry relation of an individual matrix of the form $\hat{X}(E)^*_{-n,-m} = \pm\hat{X}(E)_{n,m}$. Further simplifications can be used for symmetric coupling to the reservoirs, as the third column in table 6.1 shows.

Another symmetry relation can be used if the bias voltage is of the form $V(t) = -V(-t)$. In this highly symmetric case, the driving can again be completely included in the coupling, such that we do not need voltage-shifted replicas at $E + n\hat{\mu}_{LR}$. Furthermore, many Floquet matrix elements must vanish exactly due to the structure of the driving profile. In this special case, most Floquet matrices represent functions $f(t, s)$ in the time domain which fulfill $f(t, t-s) = \pm f(t+\frac{T}{2}, t+\frac{T}{2}-s)$, i.e., they are periodic or anti-periodic with the doubled frequency. Such functions are represented by Floquet matrices $\hat{f}(E)_{nm}$ for which at Re $E = 0$ half of the matrix elements vanish. For periodic functions of doubled frequency $\hat{f}(E)_{nm} = 0$ if $n + m$ is odd, and for anti-periodic functions all matrix elements vanish where $n + m$ is even. The last column in table 6.1 shows which Floquet matrices represent such periodic or anti-periodic functions in the time domain. Only the Floquet matrices coupling left and right reservoir in the vertices do not obey this simpler structure. For large Floquet matrices, this symmetry can be used to reduce the computational costs.

6.7. Summary

In this chapter, we have seen that many parameters can in principle influence the FRTRG results. But only the choice of approximations and the truncation order in the RG equations have a significant influence on the final results. Other aspects like the unitary transformation of the Hamiltonian can be seen as implementation details with negligible effect on the calculated observables. The redundant computation of the current and the differential conductance shows good agreement, and the comparison of RG equations truncated after leading or next-to-leading order in the coupling J indicates that the expansion in J is approximately converged.

We have seen that fast convergence of the current as a function of Λ_0 requires a good choice of the initial condition, as provided in Eq. (5.81). In the RG equations, it is sufficient to approximate the remaining frequency integral as discussed in section 4.3.4, simplifying the numerical implementation. The unitary transformation of the Hamiltonian changes the structure of the Floquet matrices and leads to strong matrix truncation effects, which can be reduced by the strategy described in section 6.4. But the results with and without unitary transformation show excellent agreement. Symmetries can be used to speed up the numerical solution of the RG equations, especially when $V_{\text{avg}} = 0$.

The FRTRG yields relatively accurate self-consistent results for transport through the periodically driven Kondo model with small numerical effort. For larger models the numerical effort grows significantly, but also for slightly larger models like the Anderson model, a numerical solution of the RG equations is possible with modest numerical resources.

7. Summary and Outlook

In this thesis, we studied two problems dealing with open quantum systems in nonequilibrium. One is quite general and more abstract, whereas the other one is concrete, involving intricate detail. Here we summarize the achieved insights and point out some connections.

The fermionic duality relation (chapter 2) is an exact property of fermionic quantum systems with bilinear, energy-independent coupling to noninteracting reservoirs in the wideband limit. We provided a new proof of this relation, which clarifies what prohibits or limits the extension of this duality relation to the calculation of transport observables and to systems with time-dependent driving. We also discussed how symmetries can be used to simplify the description of the dynamics by restricting the set of physically allowed states. Particle number conservation and the fermion superselection principle can pose such restrictions on the allowed states. It is highlighted that the restriction to physically allowed states in the evolution should not be used when calculating transport observables, when considering input states entangled with an ancilla system, or for input states that do not obey the assumed symmetries. We formulated fermionic duality relations for the simplified description of the evolution with symmetry-restricted input states in different formalisms that are commonly used for open quantum systems. The restriction of the input space and a connection of Schrödinger and Heisenberg picture by the fermionic duality relation make it possible to define different measures of divisibility for the dynamics of open systems. Such measures are used to categorize the memory of open quantum systems.

The main part of this thesis addresses the Kondo model driven by a periodic bias voltage, which is experimentally realizable in tunable quantum dots. To describe this system, we extended the RTRG in the E-flow scheme to periodically driven systems by working with a Floquet representation. This method is applicable to small open quantum systems at zero temperature with possibly strong correlations, and allows us to directly calculate observables like the current as a function of time. Through a self-consistent calculation that includes many large classes of cotunneling processes, this approach naturally considers the nontrivial interplay of various effects such as photon-assisted tunneling and dissipation due to external driving. This makes it possible to calculate the differential conductance through the periodically driven Kondo model in excellent quantitative agreement with experiments.

In agreement with experiments, the FRTRG predicts satellite peaks of the Kondo resonance in the differential conductance which are only partially suppressed by dissipation. For an asymmetric coupling to the two reservoirs, we predict that these peaks become sharper while the overall conductance is suppressed by the asymmetry. The comparison with experiments highlights the importance of decoherence leading to a broadening of the satellite peaks for a quantitative description. It furthermore reveals an important pitfall in one possible way of calibrating the oscillating bias voltage V_{osc}. When using an approximately adiabatic regime to calibrate V_{osc} by comparison of measurements to the adiabatic prediction, V_{osc} may be underestimated.

In the second part of the discussion of the Kondo model, we focussed on the time-dependence of the current. We quantitatively showed how the time-resolved current through the Kondo model explicitly reveals strong memory effects both for short voltage pulses and for strong and fast harmonic driving. These memory effects are based on a phase that is accumulated between the two reservoirs due to the bias voltage, which is very similar to a mechanism that also appears in noninteracting models like the resonant level model. But in the Kondo model, these memory effects provide evidence of the strong quantum correlations induced between the two reservoirs by the coupling to a quantum dot in the Kondo regime.

Similar effects as in the Kondo model with periodic bias voltage have been predicted [181] and observed in quantum dots in the Kondo regime coupled to bosonic modes [122, 123, 182]. An oscillating gate voltage applied to the Kondo quantum dot has also been discussed [159, 162]. An extension of the presented calculations to such similar systems poses new challenges, but seems possible. But the FRTRG is not restricted to the Kondo model, although it is especially well suited for this model. It can be applied to bosonic models like the spin-boson model, and to models with a few levels, such as the Anderson model. The ability to treat periodic fields makes it possible to analyze systems connected to superconducting reservoirs with a constant bias voltage that leads to an oscillating superconducting phase. A first attempt of such a description for the Anderson model indicated that a leading order calculation without vertex renormalization is not sufficient, but established that such problems are numerically still tractable. This highlights that when using the FRTRG, it can be challenging to estimate how well it will converge for different models. For the Kondo model, we have checked the convergence of the method in detail by comparing results from different expansion orders in the RG equations and by verifying the convergence of the numerical implementation.

A. Proof of fermionic duality

In this appendix, the full derivation of fermionic duality for systems with explicit time dependence is provided. This includes details which are left out in the motivation in section 2.2.2. The structure of the proof is the same as in section 2.2.2.

We consider a quantum system with Hamiltonian $H_S(t)$ coupled to (effectively) noninteracting reservoirs with Hamiltonian $H_R(t) = \sum_\alpha \int d\omega[\omega + \mu(t)]c^\dagger_{\alpha\omega}c_{\alpha\omega}$ by an energy-independent, bilinear coupling Hamiltonian $H_V(t) = \sum_\alpha \int d\omega\, \tau_{l\alpha}(t)c^\dagger_{\alpha\omega}d_l + \text{H.c.}$ To simplify the notation, we collect quantum numbers of fermions like spin, band index, reservoir, and level on the local system in the indices α for the reservoirs and l for the local system. This hides spin and band indices such that we can work like with spinless fermions. The local Hamiltonian, the tunneling strengths, and the chemical potentials can be time dependent.

Fermionic duality is an expression for the adjoint of the propagator describing the evolution of the local system. We start from the general form of the propagator,

$$\Pi(t,t_0) = \operatorname*{tr}_R\left\{\mathcal{T}_{\leftarrow} e^{-i\int_{t_0}^t ds[H_S(s)+H_R(s)+H_V(s)]}(\bullet\otimes\rho_R^{\text{eq}})\mathcal{T}_{\rightarrow} e^{i\int_{t_0}^t ds[H_S(s)+H_R(s)+H_V(s)]}\right\}. \tag{A.1}$$

Step 1. As in the main text, we use that for a general superoperator of the form $S = A\bullet B$, the adjoint is given by $S^\dagger = A^\dagger \bullet B^\dagger$. For the adjoint of the propagator, this yields

$$\Pi(t,t_0)^\dagger = \operatorname*{tr}_R\left\{(\mathbb{1}\otimes\rho_R^{\text{eq}})\mathcal{T}_{\rightarrow} e^{i\int_{t_0}^t ds[H_S(s)+H_R(s)+H_V(s)]}(\bullet\otimes\mathbb{1})\mathcal{T}_{\leftarrow} e^{-i\int_{t_0}^t ds[H_S(s)+H_R(s)+H_V(s)]}\right\}. \tag{A.2}$$

Step 2. To find a relation between the $\Pi(t)^\dagger$ and $\Pi(t)$, we first do a basis transformation in the reservoirs, which is a unitary transformation that maps states with energy ω to energy $-\omega$. Formally, the transformation $W_R = W_R^\dagger = W_R^{-1}$ is defined such that $W_R c^{(\dagger)}_{\alpha\omega} W_R^\dagger = c^{(\dagger)}_{\alpha-\omega}$. Using $W_R\rho_R^{\text{eq}}W_R^\dagger = \rho_R^{\text{eq}}|_{T\mapsto -T,\mu(t)\mapsto-\mu(t)} =: \bar\rho_R^{\text{eq}}|_{T\mapsto -T}$ and $W_R H_R(t) W_R^\dagger = -H_R(t)|_{\mu(t)\mapsto-\mu(t)} =: -\bar H_R(t)$, we can rewrite Eq. (A.2) in the form

$$\Pi(t,t_0)^\dagger = \operatorname*{tr}_R\left\{(\mathbb{1}\otimes\bar\rho_R^{\text{eq}}|_{T\mapsto -T})\mathcal{T}_{\rightarrow} e^{i\int_{t_0}^t ds[H_S(s)-\bar H_R(s)+H_V(s)]}(\bullet\otimes\mathbb{1})\mathcal{T}_{\leftarrow} e^{-i\int_{t_0}^t ds[H_S(s)-\bar H_R(s)+H_V(s)]}\right\}. \tag{A.3}$$

Step 3. In the next steps, we will use Wick's theorem to prove that

$$\begin{aligned}&\operatorname*{tr}_R\left\{(\mathbb{1}\otimes\rho_R^{\text{eq}}|_{T\mapsto -T})\mathcal{T}_{\rightarrow} e^{i\int_{t_0}^t ds\,[H_S(s)+H_V(s)+H_R(s)]}(\bullet\otimes\mathbb{1})\mathcal{T}_{\leftarrow} e^{-i\int_{t_0}^t ds\,[H_S(s)+H_V(s)+H_R(s)]}\right\}\\ &= \operatorname*{tr}_R\left\{\mathcal{T}_{\rightarrow} e^{i\int_{t_0}^t ds[H_S(s)+H_R(s)+iH_V(s)+i\frac{1}{2}\Gamma(s)]}(\bullet\otimes\rho_R^{\text{eq}})\mathcal{T}_{\leftarrow} e^{-i\int_{t_0}^t ds[H_S(s)+H_R(s)-iH_V(s)-i\frac{1}{2}\Gamma(s)]}\right\},\end{aligned} \tag{A.4}$$

where $\Gamma = 2\pi\sum_{l\alpha}|\tau_{l\alpha}|^2$ is the sum of all coupling rates. This relation can be shown order by order when considering that $\Gamma = O(H_V^2)$. Here the sum over α implicitly includes a sum over the

spin because α is formally a multi-index including reservoir, spin and band index. Let us consider a term in the expansion of Eq. (A.4) where the first time-ordered exponential contributes to order H_V^n in the coupling and the second exponential is of the order H_V^m. For this term, the left-hand side of Eq. (A.4) is of the form

$$\begin{aligned}\operatorname*{tr}_R\Big\{(\mathbb{1}\otimes\rho_R^{\mathrm{eq}}|_{T\mapsto -T})\mathcal{T}_{\rightarrow}\Big[e^{i\int_{t_0}^{t}ds\,[H_S(s)+H_R(s)]}iH_V(t_1)\cdots iH_V(t_n)\Big]\times\\ (\bullet\otimes\mathbb{1})\,\mathcal{T}_{\leftarrow}\Big[e^{-i\int_{t_0}^{t}ds\,[H_S(s)+H_R(s)]}[-iH_V(t'_m)]\cdots[-iH_V(t'_1)]\Big]\Big\},\end{aligned} \tag{A.5}$$

with $t > t_n > \cdots > t_1 > t_0$ and $t > t'_m > \cdots > t'_1 > t_0$. Before we proceed, we introduce a notation with digits as multi-indices, similar to the notation in chapter 4. We define a multi-index $1 = (\alpha_1, \eta_1, \omega_1)$, such that $c_1 = c_{\alpha_1\omega_1}$ if $\eta_1 = -$ and $c_1 = c^{\dagger}_{\alpha_1\omega_1}$ if $\eta = +$. We furthermore define $\tau_{1l} = \tau_{\alpha_1 l}$ if $\eta = +$ and $\tau_{1l} = \tau^*_{\alpha_1 l}$ if $\eta = -$, such that the coupling Hamiltonian is[1] $H_V(t) = \sum_{1l}\tau_{1l}c_1 d_{l\bar{\eta}_1}$. With this notation, we can factorize out the creation and annihilation operators for the reservoirs in Eq. (A.5):

$$\begin{aligned}&\mathcal{T}_{\rightarrow}e^{i\int_{t_0}^{t}[H_S(s)+H_R(s)]}iH_V(t_1)\cdots iH_V(t_n)\\ &=\Big[\mathcal{T}_{\rightarrow}e^{i\int_{t_0}^{t}H_S(s)}\tau_{1l_1}(t_1)d_{l_1\bar{\eta}_1}\cdots\tau_{nl_n}(t_n)d_{l_n\bar{\eta}_n}\Big]e^{i\int_{t_0}^{t}ds\,H_R(s)}e^{-i\eta_1\int_{t_1}^{t}ds[\omega_1+\mu(s)]-i\eta_2\int_{t_2}^{t}ds[\omega_2+\mu(s)]+\ldots}ic_1\cdots ic_n.\end{aligned} \tag{A.6}$$

This shows us that the trace over the reservoirs in Eq. (A.5) can eventually be reduced to

$$\operatorname*{tr}_R\rho_R^{\mathrm{eq}}|_{T\mapsto -T}[ic_1\cdots ic_n][(-ic_{m'})\cdots(-ic_{1'})]. \tag{A.7}$$

From Wick's theorem, we know that this can be written as the sum of all possible pair contractions of the creation and annihilation operators:

$$\langle c_1\cdots c_n\rangle = \sum_P(-1)^P\langle c_{P(1)}c_{P(2)}\rangle\cdots\langle c_{P(n-1)}c_{P(n)}\rangle, \tag{A.8}$$

where $\langle c_1c_2\rangle = \operatorname{tr}_R\rho_R^{\mathrm{eq}}c_1c_2 = \delta_{1\bar{2}}f(\eta_1\omega_1/T_1)$, $f(x) = 1/(1+e^x)$.

Here we look at individual pair contractions which appear in Eq. (A.7) when using Wick's theorem. Using that $c_1c_2 = \delta_{1\bar{2}} - c_2c_1$ and $f(-x) = 1 - f(x)$ we can rewrite these pair contractions as follows:

$$\operatorname*{tr}_R\rho_R^{\mathrm{eq}}|_{T\mapsto -T}ic_1ic_2 = \operatorname*{tr}_R(c_1c_2 - \delta_{1\bar{2}})\rho_R^{\mathrm{eq}}, \tag{A.9}$$

$$\operatorname*{tr}_R\rho_R^{\mathrm{eq}}|_{T\mapsto -T}ic_1(-ic_{2'}) = \operatorname*{tr}_R c_1\rho_R^{\mathrm{eq}}c_{2'}, \tag{A.10}$$

$$\operatorname*{tr}_R\rho_R^{\mathrm{eq}}|_{T\mapsto -T}(-ic_{1'})(-ic_{2'}) = \operatorname*{tr}_R\rho_R^{\mathrm{eq}}(c_{1'}c_{2'} - \delta_{1',\bar{2}'}). \tag{A.11}$$

[1] We define the creation and annihilation operators on different subsystems such that they commute: $[d_l, c_1] = 0$ whereas $\{c_1, c_2\} = \delta_{1\bar{2}} = \delta_{\eta_1\bar{\eta}_2}\delta_{\alpha_1\alpha_2}\delta(\omega_1 - \omega_2)$ with $\bar{\eta} = -\eta$. On the system, we use the notation $d_{l+} = d_l^{\dagger}$ and $d_{l-} = d_l$ analogous to the reservoirs.

With these relations, Eq. (A.7) becomes

$$\operatorname*{tr}_R\{\rho_R^{\mathrm{eq}}|_{T\mapsto -T}[ic_1\cdots ic_n][(-ic_{m'})\cdots(-ic_{1'})]\} = \operatorname*{tr}_R\{\vdots\, c_1\cdots c_n\,\vdots\,\rho_R^{\mathrm{eq}}\,\vdots\, c_{m'}\cdots c_{1'}\,\vdots\}, \tag{A.12}$$

where we defined $\vdots\cdots\vdots$ as adding all possible ways of replacing pairs of operators c_1c_2 by $-\delta_{1\bar{2}}$:

$$\vdots\, c_1c_2\,\vdots = c_1c_2 - \delta_{1\bar{2}}, \tag{A.13}$$

$$\begin{aligned}\vdots\, c_1c_2c_3c_4\,\vdots = {} & c_1c_2c_3c_4 - \delta_{1\bar{2}}c_3c_4 - \delta_{1\bar{3}}c_2c_4 - \delta_{1\bar{4}}c_2c_3 - \delta_{2\bar{3}}c_1c_4 - \delta_{2\bar{4}}c_1c_3 - \delta_{3\bar{4}}c_1c_2 \\ & + \delta_{1\bar{2}}\delta_{3\bar{4}} + \delta_{1\bar{3}}\delta_{2\bar{4}} + \delta_{1\bar{4}}\delta_{2\bar{3}}.\end{aligned} \tag{A.14}$$

In Eq. (A.12), we only modified the Wick contractions, such that we can directly use this result to rewrite Eq. (A.5) in the form

$$\operatorname*{tr}_R \mathcal{T}_{\rightarrow}\Big[e^{i\int_{t_0}^{t} ds\,[H_S(s)+H_R(s)]}\,\vdots\, H_V(t_1)\cdots H_V(t_n)\,\vdots\,\Big](\bullet\otimes\rho_R^{\mathrm{eq}})\mathcal{T}_{\leftarrow}\Big[e^{-i\int_{t_0}^{t} ds\,[H_S(s)+H_R(s)]}\,\vdots\, H_V(t'_m)\cdots H_V(t'_1)\,\vdots\,\Big]. \tag{A.15}$$

Step 4. This result can be simplified further by making use of the wideband limit, i.e., that τ_{1l} is independent of the energy ω_1:

$$\begin{aligned}&\vdots\, H_V(s)e^{i\int_s^t d\tau H_R(\tau)}H_V(t)\,\vdots \\ &= H_V(s)e^{i\int_s^t d\tau H_R(\tau)}H_V(t) + \sum_{1ll'}\int d\omega_1\,\tau_{1l}(s)\tau_{\bar{1}l'}(t)d_{l\bar{\eta}_1}d_{l'\eta_1}e^{-i\eta_1(t-s)\omega_1}e^{-i\eta_1\int_s^t d\tau\,\mu_{\alpha_1}(\tau)}e^{i\int_s^t d\tau H_R(\tau)}\end{aligned} \tag{A.16}$$

$$= H_V(s)e^{i\int_s^t d\tau H_R(\tau)}H_V(t) + \Gamma(t)\delta(t-s). \tag{A.17}$$

Here we explicitly wrote the integral over ω_1, which is usually hidden in the sum over 1. Now we remember that Eq. (A.15) is part of a series expansion in which we sum over n and m and integrate over $t > t_n > \cdots > t_1 > t_0$ and independently over $t > t'_m > \cdots > t'_1 > t_0$. To use Eq. (A.17) in these integrals, we need to split the delta function into $\delta(t-s) = \frac{1}{2}[\delta(t-s-0^+)+\delta(t-s+0^+)]$ such that only half of the delta function lies in the integral.[2] Putting this together, we find that the terms of the form of Eq. (A.15) form just a complicated expansion of the right-hand side of Eq. (A.4). When expanding the right-hand side of Eq. (A.4) in both $\Gamma(t)$ and $H_V(t)$ in the time-ordered integrals, one obtains precisely the terms of the form of Eq. (A.15). This completes the proof of Eq. (A.4), which we can now apply to rewrite the adjoint of the propagator:

$$\Pi(t,t_0)^\dagger = \operatorname*{tr}_R\Big\{\mathcal{T}_{\rightarrow}e^{i\int_{t_0}^{t} ds\,[H_S(s)-\bar{H}_R(s)+iH_V(s)+i\frac{1}{2}\Gamma(s)]}(\bullet\otimes\bar{\rho}_R^{\mathrm{eq}})\mathcal{T}_{\leftarrow}e^{-i\int_{t_0}^{t} ds\,[H_S(s)-\bar{H}_R(s)-iH_V(s)-i\frac{1}{2}\Gamma(s)]}\Big\}. \tag{A.18}$$

[2] This construction is mathematically very sloppy. For a more formal proof, one can include a Lorentzian cutoff function $D(\omega) = D^2/(D^2+\omega^2)$ in the frequency integral to obtain $De^{-D(t-s)}/2$ instead of $\delta(t-s)$ in Eq. (A.17) for $t > s$. In the limit $D\to\infty$, this term becomes $\delta(t-s-0^+)/2$.

Step 5. Now we can rewrite the result of step 4 using the superoperators $\mathcal{P} = (-\mathbb{1})^N \bullet$ and dual Hamiltonians $\bar{H}_V = iH_V$, $\bar{H}_S = -H_S$:

$$\Pi(t,t_0)^\dagger = e^{-\int_{t_0}^t ds\,\Gamma(s)} \times \operatorname*{tr}_R \left\{ (-\mathbb{1})^N \mathcal{T}_{\rightarrow} e^{-i\int_{t_0}^t ds\,[\bar{H}_S(s)+\bar{H}_R(s)+\bar{H}_V(s)]} (-\mathbb{1})^N (\bullet \otimes \bar{\rho}_R^{\mathrm{eq}}) \mathcal{T}_{\leftarrow} e^{i\int_{t_0}^t ds\,[\bar{H}_S(s)+\bar{H}_R(s)+\bar{H}_V(s)]} \right\}. \tag{A.19}$$

This is almost the form of the dual propagator, but the time ordering is still inverted. To obtain the duality relation, the time-ordered integrals must be invariant under reversing the time order:

$$\mathcal{T}_{\rightarrow} e^{-i\int_{t_0}^t ds\,[\bar{H}_S(s)+\bar{H}_R(s)+\bar{H}_V(s)]} \overset{!}{=} \mathcal{T}_{\leftarrow} e^{-i\int_{t_0}^t ds\,[\bar{H}_S(s)+\bar{H}_R(s)+\bar{H}_V(s)]}. \tag{A.20}$$

This relation is fulfilled if the explicitly time-dependent total Hamiltonian fulfills $H^{\mathrm{tot}}(t-s) = H^{\mathrm{tot}}(t_0+s)$ for all $s \in [0, t-t_0]$, or if the total Hamiltonian commutes with itself at all different times: $[H^{\mathrm{tot}}(s), H^{\mathrm{tot}}(s')] = 0$ for all $s, s' \in [t_0, t]$. Only if Eq. (A.20) is fulfilled, we can use the following duality relation:

$$\Pi(t,t_0)^\dagger = e^{-\int_{t_0}^t ds\,\Gamma(s)} \mathcal{P}\bar{\Pi}(t,t_0)\mathcal{P}. \tag{A.21}$$

For systems with time-dependent driving, the condition (A.20) for reversing time order is, in general, not fulfilled. One has to be especially careful when trying to apply fermionic duality for such systems. For periodically driven systems that fulfill $H^{\mathrm{tot}}(-t) = H^{\mathrm{tot}}(t)$, the condition (A.20) may be fulfilled only for special choices of t_0 and t. But also such very limited forms of fermionic duality might be helpful when computing, e.g., the stroboscopic dynamics with $t_0 = 0$ and $t = 2\pi n/\Omega$ where n is an integer and Ω is the driving frequency.

B. Resonant level model

In this appendix, the time evolution of the noninteracting resonant level model with multiple reservoirs is derived using the renormalized perturbation theory introduced in section 2.5. Alternative approaches to this model with periodic driving can be found in Refs. [167, 183]. The results of this calculation are used in figure 3.9(c).

Superfermions. We define fermionic superoperators as in Ref. [103, 104]:

$$G^q_\eta = \frac{1}{\sqrt{2}}\left[d_\eta \bullet + q(-\mathbb{1})^N \bullet (-\mathbb{1})^N d_\eta\right], \qquad J^q_{\eta\alpha} = \frac{1}{\sqrt{2}}\left[c_{\eta\alpha\omega} \bullet + q(-\mathbb{1})^{N_R} \bullet (-\mathbb{1})^{N_R} c_{\eta\alpha\omega}\right]. \tag{B.1}$$

Here the index α labels the reservoir, but we also treat separate bands and spin polarizations ($\uparrow$ or $\downarrow$) as separate reservoirs. This allows us to consider only spinless fermions in the following calculation. We define fermionic field operators such that operators of the system commute with those of the reservoirs, $[d_\eta, c_{\eta\alpha\omega}] = 0$. Some properties of these operators are (see appendix A of Ref. [93]):

$$\{G^q_\eta, G^{q'}_{\eta'}\} = \delta_{\eta\bar{\eta}'}\delta_{q\bar{q}'}, \qquad (\mathbb{1}|\, G^+_\eta = 0, \qquad G^-_\eta\,|\mathbb{1}) = 0. \tag{B.2}$$

Bare Liouvillian. For the bare Liouvillian, we use the relation

$$\sum_q G^q_- G^{\bar{q}}_+ = \mathbb{I} + \frac{1}{2}\left[(-\mathbb{1})^N, \bullet\right] = \mathbb{I} - [N, \bullet]. \tag{B.3}$$

Assuming that the state of the total system commutes with the fermion parity operator as required by the superselection principle, $[(-\mathbb{1})^{N_{\text{tot}}}, \bullet] = 0$, we can write the different components of the bare Liouvillian using fermionic superoperators in the following form:

$$L_S = \varepsilon[d^\dagger d, \bullet] = \varepsilon \sum_\eta \eta G^+_\eta G^-_{\bar{\eta}} = \varepsilon\Big(\mathbb{I} - \sum_q G^q_- G^{\bar{q}}_+\Big) = \varepsilon\Big(\sum_q G^q_+ G^{\bar{q}}_- - \mathbb{I}\Big) \tag{B.4}$$

$$L^\alpha_R = \int d\omega\,(\omega + \mu_\alpha)[c^\dagger_{\alpha\omega} c_{\alpha\omega}, \bullet] \tag{B.5}$$

$$= \int d\omega\,(\omega + \mu_\alpha) \sum_\eta J^+_{\eta\alpha\omega} J^-_{\bar{\eta}\alpha\omega} = \int d\omega\,(\omega + \mu_\alpha)\Big(\sum_q J^q_{+\alpha\omega} J^{\bar{q}}_{-\alpha\omega} - \mathbb{I}\Big) \tag{B.6}$$

$$L_V = \sum_{\eta\alpha} \tau^\eta_\alpha \left[c_{\bar{\eta}\alpha\omega} d_\eta, \bullet\right] = \sum_{\alpha\pm} L^{\pm\alpha}_V \quad \text{assuming } \left[(-\mathbb{1})^{N_{\text{tot}}}, \bullet\right] = 0 \tag{B.7}$$

$$L^{\pm\alpha}_V = \int d\omega \sum_\eta \tau^\eta_\alpha G^\pm_\eta J^\mp_{\bar{\eta}\alpha\omega} \tag{B.8}$$

Here we define the notation $\tau^+ \equiv \tau^{-*}$ for the coupling. See also appendix D of Ref. [93].

Bare current superoperator. In analogy to the bare Liouvillian, we can express the bare current superoperator using fermionic superoperators:

$$\Sigma_0^\alpha = \frac{1}{2}\{i[N^\alpha, H_V^\alpha], \bullet\} = \sum_\pm \Sigma_0^{\pm\alpha}, \qquad \Sigma_0^{\pm\alpha} = \frac{i}{2}\sum_\eta \int d\omega\, \eta \tau_\alpha^\eta G_\eta^\pm J_{\bar\eta\alpha}^\pm. \tag{B.9}$$

The component $\Sigma_0^{+\alpha}$ can be ignored because we eventually take the trace to compute the current and $(\mathbb{1}|\Sigma_0^\alpha = (\mathbb{1}|\Sigma_0^{-\alpha}$. Here, we define the current kernel with the sign convention that the current is $I^\alpha(t) = (\mathbb{1}|[\Sigma^\alpha * \rho](t)$, which differs from the convention used in chapters 1 and 4–6.

Contractions in the time domain. For this calculation, it is convenient to work in the time domain. We use Wick's theorem in frequency space with the contractions (see appendix A.2 of Ref. [93])

$$(\mathbb{1}_R|\, J^-_{\eta\alpha\omega} J^-_{\eta'\alpha'\omega'}\, |\rho_R) = -\delta(\omega-\omega')\delta_{\alpha\alpha'}\delta_{\eta\bar\eta'}\, \eta \tanh\left(\frac{\omega-\mu_\alpha}{2T}\right), \tag{B.10}$$

$$(\mathbb{1}_R|\, J^-_{\eta\alpha\omega} J^+_{\eta'\alpha'\omega'}\, |\rho_R) = \delta(\omega-\omega')\delta_{\alpha\alpha'}\delta_{\eta\bar\eta'}. \tag{B.11}$$

For contractions in the time domain, we define

$$\left\langle J^q_{\eta\alpha}(t) J^{q'}_{\eta'\alpha'}(s)\right\rangle \coloneqq \iint d\omega\, d\omega'\ (\mathbb{1}_R|\, J^q_{\eta\alpha\omega} e^{-i\int_s^t d\tau L_R(\tau)} J^{q'}_{\eta'\alpha'\omega'}\, |\rho_R) \tag{B.12}$$

$$= \delta_{q-} \iint d\omega\, d\omega'\, e^{i\eta[(t-s)\omega + A_\alpha(t) - A_\alpha(s)]}\, (\mathbb{1}_R|\, J^-_{\eta\alpha\omega} J^{q'}_{\eta'\alpha'\omega'}\, |\rho_R) \tag{B.13}$$

$$= e^{i\eta[A_\alpha(t)-A_\alpha(s)]}\delta_{q-}\delta_{\eta\bar\eta'}\delta_{\alpha\alpha'} \begin{cases} 2\pi\delta(t-s) & \text{if } q' = + \\ -i\dfrac{2\pi T_\alpha}{\sinh(\pi T_\alpha(t-s))} & \text{if } q' = -, \end{cases} \tag{B.14}$$

where $A_\alpha(t) \coloneqq \int_0^t ds\, \mu_\alpha(s)$.

Infinite temperature kernel. Defining $\Gamma_\alpha = 2\pi|\tau_\alpha|^2$ and $\Gamma = \sum_\alpha \Gamma$, we can calculate the infinite temperature coupling kernel (see appendix D of Ref. [93]):

$$\Sigma_\infty = \sum_{\alpha\alpha'\eta\eta'} \int_0^{0^+} dt\, \tau_\alpha^\eta \tau_{\alpha'}^{\eta'} G_\eta^+ e^{-iL_S t} G_{\eta'}^- \left\langle J^-_{\bar\eta\alpha}(t) J^+_{\bar\eta'\alpha'}(0)\right\rangle = -\frac{1}{2}\Gamma \sum_\eta G_\eta^+ G_{\bar\eta}^-. \tag{B.15}$$

Infinite temperature current kernel. Analogously, we obtain the infinite temperature current kernel:

$$\Sigma_\infty^{-\alpha} = \sum_{\alpha'\eta\eta'} \int_0^{0^+} dt\, \frac{1}{2}\eta \tau_\alpha^\eta \tau_{\alpha'}^{\eta'} G_\eta^- G_{\eta'}^- \left\langle J^-_{\bar\eta\alpha}(t) J^+_{\bar\eta'\alpha'}(0)\right\rangle \tag{B.16}$$

$$= \frac{1}{4}\Gamma_\alpha \eta G_\eta^- G_{\bar\eta}^- = \frac{1}{2}\Gamma_\alpha G_+^- G_-^- \tag{B.17}$$

Full effective Liouvillian. From here on, we measure the chemical potentials relative to the level ε, setting $\varepsilon = 0$ in the calculation. This also sets the bare Liouvillian of the local system to $L_S = 0$. The full effective Liouvillian or coupling kernel is

$$\Sigma(t,s) = \delta(t-s-0^+)\Sigma_\infty(t) - \tau_\alpha^\eta \tau_{\alpha'}^{\eta'} G_\eta^+ e^{\int_s^t d\tau[-iL_S(\tau)-iL_\infty(\tau)+\Sigma_\infty(\tau)]} G_{\eta'}^+ \left\langle J_{\bar\eta\alpha}^-(t) J_{\bar\eta'\alpha'}^-(s)\right\rangle \tag{B.18}$$

$$= \delta(t-s-0^+)\Sigma_\infty(t) + i\frac{\Gamma_\alpha T_\alpha e^{-i\eta[A_\alpha(t)-A_\alpha(s)]}}{\sinh(\pi T_\alpha(t-s))} G_\eta^+ e^{-\frac{1}{2}\Gamma(t-s)\sum_{\eta''} G_{\eta''}^+ G_{\bar\eta''}^-} G_{\bar\eta}^+ \tag{B.19}$$

$$= -\delta(t-s-0^+)\frac{1}{2}\Gamma G_\eta^+ G_{\bar\eta}^- + i\frac{\Gamma_\alpha T_\alpha e^{-i\eta[A_\alpha(t)-A_\alpha(s)]}}{\sinh(\pi T_\alpha(t-s))} e^{-\frac{1}{2}\Gamma(t-s)} G_\eta^+ G_{\bar\eta}^+ \tag{B.20}$$

$$= -\delta(t-s-0^+)\frac{1}{2}\Gamma G_\eta^+ G_{\bar\eta}^- + \frac{2\Gamma_\alpha T_\alpha e^{-\frac{1}{2}\Gamma(t-s)}}{\sinh[\pi T_\alpha(t-s)]} \sin[A_\alpha(t)-A_\alpha(s)] G_+^+ G_-^+. \tag{B.21}$$

Full current kernel. Analogously, we compute the full current kernel:

$$\Sigma^{-\alpha}(t,s) = \delta(t-s-0^+)\Sigma_\infty^{-\alpha}(t) + \frac{1}{2}\eta\tau_\alpha^\eta \tau_{\alpha'}^{\eta'} G_\eta^- e^{\int_s^t d\tau[-iL(\tau)-iL_\infty(\tau)+\Sigma_\infty(\tau)]} G_{\eta'}^+ \left\langle J_{\bar\eta\alpha}^-(t) J_{\bar\eta'\alpha'}^-(s)\right\rangle \tag{B.22}$$

$$= \delta(t-s-0^+)\Sigma_\infty(t) - i\eta\frac{\Gamma_\alpha T_\alpha e^{-i\eta[A_\alpha(t)-A_\alpha(s)]}}{2\sinh(\pi T_\alpha(t-s))} G_\eta^- e^{-\frac{1}{2}\Gamma(t-s)\sum_{\eta''} G_{\eta''}^+ G_{\bar\eta''}^-} G_{\bar\eta}^+ \tag{B.23}$$

$$= \delta(t-s-0^+)\Sigma_\infty(t) - i\eta\frac{\Gamma_\alpha T_\alpha e^{-i\eta[A_\alpha(t)-A_\alpha(s)]}}{2\sinh(\pi T_\alpha(t-s))} G_\eta^- e^{-\frac{1}{2}\Gamma(t-s)(G_\eta^+ G_{\bar\eta}^- + 1)} G_{\bar\eta}^+ \tag{B.24}$$

$$= \delta(t-s-0^+)\Sigma_\infty(t) - i\eta\frac{\Gamma_\alpha T_\alpha e^{-i\eta[A_\alpha(t)-A_\alpha(s)]}}{2\sinh(\pi T_\alpha(t-s))} e^{-\frac{1}{2}\Gamma(t-s)} e^{-\frac{1}{2}\Gamma(t-s)G_\eta^+ G_{\bar\eta}^-} G_\eta^- G_{\bar\eta}^+ \tag{B.25}$$

Taking the trace, we obtain

$$(\mathbb{1}|\,\Sigma^{-\alpha}(t,s) = \delta(t-s-0^+)\frac{1}{2}\Gamma_\alpha\,(\mathbb{1}|\,G_+^- G_-^- - i\frac{\Gamma_\alpha T_\alpha e^{-i\eta[A_\alpha(t)-A_\alpha(s)]}}{2\sinh(\pi T_\alpha(t-s))}\eta e^{-\frac{1}{2}\Gamma(t-s)}\,(\mathbb{1}| \tag{B.26}$$

$$= -\delta(t-s-0^+)\frac{1}{2}\Gamma_\alpha\left((-\mathbb{1})^N\right| - \frac{\Gamma_\alpha T_\alpha e^{-\frac{1}{2}\Gamma(t-s)}}{\sinh[\pi T_\alpha(t-s)]}\sin[A_\alpha(t)-A_\alpha(s)]\,(\mathbb{1}|\,. \tag{B.27}$$

Time evolution. We define $\tilde\Sigma(t,s) = \Sigma(t,s) - \Sigma_\infty(t,s)$ and use $((-\mathbb{1})^N|\Sigma_\infty = -\Gamma((-\mathbb{1})^N|$. By $A * B$, we denote a convolution of functions of two time arguments. We can expand the evolution using a Dyson equation:

$$(\mathbb{1}|\,\Pi(t,t_0) = (\mathbb{1}| \tag{B.28}$$

$$\left((-\mathbb{1})^N\right|\Pi(t,t_0) = \left((-\mathbb{1})^N\right|\Pi_\infty(t-t_0) - i\left((-\mathbb{1})^N\right|(\Pi_\infty * \tilde\Sigma * \Pi)(t,t_0) \tag{B.29}$$

$$= e^{-\Gamma(t-t_0)}\left((-\mathbb{1})^N\right| - i\iint_{t>t_2>t_1>t_0} dt_1\,dt_2\, e^{-\Gamma(t-t_2)}\left((-\mathbb{1})^N\right|\tilde\Sigma(t_2,t_1)\Pi(t_1,t_0) \tag{B.30}$$

$$= e^{-\Gamma(t-t_0)}\left((-\mathbb{1})^N\right| + \sum_\alpha \iint_{t>t_2>t_1>t_0} dt_1\,dt_2\,\frac{2\Gamma_\alpha T_\alpha e^{-\frac{1}{2}\Gamma(2t-t_1-t_2)}}{\sinh[\pi T_\alpha(t_2-t_1)]}\sin[A_\alpha(t_2)-A_\alpha(t_1)]\,(\mathbb{1}| \tag{B.31}$$

Current. The full current in reservoir α for a given initial state ρ_0 at time t_0 can be computed from $I(t) = \big(I^\alpha(t,t_0)\big|\rho(t_0)\big)$ with the left supervector

$$(I^\alpha(t,t_0)| = (\mathbb{1}|\,(\Sigma^{-\alpha} * \Pi)(t,t_0) \tag{B.32}$$

$$= -\int_{t_0}^{t} ds\, \frac{\Gamma_\alpha T_\alpha e^{-\frac{1}{2}\Gamma(t-s)}}{\sinh[\pi T_\alpha(t-s)]}\, \sin[A_\alpha(t)-A_\alpha(s)]\,(\mathbb{1}| - \frac{1}{2}\Gamma_\alpha\big((-\mathbb{1})^N\big|\,\Pi(t,t_0) \tag{B.33}$$

$$\begin{aligned} = &-\int_{t_0}^{t} ds\, \frac{\Gamma_\alpha T_\alpha e^{-\frac{1}{2}\Gamma(t-s)}}{\sinh[\pi T_\alpha(t-s)]}\, \sin[A_\alpha(t)-A_\alpha(s)]\,(\mathbb{1}| \\ &- \Gamma_\alpha \sum_{\alpha'} \iint_{t>t_2>t_1>t_0} dt_1\, dt_2\, \frac{\Gamma_{\alpha'} T_{\alpha'} e^{-\frac{1}{2}\Gamma(2t-t_1-t_2)}}{\sinh[\pi T_{\alpha'}(t_2-t_1)]}\, \sin[A_{\alpha'}(t_2)-A_{\alpha'}(t_1)]\,(\mathbb{1}| \\ &- \frac{1}{2}\Gamma_\alpha e^{-\Gamma(t-t_0)}\,\big((-\mathbb{1})^N\big|\,. \end{aligned} \tag{B.34}$$

Defining a function

$$\xi_\alpha(t,s) = -\frac{\Gamma_\alpha T_\alpha e^{-\frac{1}{2}\Gamma(t-s)}}{\sinh[\pi T_\alpha(t-s)]}\, \sin[A_\alpha(t)-A_\alpha(s)], \tag{B.35}$$

we can write the current in reservoir α in the general form

$$I(t,t_0) = \int_{t_0}^{t} ds\, \xi_\alpha(t,s) + \Gamma_\alpha \sum_{\alpha'} \iint_{t>t_2>t_1>t_0} dt_1\, dt_2\, e^{-\Gamma(t-t_2)}\xi_{\alpha'}(t_2,t_1) - \frac{1}{2}\Gamma_\alpha e^{-\Gamma(t-t_0)}\,\mathrm{tr}\left[(-\mathbb{1})^N\rho_0\right]. \tag{B.36}$$

For the case of harmonic driving with $A_\alpha(t) = \frac{V^\alpha_{\mathrm{osc}}}{\Omega}\sin(\Omega t)$ at zero temperature in the limit $t_0 \to -\infty$, the integrals can be expressed as sums,

$$\int_{-\infty}^{t} ds\, \xi(t,s) = \frac{\Gamma_\alpha}{\pi}\,\mathrm{Im}\left\{e^{i\frac{V^\alpha_{\mathrm{osc}}}{\Omega}\sin(\Omega t)} \sum_{n=-\infty}^{\infty} \mathcal{J}_n\left(\frac{V^\alpha_{\mathrm{osc}}}{\Omega}\right) e^{-in\Omega t}\log\left(\frac{\Gamma}{2}-in\Omega\right)\right\}, \tag{B.37}$$

$$\int_{-\infty}^{t} dt_2 \int_{-\infty}^{t_2} dt_1\, e^{-\Gamma(t-t_2)}\xi_{\alpha'}(t_2,t_1) = -\frac{\Gamma_{\alpha'}}{\pi}\sum_m \mathcal{J}_m\left(\frac{V^{\alpha'}_{\mathrm{osc}}}{\Omega}\right)\mathrm{Im}\left\{\log\left(\frac{\Gamma}{2}-im\Omega\right)\sum_n \frac{\mathcal{J}_n\left(\frac{V^{\alpha'}_{\mathrm{osc}}}{\Omega}\right)e^{i(n-m)\Omega t}}{\Gamma+i(n-m)\Omega}\right\}, \tag{B.38}$$

which can be computed numerically. Here $\mathcal{J}_n$ denotes again the n^{th} Bessel function.

C. Auxiliary calculations for operator sum forms

In this appendix, general relations for operator sum forms are derived, which are used in chapter 2. These calculations are based on the Choi operator.

C.1. Choi operator

We consider a superoperator $\mathcal{S}$, which acts on operators of dimension $d \times d$. The Choi operator is defined by extending the Liouville space on which $\mathcal{S}$ acts by a reference system with identical Liouville space. We choose a basis $\{|k\rangle\}_{1 \leq k \leq d}$ in both systems and define $|\mathbb{1}\rangle = \sum_k |k\rangle \otimes |k\rangle$ as the non-normalized maximally entangled state. The Choi operator is defined by [184, 185]

$$\operatorname{choi} \mathcal{S} \coloneqq (\mathcal{S} \otimes \mathbb{I})(|\mathbb{1}\rangle \langle \mathbb{1}|), \tag{C.1}$$

where $\mathbb{I}$ denotes the identity superoperator. Thus, choi $\mathcal{S}$ is an operator on the extended system consisting of physical system and reference. The map between superoperator and Choi operator is an isomorphism.

The Choi operator has multiple important properties [184, 185], of which we will need the following two. Firstly, the superoperator $\mathcal{S}$ preserves the Hermiticity of all possible states if and only if choi $\mathcal{S}$ is Hermitian. Secondly, choi $\mathcal{S}$ is positive semidefinite if and only if $\mathcal{S} \otimes \mathbb{I}$ preserves the positivity — more precisely: positive-semidefiniteness — of the states on which it acts. This property is called complete positivity and implies Hermiticity preservation. The propagator $\Pi(t)$ should always be CP because in every physical system the positivity of states must be preserved independent of possible reference systems. This property is briefly discussed in sections 2.3.1 and 2.3.4.

C.2. Kraus operator sum form

The propagator $\Pi(t)$ is CP and its Choi operator can therefore be diagonalized with positive eigenvalues:

$$\operatorname{choi} \Pi(t) = \sum_i \lambda_i(t) \, |K_i(t)\rangle\langle K_i(t)| \tag{C.2}$$

with the normalization $\langle K_i(t)|K_j(t)\rangle = \delta_{ij}$. From the definition of the Choi operator, it follows that $\operatorname{choi}(A \bullet B^\dagger) = |A\rangle\langle B|$ when we define $|A\rangle = A \otimes \mathbb{1}|\mathbb{1}\rangle = \sum_{kk'} A_{kk'}|kk'\rangle$ for arbitrary operators A and B of dimension $d \times d$. Here we used matrix elements of A and B in the previously chosen basis

$\{|k\rangle\}_k$. Since the map between superoperator and Choi operator is linear and an isomorphism, Eq. (C.2) implies that we can write $\Pi(t)$ in the form

$$\Pi(t) = \sum_i \lambda_i(t) K_i(t) \bullet K_i(t)^\dagger. \tag{C.3}$$

Using the Choi operator, one can furthermore show that also the subspace propagators and transitions $\Pi_{nm}(t)$ are CP. If choi $\Pi(t)$ is positive, then

$$\operatorname{choi} \Pi_{nm}(t) = \operatorname{choi}[\mathbb{P}_n \Pi(t) \mathbb{P}_m] = (P_n \otimes P_m^\top) \operatorname{choi}[\Pi(t)](P_n \otimes P_m^\top) \tag{C.4}$$

is positive as well. Here, $P_m^\top$ denotes the transpose of P_m with respect to the chosen basis $\{|k\rangle\}_k$. In the spectral decomposition of choi $\Pi_{nm}(t)$ we can now use the duality relation for $\Pi_{nm}(t)$,

$$\operatorname{choi}\left[\Pi_{nm}(t)^\dagger\right] = \sum_i \lambda_i \left|K_i^{nm}(t)^\dagger\right\rangle\!\left\langle K_i^{nm}(t)^\dagger\right| = e^{-\Gamma t}(-1)^{n+m} \sum_j \bar{\lambda}_j \left|\bar{K}_j^{mn}(t)\right\rangle\!\left\langle \bar{K}_j^{mn}(t)\right|, \tag{C.5}$$

proving Eq. (2.31). A more detailed proof — without the projection to subspaces — can be found in Refs. [2, 93].

C.3. GKSL form

In Eq. (2.39) it was stated that the generator can be decomposed into contributions from jumps from subspace m to subspace n which can be written in the form

$$-i\mathcal{G}^{nm} = -i\delta_{nm}[H_n', \bullet] + \sum_{i=1}^{d_n d_m - \delta_{nm}} j_i^{nm} \left(J_i^{nm} \bullet J_i^{nm\dagger} - \frac{1}{2}\left\{ J_i^{nm\dagger} J_i^{nm}, \bullet \right\}\right). \tag{C.6}$$

Here we derive this form following Ref. [186]. In this section, we will not write the time arguments to simplify the notation.

We start from the Choi operator

$$C_m \coloneqq \operatorname{choi}[-i\mathcal{G}\mathbb{P}_m] = (\mathbb{1} \otimes P_m^\top) \operatorname{choi}[-i\mathcal{G}](\mathbb{1} \otimes P_m^\top). \tag{C.7}$$

To split up C_m, we define projectors $\bar{Q}_m = |P_m\rangle\langle P_m|/d_m$ and $Q_m = \mathbb{1} \otimes P_m^\top - \bar{Q}_m$. Similar to the maximally entangled state, we use $|P_m\rangle = P_m \otimes \mathbb{1}|\mathbb{1}\rangle = \mathbb{1} \otimes P_m^\top|\mathbb{1}\rangle$. Using these projectors, we can write

$$C_m = Q_m \operatorname{choi}[-i\mathcal{G}] Q_m + |B_m\rangle\langle P_m| + |P_m\rangle\langle B_m| \tag{C.8}$$

with the definition

$$|B_m\rangle \coloneqq \frac{1}{d_m}\left(\mathbb{1} \otimes P_m^\top - \frac{1}{2d_m}|P_m\rangle\langle P_m|\right) \operatorname{choi}[-i\mathcal{G}]\,|P_m\rangle\,. \tag{C.9}$$

One can show[1] that this vector fulfills $(P_m \otimes P_m^\top)|B_m\rangle = |B_m\rangle$ and thereby $P_m B_m P_m = B_m$. Now we use that

$$|B_m\rangle\langle P_m| + |P_m\rangle\langle B_m| = \operatorname{choi}\left(B_m \bullet P_m + P_m \bullet B_m^\dagger\right) = \operatorname{choi}\left([-iH_m', P_m \bullet P_m] + \{A_m, P_m \bullet P_m\}\right) \tag{C.10}$$

[1] To show that $(P_m \otimes \mathbb{1})|B_m\rangle = |B_m\rangle$, we use that $(\mathbb{1} \otimes P_m^\top)\operatorname{choi}[-i\mathcal{G}]|P_m\rangle = -i(\mathcal{G} \otimes \mathbb{1})[|P_m\rangle\langle P_m|]|P_m\rangle = -i\sum_{kk'}[\mathcal{G}(P_m|k\rangle\langle k'|P_m)](P_m|k'\rangle) \otimes (P_m^\top|k\rangle)$ and that $\mathcal{G}(P_m \bullet P_m)$ will always yield a block-diagonal state, which commutes with P_m independent of the operator argument $\bullet$.

with the Hermitian operators $H'_m = \frac{i}{2}(B_m - B_m^\dagger)$ and $A_m = \frac{1}{2}(B_m + B_m^\dagger)$. The operator A_m only makes sure that eventually the superoperator $\mathcal{G}\mathbb{P}_m$ is trace-destroying.

To distinguish the subspaces into which the system jumps, we define the projectors $Q_{nm} = (P_n \otimes \mathbb{1})Q_m = P_n \otimes P_m^\top - \delta_{nm}\bar{Q}_m$. Since $\mathcal{G}$ preserves the block-diagonal structure of the input states, we can distinguish jumps between different subsystems:

$$Q_m \operatorname{choi}[-i\mathcal{G}]Q_m = \sum_n Q_{nm} \operatorname{choi}[-i\mathcal{G}]Q_{nm}. \tag{C.11}$$

The individual terms in this sum can be diagonalized:

$$Q_{nm} \operatorname{choi}[-i\mathcal{G}]Q_{nm} = \sum_{i=1}^{d_n d_m - \delta_{nm}} j_i^{nm} \left|J_i^{nm}\right\rangle\!\left\langle J_i^{nm}\right|. \tag{C.12}$$

Here, the number of terms is given by $\operatorname{rank} Q_{nm} = d_n d_m - \delta_{nm}$. Using again the isomorphism between superoperators and Choi operators, we find the following expression:

$$-i\mathcal{G}\mathbb{P}_m = -i[H'_m, P_m \bullet P_m] + \{A_m, \bullet\} + \sum_{ni} j_i^{nm} J_i^{nm} \bullet J_i^{nm\dagger}. \tag{C.13}$$

The operator A_m can be determined from the fact that $\mathcal{G}$ must be trace-destroying: $A_m = \frac{1}{2}\sum_{in} j_i^{nm} J_i^{nm\dagger} J_i^{nm}$. This yields the final form

$$-i\mathcal{G}\mathbb{P}_m = -i[H'_m, P_m \bullet P_m] + \sum_{ni} j_i^{nm}\left(J_i^{nm} \bullet J_i^{nm\dagger} - \frac{1}{2}\{J_i^{nm\dagger} J_i^{nm}, \bullet\}\right). \tag{C.14}$$

This still differs from the form claimed in the main text by the projectors P_m in the commutator. But since $P_m H'_m P_m = H'_m$, these projectors can be removed for input states which commute with P_m, which is the general restriction on the input states which we assume.

The result in Eq. (C.14) contains the jump operators for a reduced generator $\mathcal{G}^{\text{red}} = \mathcal{G}\sum_n \mathbb{P}_n$. These jump operators only act on one subspace, such that jump operators for different subspaces can in principle be calculated independent of each other. Furthermore, the number of jump operators is reduced by the number of subspaces minus one, comparing to the jump operators of the full generator. Thus, the GKSL form derived here is, in general, simpler than the GKSL form for the full generator, in which jump operators can act on multiple subspaces.

The duality relation for the jump operators now follows from the previous derivation and the duality relation for the generator $\mathcal{G}$. We recall that the duality relation for the generator is $\mathcal{G}^H(t) = -\mathcal{P}\bar{\mathcal{G}}(t)\mathcal{P} + i\Gamma\mathbb{I}$. We can use this relation in the projection of the Choi operator that leads to the jump operators:

$$Q_{nm} \operatorname{choi}[i\mathcal{G}^H]Q_{nm} = Q_{nm} \operatorname{choi}[-i\mathcal{P}\bar{\mathcal{G}}\mathcal{P}]Q_{nm}. \tag{C.15}$$

Here we have used that $Q_{nm}|\mathbb{1}\rangle = 0$, which implies that $Q_{nm} \operatorname{choi}[\mathbb{I}]Q_{nm} = 0$. Diagonalizing both sides of Eq. (C.15) yields the duality relation for jump operators and rates:

$$J_i^{Hnm}(t) = \bar{J}_i^{mn}, \qquad j_i^{Hnm}(t) = (-1)^{n+m}\bar{j}_i^{mn}. \tag{C.16}$$

Now we completely express the generators in their GKSL form in the duality relation for generators to obtain

$$\begin{aligned}&[{H'_m}^H, \bullet] + \sum_{ni} j_i^{Hnm}\left(J_i^{Hnm} \bullet J_i^{Hnm\dagger} - \frac{1}{2}\{J_i^{Hnm} J_i^{Hnm\dagger}, \bullet\}\right)\\ &= -[\bar{H}'_m, \bullet] - i(-1)^m \sum_{ni} \bar{j}_i^{nm}\left((-1)^n \bar{J}_i^{nm} \bullet \bar{J}_i^{nm\dagger} - \frac{1}{2}\{\bar{J}_i^{nm\dagger} \bar{J}_i^{nm}, \bullet\}\right) + i\Gamma\mathbb{P}_m. \end{aligned} \tag{C.17}$$

After cancelling the jump terms which we already know are equal, there is only one commutator and one anticommutator remaining. Thus, we can compare the commutators and find the relation ${H'_m}^H = -{\bar{H}'_m}^H$. The remaining anticommutator is equal by a sum rule that follows from the generic eigenvector $|(-\mathbb{1})^N)$ of the generator with eigenvalue $-i\Gamma$, which is itself a consequence of fermionic duality.

D. Schrieffer-Wolff transformation from Anderson to Kondo model

In this appendix, the Schrieffer-Wolff transformation from the Anderson model to the Kondo model is derived for the general time-dependent case, following Ref. [159]. We start from the Anderson Hamiltonian, where different quantities may be time-dependent:

$$H = H_0 + H_v, \tag{D.1}$$

$$H_0 = \sum_{\alpha\sigma} \int d\omega\, [\omega + \mu_\alpha(t)] c^\dagger_{\omega\sigma\alpha} c_{\omega\sigma\alpha} + \varepsilon(t) \sum_\sigma d^\dagger_\sigma d_\sigma + U d^\dagger_\uparrow d_\uparrow d^\dagger_\downarrow d_\downarrow, \tag{D.2}$$

$$H_v = + \sum_{\alpha\sigma} \int d\omega \left[\tilde{v}_\alpha(t) c^\dagger_{\omega\sigma\alpha} d_\sigma + \text{H.c.} \right]. \tag{D.3}$$

Deviating from the Anderson Hamiltonian in Eq. (3.1), we here use energy integrals instead of sums over momenta, and $c_{\omega\sigma\alpha}$ instead of $c_{k\sigma\alpha}$. This transformation is discussed for a similar setup below Eq. (2.3) and leads to the definition of $\tilde{v}_\alpha = \sqrt{\varrho_\alpha} v_\alpha$. In the Schrieffer-Wolff transformation, we aim to find a simpler Hamiltonian for the low-energy physics, which acts on a smaller low-energy Hilbert space. For the Kondo model we consider the Anderson model where the level ε lies deep in the Fermi sea, but the on-site Coulomb interaction is so strong that $\varepsilon + U$ lies far above the Fermi level. In this limit and at low temperature, the dot will always be occupied by exactly one electron and only virtual hopping processes can take place. With the Schrieffer-Wolff transformation, the Hilbert space of the quantum dot can be reduced to the two states $\uparrow$ and $\downarrow$ with occupancy one.

D.1. Deriving the transformation

The strategy for obtaining the low-energy Hamiltonian for the reduced Hilbert space is to transform the Anderson Hamiltonian to an approximately block-diagonal form. We want to construct a unitary operator W such that the transformed Hamiltonian

$$H' = WHW^\dagger - i\dot{W}W^\dagger \tag{D.4}$$

is block-diagonal, where one block describes the dynamics of the low-energy states $\uparrow, \downarrow$ and the other block describes the high-energy states with occupancies $0, 2$. The coupling Hamiltonian H_v — more precisely the coupling $\tilde{v}_\alpha$ — which connects the two subspaces in the Anderson Hamiltonian serves as the small parameter, and we will neglect terms of the order $\tilde{v}_\alpha^3$ in H'. Requiring that H' is block-diagonal when neglecting $O(\tilde{v}_\alpha^3)$ implies that all terms linear in $\tilde{v}_\alpha$ must vanish.

By writing $W = e^V$ where V is anti-Hermitian and linear in the coupling $\tilde{v}_\alpha$, this leads to the condition

$$H_v + [V, H_0] - i\dot{V} = 0. \tag{D.5}$$

Inserted in the Anderson Hamiltonian, this condition for V becomes

$$\sum_{\alpha\sigma} \int d\omega \left\{ \left(\tilde{v}_\alpha c^\dagger_{\omega\sigma\alpha} d_\sigma + \text{H.c.} \right) + (\omega + \mu_\alpha)[V, c^\dagger_{\omega\sigma\alpha} c_{\omega\sigma\alpha}] \right\} + \varepsilon \sum_\sigma [V, d^\dagger_\sigma d_\sigma] + U[V, d^\dagger_\uparrow d_\uparrow d^\dagger_\downarrow d_\downarrow] - i\dot{V} = 0. \tag{D.6}$$

A solution for $V(t)$ can be found using the ansatz [137, 159]

$$V = \sum_{\alpha\sigma} \int d\omega \, (w_{\alpha\omega} + u_{\alpha\omega} n_{\bar{\sigma}}) c^\dagger_{\omega\sigma\alpha} d_\sigma - \text{H.c.} \tag{D.7}$$

We use the convention that fermionic operators on different subsystems commute. Inserting the ansatz yields the expression

$$\begin{aligned} 0 = \sum_{\alpha\sigma} \int d\omega \Bigg\{ & \left(\tilde{v}_\alpha c^\dagger_{\omega\sigma\alpha} d_\sigma + \text{H.c.} \right) + (\omega + \mu_\alpha) \left[-c^\dagger_{\omega\sigma\alpha} d_\sigma (w_{\alpha\omega} + u_{\alpha\omega} n_{\bar{\sigma}}) + \text{H.c.} \right] \\ & + \varepsilon \left[(w_{\alpha\omega} + u_{\alpha\omega} n_{\bar{\sigma}}) c^\dagger_{\omega\sigma\alpha} d_\sigma + \text{H.c.} \right] + U \left[(w_{\alpha\omega} + u_{\alpha\omega}) c^\dagger_{\omega\sigma\alpha} d_\sigma n_{\bar{\sigma}} + \text{H.c.} \right] \\ & - i \left[(\dot{w}_{\alpha\omega} + \dot{u}_{\alpha\omega} n_{\bar{\sigma}}) c^\dagger_{\omega\sigma\alpha} d_\sigma - \text{H.c.} \right] \Bigg\}, \end{aligned} \tag{D.8}$$

which can be reduced to

$$0 = \tilde{v}_\alpha + (-\omega - \mu_\alpha + \varepsilon) w_{\alpha\omega} - i\dot{w}_{\alpha\omega}, \tag{D.9}$$

$$0 = (-\omega - \mu_\alpha + \varepsilon + U) u_{\alpha\omega} + U w_{\alpha\omega} - i\dot{u}_{\alpha\omega}. \tag{D.10}$$

Here we can see the separation of energy scales. $|\varepsilon|$ and U are large compared to μ_α, such that we can neglect μ_α in the Kondo limit. A voltage applied directly to the quantum dot, that causes an oscillation of ε, will also only affect the result if it is not much smaller than $|\varepsilon|$. In the low-energy limit when $-\varepsilon$ and $U + \varepsilon$ are much larger than all relevant energy scales, also the energy ω becomes negligible in the transformation for all relevant states.

For time-dependent driving, the solution for $V(t)$ is given by

$$w_{\alpha\omega}(t) = e^{-i\int_0^t ds\,[-\omega+\varepsilon(s)]} w'_{\alpha\omega}(t), \qquad w'_{\alpha\omega}(t) = -i \int_{t^*}^t ds\, e^{+i\int_0^s d\tau\,[-\omega+\varepsilon(\tau)]} \tilde{v}_\alpha(s), \tag{D.11}$$

$$u_{\alpha\omega}(t) = e^{-i\int_0^t ds\,[-\omega+\varepsilon(s)+U]} u'_{\alpha\omega}(t), \qquad u'_{\alpha\omega}(t) = -iU \int_{t^*}^t ds\, e^{+i\int_0^s d\tau\,[-\omega+\varepsilon(\tau)+U]} w_{\alpha\omega}(s), \tag{D.12}$$

where we have neglected μ_α. In the simpler case where μ_α is the only time-dependent quantity and is negligible compared to $|\varepsilon|$ and $U + \varepsilon$, the simpler static solution can be used:

$$w_{\alpha\omega} = \frac{\tilde{v}_\alpha}{-\varepsilon + \omega}, \tag{D.13}$$

$$u_{\alpha\omega} = \frac{\tilde{v}_\alpha U}{(\varepsilon - \omega)(U + \varepsilon - \omega)} = \frac{\tilde{v}_\alpha}{\varepsilon - \omega} - \frac{\tilde{v}_\alpha}{U + \varepsilon - \omega}. \tag{D.14}$$

If the frequency (or inverse timescale) of the driving is much smaller than $-\varepsilon$ and $U+\varepsilon$, this solution can also be used as an adiabatic approximation for the time-dependent functions $w_{\alpha\omega}$ and $u_{\alpha\omega}$. Here we can see that by including ω, one would try to take resonance effects at ε and $U+\varepsilon$ into account. However, these are far away from the low-energy dynamics, and we can neglect ω here such that $w_{\alpha\omega}$ and $u_{\alpha\omega}$ become independent of ω.

D.2. Transforming the Hamiltonian

Using the solution for $V(t)$, we can construct the transformed Hamiltonian.

$$H' = e^V H e^{-V} - i\left(\frac{d}{dt}e^V\right)e^{-V} \tag{D.15}$$

$$= H + [V,H] + \frac{1}{2}[V,[V,H]] - i\dot{V} - i\frac{1}{2}[V,\dot{V}] + O(V^3) \tag{D.16}$$

$$= H_0 + [V,H_v] + \frac{1}{2}[V,[V,H_0] - i\dot{V}] + O(V^3) \tag{D.17}$$

$$= H_0 + \frac{1}{2}[V,H_v] + O(V^3) \tag{D.18}$$

$$\begin{aligned} = H_0 + \frac{1}{2}\sum_{\alpha\alpha'\sigma}\iint d\omega\, d\omega' \Big[& \tilde{v}^*_{\alpha'}(w_{\alpha\omega} + u_{\alpha\omega}n_{\bar{\sigma}})[c^\dagger_{\omega\sigma\alpha}c_{\omega'\sigma\alpha'} - d^\dagger_\sigma d_\sigma \delta(\omega-\omega')\delta_{\alpha\alpha'}] + \text{H.c.} \\ & - \tilde{v}_{\alpha'}u_{\alpha\omega}c^\dagger_{\omega\sigma\alpha}c^\dagger_{\omega'\bar{\sigma}\alpha'}d_\sigma d_{\bar{\sigma}} - \tilde{v}^*_{\alpha'}u^*_{\alpha\omega}c_{\omega\sigma\alpha}c_{\omega'\bar{\sigma}\alpha'}d^\dagger_\sigma d^\dagger_{\bar{\sigma}} \\ & + \tilde{v}^*_{\alpha'}u_{\alpha\omega}c^\dagger_{\omega\sigma\alpha}c_{\omega'\bar{\sigma}\alpha'}d_\sigma d^\dagger_{\bar{\sigma}} + \tilde{v}_{\alpha'}u^*_{\alpha\omega}c_{\omega\sigma\alpha}c^\dagger_{\omega'\bar{\sigma}\alpha'}d^\dagger_\sigma d_{\bar{\sigma}}\Big] \end{aligned} \tag{D.19}$$

Here we find that one term only leads to a renormalization of the dot level, which we absorb in the Hamiltonian of the local level by defining

$$\tilde{H}_0 = H_0 - \sum_{\alpha\sigma}\int d\omega\ \mathrm{Re}(\tilde{v}^*_\alpha w_{\alpha\omega})n_\sigma. \tag{D.20}$$

In the following, we will only consider the low-energy block where the occupation of the dot is always one, $n_\uparrow + n_\downarrow = 1$. Terms which vanish when acting on states in this low-energy subspace are considered irrelevant:

$$\begin{aligned} H' = & \frac{1}{2}\sum_{\alpha\alpha'\sigma}\iint d\omega\, d\omega' \tilde{v}^*_{\alpha'}\left[(w_{\alpha\omega} + u_{\alpha\omega}n_{\bar{\sigma}})c^\dagger_{\omega\sigma\alpha}c_{\omega'\sigma\alpha'} - u_{\alpha\omega}c^\dagger_{\omega\sigma\alpha}c_{\omega'\bar{\sigma}\alpha'}d^\dagger_{\bar{\sigma}}d_\sigma\right] \\ & + \text{H.c.} + \tilde{H}_0 + \text{irrelevant} \end{aligned} \tag{D.21}$$

$$\begin{aligned} = & \frac{1}{2}\sum_{\alpha\alpha'\sigma\sigma'}\iint d\omega\, d\omega' \tilde{v}^*_{\alpha'}\left[\delta_{\sigma\sigma'}\left(w_{\alpha\omega} + \frac{1}{2}u_{\alpha\omega}\right)c^\dagger_{\omega\sigma\alpha}c_{\omega'\sigma\alpha'} - u_{\alpha\omega}c^\dagger_{\omega\sigma\alpha}c_{\omega'\sigma'\alpha'}\left(d^\dagger_{\sigma'}d_\sigma - \frac{1}{2}\delta_{\sigma\sigma'}\right)\right] \\ & + \text{H.c.} + \tilde{H}_0 + \text{irrelevant.} \end{aligned} \tag{D.22}$$

Of the two remaining potential scattering terms, only the second one leads to the Kondo model. For the first term, we define

$$H_s = \frac{1}{4}\sum_{\alpha\alpha'\sigma}\iint d\omega\, d\omega' \left[\tilde{v}^*_{\alpha'}\left(2w_{\alpha\omega} + u_{\alpha\omega}\right)c^\dagger_{\omega\sigma\alpha}c_{\omega'\sigma\alpha'} + \text{H.c.}\right]. \tag{D.23}$$

In the time-independent Schrieffer-Wolff transformation, which is valid even if the chemical potentials of the reservoirs are time-dependent, H_s takes the simple form

$$H_s = -\frac{1}{2}\sum_{\alpha\alpha'\sigma}\iint d\omega\, d\omega' \tilde{v}^*_{\alpha'}\tilde{v}_\alpha\left[\frac{1}{\varepsilon-\omega}+\frac{1}{U+\varepsilon-\omega}\right]c^\dagger_{\omega\sigma\alpha}c_{\omega'\sigma\alpha'} \tag{D.24}$$

and is of the order ε^{-2} at the particle-hole symmetry point $U+\varepsilon=-\varepsilon$. It is therefore legitimate to neglect it for a discussion of the universal low-energy physics of a quantum dot near particle-hole symmetry. In the Kondo model this term is not included, but it is a source of the background conductance which we need to consider when comparing to experiments in section 3.3.

This finally brings us to the low-energy Hamiltonian

$$H' = \tilde{H}_0 - \frac{1}{2}\sum_{\alpha\alpha'\sigma\sigma'}\iint d\omega\, d\omega'(\tilde{v}^*_{\alpha'}u_{\alpha\omega}+\tilde{v}_\alpha u^*_{\alpha'\omega'})\,\mathbf{S}\cdot\boldsymbol{\sigma}_{\sigma\sigma'}\,c^\dagger_{\omega\sigma\alpha}\,c_{\omega'\sigma'\alpha'}, \tag{D.25}$$

where H_s has been neglected. Here we have used that $2\mathbf{S}\cdot\boldsymbol{\sigma}_{\sigma\sigma'} = 2d^\dagger_{\sigma'}d_\sigma - \delta_{\sigma\sigma'}$ in the low-energy subspace. The Hamiltonian $\tilde{H}_0$ only contains the reservoir Hamiltonians and an irrelevant constant proportional to $\sum_\sigma n_\sigma = 1$. We can therefore write the low-energy Hamiltonian in the form

$$H' = \frac{1}{2}\sum_{\alpha\alpha'\sigma\sigma'}\iint d\omega\, d\omega'\,\bar{J}_{\alpha\alpha'}\mathbf{S}\cdot\boldsymbol{\sigma}_{\sigma\sigma'}c^\dagger_{\omega\sigma\alpha}c_{\omega'\sigma'\alpha'} + \sum_{\alpha\sigma}\int d\omega\,(\omega+\mu_\alpha)c^\dagger_{\omega\sigma\alpha}c_{\omega\sigma\alpha} \tag{D.26}$$

with the coupling matrix

$$\bar{J}_{\alpha\alpha'} = -\tilde{v}^*_{\alpha'}u_{\alpha 0} - \tilde{v}_\alpha u^*_{\alpha' 0}, \tag{D.27}$$

in which we assumed that the energy-dependence can be neglected by setting $\omega=\omega'=0$. In the time-independent Schrieffer-Wolff transformation, this coupling takes the simple form

$$\bar{J}_{\alpha\alpha'} = 2\tilde{v}_\alpha\tilde{v}^*_{\alpha'}\left(\frac{1}{-\varepsilon}+\frac{1}{U+\varepsilon}\right). \tag{D.28}$$

Now that we know the general solution for the coupling $\bar{J}_{\alpha\alpha'}$ in terms of u_α, we can explicitly calculate it for different special cases. As a first case, we have already seen that a time-dependence only in the chemical potentials μ_α does not require the time-dependent Schrieffer-Wolff transformation and leads to the time-constant result given in Eq. (D.28). For the second case, we assume that only the coupling $\tilde{v}_\alpha$ is time-dependent. The timescale for this time-dependence is assumed to be in the low-energy regime, such that $\dot{\tilde{v}}_\alpha \ll |\varepsilon|\tilde{v}_\alpha$. This implies that Eq. (D.28) — now with time-dependent $\tilde{v}_\alpha$ — can be used as an adiabatic approximation because the $\tilde{v}_\alpha$ changes only slowly in time and in Eqs. (D.9)–(D.10) the time-derivatives are negligible. For the third case, we consider an oscillating voltage that changes the level of the quantum dot in the form $\varepsilon(t) = \varepsilon_0 + V_d\cos(\Omega t)$. In this case, the adiabatic approximation can also be used. We find that $\bar{J}_{\alpha\alpha'} = \bar{J}^0_{\alpha\alpha'}[1+\gamma V_d\cos(\Omega t)]$ for $-\varepsilon, U+\varepsilon \gg \Omega$ with a constant $\gamma = O(1/\varepsilon)$ which vanishes at particle-hole symmetry and $\bar{J}^0_{\alpha\alpha'}$ denoting the coupling for $V_d = 0$ [159]. Thus, the effect of an oscillating potential on the quantum dot is suppressed in the Kondo limit.

D.3. Relation to the T-matrix formalism

The Schrieffer-Wolff transformation can be used to derive the T-matrix formalism, which is used to derive the poor man's scaling relation in section 3.1.2. For the T-matrix formalism, we assume that H_0 is diagonal and that the Hamiltonian is time-independent. From the derivation of the Schrieffer-Wolff transformation, we will only use Eqs. (D.5) and (D.18).

Like in the Schrieffer-Wolff transformation, we assume a separation of energy scales, defining a low-energy and a high-energy sector. We can write operators in a block matrix form with low and high-energy blocks:

$$H_0 = \begin{pmatrix} H_L & 0 \\ 0 & H_H \end{pmatrix}, \qquad V = \begin{pmatrix} 0 & -S^\dagger \\ S & 0 \end{pmatrix}, \qquad H_v = \begin{pmatrix} 0 & F^\dagger \\ F & 0 \end{pmatrix}. \tag{D.29}$$

With the last equation, we have added the assumption that the term H_v which we treat perturbatively does not have any components within the low or high-energy subspaces, but it only contains terms which couple these subspaces. With this notation, we can write Eq. (D.5) in matrix form as

$$\begin{pmatrix} 0 & F^\dagger \\ F & 0 \end{pmatrix} + \begin{pmatrix} 0 & H_L S^\dagger - S^\dagger H_H \\ S H_L - H_H S & 0 \end{pmatrix} = 0. \tag{D.30}$$

We can now use that H_L and H_H are diagonal and denote their eigenvalues by E_i^L and E_i^H. This allows us to directly read off the matrix elements of S from Eq. (D.30):

$$S_{ij} = \frac{F_{ij}}{E_i^H - E_j^L}. \tag{D.31}$$

The low-energy sector of the transformed Hamiltonian can now be determined using Eq. (D.18):

$$H' = \begin{pmatrix} H_L & 0 \\ 0 & H_H \end{pmatrix} + \frac{1}{2} \begin{pmatrix} -S^\dagger F - F^\dagger S & 0 \\ 0 & S F^\dagger + F S^\dagger \end{pmatrix} \tag{D.32}$$

Thus, matrix elements of the low-energy sector are given by

$$H'_{L\,ij} = \delta_{ij} E_i^L + \frac{1}{2} \sum_k \left(\frac{F_{ik}^\dagger F_{kj}}{E_j^L - E_k^H} + \frac{F_{ik}^\dagger F_{kj}}{E_i^L - E_k^H} \right). \tag{D.33}$$

This is commonly expressed using the T-matrix

$$T_{ij}(E) = \sum_k \frac{F_{ik}^\dagger F_{kj}}{E - E_k^H}, \tag{D.34}$$

such that $H'_{L\,ij} = [T_{ij}(E_i^L) + T_{ij}(E_j^L)]/2$. Eq. (D.33) directly leads to Eq. (3.5), which we used in the discussion of the poor man's scaling.

E. Floquet theory and effective density of states

Floquet theory is a common framework to treat periodically driven quantum systems. With Floquet theory, one avoids working in the time domain and instead uses infinite or truncated Floquet matrices. Here we review some basic concepts of Floquet theory in closed quantum systems and derive Eq. (3.17).

We consider the following problem. A system of noninteracting particles with unit charge and single-particle Hamiltonian H_P is driven by an oscillating voltage $V(t) = V_{\text{osc}} \cos(\Omega t)$ such that the full single-particle Hamiltonian is

$$H(t) = H_P + V_{\text{osc}} \cos(\Omega t). \tag{E.1}$$

We will denote the Fourier modes of this Hamiltonian by $H_n = \frac{1}{T}\int_0^T dt\, e^{-in\Omega t} H(t)$. As derived in Ref. [187], the eigenstates of such a system can be computed using Floquet's theorem. In close analogy to Bloch's theorem, Floquet's theorem states that a complete set of solutions of the time-dependent Schrödinger equation consists of states of the form $|\psi(t)\rangle = e^{-iEt}|\phi(t)\rangle$, where $|\phi(t+T)\rangle = |\phi(t)\rangle$ and E is the energy of the state.[1] One can now try to find the energies E and states $|\phi(t)\rangle$ by solving the Schrödinger equation in the time domain, but it is more convenient to go to Fourier space and relate the Fourier modes of $H(t)$ and $|\phi(t)\rangle$. A Fourier transform of the Schrödinger equation yields $(E - n\Omega)|\phi_n\rangle = \sum_m H_{n-m}|\phi_m\rangle$, which can be reformulated as the eigenvalue problem

$$\sum_m F^H_{nm} |\phi_m\rangle = E\,|\phi_n\rangle\,, \tag{E.2}$$

in which the Hamiltonian was replaced by the Floquet matrix

$$F^H_{nm} = H_{n-m} + n\Omega\delta_{nm} = (H_P + n\Omega)\delta_{nm} + \frac{V_{\text{osc}}}{2}(\delta_{n,m+1} + \delta_{n,m-1}). \tag{E.3}$$

On the right-hand side we have inserted the definition of the Hamiltonian. With Eq. (E.2), the solution of the time-dependent Schrödinger equation has been reduced to an eigenvalue problem for a time-constant, but infinitely large matrix.

[1] Consider the Schrödinger equation $i\partial_t|\psi(t)\rangle = H(t)|\psi(t)\rangle$. The formal solution of this ODE is $|\psi(t)\rangle = U(t)|\psi(0)\rangle$ with the unitary matrix $U(t) = \mathcal{T}_{\leftarrow} e^{-i\int_0^t ds\, H(s)}$. Since $H(s)$ is periodic, $U(t)$ must fulfill $U(t+nT) = U(t)U(T)^n$, and we can write $U(T) = e^{-iQT}$ for some Hermitian matrix Q. Now choose $\phi(0)$ to be an eigenvector of Q with eigenvalue E. Then $|\phi(t)\rangle = e^{iEt}U(t)|\phi(0)\rangle$ defines a solution $e^{-iEt}|\phi(t)\rangle$ of the Schrödinger equation of the required form. The complete set of eigenvectors of Q yields a complete set of solutions of the Schrödinger equation, from which all other solutions can be constructed by superposition.

In our example of an oscillating voltage affecting all particles, the solution of Eq. (E.2) is given by Bessel functions,

$$\left|\phi_n^{E,0}\right\rangle = \mathcal{J}_{-n}\left(\frac{V_{\text{osc}}}{\Omega}\right)\left|\psi_E^0\right\rangle, \tag{E.4}$$

where $|\psi_E^0\rangle$ is an eigenstate of the constant single-particle Hamiltonian H_P, $H_P|\psi_E^0\rangle = E|\psi_E^0\rangle$. From the structure of Eq. (E.3) it follows that for every solution $|\phi_n^{E,0}\rangle$ with energy E there exists a solution $|\phi_n^{E+k\Omega,k}\rangle := |\phi_{n-k}^{E,0}\rangle$ with energy $E + k\Omega$, where k can be any integer. Thus, the spectrum of the Floquet eigenvalue problem is periodic.

An interesting property of the system shaken by an oscillating voltage is its density of states. For strong driving, particles in the system may absorb or emit photons and jump to higher or lower levels by inter multiples of the driving frequency. Due to these processes, the driving changes the density of states. But before we can calculate it, we need to define what we mean by an effective density of states in a rapidly driven system. Assuming that the driving is fast, and we are only interested in longer timescales, we can define the effective density of states as averaged over one time period. We are thus interested in the occupancies of the modes $|\phi_0^{E,k}\rangle$ as a function of energy E. If the equilibrium density of states is known, the effective density of states of the Floquet states can be computed using the contribution of the equilibrium eigenstates to the Floquet states. The resulting effective density of states is

$$\varrho^{\text{eff}}(E) = \sum_k \left|\left\langle\phi_0^{E,-k}\middle|\psi_{E+k\Omega}^0\right\rangle\right|^2 \varrho^{\text{eq}}(E + k\Omega) = \sum_k \mathcal{J}_k^2\left(\frac{V_{\text{osc}}}{\Omega}\right)\varrho^{\text{eq}}(E + k\Omega), \tag{E.5}$$

as derived in Ref. [163] and used in section 3.2.2 to explain side peaks in the differential conductance through the Kondo model.

F. Highly asymmetric coupling

In this appendix, a formal expansion of the calculation of the current shows why the approximation by photon-assisted tunneling is exact in the limit of a strong asymmetry in the coupling. Consider the diagrammatic expansion in Floquet-Liouville space introduced in section 4.2.4. The current kernel is of the form

$$\hat{\Gamma}^L = \hat{\tilde{\mu}}_{LR}(\delta_{1L} - \delta_{2L})$$ 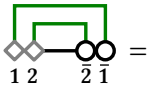

$$= \hat{\tilde{\mu}}_{LR}\Big($$ 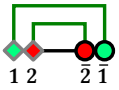

$$-$$ 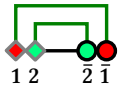

$$\Big), \tag{F.1}$$

where the left vertex is the bare current vertex (indicated by gray squares) and the right vertex is the effective coupling vertex (black circles).[1] On the right-hand side, we indicate the reservoir (L or R) in the indices $1, 2$ by the color. Red means the right reservoir and light green indicates the left reservoir. For strongly asymmetric coupling with $x_R \ll x_L$ we expand the effective coupling vertex and keep only the leading order in x_R, i.e., only terms containing just a single red index in the bare coupling vertices. Some representative diagrams in the resulting series are

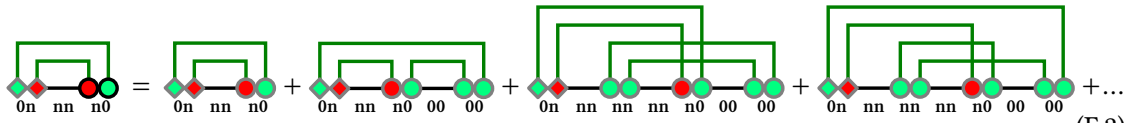

(F.2)

The indices below the diagrams will be explained below. We will see that for each diagram occurring in this expansion, the approximation of photon-assisted tunneling holds exactly.

To understand the effect of the driving, we use the unitary transformation of the Hamiltonian derived in section 5.3.2 and absorb the time-dependent part of the driving (V_{osc}) into the vertices. The average bias voltage V_{avg} is unaffected by the transformation. In this formulation, only the vertices $\hat{I}^{\gamma}_{\alpha\alpha'}$ and $\hat{G}_{\alpha\alpha'}$ connecting the two reservoirs, $\alpha \neq \alpha'$, are non-diagonal Floquet matrices. Thus, each diagram contains only two non-diagonal Floquet matrices: the bare current vertex $\hat{I}^{\gamma}_{11'}$ and the bare coupling vertex $\hat{G}_{11'}$ where $\alpha \neq \alpha'$, which is marked in red. Since we are interested in the average current, we want to compute only the Floquet matrix element $\hat{\Gamma}^L_{00}$. Taking this matrix element in the diagrams in Eq. (F.2) fixes the Floquet indices to the ones indicated below the diagrams for each Floquet matrix (vertex or resolvent), where n denotes a running index. We observe that those Floquet matrices which have indices nn or $n0$ are precisely those which also obtain a shift of the energy argument by the voltage due to the reservoir contraction lines above them. Thus, everywhere where V_{avg} occurs in the resolvents as a shift in the energy argument, we additionally need to include a shift by $n\Omega$.

Next, we recall the structure of the vertex Floquet matrices when using the unitary transformation. From section 5.3.4 we know that the bare vertices connecting different diagrams

[1] It may seem surprising that we need only two vertices, but the effective vertex is defined such that it includes all possible bare diagrams that appear in this expansion. Eq. (F.1) is exact.

($\alpha_1 \neq \alpha_2$) fulfill

$$\hat{I}_{12;0n} = \mathcal{J}_{\pm n}\left(\frac{V_{\text{osc}}}{\omega}\right) I_{12}, \qquad \hat{G}_{12;0n} = \mathcal{J}_{\pm n}\left(\frac{V_{\text{osc}}}{\omega}\right) G_{12}, \qquad \hat{G}_{12;nn} = G_{12}, \tag{F.3}$$

where I_{12} and G_{12} are superoperators that are no Floquet matrices anymore, and the sign $\pm$ is $+$ if $\alpha_1 = R$ or $-$ if $\alpha_1 = L$. Thus, each diagram in Eq. (F.2) obtains a prefactor[2] $\mathcal{J}_n^2(V_{\text{osc}}/\Omega)$.

With these considerations, we have identified two effects of the periodic driving V_{osc}. Firstly, in every diagram in Eq. (F.2) we need to sum over a Floquet index n and include a prefactor $\mathcal{J}_n^2(V_{\text{osc}}/\Omega)$. Secondly, every resolvent that includes an energy shift by V_{avg} shall additionally include a shift by $n\Omega$. Equivalently, one could replace V_{avg} by $V_{\text{avg}} + n\Omega$ in each diagram. Importantly, these are the only effects of the periodic part of the driving (V_{osc}). This implies that the approximation of only photon-assisted tunneling is exact term-by-term in this expansion as long as only the leading order in x_R is considered:

$$G(V_{\text{avg}}, V_{\text{osc}}) = \sum_{n=-\infty}^{\infty} \mathcal{J}_n^2\left(\frac{V_{\text{osc}}}{\Omega}\right) G(V_{\text{avg}} + n\Omega, 0) + O(x_R^2). \tag{F.4}$$

The structure of this proof shows that the result is not restricted to the case of harmonic driving, but holds for every splitting of the chemical potential $\mu_\alpha(t) = \mu_\alpha^j(t) + \mu_\alpha^r(t)$ where $\exp[i\int_0^t ds\, \mu_\alpha^j(s)]$ is periodic with period $T = 2\pi/\Omega$ (see section 5.3.3). For other driving profiles, the prefactor $\mathcal{J}_n^2(V_{\text{osc}}/\Omega)$ has to be replaced by $|\hat{F}_{n0}^{LR}|^2$ as defined in Eq. (5.88), and $\mu_\alpha^r(t)$ must be included on the right-hand side of Eq. (F.4).

[2] The sign $\pm$ in $\mathcal{J}_{\pm n}(x)$ is irrelevant when squaring the Bessel function.

G. Propagator in Floquet space

The central property of Floquet matrices is that the matrix product represents a convolution in the time domain. Here we repeat a proof of this property that was presented in appendix A of Ref. [3]. We consider two functions $a(t,t')$ and $b(t,t')$ and denote by $\hat{A}$ and $\hat{B}$ the corresponding Floquet matrices. As the following calculation will show, the product $\hat{C} \coloneqq \hat{A}\hat{B}$ is in the time domain

$$c(t,t') = \int_{t'}^{t} ds\, a(t,s)\, b(s,t') =: [a * b](t,t'). \tag{G.1}$$

A definition of Floquet matrices that is equivalent to Eqs. (4.1) and (4.2) is

$$\hat{A}(E)_{nm} = \frac{1}{T}\int_0^\infty ds\, e^{i(E+n\Omega)s} \int_0^T dt\, e^{i(n-m)\Omega t} a(t+s,t), \tag{G.2}$$

$$a(t+s,t) = \int_{-\infty}^{\infty} \frac{dE}{2\pi}\, e^{-i(E+n\Omega)s} \sum_{n\in\mathbb{Z}} e^{-in\Omega t} \hat{A}_{n0}(E). \tag{G.3}$$

Using this definition, we find that

$$\hat{C}(E)_{nm}$$

$$= \sum_k \iint_0^\infty ds\, ds'\, e^{i(E+n\Omega)s + i(E+k\Omega)s'} \frac{1}{T^2} \int_0^T dt \int_0^T dt'\, e^{i(n-k)\Omega t + i(k-m)\Omega t'} a(t+s,t)\, b(t'+s',t') \tag{G.4}$$

$$= \iint_0^\infty ds\, ds'\, e^{i(E+n\Omega)s + iEs'} \frac{1}{T} \int_0^T dt \int_0^T dt'\, e^{in\Omega t - im\Omega t'} \sum_k \delta(s'+t'-t+kT)\, a(t+s,t)\, b(t'+s',t') \tag{G.5}$$

$$= \iint_0^\infty ds\, ds'\, e^{i(E+n\Omega)s + iEs'} \frac{1}{T} \int_0^T dt'\, e^{in\Omega(t'+s') - im\Omega t'} a(t'+s'+s, t'+s')\, b(t'+s',t') \tag{G.6}$$

$$= \int_0^\infty ds''\, e^{i(E+n\Omega)s''} \frac{1}{T} \int_0^T dt'\, e^{i(n-m)\Omega t} \int_0^{s''} ds'\, a(t'+s'', t'+s')\, b(t'+s', t') \tag{G.7}$$

$$= \int_0^\infty ds\, e^{i(E+n\Omega)s} \frac{1}{T} \int_0^T dt\, e^{i(n-m)\Omega t} [a * b](t+s,t), \tag{G.8}$$

proving our claim that $\hat{A}\hat{B}$ is the Floquet representation of the convolution $a * b$.

The convolution property allows us to calculate the Floquet matrix of a time-ordered integral. Consider a function $f(t)$ of a single time argument which does not necessarily commute with itself at different times, $[f(t), f(s)] \neq 0$. To use the convolution property, we define $F(t,t') \equiv f(t')$ and the identity function $O(t,t') \equiv 1$. Then we can rewrite a time-ordered integral as

$$\mathcal{T}_{\leftarrow} e^{\int_{t_0}^t ds\, f(s)} = O(t,t_0) + [F * O](t,t_0) + [F * F * O](t,t_0) + \ldots = \sum_{k=0}^{\infty} [F^{*k} * O](t,t_0). \tag{G.9}$$

The Floquet matrices for $O(t,t')$ and $F(t,t')$ are

$$\hat{O}(E)_{nm} = \frac{i\delta_{nm}}{E+n\Omega} = \Big[\frac{i}{E+\hat{N}\Omega}\Big]_{nm}, \tag{G.10}$$

$$\hat{F}(E)_{nm} = \frac{i\tilde{f}_{n-m}}{E+n\Omega} = \Big[\frac{i}{E+\hat{N}\Omega}\hat{f}\Big]_{nm}. \tag{G.11}$$

Here $\tilde{f}_n = \frac{1}{T}\int_0^T dt\, e^{in\Omega t} f(t)$ denotes the Fourier coefficients of $f(t)$, and we defined the Floquet matrices $\hat{N}_{nm} = n\delta_{nm}$ and $\hat{f}_{nm} \equiv \tilde{f}_{n-m}$. The Floquet matrix representing the time-ordered integral $\mathcal{T}_{\leftarrow} e^{\int_{t_0}^{t} ds\, f(s)}$ is thus given by

$$\sum_{k=0}^{\infty}\Big[\frac{i}{E+\hat{N}\Omega}\hat{f}\Big]^k \frac{i}{E+\hat{N}\Omega} = \frac{i}{E+\hat{N}\Omega-i\hat{f}}. \tag{G.12}$$

A special case of the previously derived relation is the propagator $\Pi(t,t_0)$, which is given by the partial trace of a time-ordered integral with function $f(t) = -iL_V(t) - iL_R(t)$ and $\hat{f} = -i\hat{L}_V - i\hat{L}_R$ [see Eq. (4.5)].

H. Symmetry restrictions of a vertex

A vertex like $\bar{G}_{12}$ and $\bar{I}_{12}$ is a matrix in reservoir spin space and a superoperator acting on the Liouville space $\mathbb{C}^{2\times 2}$. In this proof, the reservoir indices of the vertices are irrelevant and will be omitted by just writing $\bar{G}_{\sigma\sigma'}$ for the coupling vertex. A general parametrization of the vertex is

$$\bar{G}_{\sigma\sigma'} = \sum_{ijk=0}^{3} g_{ijk}\sigma^i_{\sigma\sigma'} \left|\sigma_j\right)\left(\sigma_k\right|, \tag{H.1}$$

where real-valued coefficients g_{ijk} ensure Hermiticity preservation. Here $\sigma_{1,2,3}$ are the Pauli matrices and $\sigma_0 \coloneqq \mathbb{1}$. Rotational symmetry as formulated in Eq. (5.4) implies that

$$\sum_{ijk=0}^{3} g_{ijk} \left|U\sigma_j U^\dagger\right) \left(U\sigma_k U^\dagger\right| \otimes (U\sigma^i U^\dagger) = \sum_{ijk=0}^{3} g_{ijk} \left|\sigma_j\right)\left(\sigma_k\right| \otimes \sigma^i \tag{H.2}$$

or, equivalently,

$$\sum_{ijk} g_{ijk} U^{\otimes 3}(\sigma_i \otimes \sigma_j \otimes \sigma_k) {U^{\otimes 3}}^\dagger = \sum_{ijk} g_{ijk}\sigma_i \otimes \sigma_j \otimes \sigma_k \qquad \text{for all } U \in SU(2). \tag{H.3}$$

Here we prove that the most general form for g_{ijk} compatible with this symmetry is

$$g_{ijk} = A\delta_{i0}\delta_{j0}\delta_{k0} + B\delta_{i0}\delta_{jk}(1-\delta_{j0}) + C\delta_{j0}\delta_{ki}(1-\delta_{k0}) + D\delta_{k0}\delta_{ij}(1-\delta_{i0}) + E\varepsilon_{ijk}(1-\delta_{i0})(1-\delta_{j0})(1-\delta_{k0}). \tag{H.4}$$

The general vertex parametrization in Eq. (5.5) follows from this expression.

For the proof, we distinguish the four cases of how many of the indices i, j, k are zero. For $i = j = k = 0$, we find the first term in Eq. (H.4), which is obviously compatible with Eq. (H.3). When only two indices are zero — say $i = j = 0 \neq k$ — we can always choose a rotation by $U = i\sigma_i$ and find that $g_{00k} = -g_{00k}$. Thus, there is no contribution with two indies equal zero in Eq. (H.4).

Next, we consider the case that one index is zero, say $i = 0$ and $j, k \neq 0$. By choosing $U = i\sigma_j$ in Eq. (H.3), one finds that $g_{0jk} = -g_{0jk}$ if $j \neq k$. Thus, only $j = k$ remains. Choosing $U = \frac{1}{2}(\mathbb{1} - iX - iY - iZ)$, which maps $\sigma_i \mapsto U\sigma_i U^\dagger = \sigma_{i+1 \bmod 4}$, implies furthermore that $g_{011} = g_{022} = g_{033}$ such that only $g_{0jk} = B\delta_{jk}$ is compatible with the symmetry for $j, k \neq 0$. To prove that this term indeed fulfills Eq. (H.3), one can use that $\sum_{i=0}^{3}(\sigma_i \otimes \sigma_i)(|\sigma\rangle \otimes |\sigma'\rangle) = 2|\sigma'\rangle \otimes |\sigma\rangle$, which implies that $\sum_{i=0}^{3} U^{\otimes 2}\sigma_i^{\otimes 2}{U^{\otimes 2}}^\dagger = \sum_{i=0}^{3}\sigma_i^{\otimes 2}$. This shows that if one index out of i, j, k is zero, we obtain the terms with coefficients B, C, D in Eq. (H.4).

For the only remaining case, we need to consider $i, j, k \in \{1, 2, 3\}$. By choosing $U = i\sigma_i$, one finds that $g_{ijk} = 0$ except if $i = j = k$ or $i \neq j \neq k \neq i$. Choosing another Pauli matrix for U leads to the conclusion that $g_{ijk} \neq 0$ only if all indices i, j, k differ. A rotation by $U = \frac{1}{2}(\mathbb{1} - iX - iY - iZ)$

shows that g_{ijk} is invariant when incrementing all indices, e.g., $g_{123} = g_{231} = g_{312}$. Rotating by $U = (\mathbb{1} + iX)/\sqrt{2}$ shows that $g_{123} = -g_{132}$, and analogously we find $g_{321} = g_{132} = g_{213}$. This completes the proof that only $g_{ijk} = E\varepsilon_{ijk}$ can be a solution for $i, j, k \neq 0$. To prove that this solution indeed obeys the symmetry, one can write $U\sigma_i U^\dagger = \sum_j R_{ji}\sigma_j$ where $R \in SO(3)$ is a rotation matrix.[1] This brings the symmetry relation to the form

$$\varepsilon_{ijk} = \sum_{lmn} \varepsilon_{lmn} R_{il} R_{jm} R_{kn} = \begin{cases} \det(R) = 1 & \text{if } i, j, k = 1, 2, 3 \text{ or cyclic permutations} \\ -\det(R) = -1 & \text{if } i, j, k = 3, 2, 1 \text{ or cyclic permutations} \\ 0 & \text{otherwise} \end{cases} . \tag{H.5}$$

This completes the proof that the only term compatible with the symmetry relation for $i, j, k \neq 0$ is $E\varepsilon_{ijk}$.

[1] Using $R_{ij} = \frac{1}{2}\operatorname{tr}(\sigma_i U \sigma_j U^\dagger)$, one can prove that R is orthogonal, $R \in O(3)$. For $U = \mathbb{1}$, one finds $R = \mathbb{1}$ with $\det(R) = 1$. Continuous changes of U can only change R and $\det(R)$ continuously. But since the determinant of a real orthogonal matrix can only be ± 1, one can conclude that $\det(R) = 1$ for all $U \in SU(2)$. This implies $R \in SO(3)$.

I. Initial conditions for leading order RG equations

When using only the leading order terms in the RG equations, the initial conditions also need to be adapted. Here we present the initial conditions for the leading order RG flow, which is used in section 6.1.1.

As in section 5.2.5, we use the ansatz

$$G^2_{12} = -2\sqrt{x_1 x_2}J, \qquad G^3_{12} = 2\sqrt{x_1 x_2}K, \qquad I^\gamma_{12} = (\delta_{1\gamma} - \delta_{2\gamma})2\sqrt{x_1 x_2}M. \tag{I.1}$$

In leading order, the equilibrium RG equations read

$$\frac{d}{d\Lambda}\Gamma(\Lambda) = \frac{1}{Z} - 1, \tag{I.2}$$

$$\frac{d}{d\Lambda}Z(\Lambda) = 4\frac{Z^2 J^2}{\Lambda + \Gamma}, \tag{I.3}$$

$$\frac{d}{d\Lambda}J(\Lambda) = -2\frac{J^2}{\Lambda + \Gamma}, \tag{I.4}$$

$$\frac{d}{d\Lambda}K(\Lambda) = -4\frac{JK}{\Lambda + \Gamma}, \tag{I.5}$$

$$\frac{d}{d\Lambda}M(\Lambda) = -2\frac{JM}{\Lambda + \Gamma}, \tag{I.6}$$

$$\frac{d}{d\Lambda}\delta\Gamma^\gamma(\Lambda) = i12x_L x_R \frac{MK}{\Lambda + \Gamma}\delta V_{\text{avg}}. \tag{I.7}$$

Dividing by $dJ/d\Lambda$ yields

$$\frac{dZ}{dJ} = -2Z^2 \qquad \Longrightarrow \qquad Z = \frac{1}{2J + Z_0^{-1}}, \tag{I.8}$$

$$\frac{dK}{dJ} = 2\frac{K}{J} \qquad \Longrightarrow \qquad K = K_0 J^2, \tag{I.9}$$

$$\frac{dM}{dJ} = \frac{M}{J} \qquad \Longrightarrow \qquad M = M_0 J, \tag{I.10}$$

$$\frac{d\delta\Gamma^\gamma}{dJ} = -i6x_L x_R \frac{MK}{J^2}\delta V_{\text{avg}} \qquad \Longrightarrow \qquad \delta\Gamma^\gamma = -i3x_L x_R J^2 M_0 K_0\, \delta V_{\text{avg}}. \tag{I.11}$$

From section 5.2.6 we know that $K_0 = i\pi$, $M_0 = 1$ and $Z_0 = 1$. Using $\delta\Gamma^\gamma(\Lambda = 0) = \frac{4}{\pi}x_L x_R\, \delta V_{\text{avg}}$, we find that J takes a similar role like J' in the next-to-leading order initial conditions:

$$J(\Lambda = 0) = \frac{2}{\sqrt{3\pi}}. \tag{I.12}$$

By inverting both sides of Eq. (I.4), defining $\lambda = \Lambda + \Gamma$, and inserting $d\Gamma/dJ$, we find that

$$\frac{d\lambda}{dJ} = -\frac{\lambda}{2J^2} - \frac{\lambda}{J}, \tag{I.13}$$

which defines the integration constant

$$T_K'' = \lambda J e^{-\frac{1}{2J}}. \tag{I.14}$$

This is again a reference energy scale for the low-energy physics. Like for the next-to-leading order RG flow, we can use the results of the FRTRG for $V_{\text{osc}} = 0$ to connect T_K'' to T_K as defined in Eq. (3.15), which yields $T_K \approx 10.1 T_K''$. The initial conditions for the nonequilibrium RG equations can be summarized in analogy to section 5.3.5:

$$\hat{\Gamma}(E) = \Gamma(E + \hat{N}\Omega), \tag{I.15}$$
$$\hat{Z}(E) = Z(E + \hat{N}\Omega), \tag{I.16}$$
$$\hat{G}^2_{12}(E) = -2\sqrt{x_1 x_2}\hat{F}^{12} J(E + \hat{N}\Omega), \tag{I.17}$$
$$\hat{G}^3_{12}(E) = i\pi 2\sqrt{x_1 x_2}\hat{F}^{12}[J(E + \hat{N}\Omega)]^2, \tag{I.18}$$
$$\hat{G}^a_{12}(E) = 0, \tag{I.19}$$
$$\hat{I}^\gamma_{12}(E) = (\delta_{1\gamma} - \delta_{2\gamma})2\sqrt{x_1 x_2}\hat{F}^{12} J(E + \hat{N}\Omega), \tag{I.20}$$
$$\delta\hat{\Gamma}(E) = 0, \tag{I.21}$$
$$\delta\hat{\Gamma}^\gamma(E) = 3\pi x_L x_R [J(E + \hat{N}\Omega)]^2 \delta V_{\text{avg}}, \tag{I.22}$$
$$\hat{\Gamma}^L(E) = 3\pi x_L x_R \hat{\tilde{\mu}}_{LR}[J(E + \hat{N}\Omega)]^2, \tag{I.23}$$
$$\partial_E \hat{\Gamma}^L(E) = -12\pi x_L x_R \hat{\tilde{\mu}}_{LR} \frac{J(E + \hat{N}\Omega)^3}{E + i\Gamma(E + \hat{N}\Omega)}. \tag{I.24}$$

J. Optional approximations in the RG equations

In this appendix, we provide additional explanations and figures for the approximations of the RG equations, which are briefly discussed in section 6.1.

J.1. Reference energy scales

A subtle point in the comparison of results from different truncation orders is the definition of reference energy scales. For both leading and next-to-leading order truncation of the RG equations, we define all energies relative to T_K'' and T_K', respectively. To compare results from both truncation orders, we calculate T_K defined by $G(V_{\text{avg}} = T_K, V_{\text{osc}} = 0) = e^2/h$ for both cases. This yields the ratio $T_K''/T_K' \approx 2.94$ for which both methods agree on T_K, and which is used in the direct comparisons in section 6.1.

The other approximations discussed here are all based on the next-to-leading order truncation of the RG equations with the same reference energy scale T_K'. Since different approximations lead to different functions $G(V_{\text{avg}}, V_{\text{osc}} = 0)$, the ratio T_K/T_K' differs slightly between these methods. When neglecting $\hat{G}_{12}^a$, the estimate for T_K/T_K' is reduced by 4%. However, when we compare different approximations for the next-to-leading order RG equations, we use T_K' as a reference energy scale and not T_K. Here it is helpful that the results are not very sensitive to small changes of T_K' as long as the ratio $V(t)/\Omega$ is not affected.

J.2. Approximate frequency integral

In section 6.1.2 (figure 6.3), we have seen that the approximation of a frequency integral in the RG equations (discussed in section 4.3.4) leads only to very small deviations in the FRTRG results. To

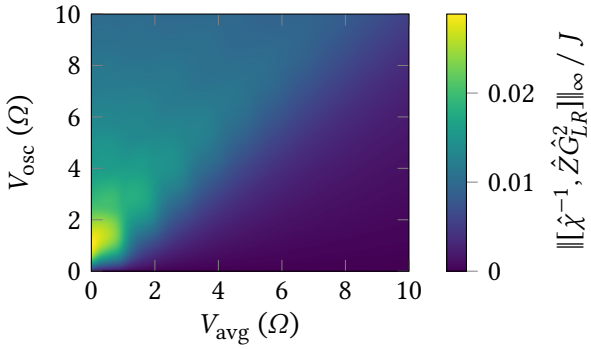

Figure J.1.: Largest matrix element of the commutator $[\hat{\chi}^{-1}, \hat{Z}\hat{G}_{12}^2]$ relative to the coupling J at the end of the RG flow ($E = 0$). Here, the matrix norm is defined by the largest matrix element in absolute value. The commutator of $\hat{\chi}^{-1}$ and $\hat{Z}\hat{G}_{12}^2$ is much smaller than the coupling J, such that it can be assumed that $\hat{\chi}^{-1}$ and $\hat{Z}\hat{G}_{12}^2$ approximately commute. Including energy shifts or $\hat{Z}$ in a different way (e.g., replacing $\hat{\chi}^{-1}$ by $\hat{R}$) does not qualitatively change the result.

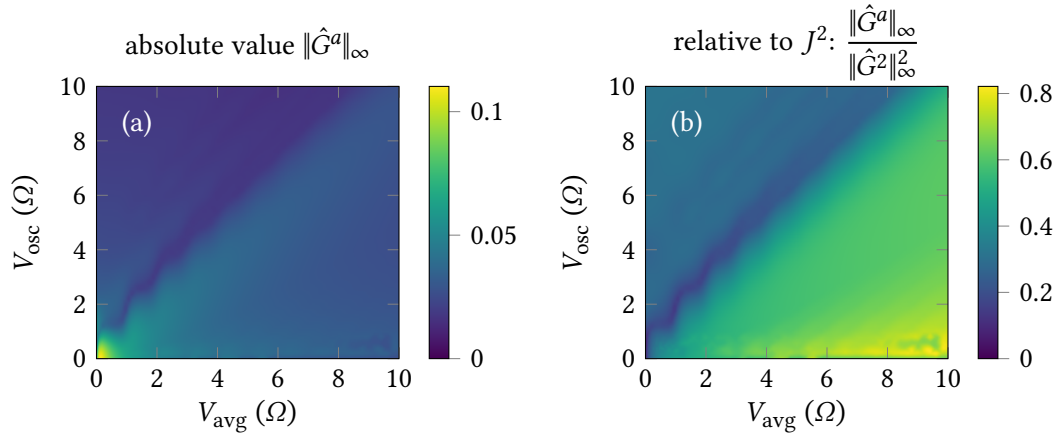

Figure J.2.: Largest matrix element $\|\hat{G}^a\|_\infty$ of $\hat{G}^a_{12}$ for $\Omega = 4.8T_K$ (a) as absolute number and (b) relative to $\|\hat{G}^2\|_\infty^2$. To answer the question whether $\hat{G}^a$ is negligible, we need to know whether $\hat{G}^a$ remains small compared to J^2. $\|\hat{G}^a\|_\infty \|\hat{G}^2\|_\infty^{-2}$ remains small in the interesting parameter regime $V_{\mathrm{avg}} \lesssim V_{\mathrm{osc}}$ and only becomes larger in the relatively boring regime $V_{\mathrm{avg}} \gg V_{\mathrm{osc}}$, far away from the region of photon-assisted tunneling with all interesting features in the differential conductance.

understand why the approximate solution of the integral is valid, we notice that the commutator $[\hat{R}, \hat{G}^2_{12}]$ is indeed small. The largest matrix element of this commutator is shown in figure J.1 and remains below $0.03J$ with the coupling defined by $J = \|\hat{G}^2\|_\infty$. This is clearly negligible for a term, which is only supposed to be correct to first order in J. Given that the resolvent $\hat{R}$ and the vertex $\hat{G}^2_{12}$ commute up to negligible higher-order terms, one can use that during most of the RG flow $\hat{\chi}(E)$ [defined in Eq. (4.56)] is a diagonal matrix with small corrections and the shifts by $\hat{\tilde{\mu}}_{12}$ are small. Under these assumptions, the approximation of the integral is justified.

J.3. Neglecting $\hat{G}^a$

Here we show why $\hat{G}^a$ has only a small influence on the results of the RG flow. We can use that we usually work with symmetric coupling to the two reservoirs ($x_L = x_R$), for which the RG equation (5.23) for $\hat{G}^a_{12}$ ensures that $\hat{G}^a_{12}$ is of the form $\hat{G}^a_{12} = (\delta_{1L} - \delta_{2R})\hat{G}^a_{LL}$ and the off-diagonal reservoir matrix elements $\hat{G}^a_{LR}$ and $\hat{G}^a_{RL}$ vanish exactly during the whole RG flow. As a consequence, $\hat{G}^a_{12}$ can only contribute to the off-diagonal reservoir matrix elements of $\hat{G}^2_{12}$, $\hat{G}^3_{12}$, and $\hat{I}^\gamma_{12}$.

The non-vanishing matrix elements of $\hat{G}^a_{12}$ also remain small during the RG flow. As shown in figure J.2, even the largest matrix elements of $\hat{G}^a_{12}$ always remain small compared to J^2 in the interesting parameter regime $V_{\mathrm{avg}} \lesssim V_{\mathrm{osc}}$. This estimate of $\hat{G}^a_{12}$ and the comparison of the result with and without $\hat{G}^a_{12}$ let us conclude that neglecting $\hat{G}^a_{12} \lesssim O(J^2)$ only leads to a deviation that is at most similar to an optimistic estimate of the overall accuracy of our method. However, neglecting $\hat{G}^a_{12}$ is an unnecessary simplification, since including it does not significantly increase the numerical or analytical effort required for setting up or solving the RG equations. In all results presented in this thesis, $\hat{G}^a_{12}$ is therefore included.

K. Notation

General notation in Liouville space

Symbol	Description	Reference
$\bullet$	argument of a superoperator, represents an arbitrary operator	
$\mathbb{1}$	identity operator or identity matrix	
$\mathbb{I}$	identity superoperator	
$\|x)$	Liouville space vector in Dirac notation, $\|x) = x$	below (2.1)
$(x\|$	Liouville space covector, $(x\| = \mathrm{tr}(x^\dagger \bullet)$	below (2.1)
$\mathcal{T}_{\leftarrow}, \mathcal{T}_{\rightarrow}$	time ordering, anti-time-ordering	
$\Pi(t, t_0)$	propagator (superoperator)	(2.6), (4.4)
$\rho(t)$	state of the local system at time t	
$\rho^{\mathrm{tot}}(t)$	total state including system and reservoirs at time t	
ρ_R^{eq}	equilibrium reservoir state	
$c^\dagger_{\alpha\sigma\omega}, c_{\alpha\sigma\omega}$	fermion creation/annihilation operators in the reservoirs	(2.4), (4.10)
$d^\dagger_\sigma, d_\sigma$	fermion creation/annihilation operators in the local system	
$\varrho_\alpha(\omega)$	density of states in reservoir α at energy ω	below (2.3)
H_S, L_S	Hamiltonian and Liouvillian of the local quantum system	
H_V, L_V	coupling Hamiltonian, Liouvillian	(2.5), (5.32)
H_R, L_R	reservoir Hamiltonian, Liouvillian	(2.3), (4.12)
$\mu_\alpha(t)$	chemical potential in reservoir α at time t	
T_α	temperature in reservoir α	
$\mathcal{J}_n(x)$	n^{th} Bessel function	

Indices

Symbol	Values	Description	Reference
α	usually L, R	reservoir index; in chapter 2 different bands and spin directions are treated like separate reservoirs	below (2.3)
σ	$\uparrow, \downarrow$	spin in z direction	
η	$\pm$	particle hole index in c_η: $c_+ = c^\dagger$, $c_- = c$	below (4.10)
ω	$\mathbb{R}$	reservoir energy level relative to the Fermi level	
q	$\pm$	superfermion causality index for $J^q_{\eta\alpha\omega}, G^q_\eta$	(2.43), (2.44)
p	$\pm$	Keldysh index of superoperators K_1^p	(4.11)

Fermionic duality

Symbol	Description	Reference
Γ	sum of all coupling rates	below (2.5)
N	fermion number operator on the local system	
$\mathcal{P}$	fermion parity superoperator $\mathcal{P} = (-\mathbb{1})^N \bullet$	section 2.1.3
$\bar{X}$	dual of X: replace $\mu_\alpha \mapsto -\mu_\alpha$, $H_S \mapsto -H_S$, and $H_V \mapsto iH_V$	below (2.2)
P_n	projector to subspace n of local system Hilbert space	section 2.3
$d_n = \operatorname{rank} P_n$	dimension of symmetry-protected subspace n	section 2.3
$\mathbb{P}_n = P_n \bullet P_n$	projector to subspace n in Liouville space	section 2.3
$\Pi_{nm}(t)$	propagator projected to $\mathbb{P}_n \Pi(t) \mathbb{P}_m$	section 2.3.1
$\Pi^{\mathrm{red}}(t)$	propagator projected on the symmetry sector	section 2.3.1
$K_i^{nm}(t)$, $\lambda_i^{nm}(t)$	normalized Kraus operators and their prefactors	(2.29)
$k(t)$, $g(t)$, $p(t)$	functions characterizing the resonant level model	(2.26)–(2.28)
$\mathcal{G}(t)$	time-local generator of the time evolution	(2.36)
$\mathcal{G}^H(t)$	time-local generator in the Heisenberg picture	(2.38)
$\mathcal{G}^{nm}(t)$	contribution of jumps from m to n in $\mathcal{G}(t)$	below (2.39)
$J_i^{nm}(t)$, $j_i^{nm}(t)$	normalized GKSL jump operators and jump rates	(2.39)
$\Pi_D(t,s)$	$\Pi(t)\Pi(s)^{-1}$, divisor in the Schrödinger picture	section 2.4
$\Pi_D^H(t,s)$	$\Pi^H(t)\Pi^H(s)^{-1}$, divisor in the Heisenberg picture	section 2.4
$J^q_{\eta\alpha\omega}$, G^q_η	superoperators for second quantization in Liouville space	(2.43), (2.44)

Periodically driven Kondo model

Symbol	Description	Reference
$\Omega = 2\pi/T$	driving frequency	
$V(t)$	time-periodic bias voltage $\mu_L(t) - \mu_R(t)$	
$V_{\mathrm{avg}}, V_{\mathrm{osc}}$	bias voltage $V(t) = V_{\mathrm{avg}} + V_{\mathrm{osc}} \cos(\Omega t)$	(3.16)
G, G_{osc}	differential conductance for direct and alternating current	
I_{avg}, I_{osc}	current, average and first harmonic	
T_K	Kondo temperature: $G(V_{\mathrm{avg}} = T_K, V_{\mathrm{osc}} = 0) = e^2/h$	(3.13), (3.15)
$\mathbf{S}$	local spin	(3.2)
$\boldsymbol{\sigma}$	vector of Pauli matrices (with matrix indices: $\boldsymbol{\sigma}_{\sigma\sigma'}$)	(3.2)
$J_0 = J^{(0)}$	bare coupling	(3.3)
x_α	asymmetry factor in the bare coupling	section 3.2.3
$\tilde{J}^{(0)}_{\alpha\alpha'}$	$= 2\sqrt{x_\alpha x_{\alpha'}} J^{(0)}$ bare coupling (reservoir matrix)	(3.3)
$D, D(\omega)$	bandwidth, cutoff function	(4.10)
φ	phase accumulated between the two reservoirs	section 3.4

Floquet real-time renormalization group

Symbol	Description	Reference
$1, 2, \ldots, n$	multi-indices: $1 = (\alpha_1, \sigma_1, \eta_1, \omega_1)$ or subset of these	section 4.2.3
$: \ldots :$	normal ordering of reservoir operators	below (4.13)
E	energy: complex Laplace variable and RG flow parameter	section 4.2.1
$\bar{\omega}_X, \hat{\bar{\mu}}_X$	$\bar{\omega}_{1\ldots} = \eta_1\omega_1 + \ldots$, analogous for $\hat{\bar{\mu}}_X$	below (4.20)
$\hat{E}_{12} = E - \hat{\bar{\mu}}_{12}$	shifted energy, Floquet matrix	below (4.49)
$\hat{N}_{nm} = n\delta_{nm}$	diagonal Floquet matrix	(4.3)
K_1^p	fermionic superoperators: $K_1^+ = c_1\bullet$, $K_1^- = \bullet c_1$	(4.11)
Δ	energy scale of the bias voltage, $\Delta \geq 0$	above (4.60)
$\tilde{E}$	renormalized energy scale: $\tilde{E} = E + i\Gamma(E) \in \mathbb{C}$	section 5.1.1
J	effective coupling, in the RG flow $J = \|\hat{G}^2\| > 0$	section 5.2.5
$\hat{\Pi}(E)$	propagator (Floquet matrix)	(4.6)
$\hat{L}(E)$	effective Liouvillian (Floquet matrix)	(4.7), (4.8)

Diagrammatic language

Symbol	Diagram	Description	Reference
$\hat{R}_X^{(0)}(E)$		bare resolvent	(4.20)
$\hat{R}(E)$, $\hat{R}_X(E)$		effective resolvent	(4.27), (4.28)
$\partial_E\hat{R}(E)$		derivative of effective resolvent	section 4.3.1
$\gamma_{11'}^{pp'}(\omega, \omega')$		reservoir contraction connecting indices 1 and 1′	(4.22)
$\gamma^{p'}(\eta\omega)$		reservoir contraction connecting indices 1 and $\bar{1}$	(4.22)
$\partial_\omega\gamma^p(\eta\omega)$		derivative of reservoir contraction	section 4.3.2
$G_{12}^{(0)pp'}$		bare coupling vertex	(4.14)
$\hat{G}_{12}^{pp'}(E)$		effective coupling vertex	(4.30)
$\partial_{\bar{\omega}_1}\hat{G}_{12}^{pp'}(E)$		derivative of effective coupling vertex	(4.39)
$\hat{G}_{1_0 2_0}^{pp'}(E)$		effective coupling vertex with $\omega_1 = \omega_2 = 0$	(4.30)
$\delta L(E)$		variation of $L(E)$	(4.73)

RG equations and initial conditions

Symbol	Description	Reference
$\delta\hat{\tilde{\mu}}_{12}$	infinitesimal variation of $\hat{\tilde{\mu}}_{12}$	section 4.3.7
$\breve{G}_{11'}$	coupling vertex summed over Keldysh indices, $1 = (\alpha, \sigma, \eta)$	section 4.3.5
$\bar{G}_{11'}$	$\breve{G}_{11'}$ with $\eta = +, \eta' = -$ and $1 = (\alpha, \sigma)$	section 4.3.5
$\hat{G}^2, \hat{G}^3, \hat{G}^a$	parametrization of the coupling vertex	(5.5)
$\bar{L}^{a,b}, L^{a,b,1,2,3}$	superoperator algebra	(5.6)–(5.7)
$I_{12}^{\gamma pp'}$	effective current vertex	(4.69)
$\bar{I}_{12}$	effective current vertex $\sum_{pp'} I_{12}^{pp'}$ with $\eta_1 = +, \eta_2 = -$	see $\bar{G}_{11'}$
$\hat{\bar{I}}_{11'}^{\gamma}(E)$	parametrization of $\bar{I}_{11'}^{\gamma}(E)$	(5.8)
$\hat{L}(E)$	effective Liouvillian	(4.8)
$\hat{\Gamma}(E)$	spin relaxation rate, parametrization of $L(E)$	(5.1)
$\hat{Z}(E)$	Z-function, Floquet matrix	(4.55)
$\hat{\chi}(E)$	needed in approximation of frequency dependence of $R_X(E)$	(4.56)
$\hat{\Sigma}_{\gamma}(E)$	current kernel	(4.68)
$\hat{\Gamma}^{\gamma}(E)$	parametrization of $\Sigma_{\gamma}(E)$	(5.2)
$\mathcal{J}^p[\cdots] = \mathcal{J}[\cdots]$	frequency integral, argument is a Floquet matrix	section 4.3.4
Λ_0	RG flow starts at $E = i\Lambda_0$	section 5.3
J, K, M	parametrization of $G_{12}^2, G_{12}^3, I_{12}^{\gamma}$ in equilibrium RG flow	(5.49)–(5.51)
T_K'	reference energy, integration constant of the RG equations	(5.63)
T_K''	reference energy of the leading order RG equations	(I.14)
$\mu_{\alpha}^{j}(t) + \mu_{\alpha}^{r}(t)$	splitting of $\mu(t)$: $\mu_{\alpha}^{j}(t)$ is transformed to coupling $\bar{J}_{\alpha\alpha'}(t)$	above (5.82)

Abbreviations

CP completely positive

FRTRG Floquet real-time renormalization group

GKSL Gorini, Kossakowski, Sudarshan, and Lindblad

ODE ordinary differential equation

RG renormalization group

RTRG real-time renormalization group

STM scanning tunneling microscope

Publications

[1] K. Nestmann, **V. Bruch**, and M. R. Wegewijs, "How quantum evolution with memory is generated in a time-local way", Phys. Rev. X **11**, 021041 (2021).

I contributed to the discussion of the stationary fixed point equation and of the resonant level model.

[2] **V. Bruch**, K. Nestmann, J. Schulenborg, and M. R. Wegewijs, "Fermionic duality: General symmetry of open systems with strong dissipation and memory", SciPost Phys. **11**, 053 (2021).

I did the calculations for general models. I contributed to writing the manuscript and to the calculations for the resonant level model.

[3] **V. Bruch**, M. Pletyukhov, H. Schoeller, and D. M. Kennes, "Floquet renormalization group approach to the periodically driven Kondo model", Phys. Rev. B **106**, 115440 (2022).

I did the calculations, implementation, and analysis of the results, and contributed to writing the manuscript.

Bibliography

[4] T. A. Fulton and G. J. Dolan, "Observation of single-electron charging effects in small tunnel junctions", Phys. Rev. Lett. **59**, 109–112 (1987).

[5] M. A. Kastner, "The single-electron transistor", Rev. Mod. Phys. **64**, 849–858 (1992).

[6] M. A. Kastner, "Artificial atoms", Phys. Today **46**, 24 (1993).

[7] R. C. Ashoori, "Electrons in artificial atoms", Nature **379**, 413–419 (1996).

[8] D. Goldhaber-Gordon, H. Shtrikman, D. Mahalu, D. Abusch-Magder, U. Meirav, and M. A. Kastner, "Kondo effect in a single-electron transistor", Nature **391**, 156–159 (1998).

[9] S. M. Cronenwett, T. H. Oosterkamp, and L. P. Kouwenhoven, "A Tunable Kondo Effect in Quantum Dots", Science **281**, 540–544 (1998).

[10] M. Bockrath, D. H. Cobden, P. L. McEuen, N. G. Chopra, A. Zettl, A. Thess, and R. E. Smalley, "Single-electron transport in ropes of carbon nanotubes", Science **275**, 1922–1925 (1997).

[11] J. Nygård, D. H. Cobden, and P. E. Lindelof, "Kondo physics in carbon nanotubes", Nature **408**, 342–346 (2000).

[12] M. R. Buitelaar, A. Bachtold, T. Nussbaumer, M. Iqbal, and C. Schönenberger, "Multiwall carbon nanotubes as quantum dots", Phys. Rev. Lett. **88**, 156801 (2002).

[13] B. Babaić, T. Kontos, and C. Schönenberger, "Kondo effect in carbon nanotubes at half filling", Phys. Rev. B **70**, 235419 (2004).

[14] P. Jarillo-Herrero, J. Kong, H. S. J. van der Zant, C. Dekker, L. P. Kouwenhoven, and S. De Franceschi, "Orbital Kondo effect in carbon nanotubes", Nature **434**, 484–488 (2005).

[15] J. Paaske, A. Rosch, P. Wölfle, N. Mason, C. M. Marcus, and J. Nygård, "Non-equilibrium singlet–triplet Kondo effect in carbon nanotubes", Nat. Phys. **2**, 460–464 (2006).

[16] J. Park, A. N. Pasupathy, J. I. Goldsmith, C. Chang, Y. Yaish, J. R. Petta, M. Rinkoski, J. P. Sethna, H. D. Abruña, P. L. McEuen, and D. C. Ralph, "Coulomb blockade and the Kondo effect in single-atom transistors", Nature **417**, 722–725 (2002).

[17] W. Liang, M. P. Shores, M. Bockrath, J. R. Long, and H. Park, "Kondo resonance in a single-molecule transistor", Nature **417**, 725–729 (2002).

[18] K. Yoshida, K. Shibata, and K. Hirakawa, "Terahertz field enhancement and photon-assisted tunneling in single-molecule transistors", Phys. Rev. Lett. **115**, 138302 (2015).

[19] R. Gaudenzi, M. Misiorny, E. Burzurí, M. R. Wegewijs, and H. S. J. van der Zant, "Transport mirages in single-molecule devices", J. Chem. Phys. **146**, 092330 (2017).

[20] C. Stampfer, E. Schurtenberger, F. Molitor, J. Güttinger, T. Ihn, and K. Ensslin, "Tunable graphene single electron transistor", Nano Lett. **8**, 2378–2383 (2008).

[21] L. A. Ponomarenko, F. Schedin, M. I. Katsnelson, R. Yang, E. W. Hill, K. S. Novoselov, and A. K. Geim, "Chaotic dirac billiard in graphene quantum dots", Science **320**, 356–358 (2008).

[22] C. Stampfer, J. Güttinger, S. Hellmüller, F. Molitor, K. Ensslin, and T. Ihn, "Energy gaps in etched graphene nanoribbons", Phys. Rev. Lett. **102**, 056403 (2009).

[23] J. Güttinger, F. Molitor, C. Stampfer, S. Schnez, A. Jacobsen, S. Dröscher, T. Ihn, and K. Ensslin, "Transport through graphene quantum dots", Rep. Prog. Phys. **75**, 126502 (2012).

[24] M. Eich, F. Herman, R. Pisoni, H. Overweg, A. Kurzmann, Y. Lee, P. Rickhaus, K. Watanabe, T. Taniguchi, M. Sigrist, T. Ihn, and K. Ensslin, "Spin and valley states in gate-defined bilayer graphene quantum dots", Phys. Rev. X **8**, 031023 (2018).

[25] L. Banszerus, B. Frohn, A. Epping, D. Neumaier, K. Watanabe, T. Taniguchi, and C. Stampfer, "Gate-defined electron–hole double dots in bilayer graphene", Nano Lett. **18**, 4785–4790 (2018).

[26] A. Kurzmann, H. Overweg, M. Eich, A. Pally, P. Rickhaus, R. Pisoni, Y. Lee, K. Watanabe, T. Taniguchi, T. Ihn, and K. Ensslin, "Charge detection in gate-defined bilayer graphene quantum dots", Nano Lett. **19**, 5216–5221 (2019).

[27] L. Banszerus, A. Rothstein, T. Fabian, S. Möller, E. Icking, S. Trellenkamp, F. Lentz, D. Neumaier, K. Watanabe, T. Taniguchi, F. Libisch, C. Volk, and C. Stampfer, "Electron–hole crossover in gate-controlled bilayer graphene quantum dots", Nano Lett. **20**, 7709–7715 (2020).

[28] L. Banszerus, S. Möller, E. Icking, C. Steiner, D. Neumaier, M. Otto, K. Watanabe, T. Taniguchi, C. Volk, and C. Stampfer, "Dispersive sensing of charge states in a bilayer graphene quantum dot", Appl. Phys. Lett. **118**, 093104 (2021).

[29] A. Kurzmann, Y. Kleeorin, C. Tong, R. Garreis, A. Knothe, M. Eich, C. Mittag, C. Gold, F. K. de Vries, K. Watanabe, T. Taniguchi, V. Fal'ko, Y. Meir, T. Ihn, and K. Ensslin, "Kondo effect and spin-orbit coupling in graphene quantum dots", Nat. Commun. **12**, 1–6 (2021).

[30] L. P. Kouwenhoven, A. T. Johnson, N. C. van der Vaart, C. J. P. M. Harmans, and C. T. Foxon, "Quantized current in a quantum-dot turnstile using oscillating tunnel barriers", Phys. Rev. Lett. **67**, 1626–1629 (1991).

[31] M. Switkes, C. M. Marcus, K. Campman, and A. C. Gossard, "An adiabatic quantum electron pump", Science **283**, 1905–1908 (1999).

[32] M. R. Buitelaar, V. Kashcheyevs, P. J. Leek, V. I. Talyanskii, C. G. Smith, D. Anderson, G. A. C. Jones, J. Wei, and D. H. Cobden, "Adiabatic charge pumping in carbon nanotube quantum dots", Phys. Rev. Lett. **101**, 126803 (2008).

[33] V. F. Maisi, Y. A. Pashkin, S. Kafanov, J.-S. Tsai, and J. P. Pekola, "Parallel pumping of electrons", New J. Phys. **11**, 113057 (2009).

[34] J. P. Pekola, O.-P. Saira, V. F. Maisi, A. Kemppinen, M. Möttönen, Y. A. Pashkin, and D. V. Averin, "Single-electron current sources: Toward a refined definition of the ampere", Rev. Mod. Phys. **85**, 1421–1472 (2013).

[35] P. W. Brouwer, "Scattering approach to parametric pumping", Phys. Rev. B **58**, R10135–R10138 (1998).

[36] G. Fève, A. Mahé, J.-M. Berroir, T. Kontos, B. Plaçais, D. C. Glattli, A. Cavanna, B. Etienne, and Y. Jin, "An on-demand coherent single-electron source", Science **316**, 1169–1172 (2007).

[37] M. D. Blumenthal, B. Kaestner, L. Li, S. Giblin, T. J. B. M. Janssen, M. Pepper, D. Anderson, G. Jones, and D. A. Ritchie, "Gigahertz quantized charge pumping", Nat. Phys. **3**, 343–347 (2007).

[38] B. Kaestner, C. Leicht, V. Kashcheyevs, K. Pierz, U. Siegner, and H. W. Schumacher, "Single-parameter quantized charge pumping in high magnetic fields", Appl. Phys. Lett. **94**, 012106 (2009).

[39] S. Hermelin, S. Takada, M. Yamamoto, S. Tarucha, A. D. Wieck, L. Saminadayar, C. Bäuerle, and T. Meunier, "Electrons surfing on a sound wave as a platform for quantum optics with flying electrons", Nature **477**, 435–438 (2011).

[40] R. P. G. McNeil, M. Kataoka, C. J. B. Ford, C. H. W. Barnes, D. Anderson, G. A. C. Jones, I. Farrer, and D. A. Ritchie, "On-demand single-electron transfer between distant quantum dots", Nature **477**, 439–442 (2011).

[41] M. Field, C. G. Smith, M. Pepper, D. A. Ritchie, J. E. F. Frost, G. A. C. Jones, and D. G. Hasko, "Measurements of Coulomb blockade with a noninvasive voltage probe", Phys. Rev. Lett. **70**, 1311–1314 (1993).

[42] D. Loss and D. P. DiVincenzo, "Quantum computation with quantum dots", Phys. Rev. A **57**, 120–126 (1998).

[43] G. Burkard, D. Loss, and D. P. DiVincenzo, "Coupled quantum dots as quantum gates", Phys. Rev. B **59**, 2070–2078 (1999).

[44] R. Hanson, B. Witkamp, L. M. K. Vandersypen, L. H. W. van Beveren, J. M. Elzerman, and L. P. Kouwenhoven, "Zeeman energy and spin relaxation in a one-electron quantum dot", Phys. Rev. Lett. **91**, 196802 (2003).

[45] A. Chatterjee, P. Stevenson, S. De Franceschi, A. Morello, N. P. de Leon, and F. Kuemmeth, "Semiconductor qubits in practice", Nat. Rev. Phys. **3**, 157–177 (2021).

[46] G. Burkard, T. D. Ladd, J. M. Nichol, A. Pan, and J. R. Petta, "Semiconductor spin qubits", accepted by Rev. Mod. Phys. (2021), arXiv:2112.08863 [cond-mat].

[47] S. Nakajima, "On quantum theory of transport phenomena", Prog. Theor. Phys. **20**, 948–959 (1958).

[48] R. Zwanzig, "Ensemble method in the theory of irreversibility", J. Chem. Phys. **33**, 1338–1341 (1960).

[49] J. Schwinger, "Brownian motion of a quantum oscillator", J. Math. Phys. **2**, 407–432 (1961).

[50] L. P. Kadanoff and G. Baym, *Quantum statistical mechanics, Green's function methods in equilibrium and nonequilibrium problems*, Frontiers in Physics: Lecture note and reprint series, A (W.A. Benjamin, 1962).

[51] R. P. Feynman and F. L. Vernon, "The theory of a general quantum system interacting with a linear dissipative system", Ann. Phys. **24**, 118–173 (1963).

[52] L. V. Keldysh, "Diagram technique for nonequilibrium processes", Sov. Phys. JETP **20**, 1018–1026 (1965).

[53] H. Schoeller and J. König, "Real-time renormalization group and charge fluctuations in quantum dots", Phys. Rev. Lett. **84**, 3686–3689 (2000).

[54] H. Schoeller, "An introduction to real-time renormalization group", Lect. Notes Phys. **544**, 137 (2000).

[55] H. Schoeller, "A perturbative nonequilibrium renormalization group method for dissipative quantum mechanics", Eur. Phys. J. Spec. Top. **168**, 179–266 (2009).

[56] H.-P. Breuer and F. Petruccione, *The theory of open quantum systems* (Oxford University Press, Oxford, England, UK, 2007).

[57] J. M. Thijssen and H. S. J. Van der Zant, "Charge transport and single-electron effects in nanoscale systems", Phys. Status Solidi B **245**, 1455–1470 (2008).

[58] K. G. Wilson and J. Kogut, "The renormalization group and the ε expansion", Phys. Rep. **12**, 75–199 (1974).

[59] L. P. Kadanoff, "Scaling laws for ising models near T_c", Physics Physique Fizika **2**, 263–272 (1966).

[60] K. G. Wilson, "Renormalization group and critical phenomena. I. Renormalization group and the Kadanoff scaling picture", Phys. Rev. B **4**, 3174–3183 (1971).

[61] L. P. Kadanoff, W. Götze, D. Hamblen, R. Hecht, E. A. S. Lewis, V. V. Palciauskas, M. Rayl, J. Swift, D. Aspnes, and J. Kane, "Static phenomena near critical points: Theory and experiment", Rev. Mod. Phys. **39**, 395–431 (1967).

[62] P. W. Anderson, G. Yuval, and D. R. Hamann, "Exact results in the Kondo problem. II. Scaling theory, qualitatively correct solution, and some new results on one-dimensional classical statistical models", Phys. Rev. B **1**, 4464–4473 (1970).

[63] P. W. Anderson, "A poor man's derivation of scaling laws for the Kondo problem", J. Phys. C: Solid State Phys. **3**, 2436–2441 (1970).

[64] K. G. Wilson, "The renormalization group: Critical phenomena and the Kondo problem", Rev. Mod. Phys. **47**, 773–840 (1975).

[65] S. Weinberg, *The quantum theory of fields, Volume II: Modern applications* (Cambridge University Press, Cambridge, England, UK, 1996).

[66] E. C. Stueckelberg and A. Petermann, "La normalisation des constantes dans la théorie des quanta", Helvetica Physica Acta **26**, 499–520 (1953).

[67] M. Gell-Mann and F. E. Low, "Quantum electrodynamics at small distances", Phys. Rev. **95**, 1300–1312 (1954).

[68] H. R. Krishna-murthy, J. W. Wilkins, and K. G. Wilson, "Renormalization-group approach to the Anderson model of dilute magnetic alloys. I. Static properties for the symmetric case", Phys. Rev. B **21**, 1003–1043 (1980).

[69] C. Wetterich, "Exact evolution equation for the effective potential", Phys. Lett. B **301**, 90–94 (1993).

[70] M. Salmhofer and C. Honerkamp, "Fermionic renormalization group flows, Technique and theory", Prog. Theor. Phys. **105**, 1–35 (2001).

[71] P. Kopietz and T. Busche, "Exact renormalization group flow equations for nonrelativistic fermions: Scaling toward the Fermi surface", Phys. Rev. B **64**, 155101 (2001).

[72] J. Berges, N. Tetradis, and C. Wetterich, "Non-perturbative renormalization flow in quantum field theory and statistical physics", Phys. Rep. **363**, 223–386 (2002).

[73] S. G. Jakobs, V. Meden, and H. Schoeller, "Nonequilibrium functional renormalization group for interacting quantum systems", Phys. Rev. Lett. **99**, 150603 (2007).

[74] M. Pletyukhov and H. Schoeller, "The nonequilibrium Kondo model: Crossover from weak to strong coupling", Phys. Rev. Lett. **108**, 260601 (2012).

[75] O. Kashuba and H. Schoeller, "Transient dynamics of open quantum systems", Phys. Rev. B **87**, 201402(R) (2013).

[76] F. Reininghaus, M. Pletyukhov, and H. Schoeller, "Kondo model in nonequilibrium: Interplay between voltage, temperature, and crossover from weak to strong coupling", Phys. Rev. B **90**, 085121 (2014).

[77] M. Bukov, L. D'Alessio, and A. Polkovnikov, "Universal high-frequency behavior of periodically driven systems: from dynamical stabilization to Floquet engineering", Adv. Phys. **64**, 139–226 (2015).

[78] T. Oka and S. Kitamura, "Floquet engineering of quantum materials", Annu. Rev. Condens. Matter Phys. **10**, 387–408 (2019).

[79] M. S. Rudner and N. H. Lindner, "Band structure engineering and non-equilibrium dynamics in Floquet topological insulators", Nat. Rev. Phys. **2**, 229–244 (2020).

[80] A. de la Torre, D. M. Kennes, M. Claassen, S. Gerber, J. W. McIver, and M. A. Sentef, "Colloquium: Nonthermal pathways to ultrafast control in quantum materials", Rev. Mod. Phys. **93**, 041002 (2021).

[81] J. M. Elzerman, S. De Franceschi, D. Goldhaber-Gordon, W. G. van der Wiel, and L. P. Kouwenhoven, "Suppression of the Kondo effect in a quantum dot by microwave radiation", J. Low Temp. Phys. **118**, 375–389 (2000).

[82] A. Kogan, S. Amasha, and M. A. Kastner, "Photon-Induced Kondo Satellites in a Single-Electron Transistor", Science **304**, 1293–1295 (2004).

[83] B. Hemingway, S. Herbert, M. Melloch, and A. Kogan, "Dynamic response of a spin-$\frac{1}{2}$ Kondo singlet", Phys. Rev. B **90**, 125151 (2014).

[84] L. E. Bruhat, J. J. Viennot, M. C. Dartiailh, M. M. Desjardins, A. Cottet, and T. Kontos, "Scaling laws of the Kondo problem at finite frequency", Phys. Rev. B **98**, 075121 (2018).

[85] J. Schulenborg, R. B. Saptsov, F. Haupt, J. Splettstoesser, and M. R. Wegewijs, "Fermion-parity duality and energy relaxation in interacting open systems", Phys. Rev. B **93**, 081411(R) (2016).

[86] J. Schulenborg, A. Di Marco, J. Vanherck, M. R. Wegewijs, and J. Splettstoesser, "Thermoelectrics of interacting nanosystems—Exploiting superselection instead of time-reversal symmetry", Entropy **19**, 668 (2017).

[87] J. Vanherck, J. Schulenborg, R. B. Saptsov, J. Splettstoesser, and M. R. Wegewijs, "Relaxation of quantum dots in a magnetic field at finite bias – Charge, spin, and heat currents", Phys. Status Solidi B **254**, 1600614 (2017).

[88] J. Schulenborg, "Dynamics of open fermionic nano-systems – a fundamental symmetry and its application to electron transport in interacting quantum dots", PhD thesis (Chalmers University of Technology, Göteborg, Sweden, 2018).

[89] J. Schulenborg, J. Splettstoesser, and M. R. Wegewijs, "Duality for open fermion systems: Energy-dependent weak coupling and quantum master equations", Phys. Rev. B **98**, 235405 (2018).

[90] J. Schulenborg, M. R. Wegewijs, and J. Splettstoesser, "Thermovoltage in quantum dots with attractive interaction", Appl. Phys. Lett. **116**, 243103 (2020).

[91] J. Monsel, J. Schulenborg, T. Baquet, and J. Splettstoesser, "Geometric energy transport and refrigeration with driven quantum dots", Phys. Rev. B **106**, 035405 (2022).

[92] L. C. Ortmanns, M. R. Wegewijs, and J. Splettstoesser, "Solution of master equations by fermionic-duality: Time-dependent charge and heat currents through an interacting quantum dot proximized by a superconductor", SciPost Phys. **14**, 095 (2023).

[93] **V. Bruch**, "Fermionic duality: dissipative symmetry for open systems dynamics beyond weak coupling", Master thesis (RWTH Aachen University, Aachen, Germany, 2019).

[94] G. C. Wick, A. S. Wightman, and E. P. Wigner, "The intrinsic parity of elementary particles", Phys. Rev. **88**, 101–105 (1952).

[95] G. C. Hegerfeldt, K. Kraus, and E. P. Wigner, "Proof of the fermion superselection rule without the assumption of time-reversal invariance", J. Math. Phys. **9**, 2029–2031 (1968).

[96] R. S. Whitney, "Non-Markovian quantum thermodynamics: Laws and fluctuation theorems", Phys. Rev. B **98**, 085415 (2018).

[97] E. C. G. Sudarshan, P. M. Mathews, and J. Rau, "Stochastic dynamics of quantum-mechanical systems", Phys. Rev. **121**, 920–924 (1961).

[98] K. Kraus, "General state changes in quantum theory", Ann. Phys. **64**, 311–335 (1971).

[99] V. Gorini, A. Kossakowski, and E. C. G. Sudarshan, "Completely positive dynamical semigroups of N-level systems", J. Math. Phys. **17**, 821–825 (1976).

[100] G. Lindblad, "On the generators of quantum dynamical semigroups", Commun. Math. Phys. **48**, 119–130 (1976).

[101] J. C. Cuevas and E. Scheer, *Molecular electronics: An introduction to theory and experiment*, Vol. 1, World Scientific Series In Nanoscience And Nanotechnology (World Scientific Publishing Company, Singapore, 2010).

[102] V. Reimer, M. R. Wegewijs, K. Nestmann, and M. Pletyukhov, "Five approaches to exact open-system dynamics: Complete positivity, divisibility, and time-dependent observables", J. Chem. Phys. **151**, 044101 (2019).

[103] R. B. Saptsov and M. R. Wegewijs, "Fermionic superoperators for zero-temperature nonlinear transport: real-time perturbation theory and renormalization group for Anderson quantum dots", Phys. Rev. B **86**, 235432 (2012).

[104] R. B. Saptsov and M. R. Wegewijs, "Time-dependent quantum transport: Causal superfermions, exact fermion-parity protected decay modes, and Pauli exclusion principle for mixed quantum states", Phys. Rev. B **90**, 045407 (2014).

[105] J. Schulenborg, J. Splettstoesser, M. Governale, and L. D. Contreras-Pulido, "Detection of the relaxation rates of an interacting quantum dot by a capacitively coupled sensor dot", Phys. Rev. B **89**, 195305 (2014).

[106] M. Tokuyama and H. Mori, "Statistical-mechanical approach to random frequency modulations and the Gaussian memory function", Prog. Theor. Phys. **54**, 918–920 (1975).

[107] M. Tokuyama and H. Mori, "Statistical-mechanical theory of random frequency modulations and generalized Brownian motions", Prog. Theor. Phys. **55**, 411–429 (1976).

[108] Á. Rivas, S. F. Huelga, and M. B. Plenio, "Entanglement and non-Markovianity of quantum evolutions", Phys. Rev. Lett. **105**, 050403 (2010).

[109] Á. Rivas, S. F. Huelga, and M. B. Plenio, "Quantum non-Markovianity: characterization, quantification and detection", Rep. Prog. Phys. **77**, 094001 (2014).

[110] Á. Rivas and S. F. Huelga, *Open quantum systems. An introduction* (Springer, Berlin, Heidelberg, 2012).

[111] H.-P. Breuer, E.-M. Laine, J. Piilo, and B. Vacchini, "Colloquium: Non-Markovian dynamics in open quantum systems", Rev. Mod. Phys. **88**, 021002 (2016).

[112] D. Chruściński and A. Kossakowski, "Markovianity criteria for quantum evolution", J. Phys. B: At. Mol. Opt. Phys. **45**, 154002 (2012).

[113] K. Nestmann and M. Wegewijs, "Renormalization group for open quantum systems using environment temperature as flow parameter", SciPost Phys. **12**, 121 (2022).

[114] K. Nestmann and M. R. Wegewijs, "General connection between time-local and time-nonlocal perturbation expansions", Phys. Rev. B **104**, 155407 (2021).

[115] L. I. Glazman and M. É. Raĭkh, "Resonant Kondo transparency of a barrier with quasilocal impurity states", JETP Lett. **47**, 452–455 (1988).

[116] T. K. Ng and P. A. Lee, "On-site Coulomb repulsion and resonant tunneling", Phys. Rev. Lett. **61**, 1768–1771 (1988).

[117] J. Schmid, J. Weis, K. Eberl, and K. V. Klitzing, "A quantum dot in the limit of strong coupling to reservoirs", Physica B **256-258**, 182–185 (1998).

[118] F. Simmel, R. H. Blick, J. P. Kotthaus, W. Wegscheider, and M. Bichler, "Anomalous Kondo Effect in a Quantum Dot at Nonzero Bias", Phys. Rev. Lett. **83**, 804–807 (1999).

[119] W. G. van der Wiel, S. De Franceschi, T. Fujisawa, J. M. Elzerman, S. Tarucha, and L. P. Kouwenhoven, "The Kondo effect in the unitary limit", Science **289**, 2105–2108 (2000).

[120] S. Sasaki, S. De Franceschi, J. M. Elzerman, W. G. van der Wiel, M. Eto, S. Tarucha, and L. P. Kouwenhoven, "Kondo effect in an integer-spin quantum dot", Nature **405**, 764–767 (2000).

[121] A. Kogan, G. Granger, M. A. Kastner, D. Goldhaber-Gordon, and H. Shtrikman, "Singlet–triplet transition in a single-electron transistor at zero magnetic field", Phys. Rev. B **67**, 113309 (2003).

[122] L. H. Yu and D. Natelson, "The Kondo effect in C_{60} single-molecule transistors", Nano Lett. **4**, 79–83 (2004).

[123] L. H. Yu, Z. K. Keane, J. W. Ciszek, L. Cheng, M. P. Stewart, J. M. Tour, and D. Natelson, "Inelastic electron tunneling via molecular vibrations in single-molecule transistors", Phys. Rev. Lett. **93**, 266802 (2004).

[124] P. Coleman, "Local moment physics in heavy electron systems", AIP Conf. Proc. **629**, 79–160 (2002).

[125] J. Kondo, "Resistance minimum in dilute magnetic alloys", Prog. Theor. Phys. **32**, 37–49 (1964).

[126] A. C. Hewson, *The Kondo problem to heavy fermions* (Cambridge University Press, Cambridge, England, UK, 1993).

[127] J. Li, W.-D. Schneider, R. Berndt, and B. Delley, "Kondo scattering observed at a single magnetic impurity", Phys. Rev. Lett. **80**, 2893–2896 (1998).

[128] V. Madhavan, W. Chen, T. Jamneala, M. F. Crommie, and N. S. Wingreen, "Tunneling into a single magnetic atom: Spectroscopic evidence of the Kondo resonance", Science **280**, 567–569 (1998).

[129] H. C. Manoharan, C. P. Lutz, and D. M. Eigler, "Quantum mirages formed by coherent projection of electronic structure", Nature **403**, 512–515 (2000).

[130] V. Madhavan, W. Chen, T. Jamneala, M. F. Crommie, and N. S. Wingreen, "Local spectroscopy of a Kondo impurity: Co on Au(111)", Phys. Rev. B **64**, 165412 (2001).

[131] K. Nagaoka, T. Jamneala, M. Grobis, and M. F. Crommie, "Temperature dependence of a single Kondo impurity", Phys. Rev. Lett. **88**, 077205 (2002).

[132] N. Knorr, M. A. Schneider, L. Diekhöner, P. Wahl, and K. Kern, "Kondo effect of single Co adatoms on Cu surfaces", Phys. Rev. Lett. **88**, 096804 (2002).

[133] M. A. Schneider, L. Vitali, N. Knorr, and K. Kern, "Observing the scattering phase shift of isolated Kondo impurities at surfaces", Phys. Rev. B **65**, 121406(R) (2002).

[134] A. F. Otte, M. Ternes, K. von Bergmann, S. Loth, H. Brune, C. P. Lutz, C. F. Hirjibehedin, and A. J. Heinrich, "The role of magnetic anisotropy in the Kondo effect", Nat. Phys. **4**, 847–850 (2008).

[135] A. F. Otte, M. Ternes, S. Loth, C. P. Lutz, C. F. Hirjibehedin, and A. J. Heinrich, "Spin excitations of a Kondo-screened atom coupled to a second magnetic atom", Phys. Rev. Lett. **103**, 107203 (2009).

[136] P. W. Anderson, "Localized magnetic states in metals", Phys. Rev. **124**, 41–53 (1961).

[137] J. R. Schrieffer and P. A. Wolff, "Relation between the Anderson and Kondo Hamiltonians", Phys. Rev. **149**, 491–492 (1966).

[138] M. Pustilnik and L. I. Glazman, "Kondo effect in quantum dots", J. Phys.: Condens. Matter **16**, R513 (2004).

[139] L. I. Glazman and M. Pustilnik, "Course 7 Low-temperature transport through a quantum dot", in *Nanophysics: Coherence and Transport*, Vol. 81, edited by H. Bouchiat, Y. Gefen, S. Guéron, G. Montambaux, and J. Dalibard, Les Houches (Elsevier, Amsterdam, 2005), pp. 427–478.

[140] P. Nozières, "A 'fermi-liquid' description of the Kondo problem at low temperatures", J. Low Temp. Phys. **17**, 31–42 (1974).

[141] P. B. Vigman, "Exact solution of $s - d$ exchange model at $T = 0$", JETP Lett. **31**, 364–370 (1980).

[142] N. Andrei, "Diagonalization of the Kondo Hamiltonian", Phys. Rev. Lett. **45**, 379–382 (1980).

[143] N. Andrei, K. Furuya, and J. H. Lowenstein, "Solution of the Kondo problem", Rev. Mod. Phys. **55**, 331–402 (1983).

[144] A. M. Tsvelick and P. B. Wiegmann, "Exact results in the theory of magnetic alloys", Adv. Phys. **32**, 453–713 (1983).

[145] R. M. Konik, H. Saleur, and A. W. W. Ludwig, "Transport through quantum dots: analytic results from integrability", Phys. Rev. Lett. **87**, 236801 (2001).

[146] R. M. Konik, H. Saleur, and A. Ludwig, "Transport in quantum dots from the integrability of the Anderson model", Phys. Rev. B **66**, 125304 (2002).

[147] T. A. Costi, A. C. Hewson, and V. Zlatic, "Transport coefficients of the Anderson model via the numerical renormalization group", J. Phys.: Condens. Matter **6**, 2519 (1994).

[148] W. Izumida, O. Sakai, and Y. Shimizu, "Kondo effect in single quantum dot systems – study with numerical renormalization group method –", J. Phys. Soc. Jpn. **67**, 2444–2454 (1998).

[149] A. Weichselbaum and J. von Delft, "Sum-rule conserving spectral functions from the numerical renormalization group", Phys. Rev. Lett. **99**, 076402 (2007).

[150] A. W. W. Ludwig and I. Affleck, "Exact, asymptotic, three-dimensional, space- and time-dependent, Green's functions in the multichannel Kondo effect", Phys. Rev. Lett. **67**, 3160–3163 (1991).

[151] I. Affleck and A. W. W. Ludwig, "Exact conformal-field-theory results on the multichannel Kondo effect: Single-fermion Green's function, self-energy, and resistivity", Phys. Rev. B **48**, 7297–7321 (1993).

[152] Y. Meir, N. S. Wingreen, and P. A. Lee, "Low-temperature transport through a quantum dot: The Anderson model out of equilibrium", Phys. Rev. Lett. **70**, 2601–2604 (1993).

[153] N. S. Wingreen and Y. Meir, "Anderson model out of equilibrium: Noncrossing-approx-i-mation approach to transport through a quantum dot", Phys. Rev. B **49**, 11040–11052 (1994).

[154] A. V. Kretinin, H. Shtrikman, D. Goldhaber-Gordon, M. Hanl, A. Weichselbaum, J. von Delft, T. Costi, and D. Mahalu, "Spin-$\frac{1}{2}$ Kondo effect in an InAs nanowire quantum dot: Unitary limit, conductance scaling, and Zeeman splitting", Phys. Rev. B **84**, 245316 (2011).

[155] A. V. Kretinin, H. Shtrikman, and D. Mahalu, "Universal line shape of the Kondo zero-bias anomaly in a quantum dot", Phys. Rev. B **85**, 201301(R) (2012).

[156] T.-K. Ng, "ac response in the nonequilibrium Anderson impurity model", Phys. Rev. Lett. **76**, 487–490 (1996).

[157] A. Schiller and S. Hershfield, "Solution of an ac Kondo model", Phys. Rev. Lett. **77**, 1821–1824 (1996).

[158] Y. Goldin and Y. Avishai, "Nonlinear Response of a Kondo System: Direct and Alternating Tunneling Currents", Phys. Rev. Lett. **81**, 5394–5397 (1998).

[159] A. Kaminski, Y. V. Nazarov, and L. I. Glazman, "Universality of the Kondo effect in a quantum dot out of equilibrium", Phys. Rev. B **62**, 8154–8170 (2000).

[160] R. López, R. Aguado, G. Platero, and C. Tejedor, "Kondo Effect in ac Transport through Quantum Dots", Phys. Rev. Lett. **81**, 4688–4691 (1998).

[161] M. H. Hettler and H. Schoeller, "Anderson model out of equilibrium: time-dependent perturbations", Phys. Rev. Lett. **74**, 4907–4910 (1995).

[162] A. Kaminski, Y. V. Nazarov, and L. I. Glazman, "Suppression of the Kondo Effect in a Quantum Dot by External Irradiation", Phys. Rev. Lett. **83**, 384–387 (1999).

[163] P. K. Tien and J. P. Gordon, "Multiphoton Process Observed in the Interaction of Microwave Fields with the Tunneling between Superconductor Films", Phys. Rev. **129**, 647–651 (1963).

[164] L. P. Kouwenhoven, S. Jauhar, J. Orenstein, P. L. McEuen, Y. Nagamune, J. Motohisa, and H. Sakaki, "Observation of photon-assisted tunneling through a quantum dot", Phys. Rev. Lett. **73**, 3443–3446 (1994).

[165] M. Grifoni and P. Hänggi, "Driven quantum tunneling", Phys. Rep. **304**, 229–354 (1998).

[166] M. Krawiec and K. I. Wysokiński, "Nonequilibrium Kondo effect in asymmetrically coupled quantum dots", Phys. Rev. B **66**, 165408 (2002).

[167] A.-P. Jauho, N. S. Wingreen, and Y. Meir, "Time-dependent transport in interacting and noninteracting resonant-tunneling systems", Phys. Rev. B **50**, 5528–5544 (1994).

[168] M. Keil and H. Schoeller, "Real-time renormalization-group analysis of the dynamics of the spin-boson model", Phys. Rev. B **63**, 180302(R) (2001).

[169] T. Korb, F. Reininghaus, H. Schoeller, and J. König, "Real-time renormalization group and cutoff scales in nonequilibrium applied to an arbitrary quantum dot in the Coulomb blockade regime", Phys. Rev. B **76**, 165316 (2007).

[170] N. Tsuji, T. Oka, and H. Aoki, "Correlated electron systems periodically driven out of equilibrium: Floquet+DMFT formalism", Phys. Rev. B **78**, 235124 (2008).

[171] B. H. Wu and J. C. Cao, "A Floquet–Green's function approach to mesoscopic transport under ac bias", J. Phys.: Condens. Matter **20**, 085224 (2008).

[172] B. H. Wu and J. C. Cao, "Noise of Kondo dot with ac gate: Floquet–Green's function and noncrossing approximation approach", Phys. Rev. B **81**, 085327 (2010).

[173] M. Genske and A. Rosch, "Floquet-Boltzmann equation for periodically driven Fermi systems", Phys. Rev. A **92**, 062108 (2015).

[174] A. K. Eissing, V. Meden, and D. M. Kennes, "Renormalization in Periodically Driven Quantum Dots", Phys. Rev. Lett. **116**, 026801 (2016).

[175] A. K. Eissing, V. Meden, and D. M. Kennes, "Functional renormalization group in Floquet space", Phys. Rev. B **94**, 245116 (2016).

[176] S. Mathey and S. Diehl, "Dynamic renormalization group theory for open Floquet systems", Phys. Rev. B **102**, 134307 (2020).

[177] G. Stefanucci, S. Kurth, A. Rubio, and E. K. U. Gross, "Time-dependent approach to electron pumping in open quantum systems", Phys. Rev. B **77**, 075339 (2008).

[178] R. P. Feynman, "Space-time approach to quantum electrodynamics", Phys. Rev. **76**, 769–789 (1949).

[179] N. M. Hugenholtz, "Quantum theory of many-body systems", Rep. Prog. Phys. **28**, 201 (1965).

[180] A. Altland and B. D. Simons, *Condensed matter field theory* (Cambridge University Press, Cambridge, UK, 2010).

[181] J. Paaske and K. Flensberg, "Vibrational Sidebands and the Kondo Effect in Molecular Transistors", Phys. Rev. Lett. **94**, 176801 (2005).

[182] J. J. Parks, A. R. Champagne, G. R. Hutchison, S. Flores-Torres, H. D. Abruña, and D. C. Ralph, "Tuning the Kondo effect with a mechanically controllable break junction", Phys. Rev. Lett. **99**, 026601 (2007).

[183] P. Wang, M. Heyl, and S. Kehrein, "Exact results for nonlinear ac transport through a resonant level model", J. Phys.: Condens. Matter **22**, 275604 (2010).

[184] M.-D. Choi, "Completely positive linear maps on complex matrices", Lin. Alg. Appl. **10**, 285–290 (1975).

[185] A. Jamiołkowski, "Linear transformations which preserve trace and positive semidefiniteness of operators", Rep. Math. Phys. **3**, 275–278 (1972).

[186] M. M. Wolf, *Quantum channels and operations – guided tour* (2012).

[187] J. H. Shirley, "Solution of the Schrödinger Equation with a Hamiltonian Periodic in Time", Phys. Rev. **138**, B979–B987 (1965).

Acknowledgments

I first wish to thank my supervisors, Dante Kennes and Maarten Wegewijs. You gave me the freedom and guidance that allowed me to follow my curiosity and has led me to interesting physical results.

The work on the real-time RG would not have been possible without inspiring discussions with Mikhail Pletyukhov and Herbert Schoeller. Some results for the real-time RG were inspired by discussions with Martin Maurer and Jens Paaske, and by the input from an anonymous referee of Ref. [3]. I am especially thankful to Andrei Kogan, Takis Kontos and Laure Bruhat for letting me use their measurement data that are shown in figures 3.5 and 3.6, and for interesting discussions. I acknowledge funding from the DFG through RTG 1995 and computation time provided by RWTH Aachen University.

An important source for inspiration were discussions with Konstantin Nestmann about many various, ranging from *E*-flow or *T*-flow RTRG to fermionic duality. The work on fermionic duality was furthermore inspired by discussions with Bassano Vacchini and Jens Schulenborg.

I very much enjoyed the inspiring atmosphere at the institute for quantum information and at the institute for statistical physics, to which so many people contributed that I will not list them all here. Thank you all!

Eidesstattliche Erklärung

Ich, Valentin Bruch, erkläre hiermit, dass diese Dissertation und die darin dargelegten Inhalte die eigenen sind und selbstständig, als Ergebnis der eigenen originären Forschung, generiert wurden.

Hiermit erkläre ich an Eides statt

1. Diese Arbeit wurde vollständig oder größtenteils in der Phase als Doktorand dieser Fakultät und Universität angefertigt;
2. Sofern irgendein Bestandteil dieser Dissertation zuvor für einen akademischen Abschluss oder eine andere Qualifikation an dieser oder einer anderen Institution verwendet wurde, wurde dies klar angezeigt;
3. Wenn immer andere eigene oder Veröffentlichungen Dritter herangezogen wurden, wurden diese klar benannt;
4. Wenn aus anderen eigenen oder Veröffentlichungen Dritter zitiert wurde, wurde stets die Quelle hierfür angegeben. Diese Dissertation ist vollständig meine eigene Arbeit, mit der Ausnahme solcher Zitate;
5. Alle wesentlichen Quellen von Unterstützung wurden benannt;
6. Wenn immer ein Teil dieser Dissertation auf der Zusammenarbeit mit anderen basiert, wurde von mir klar gekennzeichnet, was von anderen und was von mir selbst erarbeitet wurde;
7. Teile dieser Arbeit wurden zuvor veröffentlicht, und zwar in den Referenzen [2, 3].

Aachen, 19. Mai 2023
Valentin Bruch